Process and Network Level Optimization for High Salinity Brine Dewatering and Management

Submitted in partial fulfillment of the requirements for the

degree of

Doctor of Philosophy

in

Civil and Environmental Engineering

Timothy V Bartholomew

B.S., Chemical Engineering, Washington University in St. Louis
M.S., Civil and Environmental Engineering, Carnegie Mellon University

Carnegie Mellon University
Pittsburgh, PA

December, 2019

ACKNOWLEDGEMENTS

I would like to thank my funding sources. These include the James Sprauge Presidential Fellowship; Achievement Rewards for College Scientists (ARCS) Fellowship; Bradford and Diane Smith Graduate Fellowship; and appointments to the National Energy Technology Laboratory Professional Internship Program and Research Participation Program, sponsored by the U.S. Department of Energy and administered by the Oak Ridge Institute for Science and Education.

I feel fortunate to have had Dr. Meagan Mauter as my PhD advisor. I am grateful for the relationship we have developed over the course of my graduate degree and her unwavering dedication to my individual and professional development. I am especially thankful for the research and communication skills that she has instilled in me and I know I will carry them forward for the rest of my life.

I would like to thank my other thesis committee members including Dr. Jared Cohon, Dr. Ignacio Grossmann, and Dr. Nicholas Siefert for their guidance and advice over the years. Specifically, I would like to thank Ignacio for introducing me to optimization modeling and making several resources available to me. I would also like to thank Nick for our many discussions on dewatering technologies and for shaping my research to be relevant for the U.S. Department of Energy.

I would also like to thank many of my colleagues at Carnegie Mellon University who have not only supported my research but have also made life outside of research more enjoyable. Specifically, I would like to thank the graduate students in the chemical engineering department, Braulio Brunaud, David Bernal, Qi Chen, and Markus Drouven, who helped me when I had

questions about implementing and solving optimization models. I have had the privilege to work alongside my amazing colleagues and friends in the Water and Energy Efficiency for the Environment Lab (WE3 Lab), including: Conor Doherty, Alex Dudchenko, Daniel Gingerich, Niles Guo, Kathrin Kirchen, Xitong Liu, Yang Liu, Alex Newby, Sara Osipi, Amanda Quay, Sneha Shanbhag, and Paul Welle. The community we built as a research group is something that I will look back on fondly.

On a personal note, I would like to thank my family. I have been blessed with unconditional love and support from my parents, Mary and Vince Bartholomew. Without them I would not be who I am today. I also want to thank my brother Brian, who started me on the right track by teaching me some multiplication before kindergarten (I'm kidding, but not really). Lastly, I am forever grateful to my wife, Alexis Bartholomew, she has always been by my side and is easily the most significant person in my life.

ABSTRACT

High salinity brine management is an essential and costly activity for several activities, including oil and gas production, inland brackish water desalination, and geologic carbon storage. Currently most of these brines are managed with a disposal centric strategy, where the brines are minimally treated and directly disposed of via deep well injection. This common brine management strategy has several consequences including increased seismic activity and high transportation costs, energy use, and air emissions. An alternative to this brine management strategy is to dewater the brines to reduce the waste volume for transport and disposal. However, technologies that can dewater high salinity brines are generally considered prohibitively costly and energy intensive. This thesis seeks to determine the potential of brine dewatering technologies and strategies to decrease the overall cost and environmental impact of high salinity brine management.

In this thesis, the efforts to assess brine dewatering technologies and management strategies are organized across three objectives that span different scales. The first objective is to develop module-scale models for membrane-based technologies to accurately assess their dewatering performance for high salinity brines. The second objective is to develop process-scale cost optimization models that determine the technoeconomic feasibility of emerging membrane-based brine dewatering technologies. The third objective is to develop network-scale supply chain optimization models and spatially resolved analyses that identify low cost and environmental impact brine management strategies across the U.S.

A recurring theme in this thesis is that optimization modeling is a powerful tool for assessing the cost and performance of emerging dewatering technologies and strategies.

Specifically, when optimization methods are paired with detailed process modeling and sensitivity analyses, it is easier to overcome common barriers of performing a technoeconomic assessment. These barriers include: accurately modeling the separation performance at full-scale deployment, specifying the design and operation of a technology or strategy without experience or heuristics, and handling high levels of uncertainty in process and financial parameters. Throughout this thesis, detailed cost optimization models are developed to comprehensively assess the cost and performance of two emerging membrane-based brine dewatering technologies (osmotically assisted reverse osmosis and membrane distillation) and several brine management strategies for two high salinity brine applications (wastewater from shale gas production and extracted brine from geologic carbon storage).

TABLE OF CONTENTS

Acknowledgements ..... **iii**

Abstract ..... **v**

Table of Contents ..... **vii**

List of Tables ..... **x**

List of Figures and Illustrations ..... **xi**

1.0 Introduction **1**

1.1 Context 1
1.2 Overview of work 5
1.3 References 9

2.0 Computation Framework for Modeling Membrane Processes Without Process and Solution Property Simplifications **14**

2.1 Abstract 14
2.2 Introduction 14
2.3 Theory 17
2.4 Model development 23
2.5 Results and Discussion 36
2.6 Conclusions 48
2.7 Acknowledgements 49
2.8 Nomenclature 49
2.9 References 53

3.0 Osmotically Assisted Reverse Osmosis for High Salinity Brine Treatment **57**

3.1 Abstract 57
3.2 Introduction 57
3.3 Multi-staged osmotically assisted reverse osmosis process for water recovery 61
3.4 Methods 65
3.5 Results and Discussion 67
3.6 Conclusions 82
3.7 Acknowledgements 83
3.8 Nomenclature 83
3.9 References 85

4.0 Cost Optimization of Osmotically Assisted Reverse Osmosis.....90

4.1 Abstract.....90
4.2 Introduction.....90
4.3 Methods.....94
4.4 Results and Discussion.....101
4.5 Conclusions.....112
4.6 Acknowledgements.....113
4.7 References.....114

5.0 Membrane Distillation.....120

5.1 Abstract.....120
5.2 Introduction.....120
5.3 Methods.....123
5.4 Results and Discussion.....130
5.5 Conclusions.....141
5.6 Acknowledgements.....143
5.7 References.....143

6.0 Multi-Objective Optimization Model for Minimizing Cost and Environmental Impact in Shale Gas Water and Wastewater Management.....148

6.1 Abstract.....148
6.2 Introduction.....148
6.3 Methods.....150
6.4 Results and Discussion.....161
6.5 Conclusions.....167
6.6 Acknowledgements.....169
6.7 References.....171

7.0 Energy and CO_2 Emissions Penalties of Geologic Carbon Storage Brine Management 175

7.1 Abstract.....175
7.2 Introduction.....175
7.4 Results and discussion.....177
7.3 Conclusions.....190
7.4 Methods.....191
7.5 Acknowledgements.....195
7.6 References.....196

8.0 Summary and Conclusions.....202

8.1 Overview.....202
8.3 Recommendations for future work.....204

Appendices.....206
Appendix A: Supporting Information for Chapter 2 206
Appendix B: Supporting Information for Chapter 3.....223
Appendix C: Supporting Information for Chapter 4.....242
Appendix D: Supporting Information for Chapter 5 288
Appendix E: Supporting Information for Chapter 6.....318
Appendix F: Supporting Information for Chapter 7 359

LIST OF TABLES

Table 2.1 Case study parameter specifications for RO, OARO, FO, and PRO.....35

Table 2.2 Detailed process model results for the RO, OARO, FO, and PRO case studies 37

Table 3.1 User specified variables for the OARO base-case scenario 67

Table 4.1 Process and financial parameters for cost optimization model for OARO.....100

Table 5.1 Process and financial parameters for gap MD 129

Table 5.2 Cost optimal performance and financial metrics for the three gap configurations at the case study condition.....131

Table 5.3 Cost optimal design and operating variables for the three gap configurations at the case study.....134

Table 6.1 Description of the eight regulatory scenarios 160

Table 6.2 Costs of water and wastewater management activities for the three investigated objectives 164

Table 7.1. Salinity statistics for U.S. saline reservoirs 178

LIST OF FIGURES AND ILLUSTRATIONS

Figure 1.1 Overview of management activities for high salinity brines 2

Figure 2.1 Schematic of process configuration and concentration polarization for RO, OARO, PRO/FO 21

Figure 2.2 Finite difference model for hydraulic and osmotically driven membrane-based processes with five nodes and water flux profiles for a different number of nodes 25

Figure 2.3 Bulk concentration and water flux profiles along the stage for the 100 node finite difference model case studies 38

Figure 2.4 Accuracy of the n-node finite difference model relative to the 100 node model for the membrane process case studies 41

Figure 2.5 Effect of common simplifications on the accuracy of water flux estimates for the four membrane process case studies 45

Figure 3.1 Driving and retarding forces for RO, OARO, FO, PAFO, PRO 59

Figure 3.2 Process diagram of the OARO process 62

Figure 3.3 Schematic diagram of the OARO module and effects of concentration polarization 64

Figure 3.4 OARO module recovery with base case module dimensions 69

Figure 3.5 Recovery, number of modules, and energy consumption as a function of first inlet sweep concentration for the base-case module dimensions 72

Figure 3.6 The multi-module OARO process for the base-case scenario 74

Figure 3.7 Concentration profile of the feed and sweep cycles for the base case 75

Figure 3.8 First sweep concentration, number of modules, and energy consumption versus membrane area for set recoveries 77

Figure 3.9 First sweep concentration, number of modules, and energy consumption versus feed pressure for set recoveries 78

Figure 3.10 Energy consumption of RO, MVC, OARO processes and theoretical minimum work with respect to feed concentration and recovery 80

Figure 4.1 Unit water costs for RO, OARO, and MVC.....91

Figure 4.2 Process diagram of a RO and OARO system.....94

Figure 4.3 Cost-optimal unit water costs for OARO.....103

Figure 4.4 Cost-optimal concentration profile, flowrate profile, inlet feed pressure, and membrane area for OARO.....105

Figure 4.5 Cost-optimal design configurations and associated performance metrics for OARO/RO membrane-based desalination processes.....108

Figure 4.6 OARO cost sensitivity analysis.....111

Figure 5.1 Schematic of membrane distillation gap types and process configurations. 123

Figure 5.2 Case study cost optimal state variables for conductive gap MD 135

Figure 5.3 Cost optimal LCOW, design, and operating variables for conductive gap MD.....138

Figure 5.4 Cost sensitivity for conductive gap MD.....141

Figure 6.1 Simplified superstructure of shale gas FW and WW management, a case study supply chain network, and the buried and overland pipelines for the cost-optimal water management scenario.....152

Figure 6.2. Frac fluid use for the 14 wellpads in the case study.....161

Figure 6.3. Financial cost optimal water management air emissions and associated HHE costs for each pollutant.....165

Figure 6.4. Financial and HHE costs associated with air emissions for the financial cost-optimal solution and the constrained scenarios.....167

Figure 7.1 Geologic Carbon Storage Brine Characteristics of U.S. Saline Reservoirs 181

Figure 7.2 Estimated Energy Consumption of Geologic Carbon Storage Brine Management ...185

Figure 7.3. Brine management energy and emission penalties for brine management cases.....188

1.0 INTRODUCTION

1.1 Context

Recent trends, including the growing wastewater production from the oil and gas industry,[1] the increasing demand for potable water from inland brackish water desalination,[2] and the rising potential for regulations that require zero liquid wastewater discharge and geologic carbon storage,[3-4] contribute to the critical need to manage high salinity brines (>75 g/L TDS) at low cost and low environmental impact. Currently, the oil and gas industry is the largest source of high salinity brines, and the industry predominantly manages the wastewater with minimal treatment and direct disposal via injection wells or reuse.[5] This disposal-centric brine management strategy has been linked to increased seismic activity due to brine subsurface injection and high transportation costs, energy use, and air emissions.[6-8] These consequences are reduced with brine reuse practices which are becoming increasingly common for the oil and gas industry in some regions of the U.S.[1, 9] However, reuse will have limited opportunities for the other sources of high salinity brines, such as the concentrated waste from inland brackish water desalination and extracted brines from geologic carbon storage. Further, even in the oil and gas industry, the extent of reuse is limited by the water use for drilling and hydraulic fracturing and inevitably there will be times when wastewater production exceeds the demand for reuse.

The components of brine production and management are shown in Figure 1.1. If high salinity brines are treated and dewatered, the brine volume that is transported and disposed of is reduced and a high-quality product water is produced. Generally, this strategy has not been preferred because the pretreatment and dewatering of the brines is costly.[10] However, there have been recent developments and plans for commercial scale facilities for high salinity brine

dewatering.[11] This thesis seeks to assess the potential of brine dewatering strategies by addressing two questions: 1) What dewatering technologies are most cost effective across a broad range of brine salinities and water recoveries? and 2) What impact would dewatering strategies have on the overall cost and environmental impact of high salinity brine management?

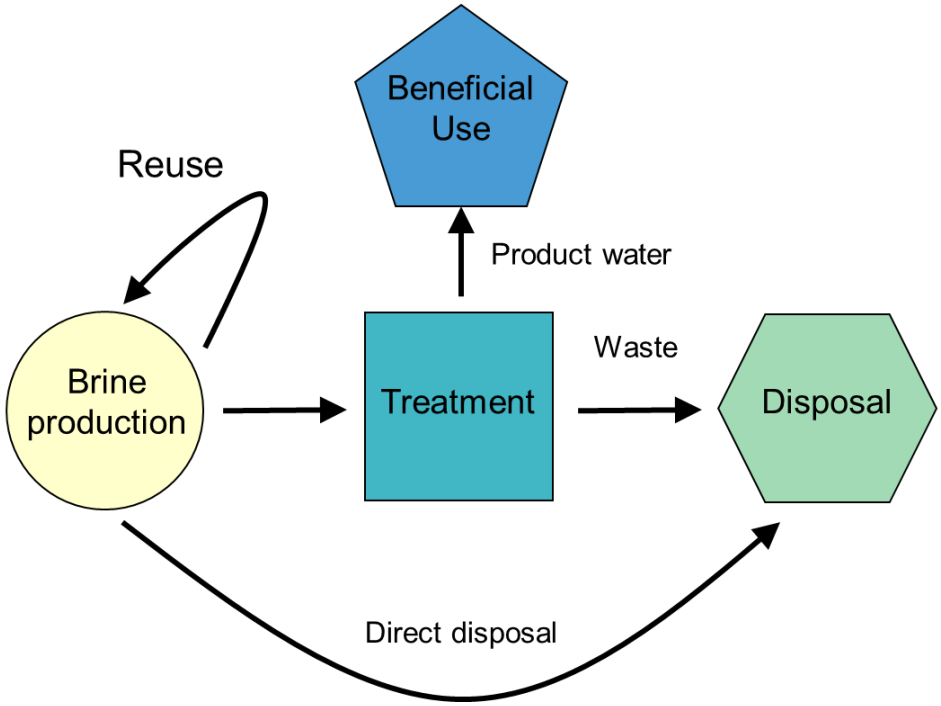

Figure 1.1. *Overview of management activities for high salinity brines (>75 g/L TDS)*

Review of current and emerging brine dewatering technologies

The two major categories of dewatering technologies are evaporative and non-evaporative. Evaporative dewatering technologies can achieve high water recoveries from high salinity brines, but they are generally considered to have high energy consumption and costs. The mature evaporative technologies are multi-stage flash distillation (MSF), multi-effect distillation (MED), and mechanical vapor compression (MVC).[12-13]

Non-evaporative technologies are generally less costly and energy intensive than evaporative technologies, but they have limited or no effectiveness for high salinity brines. The mature non-evaporative technologies are reverse osmosis (RO) and electrodialysis (ED).[2, 14-15] While RO is the predominant seawater desalination technology due to its relatively low cost and energy consumption, the process is physically limited by the membrane burst pressure and typical RO operation does not concentrate brines above 70-75 g/L TDS.[16] ED is generally used at low salinities (<10 g/L TDS) and is not cost competitive at higher salinities due to parasitic energy loss and cost of ion-exchange membranes.[17]

This thesis investigates two emerging membrane-based technologies that have the potential to lower the energy consumption and cost of high salinity brine dewatering, membrane distillation (MD) and osmotically assisted reverse osmosis (OARO). MD is an evaporative process that may reduce costs because it can be operated at a temperature lower than the boiling point.[18] OARO is a non-evaporative process that can effectively dewater high salinity brines at a lower energy consumption than evaporative processes.[19-20] Both emerging membrane technologies have not been deployed at the commercial scale because of remaining questions about their technoeconomic feasibility. Specifically, it is not known if the technologies would be cost competitive and perform reliably at scale.

Barriers to assessing the technoeconomic feasibility of emerging high salinity brine dewatering technologies and management strategies

There are a few critical barriers to estimating the performance and cost of emerging dewatering technologies and management strategies. These barriers include: 1) creating models that accurately predict performance at full-scale deployment, 2) specifying the design and operation of the technology or strategy without experience or heuristics, 3) handling the high

uncertainty that is inherent in emerging technologies and strategies for both process and financial parameters.

The first barrier of developing accurate models is challenging because of the need to balance simplicity with complexity. Simple models are more computationally efficient and easier to interpret, while complex models may be more accurate. In general, technoeconomic assessments for membrane-based technologies use one dimensional models that explicitly calculate the state and process variables along the module.[21-24] These models are popular because they account for the decreasing driving force along the module. Some models in the literature simplify the process even further by estimating the separation performance by averaging the state and process variables.[25-26] While inlet-outlet modeling provides less detail and is likely less accurate, the models have reduced computational demand. Similarly, researchers use common process and solution property simplifications to reduce computational demand, such as no salt flux, no pressure drop, ideal solution, constant solution properties (e.g. density, diffusivity, viscosity, specific heat), and constant heat and mass transfer coefficients. Despite their common use, the literature lacks a quantitative discussion of the errors introduced by these simplifications. Further, the rationale for using these common simplifications has been greatly reduced due to advances in computational processing speed and the efficiency of algorithms (e.g. the solver CONOPT).[27]

The second barrier of specifying the design and operation of the emerging technologies is challenging because they are characterized by large decision spaces with complex tradeoffs. Traditionally, technoeconomic assessments vary one to three design and operating variables to assess the effect on the outcome metrics (e.g. energy consumption, levelized cost of water production). This approach requires the decision space to be reduced to a few variables and

assumes they are decoupled, which greatly limits the relevance of the results. Optimization modeling can more appropriately address a large decision space because it does not require the design and operating variables to be set in advance. Instead, optimization approaches determine the optimal design and operation and balance complex tradeoffs associated with capital and operating costs which greatly enhances the relevance of the technoeconomic assessment. This type of approach has been applied to several dewatering technologies; examples include: RO,[25-26, 28] MVC,[29] MED[30], and direct contact MD.[31] However, there is a need to assess other high salinity membrane-based dewatering technologies like OARO and other types of MD. While optimization approaches have also been used extensively to assess oil and gas wastewater management strategies,[9, 32-35] they have been generally limited to crude dewatering modeling with fixed water recovery and do not consider human health impacts associated with the water management activities.

The third barrier of handling the uncertainty in parameters for emerging high salinity dewatering technologies and strategies is challenging because the relatively high uncertainty can span a wide range of results and conclusions. The uncertainty for these emerging processes can be high because there is little to no available data on their performance in the field. The most appropriate ways to address this uncertainty for a technoeconomic assessment are parametric sensitivity analyses to describe the trends associated with the parameter and stochastic simulation (e.g. Monte Carlo) that can develop distributions of the results. These types of analyses can more appropriately give ranges for the technoeconomic results and identify the key parameters that need to be further investigated.

1.2 Overview of work

The main goal of this thesis is to quantify the costs, benefits, and tradeoffs of using dewatering technologies for high salinity brine management. This thesis is composed of three objectives that cover different scales of high salinity brine dewatering and management. The first objective is to develop module-scale models for membrane-based technologies that accurately predict the separation performance for high salinity brines. The second objective is to develop process-scale cost optimization models that determine the technoeconomic feasibility of emerging membrane-based brine dewatering processes. The third objective is to develop network-scale supply chain optimization models and spatially resolved analyses that identify low cost and environmental impact brine management strategies across the U.S.

Chapter 2 addresses the first objective by developing detailed module-scale models for hydraulic and osmotic pressure driven membrane technologies. These models avoid using common simplifications found in the literature, including approximations for the process (i.e. no salt flux, no pressure drop) and for the solution properties (i.e. ideal solution, and constant density, viscosity, and diffusivity). We then leverage these models to quantify the errors introduced by these simplifications. We find that some of these common approximations in the literature can under or overestimate the average water flux across the module by up to 50% at typical operating conditions. Additionally, this chapter assesses the accuracy of less detailed inlet-outlet models and proposes novel formulations that can have greater accuracy when describing non-linear water flux profiles.

Chapter 3 addresses the second objective by developing a process-scale model for osmotically assisted reverse osmosis (OARO). This chapter is the first work that describes and models the OARO process, which is a novel membrane-base technology for dewatering high salinity brines. Our model determines the technical feasibility of the OARO process by

determining the water recovery and energy consumption for a range of feed salinities. We find that the OARO process can dewater high salinity brines (up to 150 g/L TDS) with 35-50% water recovery at a lower energy consumption than mechanical vapor compression, the leading high salinity brine dewatering technology.

Chapter 4 expands beyond the work in chapter 3 by developing a cost optimization model for OARO. The model synthesizes the complex decision space of the novel technology and minimizes the levelized cost of water across a wide range of feed salinities and water recoveries. We find that the OARO process could cost between $3 and $15 per m^3 and could be economically feasible for some high salinity brine dewatering applications. We also develop generalizable guidelines for low cost design and operation and estimate the value of process improvements, such as increasing the membrane water permeability or the burst pressure.

Chapter 5 also addresses the second objective by developing a process-scale cost optimization model for membrane distillation. As in chapter 4, we use the model to comprehensively assess the technoeconomic feasibility of the process for a broad range of potential dewatering applications. We estimate that gap membrane distillation can dewater high salinity brines with costs ranging from $6 to $10 per m^3 of product water. Besides extracting generalizable guidelines for low cost design and operation and assessing the sensitivity of parameters, this work also emphasizes the strong effect salinity has on MD process performance and costs, which is often understated in MD literature.

Chapter 6 addresses the third objective at the network-scale by leveraging a multiobjective optimization model to assess the tradeoffs between cost and environmental impact for various brine management strategies. The model expands beyond the previous chapters that investigated dewatering processes by accounting for additional brine management activities,

such as, freshwater acquisition, wastewater production, transport, storage, and scheduling. This model is the first optimization model for oil and gas wastewater management that includes the human health impacts of air emissions from the brine management activities. In the chapter, we demonstrate the usefulness of the model by applying it to a case study of shale gas extraction in the Marcellus play and quantify the effects of various potential regulations on the financial and human health and environmental costs.

Chapter 7 also addresses the third objective at the network-scale by analyzing several brine management strategies for geologic carbon storage (GCS) across the U.S. This work estimates the energy and emission penalties of GCS brine management by spatially integrating data sources on CO_2 emission sources, CO_2 storage reservoirs, and brine salinity and using stochastic simulation. We find that the median energy penalty ranges from 4.4 to 35 kWh/tonne of CO_2 stored across three brine management strategies with different extents of dewatering. These estimates suggest that brine management dominates the energy consumption of post-capture CO_2 storage and that brine management should be a top consideration when designing a CO_2 storage system.

Chapter 8 summarizes the key findings and conclusions of the presented work, as well as providing recommendations for future research.

1.3 References

1. *Hydraulic Fracturing for Oil and Gas: Impacts from the Hydraulic Fracturing Water Cycle on Drinking Water Resources in the United States (Final Report).* Environmental Protection Agency: U.S.A, Washington, DC, 2016.

2. Elimelech, M.; Phillip, W. A., The Future of Seawater Desalination: Energy, Technology, and the Environment. *Science* **2011,** *333* (6043), 712.

3. Tong, T.; Elimelech, M., The Global Rise of Zero Liquid Discharge for Wastewater Management: Drivers, Technologies, and Future Directions. *Environmental Science & Technology* **2016,** *50* (13), 6846-6855.

4. Arena, J. T.; Jain, J. C.; Lopano, C. L.; Hakala, J. A.; Bartholomew, T. V.; Mauter, M. S.; Siefert, N. S., Management and dewatering of brines extracted from geologic carbon storage sites. *International Journal of Greenhouse Gas Control* **2017,** *63*, 194-214.

5. Veil, J. A. *U.S. Produced Water Volumes and Management Practices in 2012*; Ground Water Protection Council: Oklahoma City, Oklahoma, 2015.

6. Ellsworth, W. L., Injection-Induced Earthquakes. *Science* **2013,** *341* (6142).

7. Behrer, A. P.; Mauter, M. S., Allocating Damage Compensation in a Federalist System: Lessons from Spatially Resolved Air Emissions in the Marcellus. *Environmental Science & Technology* **2017,** *51* (7), 3600-3608.

8. Litovitz, A.; Curtright, L.; Abramzon, S.; Burger, N.; Samaras, C., Estimation of regional air-quality damages from Marcellus Shale natural gas extraction in Pennsylvania. *Environmental Research Letters* **2013,** *8* (1), 014017.

9. Yang, L.; Grossmann, I. E.; Manno, J., Optimization Models for Shale Gas Water Management. *Aiche J* **2014,** *60* (10), 3490-3501.

10. Shaffer, D. L.; Arias Chavez, L. H.; Ben-Sasson, M.; Romero-Vargas Castrillon, S.; Yip, N. Y.; Elimelech, M., Desalination and reuse of high-salinity shale gas produced water: drivers, technologies, and future directions. *Environ Sci Technol* **2013,** *47* (17), 9569-83.

11. Veolia to build, operate water treatment plant for Antero Resources. *Pump Industry Analyst* **2015,** *2015* (10), 3.

12. Al-Sahali, M.; Ettouney, H., Developments in thermal desalination processes: Design, energy, and costing aspects. *Desalination* **2007,** *214* (1), 227-240.

13. Thiel, G. P.; Tow, E. W.; Banchik, L. D.; Chung, H. W.; Lienhard V, J. H., Energy consumption in desalinating produced water from shale oil and gas extraction. *Desalination* **2015,** *366*, 94-112.

14. Ghaffour, N.; Missimer, T. M.; Amy, G. L., Technical review and evaluation of the economics of water desalination: Current and future challenges for better water supply sustainability. *Desalination* **2013,** *309*, 197-207.

15. Xu, T.; Huang, C., Electrodialysis-based separation technologies: A critical review. *Aiche J* **2008,** *54* (12), 3147-3159.

16. Fritzmann, C.; Löwenberg, J.; Wintgens, T.; Melin, T., State-of-the-art of reverse osmosis desalination. *Desalination* **2007,** *216* (1), 1-76.

17. Fakhru'l-Razi, A.; Pendashteh, A.; Abdullah, L. C.; Biak, D. R. A.; Madaeni, S. S.; Abidin, Z. Z., Review of technologies for oil and gas produced water treatment. *Journal of Hazardous Materials* **2009,** *170* (2), 530-551.

18. Deshmukh, A.; Boo, C.; Karanikola, V.; Lin, S.; Straub, A. P.; Tong, T.; Warsinger, D. M.; Elimelech, M., Membrane distillation at the water-energy nexus: limits, opportunities, and challenges. *Energy & Environmental Science* **2018,** *11* (5), 1177-1196.

19. Bartholomew, T. V.; Mey, L.; Arena, J. T.; Siefert, N. S.; Mauter, M. S., Osmotically assisted reverse osmosis for high salinity brine treatment. *Desalination* **2017,** *421*, 3-11.

20. Chen, X.; Yip, N. Y., Unlocking High-Salinity Desalination with Cascading Osmotically Mediated Reverse Osmosis: Energy and Operating Pressure Analysis. *Environmental Science & Technology* **2018,** *52* (4), 2242-2250.

21. Banchik, L. D.; Weiner, A. M.; Al-Anzi, B.; Lienhard V, J. H., System scale analytical modeling of forward and assisted forward osmosis mass exchangers with a case study on fertigation. *Journal of Membrane Science* **2016,** *510*, 533-545.

22. Davenport, D. M.; Deshmukh, A.; Werber, J. R.; Elimelech, M., High-Pressure Reverse Osmosis for Energy-Efficient Hypersaline Brine Desalination: Current Status, Design Considerations, and Research Needs. *Environmental Science & Technology Letters* **2018**.

23. Deshmukh, A.; Yip, N. Y.; Lin, S.; Elimelech, M., Desalination by forward osmosis: Identifying performance limiting parameters through module-scale modeling. *Journal of Membrane Science* **2015,** *491*, 159-167.

24. Straub, A. P.; Lin, S.; Elimelech, M., Module-Scale Analysis of Pressure Retarded Osmosis: Performance Limitations and Implications for Full-Scale Operation. *Environmental Science & Technology* **2014,** *48* (20), 12435-12444.

25. Vince, F.; Marechal, F.; Aoustin, E.; Bréant, P., Multi-objective optimization of RO desalination plants. *Desalination* **2008,** *222* (1), 96-118.

26. Lu, Y.-Y.; Hu, Y.-D.; Zhang, X.-L.; Wu, L.-Y.; Liu, Q.-Z., Optimum design of reverse osmosis system under different feed concentration and product specification. *Journal of Membrane Science* **2007,** *287* (2), 219-229.

27. Drud, A. S., CONOPT—A Large-Scale GRG Code. *ORSA Journal on Computing* **1994,** *6* (2), 207-216.

28. Marcovecchio, M. G.; Aguirre, P. A.; Scenna, N. J., Global optimal design of reverse osmosis networks for seawater desalination: modeling and algorithm. *Desalination* **2005,** *184* (1), 259-271.

29. Onishi, V. C.; Carrero-Parreño, A.; Reyes-Labarta, J. A.; Fraga, E. S.; Caballero, J. A., Desalination of shale gas produced water: A rigorous design approach for zero-liquid discharge evaporation systems. *Journal of Cleaner Production* **2017,** *140,* 1399-1414.

30. Onishi, V. C.; Carrero-Parreño, A.; Reyes-Labarta, J. A.; Ruiz-Femenia, R.; Salcedo-Díaz, R.; Fraga, E. S.; Caballero, J. A., Shale gas flowback water desalination: Single vs multiple-effect evaporation with vapor recompression cycle and thermal integration. *Desalination* **2017,** *404,* 230-248.

31. Carrero-Parreño, A.; Onishi, V. C.; Ruiz-Femenia, R.; Salcedo-Díaz, R.; Caballero, J. A.; Reyes-Labarta, J. A., Optimization of multistage membrane distillation system for treating shale gas produced water. *Desalination* **2019,** *460,* 15-27.

32. Yang, L.; Grossmann, I. E.; Mauter, M. S.; Dilmore, R. M., Investment optimization model for freshwater acquisition and wastewater handling in shale gas production. *Aiche J* **2015,** *61* (6), 1770-1782.

33. Lira-Barragán, L. F.; Ponce-Ortega, J. M.; Serna-González, M.; El-Halwagi, M. M., Optimal reuse of flowback wastewater in hydraulic fracturing including seasonal and environmental constraints. *Aiche J* **2016,** *62* (5), 1634-1645.

34. Gao, J.; You, F., Optimal design and operations of supply chain networks for water management in shale gas production: MILFP model and algorithms for the water-energy nexus. *Aiche J* **2015,** *61* (4), 1184-1208.

35. Guerra, O. J.; Calderón, A. J.; Papageorgiou, L. G.; Siirola, J. J.; Reklaitis, G. V., An optimization framework for the integration of water management and shale gas supply chain design. *Computers & Chemical Engineering* **2016,** *92*, 230-255.

2.0 COMPUTATIONAL FRAMEWORK FOR MODELING MEMBRANE PROCESSES WITHOUT PROCESS AND SOLUTION PROPERTY SIMPLIFICATIONS

2.1 Abstract

Accurately modeling membrane processes is critical to evaluating novel process configurations, designing scalable membrane systems, informing process cost estimates, and directing future research. Most membrane process models trade accuracy for computational efficiency by employing simplified approximations of the process (i.e. no salt flux, no pressure drop) and solution properties (i.e. ideal solution, and constant density, viscosity, and diffusivity). This work presents a detailed one-dimensional finite difference model for evaluating membrane processes that avoids these common simplifications. We apply this model to quantify the error introduced by these simplifications for case studies of reverse osmosis, osmotically assisted reverse osmosis, forward osmosis, and pressure retarded osmosis. While the magnitude of error introduced by these simplifications is dependent on the case study parameters and specifications, we find that existing model formulations can underestimate or overestimate average water flux by nearly 50% for some membrane processes operating under standard conditions. Finally, we investigate the error introduced by simplified inlet-outlet models that do not solve the governing system of differential equations, and we assess the accuracy of novel inlet-outlet formulations that use a log and geometric mean, instead of the typical arithmetic mean, to represent non-linear water flux profiles.

2.2 Introduction

Computational models are essential to describing and predicting the performance of pressure and osmotically driven membrane based processes, but the modeling framework and

embedded assumptions used to describe these membrane processes vary widely. For example, some models provide simple point estimates of water flux,[1] while others use two and three dimensional computational fluid dynamics models to estimate membrane performance.[2-3] As a result, there is often significant deviation in performance estimates between process models, and few models exhibit high experimental fidelity across a range of process conditions. Shortcomings in these performance models can obscure high impact research needs for technology development, inhibit direct comparisons between processes or process configurations, impede technology scale up from the lab and facilitate sustained research in non-competitive technologies.

Detailed one-dimensional process models relate the design, operating, state, and process variables of a membrane stage using a system of differential equations. When these models are solved for a given design and operating condition, the solution describes the profiles of variables along the membrane stage (e.g. solute concentration, flow rate, water flux, etc.) and provides estimates of the overall process performance (e.g. water recovery, average water flux, pressure drop, salt passage, etc.). These stage-level process models can also be integrated into systems-scale models to estimate and optimize other key metrics like net energy consumption and cost.[4]

These detailed process models of reverse osmosis (RO) assume that the permeate side of the membrane has a negligible impact on the driving force and solve this system of differential equations using traditional ordinary differential equation solvers (e.g. Runge-Kutta method and its modified forms).[5] For counterflow membrane processes, such as osmotically assisted reverse osmosis (OARO),[4, 6-7] forward osmosis (FO),[8-9] and pressure retarded osmosis (PRO),[10] the system of differential equations is implicit and cannot be solved with traditional differential equation solvers. Instead this system of differential equations is commonly approximated using

a finite difference approach and solved using numerical methods (e.g. Newton's method and trust-region methods).[10] The accuracy of the finite difference approximation is dependent on the number of finite nodes, which are typically increased until there is little change between the nth and nth plus one solutions.

In contrast to detailed process models that solve for the profiles of variables along the length of the module, simplified inlet-outlet models estimate the overall process performance by averaging the inlet and outlet values of the variables.[11-12] For instance, an arithmetic mean of the inlet and outlet of a variable could be used to precisely represent the average value of a variable with a linear profile. This formulation preserves the key decision variables and reduces the number of variables and equations, making it attractive for use in optimization models.

The accuracy of the arithmetic mean inlet-outlet model solution breaks down, however, if there is low fidelity between the actual and assumed linear profile of the variables along the length of the module. For example, many membrane processes exhibit non-linear water flux profiles. The average of these non-linear profiles may be more accurately represented with a log or geometric mean, where the average is more heavily weighted to the lower values. This weighting reflects the common shape of non-linear water flux profiles in membrane processes, but we are unaware of previous work applying these means to inlet-outlet modeling formulations for membrane systems.

In addition to assumptions embedded in the modeling structure, most detailed process models and simplified inlet-outlet models make several additional simplifying assumptions about the process and solution properties. Common simplifications include no salt flux across the membrane, no pressure drop across the length of the stage, ideal solution properties, and constant density, viscosity, and solute diffusion coefficient (diffusivity). While these simplifications

reduce the computational demand of the models, most studies do not perform a sensitivity analysis or quantitatively assess the error introduced by these simplifications. Further, even though a more accurate representation without the common simplifications may not be essential for clarifying a specific phenomenon in membrane separation processes, accurate water fluxes are important when assessing the techno-economic feasibility of membrane technologies.

The present work formulates detailed process models and simplified inlet-outlet models for RO, OARO, FO, and PRO membrane processes that do not employ common simplifications for the process and solution properties described above. We use these models to quantify the error associated with each simplification. We also investigate the effect of assumptions embedded in modeling structure by assessing the impact of the number of nodes on the accuracy of the finite difference approximation method. Finally, we propose and assess the accuracy of novel simplified inlet-outlet models that use either a log or a geometric mean, as opposed to the traditional arithmetic mean, to determine the average water flux.

2.3 Theory

Water and salt flux

Water and salt transport in pressure driven membrane processes are generally described by Eq. 2.1 and 2.2.

$$Jw = A(\Delta P - \Delta\pi) \quad (2.1)$$

$$Js = B\,\Delta C \quad (2,2)$$

Where Jw is the water flux [m^3/m^2-h], A is the water permeability coefficient [m/bar-h], ΔP (Pf-Pp) is the hydraulic pressure difference [bar], $\Delta\pi$ (πf-πp) is the osmotic pressure difference [bar], Js is the salt flux [kg/m^2-h], B is the salt permeability coefficient [m/h], and ΔC (Cf-Cp) is

the salt concentration difference [kg/m^3 or g/L]. The direction of the water and salt flux is defined as from the feed (f) to the permeate (p) side. For the specified flux direction, the salt flux is positive for RO and OARO and is negative for FO and PRO. These water and salt flux equations assume the effect of the reflection coefficient in the Spiegler-Kedem model is negligible (i.e. a value of 1),[13] which is typical for membranes with high salt rejection and low salt permeability.[14-15] If the reflection coefficient is substantially less than 1, as is common in nanofiltration membranes or solutions with poorly rejected solutes, then our model will underestimate the water flux for hydraulically driven processes (RO, OARO) and overestimate the water flux osmotically (FO, PRO) driven processes.[14, 16]

Solution properties

The osmotic pressure is a function of the salt concentration, as shown in Eq. 2.3a.

$$\pi = i\,\phi\,C\,\frac{1}{MW}\,R\,T \qquad (2.3a)$$

Where π is the osmotic pressure [bar], i is the number of dissociating ions [-], ϕ is the osmotic coefficient [-], C is the salt concentration [g/L], MW is the molecular weight [g/mol], R is the gas constant [8.314E-2 L-bar/mol-K], and T is the temperature [K]. When the solution is assumed to be ideal, the osmotic coefficient (ϕ) is 1. In this work, we assume the solute is NaCl and the temperature is 25°C and we account for non-ideal behavior by modeling the osmotic coefficient as a function of concentration.[17] We determine the osmotic coefficient function from a quadratic fit of experimental results, observing close agreement (less than 1% or 0.1 bar) to a more detailed osmotic coefficient relationship presented in Mistry and Lienhard 2013.[17-19] The osmotic pressure of a NaCl solution as a function of only concentration is presented in Eq. 2.3b.

$$\pi = K\,\phi(C)\,C = 0.848\,(3.14E\text{-}6\,\mathrm{C}^2 + 2.13E\text{-}4\,\mathrm{C} + 0.917)\,C \qquad (2.3b)$$

Where K is the lumped constants in Eq. 2.3a (i.e. $i\ R\ T/MW$) and $\phi(C)$ is the osmotic coefficient as a function of concentration.

In addition to osmotic pressure, other key solution properties are a function of salt concentration or mass fraction, including: density, viscosity, and diffusivity, as shown in Eq. 2.4-2.6. We determine these relationships from polynomial fits of NaCl solution property tables.[18, 20-21] Additional details on the osmotic pressure, density, viscosity, and diffusivity are included in SI Section S1.

$$\rho = 756\,X + 995 \tag{2.4}$$

$$\mu = 2.15E\text{-}3\,X + 9.80E\text{-}4 \tag{2.5}$$

$$D = 153\,X^4 - 122\,X^3 + 30.1\,X^2 - 2.00\,X + 1.51 \tag{2.6}$$

Where ρ is the density [kg/m^3 or g/L], μ is the viscosity [Pa-s], D is the diffusivity [1E-9 m^2/s], and X is the salt mass fraction [kg of solute/kg of solution]. The salt concentration is related to the density and salt mass fraction as shown in Eq. 2.7.

$$C = \rho\,X\ = 756\,X^2 + 995\,X \tag{2.7}$$

Concentration polarization

The concentration and osmotic pressure difference in Eq. 2.1 and 2.2 are evaluated at the membrane interface. The qualitative relationship between the concentration at the membrane interface and bulk concentration for RO, OARO, FO, and PRO on both the feed and permeate side are shown in Figure 2.1. When internal and external concentration polarization are accounted for with steady state film theory, the quantitative relationship between the feed and permeate side concentration at the membrane interface and bulk concentration are determined in

Eq. 2.8 and 2.9. For all membrane processes, we assume the porous support is on the side with low pressure (i.e. permeate side for RO, OARO, and FO and feed side for PRO).

$$Cm_f = Cb_f \exp\left(\frac{Jw}{k_f}\right) - \frac{Js}{Jw}\left(\exp\left(\frac{Jw}{k_f}\right) - 1\right) \quad (2.8a)$$

$$Cm_f = Cb_f \exp\left(Jw\left[\frac{1}{k_f} + \frac{S}{D}\right]\right) - \frac{Js}{Jw}\left(\exp\left(Jw\left[\frac{1}{k_f} + \frac{S}{D}\right]\right) - 1\right) \quad (2.8b)$$

$$Cm_p = Cb_p \exp\left(-Jw\left[\frac{S}{D} + \frac{1}{k_p}\right]\right) + \frac{Js}{Jw}\left(1 - \exp\left(-Jw\left[\frac{S}{D} + \frac{1}{k_p}\right]\right)\right) \quad (2.9a)$$

$$Cm_p = Cb_p \exp\left(-\frac{Jw}{k_p}\right) + \frac{Js}{Jw}\left(1 - \exp\left(-\frac{Jw}{k_p}\right)\right) \quad (2.9b)$$

Where Eq. 2.8a and 2.9a are valid for processes with the porous support on the permeate side (i.e. RO, OARO, and FO) and Eq. 2.8b and 2.9b are valid for processes with the porous support on the feed side (i.e. PRO). The concentrations are subscripted for the side, feed (f) and permeate (p), and location, membrane interface (m) and bulk (b). The external concentration polarization on each side is modeled with the mass transfer coefficient, k, [m/h]. We assume that internal and external concentration polarization on the permeate side is negligible for RO. The internal concentration polarization is modeled with the structural parameter, S, [m] and diffusion coefficient of the solute, D, [m^2/s]. These concentration polarization relationships are similar to other work on the individual processes.[4, 22-24] However, differences may arise due to the specified direction of the salt flux. The derivations of these relationships are included in SI section S.2.

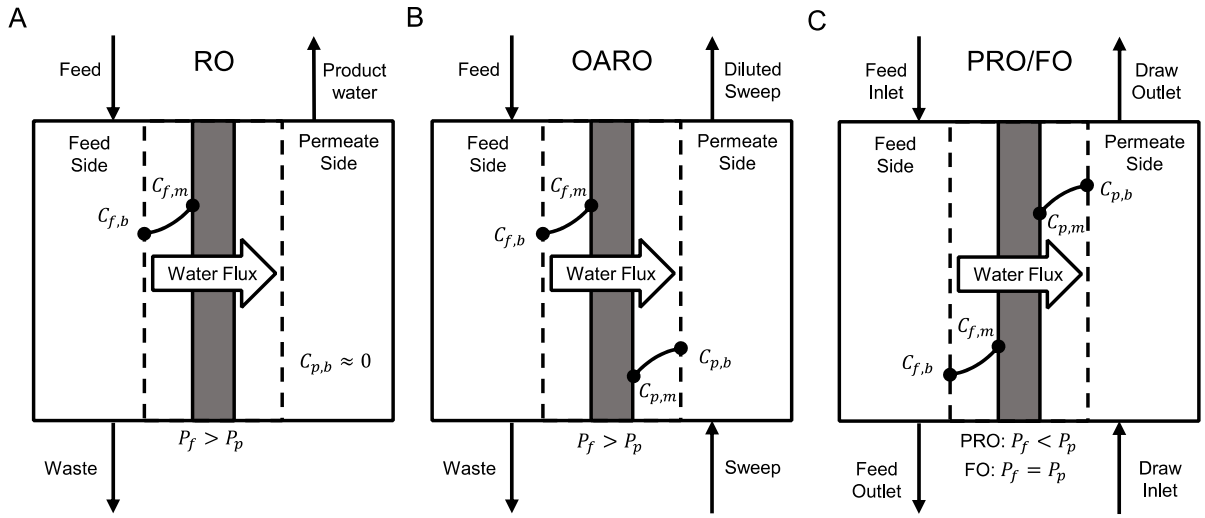

Figure 2.1. *Schematic of process configuration and concentration polarization for A) RO, B) OARO, C) PRO/FO. The relationship between the feed and permeate-side concentration (Cf, Cp) in the bulk (b) and at the membrane interface (m) is noted within the boundary layer (dotted line). An inequality indicates whether the feed or permeate-side hydraulic pressure (Pf, Pp) is greater. We assume that the membrane porous support is on the side with the lower hydraulic pressure and on the draw-side for FO.*

The mass transfer coefficient, k, is determined by Eq. 2.10.

$$k = \frac{D\ Sh}{d_h} \tag{2.10}$$

Where Sh is the Sherwood number [-] and d_h is the hydraulic diameter [m]. The Sherwood number is a dimensionless number that is a function of the Reynolds (Re) and Schmidt (Sc) number. We estimate the Sherwood number with Eq. 2.11, which was developed from computational fluid dynamic simulations of mesh filled rectangular channels.[25] The definition of the hydraulic diameter is shown in Eq. 2.12 and is determined based on channel dimensions and mesh configuration as described further in SI Section S3.

$$Sh = 0.46(Re\ Sc)^{0.36} \quad (2.11)$$

$$d_h = \frac{4\ (flow\ area)}{(wetted\ perimeter)} \quad (2.12)$$

Pressure drop

In addition to the water and salt flux, another key phenomenon is the pressure drop across the membrane stage. The pressure loss per unit length can be determined by Eq. 2.13.

$$PL = \frac{F\ \rho\ v^2}{2\ d_h}\ \left[\frac{1\ bar}{1E5\ Pa}\right] \quad (2.13)$$

Where PL is the pressure loss per unit length [bar/m], F is the friction factor [-], ρ is the fluid density [kg/m^3], v is the fluid velocity [m/s]. For both the pressure drop and Reynolds number calculations, the fluid velocity is the average axial velocity determined from the fluid flowrate, channel cross-sectional area, and mesh void space. F is approximated in Eq. 2.14 by a correlation developed for a simulated mesh filled channel.[25] The presented α and β parameters are for a filament with a circular cross section and effective cross-section of 25% (diameter of filament/height of channel).

$$F = \alpha + \frac{\beta}{Re} = 0.42 + \frac{189.3}{Re} \quad (2.14)$$

Governing system of equations

The governing system of differential equations for a one-dimensional model is composed of mass transfer and pressure drop equations shown in Eq. 2.15-2.20.

$$\frac{dM_f}{dz} = -(Jw\ \rho w + Js)\ W \quad (2.15)$$

$$\frac{d(M_f\ X_f)}{dz} = -Js\ W \quad (2.16)$$

$$\frac{dM_p}{dz} = (Jw\ \rho w + Js)\ W \quad (2.17)$$

$$\frac{d(M_p\ X_p)}{dz} = Js\ W \quad (2.18)$$

$$\frac{dP_f}{dz} = \text{-}PL_f \quad (2.19)$$

$$\frac{dP_p}{dz} = \text{-}PL_p \quad (2.20)$$

Where M, X, and P are the state variables: mass flow rate [kg/h], salt mass fraction [-], and hydraulic pressure [bar], respectively, for the feed (f) and permeate (p) side; Jw, Js, and PL are the process variables: water flux [m^3/m^2-h or LMH], salt flux [kg/m^2-h], and pressure loss [bar/m], respectively; z is the dimension along the length of membrane [m]; and ρw is the density of water [kg/m^3]. z is defined such that z=0 at the inlet (e.g. $M_f(0) = M_{f_{in}}, M_p(0) = M_{p,in}$) and z=$L$, the stage length, at the outlet (e.g. $M_f(L) = M_{f,out}$, $M_p(L) = M_{p,out}$). Note that the process variables (i.e. Jw, Js, PL) are functions of the state variables as described in the preceding section. The initial conditions of this system of differential equations are the specified inlet values for the state variables. The solution of the system of differential equations provides the profiles of the state and process variables along the stage, which can be used to extract key metrics, including: average water and salt flux, water recovery, salt passage, and feed and permeate side outlet flow rate, concentration, and pressure drop.

2.4 Model development

Detailed process model

We develop a detailed process model based on the finite difference approximation of the governing system of equations (Eq. 2.15-2.20). This finite difference approach discretizes the

membrane stage into a series of nodes (Fig. 2.2). At each node, the state variables (i.e. flow rate, concentration, and pressure) and process variables (i.e. water flux, salt flux, and pressure drop) are evaluated. The process model spans the level of detail presented in section 2.3, where solution properties are a function of concentration and mass transfer coefficients and friction factors are determined from dimensionless numbers (i.e. Reynolds, Schmidt) that vary along the stage. The solution of this model provides the key performance metrics (i.e. average water flux, water recovery, and pressure drop) and the one-dimensional profiles of the state and process variables along the stage for a specified case.

We formulated and specified the detailed process model with the following specifications and assumptions. First, we formulate the model on a mass basis instead of a volumetric basis. The volumetric basis is the most common approach for membrane models that assume constant density. However, when density is modeled as a function of concentration, the volumetric balance does not satisfy conservation of mass. Second, we make several assumptions that are consistent with our previous work regarding the design and operation of the membrane process.[4] Specifically, we assume:

- The solute is NaCl and the non-ideal solution osmotic pressure matches experimental results.[17]
- The membrane units have a flat plate geometry with counter-current flow and are composed of an asymmetric membrane with the porous support on the low hydraulic pressure-side.
- The mass transfer coefficient and pressure drop are adequately estimated by Sherwood number and friction factor correlations that were developed by Guillen and Hoek (2009) from simulations on channels with a mesh spacer.[25] Despite the limitations of this study,

including assumptions of constant solution properties, isolated filaments, and a Reynolds number between 10-400, these are currently the best available correlations relevant to membrane channels with a mesh.

- The continuous membrane dimensions, length and width, adequately represent a membrane stage that may be comprised of multiple modules in series and parallel.
- The outlet hydraulic pressure is 1 bar for the non-pressurized streams.

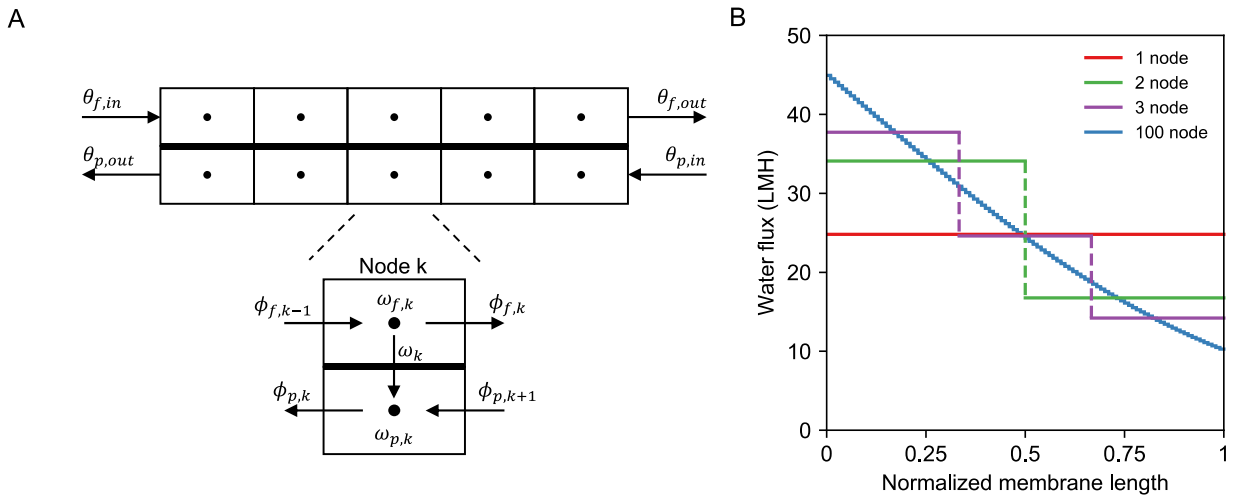

Figure 2.2. *A) Finite difference model for hydraulic and osmotically driven membrane-based processes with five nodes. Θ are inlet and outlet stage variables that include: mass flowrate, mass fraction, and hydraulic pressure. Φ are inter-node variables that include: mass flowrate, mass fraction, and pressure loss. ω are nodal variables that include: bulk concentration, concentration at the membrane interface, hydraulic and osmotic pressure, and water and salt flux. B) Water flux profiles for a different number of nodes. Water flux values are representative of the RO case study for a feed of 35 g/L TDS with 50% water recovery. Additional details are provided in Section 2.4.*

The finite difference approximations of the governing mass transfer equations (Eq. 2.15-2.18) are shown in Eq. 2.21-2.32.

$$M_{f,k} = M_{f,k-1} - \frac{Amem}{N}\ (Jw_k\ \rho_w + Js_k) \quad \forall k, k \neq k1 \tag{2.21}$$

$$M_{f,k}X_{f,k} = M_{f,k-1}X_{f,k-1} - \frac{Amem}{N}\ Js_k \quad \forall k, k \neq k1 \tag{2.22}$$

$$M_{f,k1} = M_{f,in} - \frac{Amem}{N}(\ Jw_{k1}\ \rho_w + Js_{k1}) \tag{2.23}$$

$$M_{f,k1}M_{f,k1} = M_{f,in}X_{f,in} - \frac{Amem}{N}\ Js_{k1} \tag{2.24}$$

$$M_{f,out} = M_{f,kN} \tag{2.25}$$

$$X_{f,out} = X_{f,kN} \tag{2.26}$$

$$M_{p,k} = M_{p,k+1} + \frac{Amem}{N}\ (Jw_k\ \rho_w + Js_k) \quad \forall k, k \neq kN \tag{2.27}$$

$$M_{p,k}X_{p,k} = M_{p,k+1}X_{p,k+1} + \frac{Amem}{N}\ Js_k \quad \forall k, k \neq kN \tag{2.28}$$

$$M_{p,kN} = M_{p,in} + \frac{Amem}{N}\ (Jw_{kN}\ \rho_w + Js_{kN}) \tag{2.29}$$

$$M_{p,kN}X_{p,kN} = M_{p,in}X_{p,in} + \frac{Amem}{N}\ Js_{kN} \tag{2.30}$$

$$M_{p,out} = M_{p,k1} \tag{2.31}$$

$$X_{p,out} = X_{p,k1} \tag{2.32}$$

Where $Amem$ is the total stage membrane area and the state and process variables are either indexed by the node (k), stage inlet (in), or stage outlet (out). The set of nodes, K, has N

number of nodes and is enumerated from $k1$ to kN, starting at the feed side inlet (permeate side outlet) and ending at the feed side outlet (permeate side inlet).

The finite difference approximations of the governing pressure drop equations (Eq. 2.19 and 2.20) are shown in Eq. 2.33-2.38. The slight difference between the mass transfer and pressure drop approximations (e.g. $1/N$ term in Eq. 2.23 compared to $1/2N$ term in Eq. 2.34) arises because hydraulic pressure is a nodal variable (w in Fig. 2.2) and mass flow rate and mass fraction are inter-node variables (ϕ in Fig. 2.2).

$$P_{f,k} = P_{f,k-1} - PL_{f,k-1}\frac{L}{N} \quad \forall k, k \neq k1 \tag{2.33}$$

$$P_{f,k1} = P_{f,in} - PL_{f,in}\frac{L}{2N} \tag{2.34}$$

$$P_{f,out} = P_{f.kN} - PL_{f,kN}\frac{L}{2N} \tag{2.35}$$

$$P_{p,k} = P_{p,k+1} - PL_{p,k+1}\frac{L}{N} \quad \forall k, k \neq kN \tag{2.36}$$

$$P_{p,kN} = P_{p,in} - PL_{p,in}\frac{L}{2N} \tag{2.37}$$

$$P_{p,out} = P_{p,k1} - PL_{p,k1}\frac{L}{2N} \tag{2.38}$$

In the following model description, we frequently use functions (f_*) that relate the specified variable to other variables (e.g. the osmotic pressure as a function of concentration is represented by $f_\pi(C)$). Previously described functions include: $f_\pi(C)$ as Eq. 2.3, $f_\rho(X)$ as Eq. 2.4, $f_\mu(X)$ as Eq. 2.5, $f_D(X)$ as Eq. 2.6, $f_C(X)$ as Eq. 2.7, $f_{Cm_f}\left(Cb_f, Jw, Js, k_f, D\right)$ as Eq. 2.8, and $f_{Cm_p}\left(Cb_p, Jw, Js, k_p, D\right)$ as Eq. 2.9. Additionally, functions for the mass transfer coefficient (f_k),

pressure loss per unit length (f_{PL}), and Reynolds number (f_{Re}) are formulated for the variables considered in our model, as shown in Eq. 2.39-2.41.

$$f_k(X, Re, Sc) = \frac{f_D(X)}{d_h}\ 0.46(Re\ Sc)^{0.36} \tag{2.39}$$

$$f_{PL}(M, X, Re, W) = \frac{\left(0.42+\frac{189.3}{Re}\right)M^2}{2\ d_h\ f_\rho(X)\ H^2\ W^2\ \varepsilon^2}\left[\frac{1\ h}{3600\ s}\right]^2\left[\frac{1\ bar}{1E5\ Pa}\right] \tag{2.40}$$

$$f_{Re}(M, X, W) = \frac{M\ d_h}{f_\mu(X)\ H\ W\ \varepsilon}\left[\frac{1\ h}{3600\ s}\right] \tag{2.41}$$

Where ε is the void space of the mesh filled channel (assumed to be 97% for consistency with the Sherwood number and friction factor assumptions).

The nodal variables (ω in Fig. 2.2): water flux, salt flux, osmotic pressure, concentration at the membrane interface, bulk concentration, mass transfer coefficient, and diffusivity are determined with Eq. 2.42-2.57.

$$Jw_k = A\left(\left(P_{f,k} - P_{p,k}\right) - \left(\pi_{f,k} - \pi_{p,k}\right)\right) \quad \forall k \tag{2.42}$$

$$Js_k = B\left(Cm_{f,k} - Cm_{p,k}\right) \quad \forall k \tag{2.43}$$

$$\pi_{s,k} = f_\pi\left(Cm_{s,k}\right) \quad \forall s \in (f,p), \forall k \tag{2.44}$$

$$Cm_{s,k} = f_{Cm_s}\left(Cb_{s,k}, Jw_k, Js_k, k_{s,k}, D_{s,k}\right) \quad \forall s \in (f,p), \forall k \tag{2.45}$$

$$Cb_{f,k} = \frac{f_C(X_{f,k}) + f_C(X_{f,k-1})}{2} \quad \forall k, k \neq k1 \tag{2.46}$$

$$Cb_{f,k1} = \frac{f_C(X_{f,in}) + f_C(X_{f,k1})}{2} \tag{2.47}$$

$$Cb_{p,k} = \frac{f_C(X_{p,k}) + f_C(X_{p,k+1})}{2} \quad \forall k, k \neq kN \tag{2.48}$$

$$Cb_{p,kN} = \frac{f_C(X_{p,in}) + f_C(X_{p,kN})}{2} \tag{2.49}$$

$$k_{f,k} = \frac{f_k(X_{f,k}, Re_{f,k}, Sc_{f,k}) + f_k(X_{f,k-1} Ref_{k-1}, Scf_{k-1})}{2} \quad \forall k, k \neq k1 \tag{2.50}$$

$$k_{f,k1} = \frac{f_k(X_{f,in}, Re_{f,in}, Sc_{f,in}) + f_k(X_{f,k}, Re_{f,k}, Sc_{f,k})}{2} \tag{2.51}$$

$$k_{p,k} = \frac{f_k(X_{p,k}, Re_{p,k}, Sc_{p,k}) + f_k(X_{p,k+1}, Re_{p,k+1}, Sc_{p,k+1})}{2} \quad \forall k, k \neq kN \tag{2.52}$$

$$k_{p,kN} = \frac{f_k(X_{p,in}, Re_{p,in}, Sc_{p,in}) + f_k(X_{p,kN}, Re_{p,kN}, Sc_{p,kN})}{2} \tag{2.53}$$

$$D_{f,k} = \frac{f_D(X_{f,k}) + f_D(X_{f,k-1})}{2} \quad \forall k, k \neq k1 \tag{2.54}$$

$$D_{f,k1} = \frac{f_D(X_{f,in}) + f_D(X_{f,k1})}{2} \tag{2.55}$$

$$D_{p,k} = \frac{f_D(X_{p,k}) + f_D(X_{p,k+1})}{2} \quad \forall k, k \neq kN \tag{2.56}$$

$$D_{p,kN} = \frac{f_D(X_{p,in}) + f_D(X_{p,kN})}{2} \tag{2.57}$$

Where the subscript s denotes either the feed (f) or sweep (s) side. Note that the bulk concentration, the mass transfer coefficient, and the solute diffusion coefficient (nodal variables) are determined from the average of their functions evaluated at the adjacent inter-node variables.

The inter-node variables (ϕ in Fig. 2.2) - pressure loss per unit length, Reynolds number, and Schmidt number - are determined with Eq. 2.58-2.60.

$$PL_{s,u} = f_{PL}\left(M_{s,u}, X_{s,u}, Re_{s,u}, W\right) \quad \forall s \in (f,p), \forall u \in (K, in) \tag{2.58}$$

$$Re_{s,u} = f_{Re}(Mf_u, Xf_u, W) \quad \forall s \in (f,p), \forall u \in (K, in) \tag{2.59}$$

$$Sc_{s,u} = \frac{f_{\mu}(X_{s,u})}{f_{\rho}(X_{s,u})\, f_D(X_{s,u})} \quad \forall s \in (f,p), \forall u \in (K,in) \tag{2.60}$$

Previously described stage level variables - membrane area, length, and width - are related by Eq. 2.61. Other stage level variables include: average water flux (Jw_{avg}), average salt flux (Js_{avg}), water recovery (Rw), salt passage (Rs), and pressure drop on the feed and permeate side (ΔP_f, ΔP_p). These variables are determined in Eq. 2.62-2.66.

$$Amem = W\, L \tag{2.61}$$

$$Jw_{avg} = \frac{1}{N} \sum_k Jw_k \tag{2.62}$$

$$Js_{avg} = \frac{1}{N} \sum_k Js_k \tag{2.63}$$

$$Rw = \frac{Jw_{avg}\, Amem}{M_{f,in}\,(1 - X_{f,in})} \tag{2.64}$$

$$Rs = \frac{Js_{avg}\, Amem}{M_{f,in}\, X_{f,in}} \tag{2.65a}$$

$$Rs = \frac{-Js_{avg}\, Amem}{M_{p,in}\, X_{p,in}} \tag{2.65b}$$

$$\Delta P_s = P_{s,in} - P_{s,out} \quad \forall s \in (f,p) \tag{2.66}$$

Where Eq. 2.65a is valid for processes with positive salt flux (i.e. RO and OARO) and Eq. 2.65b is valid for processes with negative salt flux (i.e. FO and PRO). Note that water recovery is defined as the fraction of permeated water mass flow rate over the feed inlet water mass flow rate, as opposed to the inlet feed volume reduction, which is commonly used in the literature. An issue with the volumetric reduction definition of water recovery is that it determines the solution recovery rather than the water recovery. The deviation between the mass and volumetric-based

water recovery is small when the initial feed concentration is dilute, but they deviate at higher salinities that are common for OARO and FO.

Simplified inlet-outlet model

The detailed process model can be simplified to an inlet-outlet model. This approach reduces the dimension of the model from one to zero by disregarding the governing system of differential equations. Instead, the inlet-outlet model estimates the overall performance of the membrane process by averaging variables at the inlet and outlet of the stage. The inlet-outlet model is computationally leaner because it has significantly fewer variables and constraints; however, its solutions are less detailed and accurate (i.e. no profiles of variables along the membrane stage).

In this work, we consider three inlet-outlet model formulations that estimate the average with: 1) the arithmetic mean, 2) the log mean, and 3) the geometric mean. These means are specified in Eq. 2.67a, 2.67b, and 2.67c, respectively. We approximate the log mean with an approximation developed by Chen 1987 because the log mean can be undefined over the domain of feasible variables.[26-27]

$$f_{avg}(Y_1, Y_2) = \frac{(Y_1 + Y_2)}{2} \tag{2.67a}$$

$$f_{avg}(Y_1, Y_2) = \frac{Y_1 - Y_2}{\ln\left(\frac{Y_1}{Y_2}\right)} \approx \left(Y_1\, Y_2\, \frac{(Y_1 + Y_2)}{2}\right)^{\frac{1}{3}} \tag{2.67b}$$

$$f_{avg}(Y_1, Y_2) = (Y_1\, Y_2)^{\frac{1}{2}} \tag{2.67c}$$

The mass balance and pressure drop equations around the membrane stage are shown in Eq. 2.68-2.72.

$$M_{f,out} = M_{f,in} - Amem\left(Jw_{avg}\, \rho_w + Js_{avg}\right) \tag{2.68}$$

$$M_{f,out}\, X_{f,out} = M_{f,in}\, X_{f,in} - Amem\, Js_{avg} \tag{2.69}$$

$$M_{p,out} = M_{p,in} + Amem\left(Jw_{avg}\, \rho_w + Js_{avg}\right) \tag{2.70}$$

$$M_{p,out}\, X_{p,out} = M_{p,in}\, X_{p,in} + Amem\, Js_{avg} \tag{2.71}$$

$$P_{s,out} = P_{s,in} + PL_{s,avg}\, L \quad \forall s \in (f,p) \tag{2.72}$$

The averaged process variables Jw_{avg}, Js_{avg}, and $PL_{s,avg}$ are determined in Eq. 2.73-2.75.

$$Jw_{avg} = f_{avg}(Jw_1, Jw_2) \tag{2.73}$$

$$Js_{avg} = \frac{Js_1 + Js_2}{2} \tag{2.74}$$

$$PL_{s,avg} = f_{avg}\left(PL_{s,in}, PL_{s,out}\right) \tag{2.75}$$

Where f_{avg} is Eq. 2.67a, 2.67b, or 2.67c depending on the mean formulation, the numbered subscript denotes the membrane stage end: 1 for feed side inlet and permeate side outlet, and 2 for feed side outlet and permeate side inlet. We determine the average salt flux using the arithmetic mean for all inlet-outlet models since we observe nearly constant or linear salt flux profiles from our detailed one-dimensional model.

The water flux, salt flux, and pressure loss are determined at each end of the membrane stage with Eq. 2.76-2.80.

$$Jw_1 = A\, \left(\left(P_{f,in} - P_{p,out}\right) - \left(\pi_{f,in} - \pi_{p,out}\right)\right) \tag{2.76}$$

$$Jw_2 = A\, \left(\left(P_{f,out} - P_{p,in}\right) - \left(\pi_{f,out} - \pi_{p,in}\right)\right) \tag{2.77}$$

$$Js_1 = B\left(Cm_{f,in} - Cm_{p,out}\right) \tag{2.78}$$

$$Js_2 = B\left(Cm_{f,out} - Cm_{p,in}\right) \tag{2.79}$$

$$PL_{s,u} = f_{PL}\left(M_{s,u}, X_{s,u}, Re_{s,u}, W\right) \quad \forall s \in (f,p), \forall u \in (in,out) \tag{2.80}$$

All other variables, including osmotic pressure, concentration at the membrane interface, bulk concentration, mass transfer coefficient, Reynolds number, and Schmidt number, are determined in Eq. 2.81-2.89.

$$\pi_{s,u} = f_{\pi}\left(Cm_{s,u}\right) \quad \forall s \in (f,p), \forall u \in (in,out) \tag{2.81}$$

$$Cm_{f,in} = f_{Cm_f}\left(Cb_{f,in}, Jw_1, k_{f,in}, D_{f,in}\right) \tag{2.82}$$

$$Cm_{f,out} = f_{Cm_f}\left(Cb_{f,out}, Jw_2, k_{f,out}, D_{f,out}\right) \tag{2.83}$$

$$Cm_{p,in} = f_{Cm_p}\left(Cb_{p,in}, Jw_2, k_{p,in}, D_{p,in}\right) \tag{2.84}$$

$$Cm_{p,out} = f_{Cm_p}\left(Cb_{p,out}, Jw_1, k_{p,out}, D_{p,out}\right) \tag{2.85}$$

$$Cb_{s,u} = f_{C}\left(X_{s,u}\right) \quad \forall s \in (f,p), \forall u \in (in,out) \tag{2.86}$$

$$D_{s,u} = f_{D}\left(X_{s,u}\right) \quad \forall s \in (f,p), \forall u \in (in,out) \tag{2.87}$$

$$Re_{s,u} = f_{Re}(Mf_u, Xf_u, W) \quad \forall s \in (f,p), \forall u \in (in,out) \tag{2.88}$$

$$Sc_{s,u} = \frac{f_{\mu}(X_{s,u})}{f_{\rho}(X_{s,u}) D_{s,u}} \quad \forall s \in (f,p), \forall u \in (in,out) \tag{2.89}$$

The inlet-outlet model uses the same equations as the detailed process model (Eq. 2.61 and 2.64-2.66) for the stage level variables.

Case studies

We apply our detailed process model and inlet-outlet models to case studies for RO, OARO, FO, and PRO membrane technologies. The membrane properties (Table 2.1) were estimated from the literature.[12, 28-30] The case study specifications (Table 2.1) were selected for representativeness and ease of comparison with similar process modeling exercises.[4, 8, 10, 12] In addition to the values defined by the case studies, we also perform a Monte Carlo analysis to assess the sensitivity of our results to the specified parameters. In the Monte Carlo simulations, we develop a set of 100 cases that are created by randomly sampling the parameters between +/- 5% of the specified case study value.

Table 2.1. *Case study parameter specifications. Not applicable (NA) and not specified (NS) variables are noted. We assume a basis of 1000 kg/h of feed side inlet mass flowrate. The permeate side inlet mass flowrate is determined with its mass flowrate fraction defined as* $Mp_{in}/(Mp_{in} + Mf_{in})$*. Specifications that are varied in the Monte Carlo analysis are noted with ±5%.*

	RO	OARO	FO	PRO
Membrane and module properties				
Water permeability coefficient [1E-12 m Pa^{-1} s^{-1}]	4.2 ±5% [12]	1.0 ±5% [28]	3.2 ±5% [29]	6.9 ±5% [30]
Salt permeability coefficient [1E-8 m s^{-1}]	3.5 ±5% [12]	7.7 ±5% [28]	13 ±5% [29]	11 ±5% [30]
Structural parameter [μm]	NA	1200 ±5% [4]	500 ±5% [29]	560 ±5% [30]
Inlet specifications				
Feed side inlet mass flowrate [kg h^{-1}]	1000	1000	1000	1000
Feed side inlet concentration [g L^{-1}]	35 ±5%	75 ±5%	35 ±5%	2.9 ±5%
Feed side inlet pressure [bar]	70 ±5%	65 ±5%	NS	NS
Permeate side inlet mass flowrate fraction [-]	0	0.33 ±5%	0.33 ±5%	0.5 ±5%
Permeate side inlet concentration [g L^{-1}]	0	100 ±5%	175 ±5%	35 ±5%
Permeate side inlet pressure [bar]	NS	NS	NS	13 ±5%
Outlet specifications				
Feed side outlet pressure [bar]	NS	NS	1	1
Permeate side outlet pressure [bar]	1	1	1	NS
Additional specifications				
Water recovery [%]	50 ±5%	50 ±5%	50 ±5%	50 ±5%
Feed side inlet Reynolds number [-]	400 ±5%	400 ±5%	400 ±5%	300 ±5%
Channel height [mm]	1 ±5%	2 ±5%	2 ±5%	2 ±5%

Solving the models

The size of the detailed process model is dependent on the number of nodes (N): 24N+27 variables, and 24N + 19 equality constraints. The simplified inlet-outlet model has 53 variables and 45 equality constraints. Both models have 8 degrees of freedom, which are reduced to zero with the case study specifications in Table 2.1. We create the models in Python using the open source software package Pyomo and solve for the single feasible solution using GAMS

24.5.6/CONOPT3. Additional details on bounding and initializing the variables is provided in SI Section S4.

2.5 Results and Discussion

This work systematically evaluates the accuracy implications of common simplifications adopted in RO, OARO, FO, and PRO membrane process models. We begin by assessing the effect of the number of nodes on the results of the finite difference approximation for water flux. We then evaluate the effect of common simplifications used in describing the process and solution properties by quantifying the difference in average water flux with and without implementation of these simplifications. Finally, we quantify the average water flux error that originates from the use of simplified inlet-outlet modeling and evaluate the performance of novel inlet-outlet model formulations that use the log and geometric means to estimate the average water flux and pressure loss.

Detailed process model results

The detailed process model with 100 nodes (2427 variables) is solved in less than 2 seconds when using an Intel i7 CPU 2.6 GHz processor with 8 GB of memory for each of the four membrane processes. While we obtain short solution times with the solver CONOPT, the largest benefit of the commercial solver is that the solution is tractable with crude variable bounds and initialization (SI Section S4). This solver performance contrasts with the Matlab nonlinear systems of equations solver, fsolve, which was unable to converge on a solution for the same bounds and initialization.

Table 2.2 presents the solutions to the optimal process specifications and performance metrics, including average water and salt flux; salt recovery; membrane area; and feed and permeate side pressure drop, outlet concentration, average Reynolds number, and average mass

transfer coefficient. We observe that our process model results are consistent with expected modeling results for the outlet concentrations, average water flux, and pressure drop.[4, 8, 10, 12]

Table 2.2. *Detailed process model results for the RO, OARO, FO, and PRO case studies.*

Key variables and performance metrics	RO	OARO	FO	PRO
Average water flux [L m^{-2} h^{-1}]	25.6	3.0	6.1	4.5
Average salt flux [g m^{-2} h^{-1}]	8.1	17.4	-3.1	-6.6
Salt passage [%]	0.5	4.0	0.3	2.2
Feed side pressure drop [bar]	1.5	1.9	0.9	0.5
Permeate side pressure drop [bar]	NA	1.7	0.9	1.0
Feed side outlet concentration [g L^{-1}]	69	131.5	69.8	7.3
Permeate side outlet concentration [g L^{-1}]	0.3	52.9	84.1	22.7
Membrane area [m^2]	19	155	80	112
Membrane width [m]	1.2	1.1	1.2	1.7
Membrane length [m]	16	141	68	67
Feed side average Reynolds number	272	273	297	226
Permeate side average Reynolds number	NA	274	261	359
Feed side average mass trans. coef. [mm h^{-1}]	113	58	58	52
Permeate side average mass trans. coef. [mm h^{-1}]	NA	57	58	62

The detailed process model also provides the profile of each variable along the length of the membrane. Profiles for feed concentration, permeate concentration, and water flux are plotted in Figure 2.3. In RO and OARO, we observe the characteristically steep water flux decline along the membrane length that results from the pressure drop and the increasing feed side

concentration, and in OARO, from the dilution of the sweep. In contrast, we observe a modest water flux increase from the feed inlet to the feed outlet for FO and PRO.

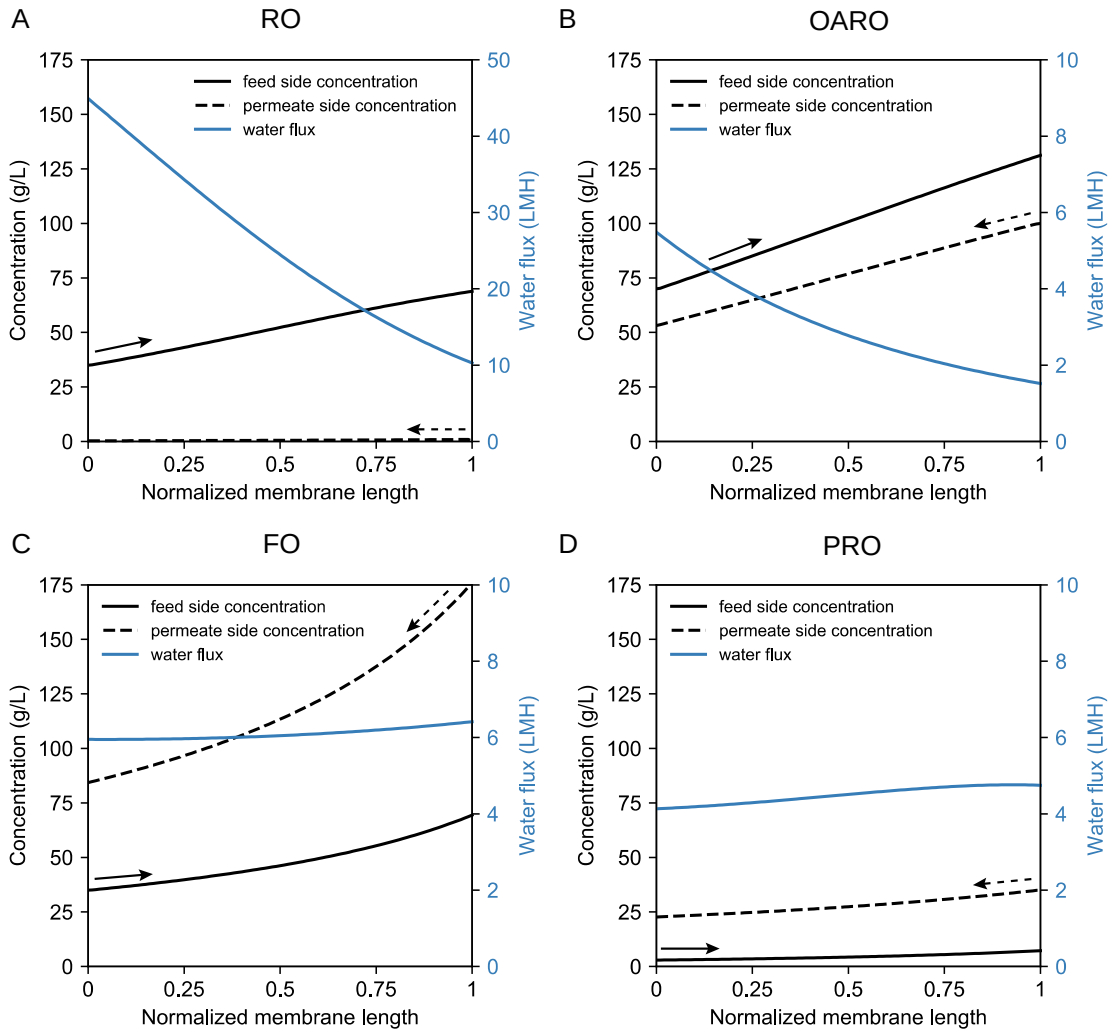

Figure 2.3. Bulk concentration (black) and water flux (blue) profiles along the stage for the 100 node finite difference model case studies: A) RO, B) OARO, C) FO, and D) PRO. The feed side (solid) and permeate side (dotted) concentrations are noted with line style and the flowrate directions for the streams are noted with arrows. The case study specifications and parameters are described in Section 2.4 and Table 2.1. Note that the RO water flux has a different scale than the other processes.

The fidelity between the detailed process model outputs and experimental measurements will depend upon the accuracy of the underlying assumptions. As noted above, the model assumes that the membranes are configured in a flat plate geometry, modules are operated in counter-current flow, friction factors and mass transfer coefficients can be described with correlations from a simulated computational fluid dynamics model, and the membrane parameters (e.g. A, B, and S) are independent of operating variables (e.g. feed and sweep side pressure and concentration). Thus, this model will not accurately describe membrane modules with different geometries (e.g. spiral wound or hollow fiber), cross flow operation, and large dead zones. We expect that our assumed flat plate geometry with only one membrane active layer bordering the flow will have longer modules than spiral wound (2 layers) or hollow fiber modules and that our assumed counter-current flow operation will have a higher average permeate-side concentration compared to the more common cross flow operation for RO processes. Finally, our model does not reflect the greater pressure drop that is expected on the low hydraulic pressure side of OARO and PRO processes due to the lack of experimental data and friction factor correlations for those conditions.

Accuracy implications of decreasing the number of nodes in the finite difference approximation.

We assess the accuracy implications of decreasing the computational intensity of the finite difference model by decreasing the number of model nodes. In Figure 2.4, we plot the average difference in water flux between the n node approximation and the 100 node approximation. For each approximation, we use a Monte Carlo simulation that perturbs the specified inlet variables by ±5%, as described in Section 2.4, to assess the sensitivity of the average water flux error to the specified conditions.

We observe that the 1 node approximation deviates from the 100 node approximation of average water flux by less than 11% for each membrane process. As the number of nodes increases, the deviation decreases to less than 1% and 0.1% for 5 and 10 nodes, respectively. Deeming 0.1% accuracy sufficient for our current work, we use the 10 node approximation for all subsequent simulations.

Generally, deviations tend to increase with decreasing driving force and increasing membrane area, as low node approximations are less accurate at representing the profile of long modules. Whether the average water flux is over or underestimated is highly dependent on the case study parameters, and we observe that even the relatively small perturbation of ±5% can result in either an over or underestimate for RO and PRO.

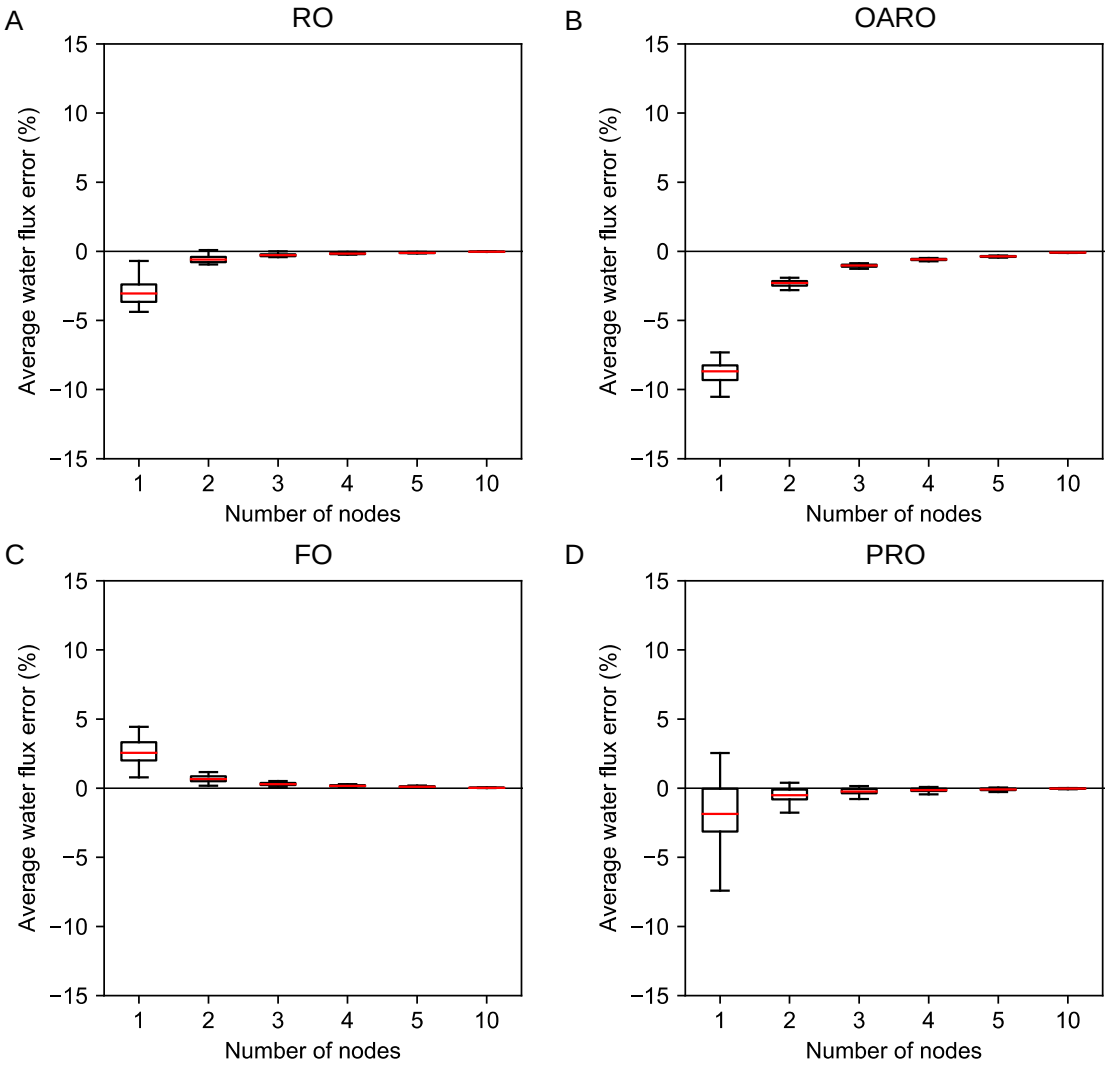

Figure 2.4. *Accuracy of the n-node finite difference model relative to the 100 node model for A) RO, B) OARO, C) FO, and D) PRO. The water flux solution for the 100 node model is assumed to be the true value because there is an undetectable change (less than 0.001%) associated with a further increase in the number of nodes. The distribution of average water flux errors was developed using a Monte Carlo simulation that varied the specified parameters by ±5%, as noted in Table 2.1.*

Effect of process and solution property simplifications on model accuracy

We determine the average water flux percent error for common modeling simplifications, including: no salt flux, no pressure drop, ideal solution, and constant density, viscosity, and diffusivity for the 10 node case (Figure 2.5). We find that the simplifications result in water flux errors in our case studies of up to 20% for RO, 30% for OARO, 10% for FO, and 40% for PRO.

The no salt flux simplification can result in large errors (>30%) for osmotically driven membrane processes. In these processes, salt flux has a large effect on the interfacial solute concentration and therefore on the osmotic driving force. In RO and OARO, the no salt flux simplification artificially increases the interfacial solute concentration on the feed side and decreases the concentration on the permeate side, decreasing the overall driving force and leading to an underestimation of average water flux. The inverse is true for both FO and PRO processes, which exhibit negative salt flux. Note that the no salt flux simplification results in significantly smaller errors in FO than in PRO because 1) the FO case study resulted in a lower average salt flux (Table 2.1), and 2) the orientation of the porous support on the permeate side in the FO case study reduces the feed side concentration polarization, which dampens the effect of assuming no salt flux.

The no pressure drop simplification results in large errors (up to 30%) for PRO and small errors (<10%) for the other membrane processes. We observe a large error for the PRO case study because neglecting the pressure drop decreases the overall driving force. When pressure drop is included, the inlet feed side pressure is greater than 1 bar and the outlet permeate side pressure is less than the specified permeate side inlet pressure. The pressure drop therefore increases the driving force at the end of the membrane stage with the feed inlet.

In contrast, when pressure drop is included for RO and OARO, the driving force decreases along the membrane length. If RO and OARO are operated at higher Reynolds numbers than those specified in our case study, the associated error with neglecting pressure drop would increase. We observe the smallest error from the no pressure drop simplification for FO because, while including the pressure drop increases the driving force at the feed inlet, it also decreases the driving force at the feed outlet and mitigates the change in average driving force along the stage. While this work only assesses the error on the average water flux, neglecting the pressure drop could result in large errors in the estimated energy consumption (or production, in the case of PRO) of the membrane processes.

The ideal solution simplification results in larger errors (>10%) for RO and PRO modeling and small errors (<5%) for RO and FO. OARO and FO are less impacted by the ideal solution assumption because the error in the osmotic pressure calculation occurs on both the feed and permeate side, effectively mitigating the net error. In contrast, the error in RO and PRO is large because only one side has a significant amount of osmotic pressure. This finding is especially significant because low concentration feeds are often used to justify the use of the ideal solution simplification in RO and PRO models.

The constant density assumption results in moderate errors (5-10%) for RO, OARO, FO, and PRO. Even though the density does not change by more than 5% between the inlet and outlet of each stream in the case studies, the constant density assumption results in moderate errors because assuming constant density leads to underestimates of the change in concentration. The magnitude of this error is directly related to the concentrations of the feed and permeate streams, with OARO and FO having the highest concentrations and the highest errors.

The constant viscosity assumption results in negligible errors (<2%) for all processes, despite the large viscosity change of over 50% across the solubility of NaCl. While viscosity has a proportional effect on the Reynolds number, it does not significantly affect the overall driving force when operating the membrane system at typical flow velocities.

The constant diffusivity assumption results in negligible errors (<0.1%) for all processes. This finding is unsurprising given that diffusivity has a limited effect on the average water flux and only varies by 10% across the solubility of NaCl at 25 °C. For processes with depressed, elevated, or non-constant temperatures, the constant diffusivity assumption may contribute to higher average water flux errors.

The cumulative error of these simplifications depends upon the process and the case study specifications. For RO and OARO, the cumulative error is less than the maximum error from a single simplification because some simplifications result in an overestimation of flux, while others result in underestimation. In contrast, the cumulative error is largest for FO and PRO. We observe that the cumulative errors are less than 15%, 10%, 10%, and 50% for the RO, OARO, FO, and PRO cases, respectively. While these errors may be significant for some cases, we find that adopting these simplifications reduces the solution time of the detailed model by roughly a factor of 3.

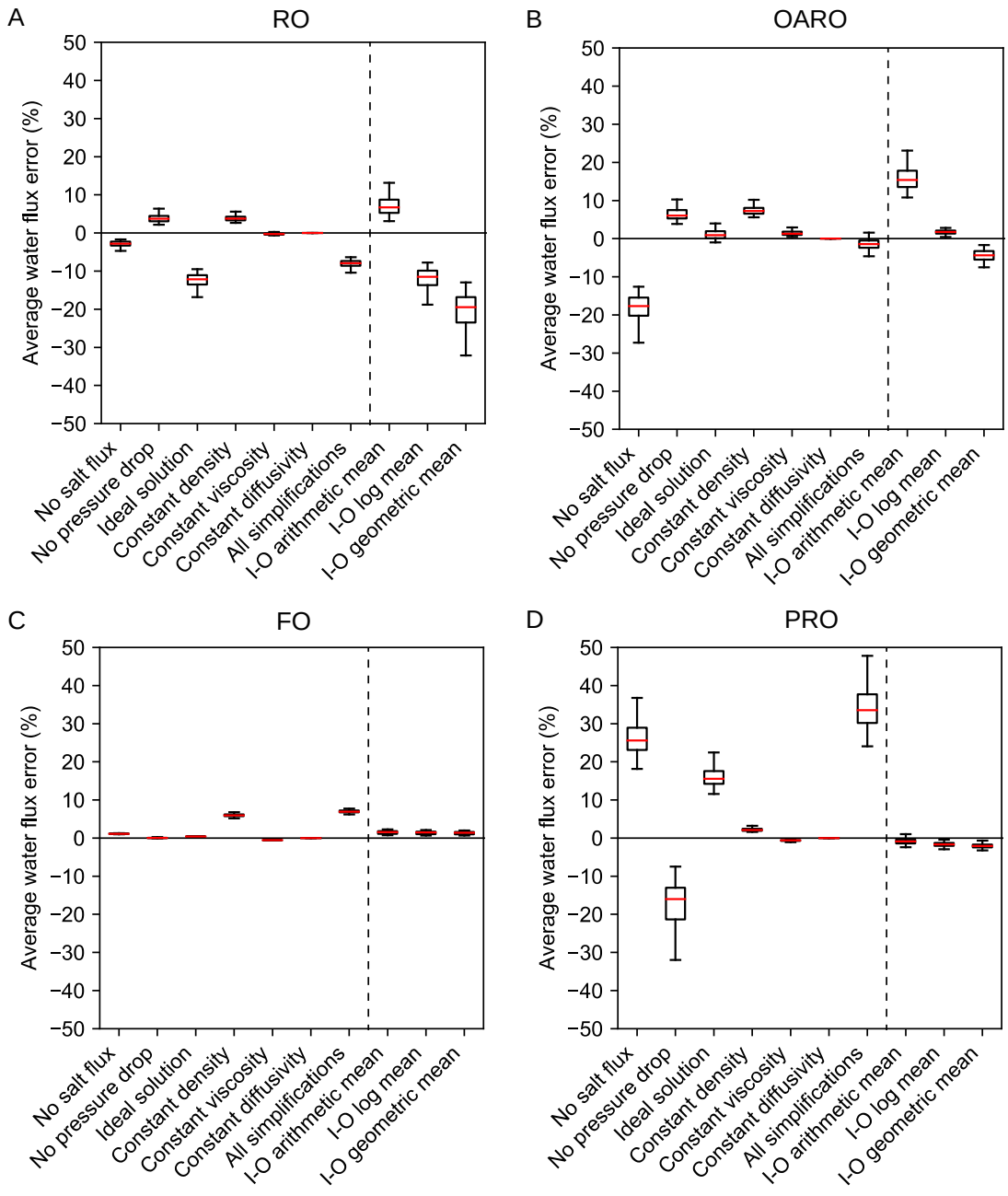

Figure 2.5*. Effect of common simplifications on the accuracy of water flux estimates for the four membrane process case studies: A) RO, B) OARO, C) FO, and D) PRO. All water flux errors are relative to the 10 node finite difference model without employing common simplifications. "All simplifications" includes the no salt flux, no pressure drop, ideal solution, and constant density, viscosity, and diffusivity assumptions. The right-hand side of the dotted line reports the accuracy*

of the simplified inlet-outlet (I-O) model formulated with an arithmetic, log, and geometric means.

Effect of inlet-outlet formulation on model accuracy

In contrast to the process model described above, inlet-outlet models do not directly estimate the profiles of variables along the membrane stage. Instead, they estimate the process performance by averaging the inlet and outlet variables. These models are frequently used because they have reduced computational complexity and are readily incorporated into system-scale optimization models that have higher degrees of freedom. In our work, we find that the inlet-outlet model solves 10 times faster than the detailed model.

We determine the water flux percent error relative to the 10 node finite difference model of the three inlet-outlet modeling formulations. We observe that the arithmetic mean formulation results in large errors (>10%) for the RO and OARO case studies and small errors (<5%) for FO and PRO case studies (Fig. 2.5). Generally, the arithmetic mean overestimates the average water flux for the membrane processes with non-linear water flux profiles.

The log and geometric mean formulations will yield lower average water flux compared to the arithmetic mean. We find that these means underestimate the water flux by up to 40% in the RO case study. In contrast, for the OARO case, the log mean has significantly lower average water flux errors than the geometric or arithmetic means. Finally, in the FO and PRO cases, we find that there is little difference between the means because both cases have relatively flat water flux profiles. When we modify the specifications in the case studies to produce steeper water flux profiles, we find that there is no consistent formulation that results in the lowest error for FO and PRO (Fig. S6). FO and PRO do not have a most accurate formulation because they can be operated with a variety of water flux profiles (e.g. linear or non-linear, increasing or decreasing

along the stage), whereas the shape of the water flux profile in RO and OARO is more consistent. Further discussion of the additional FO and PRO case studies are provided in SI section S.5.

One drawback of the log and geometric mean models is that they can incorrectly predict some process configurations as infeasible, meaning that while the target water recovery can be achieved with specified parameters for the detailed one-dimensional model, the water recovery cannot be achieved for the inlet-outlet models. We observe this behavior in 4% and 2% of the Monte Carlo simulations from the RO case study for the log and geometric mean formulations, respectively. The simulations are infeasible for these formulations because they significantly underestimate the average water flux and, thus, overestimate the total membrane area (including membrane length) and total pressure drop. These inflated pressure drops cause the specified water recovery and operating conditions to be infeasible. We do not observe this diverging behavior for the other membrane processes (i.e. OARO, FO, and PRO) because the difference between the water flux at both ends of the membrane stage is significantly smaller.

Collectively, these results suggest that the arithmetic and log mean formulations are the most accurate approaches for inlet-outlet modeling of RO and OARO, respectively. While inlet-outlet modeling can be applied to accurately represent FO and PRO, it is important to begin by using a one-dimensional model to predict the shape of the water flux profile prior to selecting an appropriate mean for estimating the average.

2.6 Conclusions

While all membrane models are approximations of the process conditions observed in real-world membrane systems, accurate models are critical for developing and predicting the performance of novel membrane technologies. Fully understanding the limitations of existing models and the tradeoffs between model simplicity and model accuracy will further improve our ability to use these models to assess and design novel membrane processes.

This work quantified the errors introduced by common simplifications for the membrane process, solution properties, and modeling. We demonstrated that the finite difference approximation with 10 nodes is sufficient to accurately describe the average water flux to within 0.1%. We also demonstrated that the no salt flux, ideal solution, and constant density simplifications result in the largest water flux errors. Finally, we demonstrated the value of replacing arithmetic mean approximations with a log mean approximation in inlet-outlet models for OARO and FO processes where the water flux is significantly affected by solution conditions on both side of the membrane.

This work has several implications for modeling membrane processes. The first is that the presented finite difference model can be solved efficiently without making common simplifications that are typically rationalized as a means of lowering the computational intensity of the model. Second, both low node approximations and process and solution property simplifications can result in significant errors in predicted water flux. While these simplifications are specific to the case study parameters, we observe water flux errors as large a 50% for some membrane processes operating under standard conditions. Finally, for applications where simplified inlet-outlet modeling is preferred (e.g. system-scale optimization problems), we have explored the accuracy implications of using different means for all four

membrane processes and found that a novel log mean formulation more accurately represents the non-linear water flux in the OARO process.

Supporting Information

The additional supporting information for this chapter is included in Appendix A.

2.7 Acknowledgements

We would like to thank Dr. Nick Siefert of the National Energy Technology Laboratory. This work was funded via the U.S. Department of Energy's National Energy Technology Laboratory under the Crosscutting Technologies Division and via NSF CBET-1554117. Support for T.V.B. was provided by appointment to the National Energy Technology Laboratory Research Participation Program, sponsored by the U.S. Department of Energy and administered by the Oak Ridge Institute for Science and Education. T.V.B. was also supported by the ARCS Foundation Fellowship.

2.8 Nomenclature

Roman symbols

A – Water permeability coefficient [m/bar-h]

$Amem$ – Stage membrane area [m^2]

B – Salt permeability coefficient [m/h]

C – Concentration [g/L]

Cb – bulk concentration [g/L]

Cm – concentration at the membrane interface [g/L]

D – diffusion coefficient of the solute [m^2/s]

d_h – Hydraulic diameter [m]

F – Friction factor [-]

H – Channel height [m]

Js – Salt flux [kg/h]

Jw – Water flux [m^3/m^2-h]

k – mass transfer coefficient [m/h]

L – Membrane stage length [m]

M – mass flowrate [kg/h]

MW – Molecular weight [g/mole]

N – number of nodes

P – Hydraulic pressure [bar]

PL – Pressure loss per unit length [bar/m]

Re – Reynolds number [-]

Rs – salt passage [%]

Rw – water recovery [%]

S – structural parameter [m]

Sc – Schmidt number [-]

Sh – Sherwood number [-]

T – Temperature [K]

W – Membrane stage width [m]

X – mass fraction [kg of solute/kg of solution]

Greek symbols

ε – Void space of mesh

θ – Inlet and outlet stage variables

μ – Viscosity [Pa-s]

π – Osmotic pressure [bar]

ρ – Density [kg/m^3]

ρw – Pure water density [kg/m^3]

ϕ – Inter-node variables

ω – Nodal variables

Subscript

avg – average

f – feed-side

p – permeate-side

in – inlet

out – outlet

k – node in set K $(k1, k2, \dots, kN)$

Miscellaneous

$f_y(x)$ – function that determines y from variables x

Abbreviations

FO – Forward osmosis

OARO – Osmotically assisted reverse osmosis

PRO – Pressure retarded osmosis

RO – Reverse osmosis

2.9 References

1. Mazlan, N. M.; Peshev, D.; Livingston, A. G., Energy consumption for desalination — A comparison of forward osmosis with reverse osmosis, and the potential for perfect membranes. *Desalination* **2016,** *377*, 138-151.

2. Sagiv, A.; Zhu, A.; Christofides, P. D.; Cohen, Y.; Semiat, R., Analysis of forward osmosis desalination via two-dimensional FEM model. *Journal of Membrane Science* **2014,** *464* (Supplement C), 161-172.

3. Fimbres-Weihs, G. A.; Wiley, D. E., Review of 3D CFD modeling of flow and mass transfer in narrow spacer-filled channels in membrane modules. *Chemical Engineering and Processing: Process Intensification* **2010,** *49* (7), 759-781.

4. Bartholomew, T. V.; Siefert, N. S.; Mauter, M. S., Cost Optimization of Osmotically Assisted Reverse Osmosis. *Environmental Science & Technology* **2018,** *52* (20), 11813-11821.

5. Davenport, D. M.; Deshmukh, A.; Werber, J. R.; Elimelech, M., High-Pressure Reverse Osmosis for Energy-Efficient Hypersaline Brine Desalination: Current Status, Design Considerations, and Research Needs. *Environmental Science & Technology Letters* **2018**.

6. Bartholomew, T. V.; Mey, L.; Arena, J. T.; Siefert, N. S.; Mauter, M. S., Osmotically assisted reverse osmosis for high salinity brine treatment. *Desalination* **2017,** *421*, 3-11.

7. Kim, J.; Kim, J.; Kim, J.; Hong, S., Osmotically enhanced dewatering-reverse osmosis (OED-RO) hybrid system: Implications for shale gas produced water treatment. *Journal of Membrane Science* **2018,** *554*, 282-290.

8. Deshmukh, A.; Yip, N. Y.; Lin, S.; Elimelech, M., Desalination by forward osmosis: Identifying performance limiting parameters through module-scale modeling. *Journal of Membrane Science* **2015,** *491*, 159-167.

9. Banchik, L. D.; Weiner, A. M.; Al-Anzi, B.; Lienhard V, J. H., System scale analytical modeling of forward and assisted forward osmosis mass exchangers with a case study on fertigation. *Journal of Membrane Science* **2016,** *510*, 533-545.

10. Straub, A. P.; Lin, S.; Elimelech, M., Module-Scale Analysis of Pressure Retarded Osmosis: Performance Limitations and Implications for Full-Scale Operation. *Environmental Science & Technology* **2014,** *48* (20), 12435-12444.

11. Vince, F.; Marechal, F.; Aoustin, E.; Bréant, P., Multi-objective optimization of RO desalination plants. *Desalination* **2008,** *222* (1), 96-118.

12. Lu, Y.-Y.; Hu, Y.-D.; Zhang, X.-L.; Wu, L.-Y.; Liu, Q.-Z., Optimum design of reverse osmosis system under different feed concentration and product specification. *Journal of Membrane Science* **2007,** *287* (2), 219-229.

13. Spiegler, K. S.; Kedem, O., Thermodynamics of hyperfiltration (reverse osmosis): criteria for efficient membranes. *Desalination* **1966,** *1* (4), 311-326.

14. Hoek, E. M. V.; Kim, A. S.; Elimelech, M., Influence of Crossflow Membrane Filter Geometry and Shear Rate on Colloidal Fouling in Reverse Osmosis and Nanofiltration Separations. *Environmental Engineering Science* **2002,** *19* (6), 357-372.

15. McCutcheon, J. R.; McGinnis, R. L.; Elimelech, M., Desalination by ammonia–carbon dioxide forward osmosis: Influence of draw and feed solution concentrations on process performance. *Journal of Membrane Science* **2006,** *278* (1), 114-123.

16. Yong, J. S.; Phillip, W. A.; Elimelech, M., Coupled reverse draw solute permeation and water flux in forward osmosis with neutral draw solutes. *Journal of Membrane Science* **2012,** *392-393*, 9-17.

17. Scatchard, G.; Hamer, W. J.; Wood, S. E., Isotonic Solutions. I. The Chemical Potential of Water in Aqueous Solutions of Sodium Chloride, Potassium Chloride, Sulfuric Acid, Sucrose, Urea and Glycerol at 25°1. *Journal of the American Chemical Society* **1938,** *60* (12), 3061-3070.

18. Pitzer, K. S.; Peiper, J. C.; Busey, R. H., Thermodynamic Properties of Aqueous Sodium Chloride Solutions. *Journal of Physical and Chemical Reference Data* **1984,** *13* (1), 1-102.

19. Mistry, K. H.; Lienhard V, J. H., Effect of Nonideal Solution Behavior on Desalination of a Sodium Chloride Solution and Comparison to Seawater. *Journal of Energy Resources Technology* **2013,** *135* (4), 042003-042003-10.

20. Washburn, E. W., International Critical Tables of Numerical Data, Physics, Chemistry and Technology (1st Electronic Edition). Knovel.

21. Lobo, V. M. M., Mutual diffusion coefficients in aqueous electrolyte solutions (Technical Report). In *Pure and Applied Chemistry*, 1993; Vol. 65, p 2613.

22. Yip, N. Y.; Tiraferri, A.; Phillip, W. A.; Schiffman, J. D.; Hoover, L. A.; Kim, Y. C.; Elimelech, M., Thin-Film Composite Pressure Retarded Osmosis Membranes for Sustainable Power Generation from Salinity Gradients. *Environmental Science & Technology* **2011,** *45* (10), 4360-4369.

23. Tiraferri, A.; Yip, N. Y.; Straub, A. P.; Romero-Vargas Castrillon, S.; Elimelech, M., A method for the simultaneous determination of transport and structural parameters of forward osmosis membranes. *Journal of Membrane Science* **2013,** *444*, 523-538.

24. Bui, N.-N.; Arena, J. T.; McCutcheon, J. R., Proper accounting of mass transfer resistances in forward osmosis: Improving the accuracy of model predictions of structural parameter. *Journal of Membrane Science* **2015,** *492*, 289-302.

25. Guillen, G.; Hoek, E. M. V., Modeling the impacts of feed spacer geometry on reverse osmosis and nanofiltration processes. *Chemical Engineering Journal* **2009,** *149* (1), 221-231.

26. Chen, J., Comments on improvements on a replacement for the logarithmic mean. *Chemical Engineering Science* **1987,** *42* (10), 2488-2489.

27. Mistry, M.; Misener, R., Optimising heat exchanger network synthesis using convexity properties of the logarithmic mean temperature difference. *Computers & Chemical Engineering* **2016,** *94*, 1-17.

28. She, Q.; Jin, X.; Tang, C. Y., Osmotic power production from salinity gradient resource by pressure retarded osmosis: Effects of operating conditions and reverse solute diffusion. *Journal of Membrane Science* **2012,** *401–402*, 262-273.

29. Yip, N. Y.; Tiraferri, A.; Phillip, W. A.; Schiffman, J. D.; Elimelech, M., High Performance Thin-Film Composite Forward Osmosis Membrane. *Environmental Science & Technology* **2010,** *44* (10), 3812-3818.

30. Straub, A. P.; Yip, N. Y.; Elimelech, M., Raising the Bar: Increased Hydraulic Pressure Allows Unprecedented High Power Densities in Pressure-Retarded Osmosis. *Environmental Science & Technology Letters* **2014,** *1* (1), 55-59.

3.0 OSMOTICALLY ASSISTED REVERSE OSMOSIS FOR HIGH SALINITY BRINE TREATMENT

3.1 Abstract

This work evaluates a novel osmotically assisted reverse osmosis (OARO) process for dewatering high salinity brines using readily available membranes and equipment. While traditional reverse osmosis processes are limited to treating brines with osmotic pressures below the membrane burst pressure, in OARO, the osmotic pressure difference across a membrane is reduced with a permeate side saline sweep. A series of OARO stages can be used to sequentially reduce the concentration of the feed until a traditional RO process can obtain fully desalinated water. This paper develops an OARO model to identify feasible operating conditions for this process and to estimate the water recovery and energy consumption across a range of brine feed concentrations. For a feed of 100-140 g/L sodium chloride, we estimate that the OARO process is capable of a 35-50% water recovery with an energy consumption of 6-19 kWh per m^3 of product water. The results suggest that an OARO dewatering process improves upon the recovery of reverse osmosis for high salinity brines and has a comparable or lower energy consumption than mechanical vapor recompression.

3.2 Introduction

There is growing demand from the oil and gas, electric power, and industrial sectors for processes to desalinate high salinity brines with 50-350 g/L of total dissolved solids (TDS).[1-3] Current brine dewatering techniques are expensive, energy intensive, or limited to low water recovery. There is an urgent need for new, scalable methods for concentrating brine prior to crystallization or disposal.

Current technologies for brine dewatering include both evaporative and non-evaporative approaches. The most common evaporative technologies include multi-stage flash distillation (MSF), multi-effect distillation (MED), membrane distillation (MD), and mechanical vapor compression (MVC).[4,5] MSF, MED, and MD processes use thermal energy, commonly steam, which limits the practicality of these processes on field-deployable skids.[1,4] In contrast, the MVC process uses only electricity and is now widely adopted for dewatering high salinity brines in the oil and gas industry.[1] As an evaporative process, the energy consumption of MVC ranges from 11-25 kWh per m^3 of produced water, which is significantly greater than the theoretical minimum work of approximately 1 - 5 kWh per m^3 to dewater a brine with TDS of 35 - 150 g/L at 50% recovery.[6]

By avoiding a phase change, non-evaporative membrane based technologies may reduce the energy intensity of desalination and brine dewatering processes. Reverse osmosis (RO), forward osmosis (FO), and pressure assisted forward osmosis (PAFO) offer several pathways for brine dewatering across a semi-permeable membrane.[7-10] Figure 3.1A presents the set driving and retarding forces in membrane-based separation processes where positive water flux is defined as flow against the osmotic pressure difference from the feed side (f) to the permeate side (p) of the membrane. A positive hydraulic pressure difference ($P_f - P_p$, ΔP) drives water transport, while a negative ΔP retards water transport. In contrast, a positive osmotic pressure difference ($\pi_f - \pi_p$, $\Delta\pi$) retards water transport, while a negative $\Delta\pi$ drives water transport.

In RO, a positive hydraulic pressure difference ($+\Delta P$) drives water transport against the retarding force of a positive osmotic pressure difference ($+\Delta\pi$). In FO, there is a negligible hydraulic pressure difference ($\Delta P \approx 0$) and a highly concentrated draw solution establishes a negative osmotic pressure difference ($-\Delta\pi$) to drive water flux from the feed to the draw. In

PAFO, a positive hydraulic pressure gradient is used to augment the negative osmotic gradient of FO (+ΔP, –Δπ). While not a separation process, pressure retarded osmosis (PRO) processes utilize the hydraulic pressure as a retarding force (–ΔP) and the osmotic pressure as the driving force (–Δπ). Of these membrane processes, only RO directly dewaters brines. FO and PAFO require a second process, most commonly a RO or thermal draw solute regeneration step, to produce a pure water permeate.

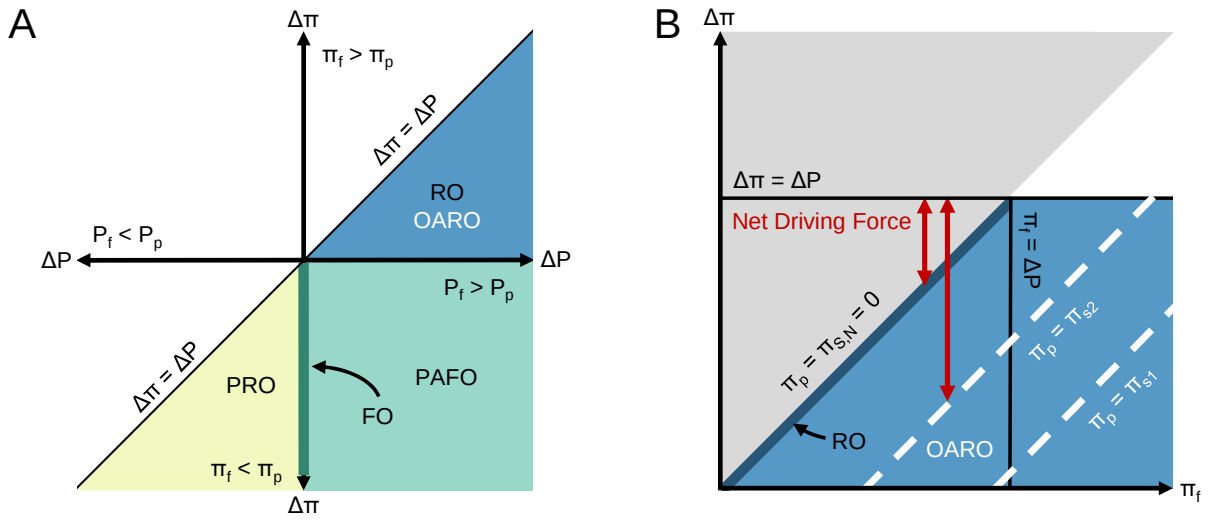

Figure 3.1. *A) Driving and retarding forces for reverse osmosis (RO), osmotically assisted reverse osmosis (OARO), forward osmosis (FO), pressure assisted forward osmosis (PAFO), and pressure retarded osmosis (PRO) membrane processes. We define the feed side (f) and permeate side (p) of the processes by the direction of the water flux (feed to permeate). Hydraulic pressure difference ($P_f – P_p$, ΔP) is a driving force when positive and is a retarding force when negative. Osmotic pressure difference ($\pi_f – \pi_p$, $\Delta\pi$) is a retarding force when positive and is a driving force when negative. The white region is where the driving force is smaller than the retarding force, thereby changing the direction of water transport and inverting the definition of the feed side and permeate side. B) RO (dark blue line, $\pi_p=0$) and OARO process region (blue) for two potential sweep concentrations (white dotted lines, $\pi_p=\pi_{s,1}$, $\pi_p=\pi_{s,2}$) at a*

constant applied hydraulic pressure difference (ΔP). The net driving force (ΔP – Δπ) of OARO is greater than the net driving force of RO with the same π_f. The grey region represents the infeasible case of π_p being negative.

While non-evaporative membrane-based processes more closely approach the thermodynamic minimum of separation for seawater desalination, they are limited in their effectiveness for treating high salinity brines.[11] RO water recovery is limited for high salinity brines (> 50 g/L) because the hydraulic pressure cannot exceed the membrane burst pressure (membrane dependent, but typically about 70-80 bar).[7] While ongoing research is focused on increasing this burst pressure, operating at ultra-high pressures may lead to severe compression of the polymer active layer and greater irreversible fouling. FO processes simply perform a salt exchange across a membrane, and thus do not dewater brines in the traditional sense without a second membrane, thermal, or solvent induced separations step.

Osmotically assisted reverse osmosis (OARO) is a non-evaporative, membrane-based process for high recovery, energy efficient desalination of high salinity brines.[3,12-14] OARO, like RO, uses hydraulic pressure to transport water across a semi-permeable membrane against the osmotic pressure difference between the feed and permeate ($+\Delta P$, $-\Delta\pi$). Unlike RO, where the permeate TDS approaches zero, OARO has a permeate-side saline sweep to reduce the osmotic pressure difference across the membrane and enable water transport even when the osmotic pressure of the feed exceeds the burst pressure of the membrane. Therefore, OARO expands the maximum TDS from which water can be recovered from hydraulic pressure driven membrane processes (Figure 3.1B). When multiple OARO stages are linked in series, this process enables the recovery of freshwater from high salinity brines.

The present work explores the theoretical limits of OARO processes and quantifies key performance metrics. We develop a discrete model that includes concentration polarization effects, and we apply this model to estimate the water recovery and energy consumption of the OARO process. We also explore the decision space of the OARO process by varying inlet feed and sweep concentrations, the feed pressure, the number of OARO stages, and the membrane area. Additionally, we compare the performance of OARO to other electricity driven desalination technologies, MVC and RO. Finally, we discuss the limitations of our model and identify the critical research steps necessary to fully assess the technical and economic feasibility of the OARO process.

3.3 Multi-staged osmotically assisted reverse osmosis process for water recovery

OARO is a novel process for realizing moderate water recoveries from high salinity brines at ambient temperatures via a membrane-based separation process. Figure 3.2 presents a schematic diagram of the proposed OARO process requiring multiple stages to produce desalinated water. Here, a high salinity feed is fed into an OARO module at a high hydraulic pressure. On the permeate-side of the module, a low-pressure sweep with a lower salinity flows counter-current to the feed. The high-pressure feed and low-pressure sweep establishes a hydraulic pressure difference that is greater than the osmotic pressure difference across the membrane. The resulting water flux concentrates the feed and dilutes the sweep. The concentrated feed is the reject from the OARO process and may be crystallized or otherwise disposed.

If the diluted sweep concentration is relatively high and the target recovery is not achievable via RO, then the diluted sweep can be pressurized and fed into a second OARO module. Since the diluted sweep has a lower concentration than the original feed, an equivalent

permeate volume can be realized with a lower sweep concentration. This second OARO module re-concentrates the diluted first sweep and dilutes the second sweep. The re-concentrated first sweep can be reused as the sweep inlet for the first OARO module and the diluted second sweep may require another OARO stage. The sweep concentrations successively decrease over a series of OARO stages until the sweep concentration is sufficiently low for RO. Ultimately, the OARO process will involve a feed inlet, a concentrated waste outlet, closed cycles of saline sweeps, and a product water outlet.

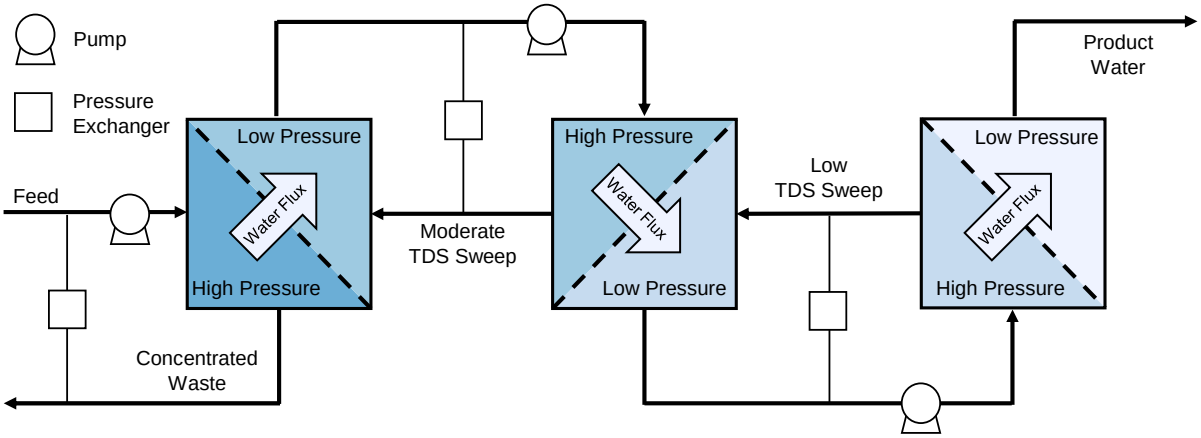

Figure 3.2. *Process diagram of the OARO process. The first two stages are OARO, while the final stage is RO.*

Energy consumption of the OARO process

The primary energy demand of the OARO process is the electricity required to power the pumps to pressurize the feed. A pressure exchanger, represented as a box linking the feed and the permeate streams in Figure 3.2, lowers the energy demand by transferring energy from the high pressure waste stream to the low pressure feed before the feed is pumped to the designed pressure.[7] In OARO, not only can the pressure exchanger be used for the feed, it can also be used

for each sweep cycle, as shown in Figure 3.2. An effective use of multiple pressure exchangers will lower the energy consumption of the OARO process.

OARO water flux and concentration polarization

Water flux in OARO processes depends upon the hydraulic and osmotic pressure difference across the membrane (Equation 3.1).

$$J_w = A\left[\left(P_f - P_s\right) - \left(\pi_{f,m} - \pi_{s,m}\right)\right] \quad (3.1)$$

Here, J_w is the water flux from the feed to the sweep, A is the pure water permeability coefficient, P_f and P_s are the hydraulic pressures for the feed and sweep, and $\pi_{f,m}$ and $\pi_{s,m}$ are the osmotic pressure at the membrane surface for the feed and sweep. The osmotic pressure of a solution can be estimated as a function of solute concentration (Equation 3.2).

$$\pi(C) = i\phi CRT \quad (3.2)$$

Here, i is the number of dissociating ions, ϕ is the osmotic coefficient, C is the solute concentration, R is the gas constant, and T is the temperature. Oftentimes, the solution is assumed to be ideal, ϕ = 1. However, solutions with high solute concentrations significantly deviate from ideal behavior. To account for non-ideal behavior, we model the osmotic coefficient as a function of solute concentration based on experimental results.

The osmotic pressure at the membrane surface is determined by adjusting the bulk solute concentration for concentration polarization effects.[15] In concentration polarization, water flux increases solute concentration at the membrane on the feed side and decreases solute concentration at the membrane on the sweep side relative to the bulk concentration, as shown in Figure 3.3. The solute concentration at the membrane surface for the feed and sweep can be calculated from equations 3.3 and 3.4.[16]

$$C_{f,m} = C_{f,b} \exp\left(\frac{J_w}{k}\right) \quad (3.3)$$

$$C_{s,m} = C_{s,b} \exp(-J_w K) \quad (3.4)$$

Where, $C_{f,m}$ and $C_{s,m}$ are the solute concentrations at the membrane surface for the feed and sweep, $C_{f,b}$ and $C_{s,b}$ are the respective bulk solute concentrations of the feed and sweep, k is the feed mass transfer coefficient, and K is the solute resistivity for diffusion in the sweep side porous support; refer to McCutcheon and Elimelech for further direction in determining these parameters.[16]

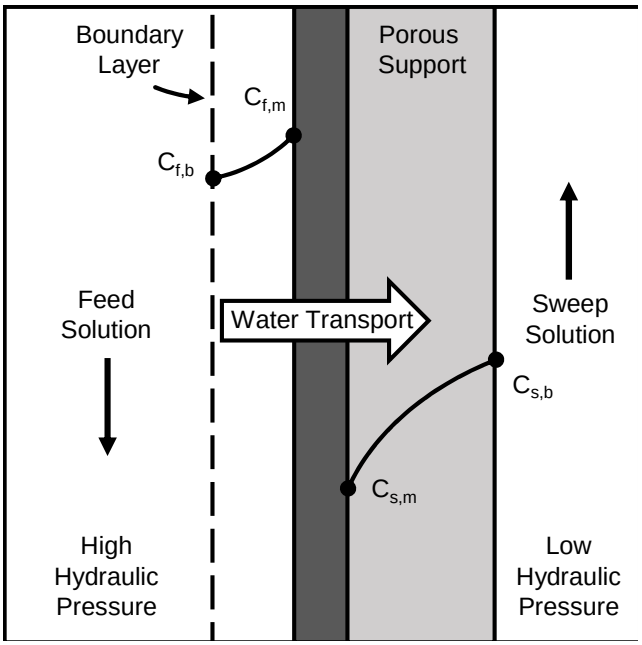

Figure 3.3. *Schematic diagram of an OARO module and the effects of concentration polarization on the solute concentration at the membrane surface ($C_{*,m}$) relative to the bulk concentration ($C_{*,m}$) of the feed (f) and sweep (s).*

3.4 Methods

Discrete element model for the OARO module

We model the OARO module as a flat plate with counter-current flow. The model uses a discrete element approach and an iterative method to solve the implicit flux and counter-current operation. Additional details on the mass balance equations and solution methods are provided in SI Section 2. The model input variables include: the module dimensions, and inlet flow rates, concentrations, and hydraulic pressures for the feed and sweep. The model output variables include: water recovery, and outlet flow rates, concentrations, and hydraulic pressures of the feed and sweep. For simplicity, we assume that the solute for the feed and sweep is sodium chloride, though any solute with low reverse flux, high osmotic pressure, and high diffusivity could be used in principle.[17] We source membrane specific parameters from the literature and use regressions of literature sources and databases to determine the concentration dependent solution properties: osmotic coefficient, diffusivity, and density.[18-20]

Salt rejection

The amount of salt flux will vary for each OARO module and will lead to salt accumulation or depletion within the sweep cycles. We assume there is no salt flux (100% salt rejection) to simplify the model and assess steady state operation. We consider salt flux and assess the expected salt rejection in SI Section 5.

Transitional flow regime

We assume a Reynolds number of 1000 for the feed and sweep flow. This transitional flow regime is typical of RO and FO processes in which spacers are utilized to promote mixing.[21-24] The effect of different spacer shapes is outside the scope of this work.

Pressure drop

Pressure drop is dependent on a multitude of factors: module design, spacers, flow regime, and membrane roughness. We assume a 5 kPa pressure drop per meter of membrane

length, which aligns with a combination of previous modeling and experimental work, as well as a friction based analytical calculation.[25,26] The sensitivity of the pressure drop on the performance of the OARO process is presented in SI Section 6.

Determining the number of modules and estimating the energy consumption

The OARO process is a system of modules that successively decreases the sweep concentration until a RO unit can be used to dewater a brine without exceeding the burst pressure of the membrane. To model this process, we require the OARO process to operate at steady state such that the permeate volume is equivalent across the multiple modules. Therefore, after the first OARO module is specified, successive OARO module design is deterministic.

We determine the operating parameters for successive modules by fixing design variables and adjusting the sweep concentration. We hold the module dimensions, inlet pressure, and sweep flow constant across all stages. We then adjust the sweep concentration for each OARO module to obtain the same permeate volume as the first module. Eventually, the last module will require a sweep TDS of zero; therefore, a RO module is used instead. Since there is no sweep for the RO module, we adjust the feed pressure to obtain the same permeate volume as the first module. Once the entire OARO process is specified, we can determine the total number of modules and estimate the energy consumption of the high-pressure pumps. In calculating the energy consumption, we assume the pumps have an 80% isentropic efficiency and the pressure exchangers are 96% efficient.[7]

Base case

We define a base-case scenario to provide a thorough example of the OARO process and establish a basis from which to compare other operating conditions. Our base case achieves the

goal of greater than 30% freshwater recovery for a 125 g/L sodium chloride brine. Table 3.1 provides the user specified variables of the base-case scenario. We use a common RO operating pressure of 65 bar, which is below the assumed membrane burst pressure of 70 bar. The module dimensions are arbitrary and are proportionally related to the feed flow rate. We assume the sweep inlet flowrate is half of the feed inlet flowrate, so that the diluted sweep outlet would have a similar flowrate and fluid flow regime as the feed inlet. We assume the membrane specific parameters are 1.0×10^{-12} m/(s-Pa) for the water permeability coefficient and 1000 μm for the structural parameter, which is representative of a commercial, asymmetric, cellulose triacetate membrane.[19] We assume a temperature of 298 K for both the feed and sweep solutions.

Table 3.1. *User specified variables for the OARO base-case scenario.*

Parameter	Symbol	Value	Units
Module length	L	10	m
Module width	W	1	m
Module height	H	1	mm
Feed inlet flowrate	Qf	1.0E-05	m^3/s
Sweep inlet flowrate	Qs	5.0E-06	m^3/s
Feed inlet pressure	Pf	65	bar
Feed TDS	C_f	125	g/L
Sweep inlet pressure	Ps	2	bar
First sweep TDS	C_s	175	g/L

3.5 Results and Discussion

The OARO process expands the use of membrane-based separation processes for high salinity brine dewatering. OARO can increase water recovery at hydraulic pressures below the membrane burst pressure by utilizing a saline sweep to reduce the osmotic pressure difference across the membrane. The sweep concentration is reduced in successive stages until the diluted sweep can be effectively treated using a traditional RO process. The OARO process has several key design considerations, such as: freshwater recovery, inlet feed and sweep concentration,

hydraulic pressure of the feed, number of stages, and membrane area. We assess these design variables by systematically varying the parameters around the base-case scenario established in Table 3.1.

Systematic analysis of OARO performance as a function of key design parameters

The purpose of the OARO process is to obtain higher water recoveries than RO by utilizing saline sweeps to reduce the osmotic pressure difference across the membrane. Figure 3.4A provides the simulated recovery for an OARO module with the base case module dimensions and a feed pressure of 65 bar across a range of inlet feed and sweep concentrations. The sweep with zero TDS has a recovery of 54% for a feed TDS of 35 g/L, which matches the expected performance of RO processes. As the feed concentration increases, the recovery rate from the RO process drops sharply to only 4% for a feed TDS of 75 g/L. This sharp decrease in recovery at higher feed concentrations demonstrates the value of the OARO process for enhancing recovery of high salinity brines. Using saline sweeps increases the recovery for a given feed concentration, and recoveries greater than 30% are obtained for feed TDS up to 145 g/L with sweep TDS up to 200 g/L.

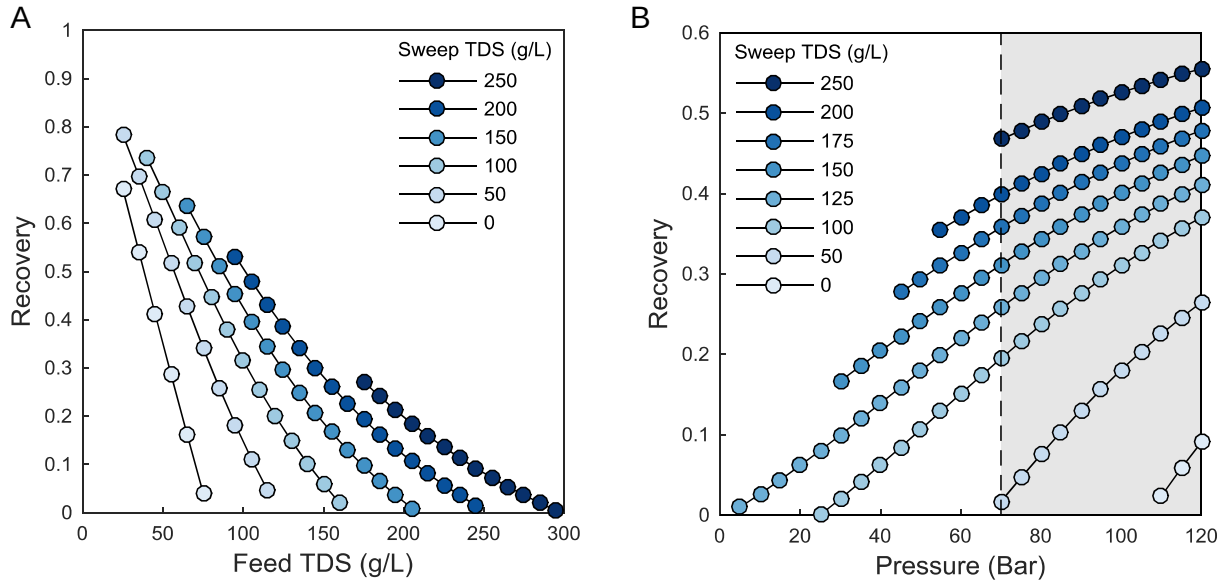

Figure 3.4. *OARO module recovery with base case module dimensions. A) OARO module recovery for a constant feed pressure of 65 bar and variable feed and sweep concentration. Cases with high sweep concentration and low feed concentrations operate as PAFO and are omitted from this graph. B) OARO module recovery for a feed with a TDS of 125 g/L sodium chloride and variable feed pressure and sweep concentration. The shaded region represents infeasible operating pressures based on the assumed membrane burst pressure of 70 bar (dotted line). Cases with high sweep concentrations and low feed pressure operate as PAFO and are omitted from this graph.*

Figure 3.4B provides the simulated recovery for an OARO module with an inlet feed TDS of 125 g/L across a range of feed pressures and sweep inlet concentrations. For this high salinity feed, RO processes (sweep TDS of 0 g/L) are not capable of recovering any freshwater using membranes with a burst pressure of 70 bar. Therefore, it is necessary to use a saline sweep to obtain operating conditions with higher recoveries and feasible operating pressures. Recoveries above 30% at feasible operating pressures occur only for sweep TDS above 150 g/L. In these instances, the inlet sweep TDS is greater than the inlet feed TDS of 125 g/L. However, the feed concentration is greater than the sweep concentration along the membrane because the module operates in counter-current flow. SI Section 4 provides a detailed description of the modeled concentration profile along the OARO module for the base-case scenario.

The OARO process has a set of physical, process, and operator imposed constraints that define a window of feasible OARO operating conditions. As discussed above, the feed pressure must be below the membrane burst pressure and the concentration of the sweep outlet must be less than that of the feed inlet to realize a series of successively decreasing sweep concentrations.

This second constraint is violated at low feed concentrations and high sweep concentrations for some set of feed pressures (Figure 3.4A). It is also violated at low feed pressures and high sweep concentrations for some set of feed concentrations (Figure 3.4B). In both cases, the water permeate volume is not sufficient to dilute the sweep below the feed inlet concentration, causing the module to operate in a PAFO regime (Figure 3.1). Figure 3.4 plots only OARO processes, and excludes the PAFO conditions.

In addition to the above physical and process constraints, a minimum target recovery is typically set to achieve water treatment goals. With these three constraints, a defined range for feasible OARO operation can be determined. Given a feed TDS of 125 g/L sodium chloride, minimum recovery of 30%, base-case module dimensions, and membrane burst pressure of 70 bar, the range of feasible inlet sweep TDS is 150 - 250 g/L and the maximum recovery is ~47%. For much higher feed TDS, the solubility of the solute may be an upper limit of sweep TDS, which for sodium chloride is 357 g/L at ambient tempeartures.[27]

While a high sweep concentration in the first module enhances water recovery, it also has a profound effect on the multi-module configuration and energy consumption of the process. Here, the multi-module configuration is determined from the first OARO module by requiring successive modules to operate at steady state and assuming all module and operating variables are constant, except for the sweep concentration, as described in Section 3.4. Once the entire OARO process is specified, we estimate the energy consumption of the high-pressure pumps. Figure 3.5 provides the freshwater recovery, number of modules, and energy consumption of the OARO process with the base case module dimensions, feed inlet pressure of 65 bar, and a feed TDS of 125 g/L sodium chloride.

As the first sweep TDS ranges from 100 to 225 g/L, the recovery, the number of modules, and the energy consumption increase from 17 to 42%, 3 to 7 modules, and 5.7 to 14 kWh per m^3 of produced water, respectively (Figure 3.5). Freshwater recovery increases because a higher sweep concentration decreases the osmotic pressure difference across the membrane and increases water flux. The number of modules increases because a higher first sweep concentration directly increases the concentration of the first diluted sweep and requires additional stages to lower the concentration to the point at which an RO module can be used. The energy consumption increases with a higher first sweep concentration for two reasons. First, an increase in the number of modules increases the mechanical energy loss for the system from the pressure drop along the additional modules and inefficiencies of the additional high pressure pumps and pressure exchangers. Second, in instances where the number of modules stays constant, a higher first sweep concentration will result in a higher diluted sweep concentration into the RO module. Recovering freshwater will thus require higher RO operating pressures and increased energy consumption. The trade-offs associated with the first sweep concentration on recovery, number of modules, and energy consumption will be key design considerations. While higher freshwater recovery will be beneficial, increasing the number of modules and energy consumption will also increase the capital and operating costs of the OARO system.

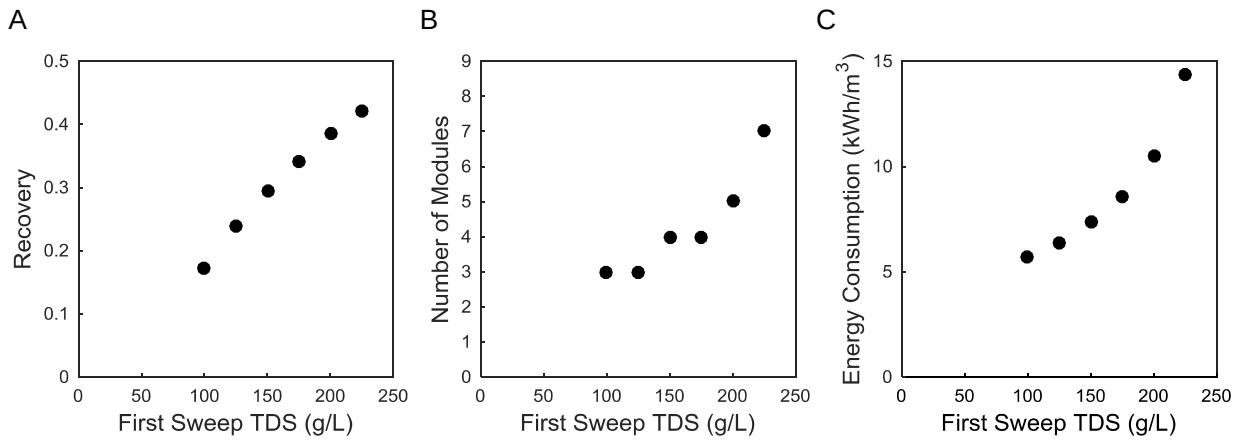

Figure 3.5*. Recovery (A), number of modules (B), and energy consumption (C) as a function of first inlet sweep concentration for the base-case module dimensions, feed pressure of 65 bar, and inlet feed TDS of 125 g/L sodium chloride.*

In addition to the process configurations, the type and dimensions of the module will influence the OARO process. In principle, the OARO module could adopt any configuration with a permeate side sweep. An ideal OARO module configuration will have counter-current feed and sweep flow, relatively high turbulence, and relatively low pressure drop. Counter-current feed and sweep flow minimizes the osmotic pressure difference across the membrane. As in RO, a relatively high turbulence is preferred to reduce concentration polarization effects and a relatively low hydraulic pressure drop across the module will increase water flux and pressure recovery. However, turbulence and pressure drop increase together, so the trade-off between increasing the turbulence and lowering the pressure drop will be a key design consideration. Another design consideration is the membrane area for each module. While increasing membrane area will increase the freshwater recovery, it also increases the pressure drop, salt permeate, and capital and operating costs of the OARO module. Varying the

membrane area adds another dimension to the OARO operating decision space, and this dimension is investigated further in SI Section 6.3 when the recovery of the process is set.

In addition to the design considerations already noted, the OARO process is also dependent upon membrane properties. An ideal OARO membrane would have high water permeability, high water selectivity, high membrane burst pressure, and a low structural parameter. Meanwhile, RO membranes are designed for only three of the four ideal properties: high water permeability, high water selectivity, and high membrane burst pressure.[28] RO membrane design has not prioritized reducing the structural parameter of the membrane support layer because RO does not experience permeate-side concentration polarization. In contrast, FO membranes are designed with low structural parameters, but they are not typically designed for high membrane burst pressures.[28] Ultimately, ideal OARO membranes most closely resemble ideal PRO and PAFO membranes, with high membrane burst pressures and low structural parameters.[29,30] Thus, we base the membrane properties on a commercially available cellulose triacetate asymmetric membrane commonly used in FO, PRO, and PAFO experiments.[19]

This section has detailed the general operating conditions for OARO processes over the range of feedwater salinities and recovery rates attractive for brine treatment associated with common industrial processes. In the subsequent sections, we detail the process variables and separation performance for the base case established in Table 3.1, providing detailed information about the process configuration, the concentration of each sweep, and the process performance as a function of membrane area and feed pressure.

Detailed process conditions in base case

The base case requires four modules, as shown in Figure 3.6, and has an average water flux of 1.3 L/(m^2 h), a recovery of 34%, and energy consumption of 8.6 kWh per m^3 of produced water. Figure 3.7 provides the corresponding concentration profiles of the feed and sweep cycles. The three OARO modules decrease the sweep TDS to 37 g/L (stream 8 in Figure 3.6), which is sufficiently low for the final RO module to achieve the same permeate volume as the upstream OARO modules. The detailed process configuration and variables of the base case demonstrates that the OARO treatment process can treat a high salinity feed (125 g/L TDS) through successively decreasing the concentration of the sweeps, but that the flux for this OARO example lies significantly below that which is typical for RO.

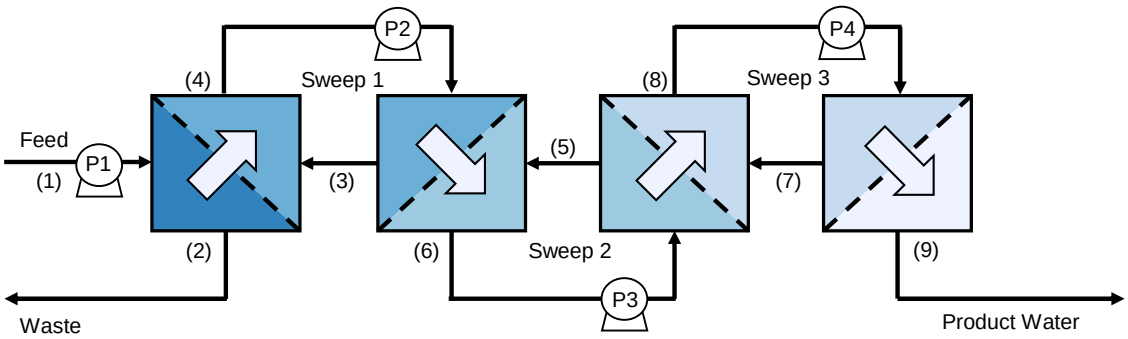

Figure 3.6. *The multi-module OARO process for the base-case scenario. The first three modules are OARO and the last module is RO. The streams are numbered (1)-(9). There are four pumps (P1-P4) and four pressure exchangers for the feed and sweep cycles (not shown).*

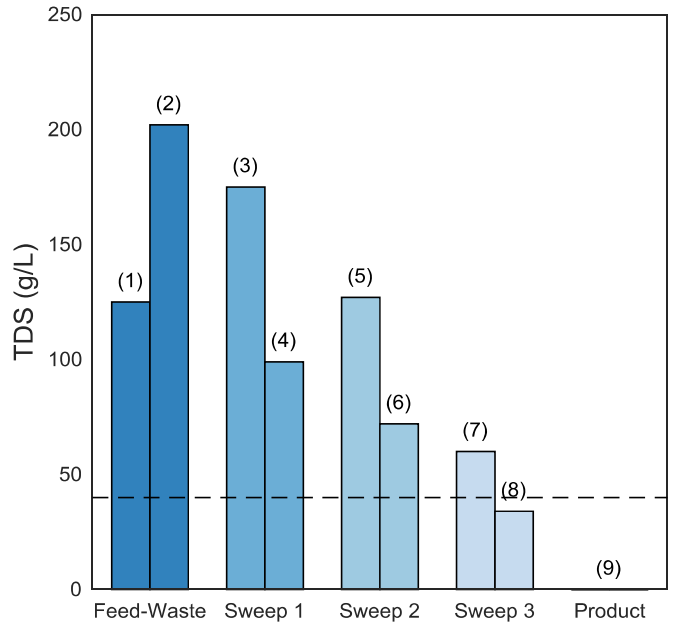

Figure 3.7. *Concentration profile of the feed and sweep cycles for the base case. The streams (1)-(9) are labeled in Figure 3.6. The dotted line represents the typical TDS upper limit (40 g/L) of economically viable reverse osmosis.*

Effect of membrane area on energy consumption for a set recovery

To evaluate the effect of membrane area on OARO process performance, we set the freshwater recovery at 35 and 40% and assess how increasing the module membrane area (10 m^2 in the base-case scenario) influences the energy consumption of the OARO process. We adjust the first sweep inlet concentration to maintain a constant recovery for the variable membrane area per module. Increasing the membrane area per module from 9 to 13 m^2 decreases the first stage sweep TDS from 185 to 165 g/L and 215 to 190 g/L, the number of modules from 5 to 4 and 7 to 5, and energy consumption from 9.7 to 7.8 and 14.4 to 9.3 kWh per m^3 of produced water for a recovery of 35 and 40%, respectively (Figure 3.8). As membrane area increases, the

water flux can be lower to obtain the same desired recovery, thereby allowing a lower first sweep concentration. As discussed previously, a lower first sweep concentration results in either fewer modules or a lower concentration of the diluted sweep into the final RO module. Ultimately, fewer modules or a lower operating pressure requirement on the RO unit decreases energy consumption.

Although larger membrane area per module decreases energy consumption, continued increases in membrane area are limited economically. Larger membrane areas will have greater capital and operating costs so the trade-off between the marginal performance improvement with increased cost will be a critical design consideration. In instances where a small increase in membrane area per module decreases the number of modules, the total membrane area of the OARO process decreased. For example, when the area per module increased from 9 to 10 m^2 for a 35% recovery, the total membrane area decreased from 45 m^2 (5 modules at 9 m^2 each) to 40 m^2 (4 modules at 10 m^2 each). In these cases, not only did increasing the membrane area per module decrease the energy consumption but it also decreased the total amount of membrane area and likely the associated membrane costs. This finding suggests that for a given recovery it is better to have fewer large OARO modules rather than more numerous small modules to decrease energy consumption and membrane costs.

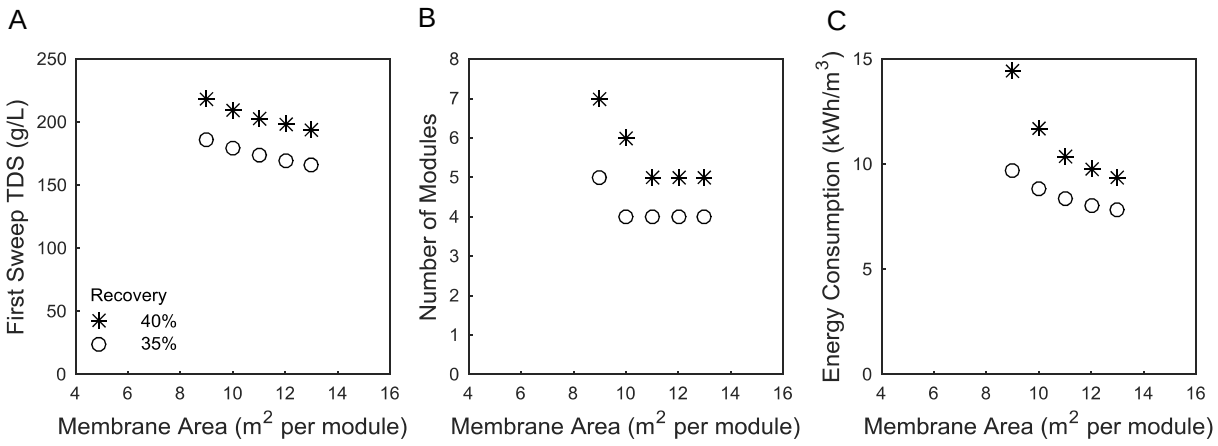

Figure 3.8. *First sweep concentration (A), number of modules (B), and energy consumption (C) versus membrane area for set recoveries of 35% and 40% (circle and asterisk, respectively). The inlet feed TDS is 125 g/L and feed pressure is 65 bar.*

Effect of hydraulic pressure on energy consumption for a set recovery

We assess the effect of feed pressure on OARO energy consumption, for a set freshwater recovery at 35 and 40%. We maintain a constant recovery for the variable feed pressure by adjusting the first sweep concentration. Increasing the feed pressure from 55 to 75 bar decreases the first sweep TDS from 195 to 160 g/L and 220 to 190 g/L, the number of modules from 6 to 3 and 8 to 4, and energy consumption from 11.1 to 7.8 and 14.7 to 9.6 kWh per m^3 of produced water for a recovery of 35 and 40%, respectively (Figure 3.9). The feed pressure relationship to the first sweep concentration, number of modules, and energy consumption is similar to the membrane area per module for the same reasons. Feed pressure increases the driving force for water flux, thereby allowing a lower first sweep concentration to obtain the target recovery. The lower first sweep concentration results in lower energy consumption through either fewer modules or a lower pressure demand in the final RO module. While higher feed pressures

decrease the number of modules and energy consumption, further increases in feed pressure are physically limited by the membrane burst pressure.

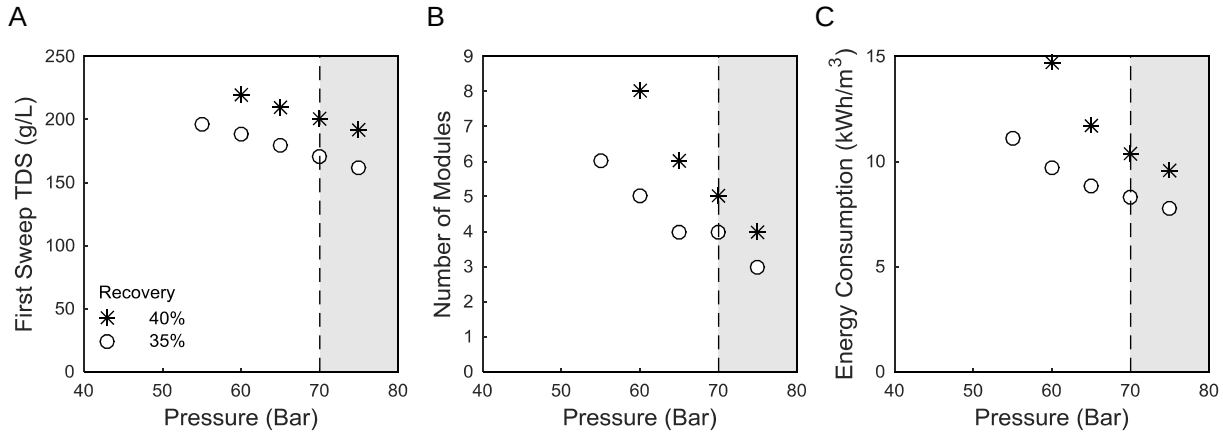

Figure 3.9. *First sweep concentration (A), number of modules (B), and energy consumption (C) versus feed pressure for set recoveries of 35% and 40% (circle and asterisk, respectively). The inlet feed TDS is 125 g/L sodium chloride and membrane area per module is 10 m^2. The shaded region represents infeasible operating pressures based on our assumed membrane burst pressure of 70 bar (dotted line).*

Comparison of OARO energy consumption to other brine treatment processes

The energy consumption is a key metric for assessing the effectiveness and economic feasibility of the OARO process relative to state of the art evaporative processes, such as MVC. Figure 3.10 provides literature-reported energy consumption values for RO and MVC, as well as our OARO simulations at a feed pressure of 65 bar and a membrane area per module of 10 and 20 m^2 for recoveries of 35 and 50%, respectively. RO energy consumption ranges from 1 to 2 kWh per m^3 of produced water for brackish (~5 g/L TDS) and seawater (35 g/L TDS) at a 50% recovery.[7] MVC energy consumption ranges from 11 to 25 kWh per m^3 of produced water for seawater (35 g/L TDS) to high salinity brines (150 g/L TDS) at recoveries of 35 to 50%.[1,6,31] The

OARO energy consumption is estimated as 2.9 to 3.7 kWh per m^3 of produced water for feed TDS of 60 g/L at 35 and 50% recovery, respectively. At a higher feed TDS of 140 g/L, these values increase to 12.4 and 19.3 kWh per m^3 of produced water for recoveries of 35 and 50%, respectively. These estimates of OARO energy consumption account for losses associated with pressure drop across the module, losses in the pressure exchangers, and the isentropic efficiency of the high pressure pump. Figure 3.10 also presents the theoretical minimum work to dewater the brines, which was calculated as the difference between Gibbs free energy of the inlet feed and the two products (freshwater and concentrated brine).[3] The Electrolyte NRTL method in AspenPlus is used to determine the Gibbs free energy of the solutions. The dewatering efficiency, defined as the ratio of the minimum theoretical work to the energy consumption, ranges from 30-55% for the membrane processes (RO and OARO) and 10-20% for MVC.

As anticipated, the energy consumption of treatment processes increases significantly with increasing feed concentration and freshwater recovery. For all investigated salinities, the membrane-based processes (RO and OARO) have lower energy consumption than MVC. The membrane-based process becomes less efficient at increasing salinities, while MVC has the opposite relationship and becomes more efficient. MVC can obtain recoveries as high as 90% for brines, which is well above the OARO recoveries from the base case examined in this study.[32] However, in instances where a recovery of 30-50% is desirable, such as volume reduction of wastewater before transport to disposal or further treatment, the OARO process may provide a lower energy consumption alternative to MVC. Additionally, it is possible to increase the recovery of the OARO process by increasing the total membrane area, the sweep concentrations, and number of modules. These changes to increase recovery would increase the energy consumption and the costs of the OARO process.

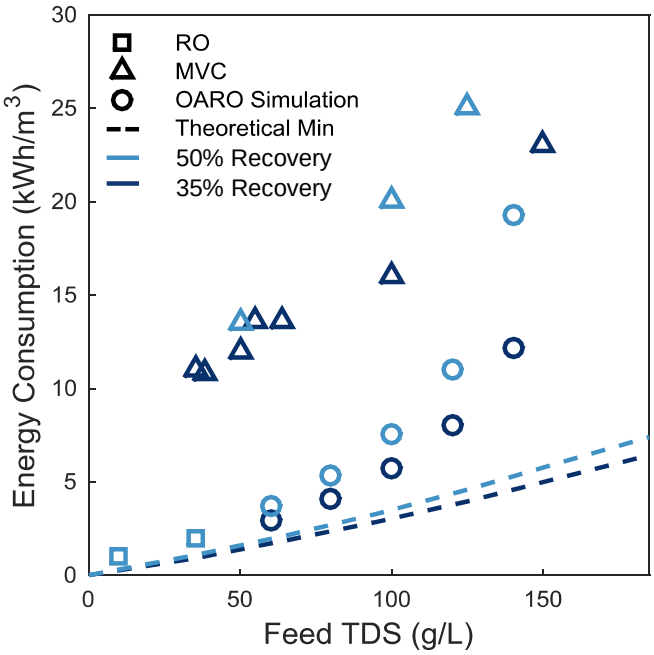

Figure 3.10. *Energy consumption of RO, MVC, OARO processes and theoretical minimum work with respect to feed concentration and recovery (35% dark blue, 50% light blue). The RO energy consumption is for the desalination of brackish and seawater at a recovery of 50%.*[7] *The MVC energy consumption spans seawater and higher salinity brines from the oil and gas industry at recoveries of 35-50%.*[1,6,31] *The OARO simulation uses a feed pressure of 65 bar and a membrane area per module of 10 and 20 m*^{2} *for a recovery of 35 and 50%, respectively. The theoretical minimum work is based on the difference in Gibbs free energy from the inlet feed and outlet products.*[3]

OARO model limitations

This work presents a first order model to estimate key performance metrics of the OARO process. Though the model estimates reasonable recovery rates and energy consumption, there

are several other factors including capital costs and pretreatment requirements that will contribute to determining the technical and economic viability of OARO process.

This work does not assess the economics of the OARO process. Without an economic analysis, we cannot determine whether our base case module assumptions and results are feasible. We recognize that many of the critical design variables, such as the membrane area and the number of modules, are solely constrained by costs. In general, the OARO process is expected to have high capital costs due to using multiple membrane modules, high pressure pumps, and pressure exchangers. While multiple modules suggest a high total membrane area, it is expected that the bulk of the capital costs will stem from the physical modules, pumps, and pressure exchangers. This realization suggests that a cost optimal OARO process will likely have a small number of stages, e.g. 2 to 3 large modules. While the maintenance of the membrane and equipment contributes to the operating costs, it is expected that energy consumption will dominate.

In addition, this work does not address pretreatment processes that are essential for reducing membrane fouling. Pretreatment is especially pertinent for high salinity brines sourced from the oil and gas industry that include many contaminants.[1] Further work to provide cost estimates and energy consumption of pretreatment will be critical to fully assess the feasibility of the OARO process.

Finally, we make several simplifying assumptions in our analysis that require further investigation. First, we simplify the OARO model by assuming 100% salt rejection. In reality, salt will diffuse across the membrane and the salt flux will vary for each module in the OARO process . The resulting non-steady state conditions will lead to salt accumulation or depletion within the sweep cycles and will require the addition of a purge stream and/or input of a saline

solution for sweep TDS and volume adjustment. Other non-steady state processes, e.g. variable feed quality and membrane scaling and fouling, were also not assessed. Finally, we assume that the membrane properties from experiments with relatively low concentrations and applied hydraulic pressure are applicable for the OARO process.[19] There is significant need for experimental work on the performance of membranes in the high salinity and high pressure operating conditions associated with the OARO process to complement the modeling work performed in this study. Preliminary experimental work for OARO conditions has recently been reported by Arena et. al.[33]

3.6 Conclusions

The dewatering of high salinity brines is costly due to the high energy demand or low recovery of existing treatment technologies. In this work, we introduce the OARO process and provide first order estimates of physically feasible operating conditions and performance metrics, such as recovery and energy consumption. We observe that the OARO process can obtain reasonable recoveries for reduced or comparable energy consumption as the MVC process, the dominant high salinity brine treatment technology. Future work to determine the feasibility of the OARO process will need to address the implications of our simplifying assumptions, consider the pretreatment requirements for long-term operation, and estimate the cost-competitiveness of this technology.

Supporting Information

The additional supporting information for this chapter is included in Appendix B. The supporting information includes further elaboration on: 1) osmotic pressure calculation, 2) discrete element model for a single OARO module, 3) multi-module model for the OARO process, 4) base case concentration profile, 5) salt rejection, 6) pressure drop.

3.7 Acknowledgements

This work was completed as part of National Energy Technology Laboratory (NETL) research for the U.S. Department of Energy's (DOE) Fossil Energy (FE) program and NSF CBET-1554117 and CBET-1215845. Support for T.V.B and J.T.A was provided by appointment to the National Energy Technology Laboratory Research Participation Program, sponsored by the U.S. Department of Energy and administered by the Oak Ridge Institute for Science and Education. T.V.B was also supported by the ARCS Foundation Fellowship.

3.8 Nomenclature

Treatment technology

RO - Reverse osmosis

MD - Membrane distillation

MED - Multi-effect distillation

MSF - Multi-stage flash distillation

MVC - Mechanical vapor compression

FO - Forward osmosis

PAFO - Pressure assisted forward osmosis

PRO - Pressure retarded osmosis

TDS - Total dissolved solids

Variables

P – Hydraulic pressure

ΔP - Hydraulic pressure difference across the membrane

π – Osmotic pressure

$\Delta\pi$ – Osmotic pressure difference across the membrane

A – Water permeability coefficient

J_w – Water flux

i – Number of dissociating ions

ϕ – Osmotic coefficient

C – Solute concentration

R – Gas constant

T – Temperature

k – Mass transfer coefficient

K – Solute resistivity for diffusion in the porous support

Subscripts

f – Feed side

p – Permeate side

s – Sweep side

b – bulk

m – Membrane surface

3.9 References

(1) Shaffer, D. L.; Arias Chavez, L. H.; Ben-Sasson, M.; Romero-Vargas Castrillon, S.; Yip, N. Y.; Elimelech, M. Desalination and reuse of high-salinity shale gas produced water: drivers, technologies, and future directions. *Environ Sci Technol* **2013,** *47* (17), 9569.

(2) Kaplan, R.; Mamrosh, D.; Salih, H. H.; Dastgheib, S. A. Assessment of desalination technologies for treatment of a highly saline brine from a potential CO2 storage site. *Desalination* **2017,** *404*, 87.

(3) Arena, J. T.; Jain, J. C.; Lopano, C. L.; Hakala, J. A.; Bartholomew, T. V.; Mauter, M. S.; Siefert, N. S. Management and dewatering of brines extracted from geologic carbon storage sites. *International Journal of Greenhouse Gas Control* **2017**.

(4) Al-Sahali, M.; Ettouney, H. Developments in thermal desalination processes: Design, energy, and costing aspects. *Desalination* **2007,** *214* (1), 227.

(5) Alkhudhiri, A.; Darwish, N.; Hilal, N. Membrane distillation: A comprehensive review. *Desalination* **2012,** *287*, 2.

(6) Thiel, G. P.; Tow, E. W.; Banchik, L. D.; Chung, H. W.; Lienhard V, J. H. Energy consumption in desalinating produced water from shale oil and gas extraction. *Desalination* **2015,** *366*, 94.

(7) Fritzmann, C.; Löwenberg, J.; Wintgens, T.; Melin, T. State-of-the-art of reverse osmosis desalination. *Desalination* **2007,** *216* (1), 1.

(8) Cath, T. Y.; Childress, A. E.; Elimelech, M. Forward osmosis: Principles, applications, and recent developments. *Journal of Membrane Science* **2006,** *281* (1–2), 70.

(9) Oh, Y.; Lee, S.; Elimelech, M.; Lee, S.; Hong, S. Effect of hydraulic pressure and membrane orientation on water flux and reverse solute flux in pressure assisted osmosis. *Journal of Membrane Science* **2014,** *465*, 159.

(10) Achilli, A.; Childress, A. E. Pressure retarded osmosis: From the vision of Sidney Loeb to the first prototype installation — Review. *Desalination* **2010,** *261* (3), 205.

(11) Elimelech, M.; Phillip, W. A. The Future of Seawater Desalination: Energy, Technology, and the Environment. *Science* **2011,** *333* (6043), 712.

(12) Sawyer, J. E.; Lucas, A. L.; Davis, V. M.; Dombek, B. D.; George, E. K., Treatment of waters with multiple contaminants. United States Patent US20140021135 A1, Jan 23, **2014**.

(13) Wohlert, C. W., Apparatus and methods for solution processing using reverse osmosis. United States Patent US20130270186 A1, Oct 17, **2013**.

(14) Lakerveld, R.; Kuhn, J.; Kramer, H. J. M.; Jansens, P. J.; Grievink, J. Membrane assisted crystallization using reverse osmosis: Influence of solubility characteristics on experimental application and energy saving potential. *Chemical Engineering Science* **2010,** *65* (9), 2689.

(15) Loeb, S.; Titelman, L.; Korngold, E.; Freiman, J. Effect of porous support fabric on osmosis through a Loeb-Sourirajan type asymmetric membrane. *Journal of Membrane Science* **1997,** *129* (2), 243.

(16) McCutcheon, J. R.; Elimelech, M. Influence of concentrative and dilutive internal concentration polarization on flux behavior in forward osmosis. *Journal of Membrane Science* **2006,** *284* (1–2), 237.

(17) Achilli, A.; Cath, T. Y.; Childress, A. E. Selection of inorganic-based draw solutions for forward osmosis applications. *Journal of Membrane Science* **2010,** *364* (1–2), 233.

(18) Scatchard, G.; Hamer, W. J.; Wood, S. E. Isotonic Solutions. I. The Chemical Potential of Water in Aqueous Solutions of Sodium Chloride, Potassium Chloride, Sulfuric Acid, Sucrose, Urea and Glycerol at 25°1. *Journal of the American Chemical Society* **1938,** *60* (12), 3061.

(19) She, Q.; Jin, X.; Tang, C. Y. Osmotic power production from salinity gradient resource by pressure retarded osmosis: Effects of operating conditions and reverse solute diffusion. *Journal of Membrane Science* **2012,** *401–402*, 262.

(20) Washburn, E.W., International Critical Tables of Numerical Data, Physics, Chemistry and Technology (1st Electronic Edition). Knovel. (**2003**). Online version available at http://app.knovel.com/hotlink/toc/id:kpICTNDPC4/international-critical/international-critical

(21) Cohen, R. D.; Probstein, R. F. Colloidal fouling of reverse osmosis membranes. *Journal of Colloid and Interface Science* **1986,** *114* (1), 194.

(22) Kim, S.; Hoek, E. M. V. Modeling concentration polarization in reverse osmosis processes. *Desalination* **2005,** *186* (1), 111.

(23) McCutcheon, J. R.; McGinnis, R. L.; Elimelech, M. Desalination by ammonia–carbon dioxide forward osmosis: Influence of draw and feed solution concentrations on process performance. *Journal of Membrane Science* **2006,** *278* (1–2), 114.

(24) Tan, C. H.; Ng, H. Y. Modified models to predict flux behavior in forward osmosis in consideration of external and internal concentration polarizations. *Journal of Membrane Science* **2008,** *324* (1–2), 209.

(25) Schwinge, J.; Wiley, D. E.; Fane, A. G. Novel spacer design improves observed flux. *Journal of Membrane Science* **2004,** *229* (1–2), 53.

(26) Xie, P.; Murdoch, L. C.; Ladner, D. A. Hydrodynamics of sinusoidal spacers for improved reverse osmosis performance. *Journal of Membrane Science* **2014,** *453*, 92.

(27) Maynard, R. L. The Merck Index: 12th edition 1996. *Occupational and Environmental Medicine* **1997,** *54* (4), 288.

(28) Tiraferri, A.; Yip, N. Y.; Phillip, W. A.; Schiffman, J. D.; Elimelech, M. Relating performance of thin-film composite forward osmosis membranes to support layer formation and structure. *Journal of Membrane Science* **2011,** *367* (1–2), 340.

(29) Anastasio, D. D.; Arena, J. T.; Cole, E. A.; McCutcheon, J. R. Impact of temperature on power density in closed-loop pressure retarded osmosis for grid storage. *Journal of Membrane Science* **2015,** *479*, 240.

(30) Coday, B. D.; Heil, D. M.; Xu, P.; Cath, T. Y. Effects of Transmembrane Hydraulic Pressure on Performance of Forward Osmosis Membranes. *Environmental Science & Technology* **2013,** *47* (5), 2386.

(31) Koren, A.; Nadav, N. Mechanical vapour compression to treat oil field produced water. *Desalination* **1994,** *98* (1), 41.

(32) Xu, P.; Hancock, N.; Guerra, K.; Cath, T.; Drewes, J. "An Integrated Framework for Treatment and Management of Produced Water: Technical Assessment of Produced Water Treatment Technologies," Department of Energy, Research Partnership to Secure Energy for America Project 07122–12. **2009**.

(33) Arena, J.T.; Bartholomew T.V.; Mauter, M.S.; Siefert, N.S. Dewatering of High Salinity Brines by Osmotically Assisted Reverse Osmosis. Proceedings of the 2017 AWWA-

AMTA Membrane Technology Conference and Exposition. February 13-17, **2017**, Long Beach, CA, USA

4.0 COST OPTIMIZATION OF OSMOTICALLY ASSISTED REVERSE OSMOSIS

4.1 Abstract

We develop a nonlinear optimization model to identify minimum cost designs for osmotically assisted reverse osmosis (OARO), a multi-staged membrane-based process for desalinating high salinity brines. The optimization model enables comprehensive evaluation of a complex process configuration and operational decision space that includes nonlinear process performance and implicit relationships between membrane stages, saline sweep cycles, and make-up, purge, and recycle streams. The objective function minimizes cost, rather than energy or capital expenditures, to accurately account for the tradeoffs in capital and operational expenses inherent in multi-staged membrane processes. Generally, we find that cost-optimal OARO processes minimize the number of stages, eliminate the use of saline make-up streams, purge from the first sweep cycle, and successively decrease stage membrane area and sweep flowrates. The optimal OARO configuration for treating feed salinities of 50-125 g/L total dissolved solids with water recoveries between 30-70% results in process costs less than or equal to \$6 per m^3 of product water. Sensitivity analysis suggests that future research to minimize OARO costs should focus on minimizing the membrane structural parameter while maximizing the membrane burst pressure and reducing the membrane unit cost.

4.2 Introduction

Safe and cost effective management of saline brines is a critical enabler of inland brackish water desalination,[1] produced water treatment,[2] geothermal energy production,[3] and CO_2 sequestration.[4-5] Current best practices for managing the vast majority of these brines is direct disposal via deep well injection or minimal treatment followed by discharge to the

environment.[6-7] The financial and environmental consequences of this disposal-centric management strategy are significant, including high capital and operational costs of transporting water,[8] environmental costs associated with brine transport and discharge,[9] and increased seismic risks associated with high volume brine injection.[10] These risks are driving the design of brine management networks that couple increased direct water reuse with desalination technologies that reduce brine disposal volume and produce high quality water for beneficial secondary applications.[11-15]

Unfortunately, there are few cost-effective technologies for managing high salinity brines. Membrane-based desalination technologies, such as reverse osmosis (RO), are designed to concentrate brines to approximately 75 g/L. Evaporative desalination technologies, such as mechanical vapor compression, can concentrate brines to near saturation (310 g/L TDS for pure NaCl solutions), but they are energy intensive[2, 16] and expensive (Figure 4.1).

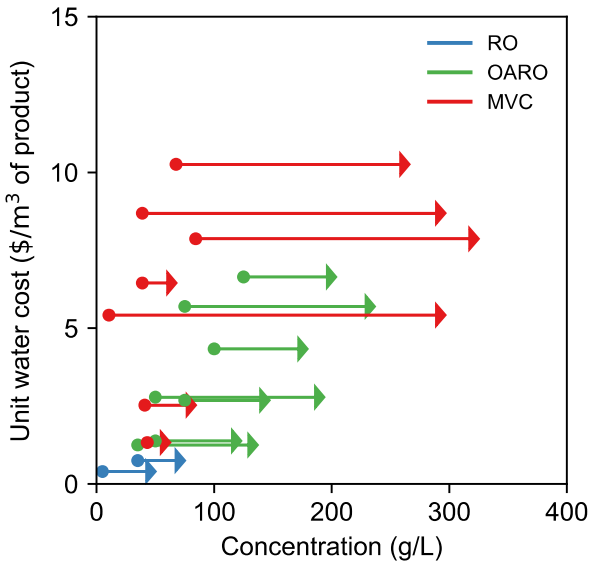

Figure 4.1. *Unit water costs for reverse osmosis (RO), osmotically assisted reverse osmosis (OARO), and mechanical vapor compression (MVC). Each arrow represents one case study for*

concentrating an inlet feed from an initial (circle) to final (arrow head) salinity. Life-cycle RO and MVC costs were obtained from literature,[7,17-21] while life-cycle OARO costs were estimated in this work. All cost estimates exclude pretreatment and post-treatment.

In our previous work,[22] we introduced osmotically assisted reverse osmosis (OARO), a non-evaporative membrane-based desalination process capable of concentrating high salinity brines. OARO modifies RO by adding a saline sweep to decrease the osmotic pressure difference across the membrane and increase water flux; further details on the OARO process are provided elsewhere.[22-25] We used a numeric modeling approach to demonstrate the feasibility of combining multiple OARO stages with a single RO stage to form an OARO brine concentration system (Figure 4.2). We estimated that an OARO process could produce a desalinated outlet stream from 50-140 g/L TDS brines with a water recovery of 35-50% and an energy consumption of 3-16 kWh/m^3 of product water.[22] This energy consumption of the OARO process is 30-60% lower than the state-of-the-art evaporative MVC process.[16] However, these energy benefits are greatest when the number of OARO stages are infinite and each stage has low water and high membrane areas. Given the high capital costs of OARO components, energy optimal configurations are not economically optimal. Evaluating the window of economic viability for OARO processes requires a full life-cycle cost estimate that captures the unique complexities of OARO performance.

Designing a cost-optimal OARO system is challenging due to the large and complex decision space for both process design and operation. The design space includes: water recovery; the number of stages; the use and flowrates of make-up, purge, and recycle streams; and the operating pressure, membrane area, sweep concentration, and sweep flowrate for each stage.

These numerous variables affect the OARO process performance and cost and interact in competing ways, thereby increasing the complexity of determining optimal system designs. While past work has evaluated the costs and energy intensity of specified OARO process configurations, the present work makes significant advances by evaluating the full process design and operational decision space.[22, 24, 26-27]

We address this large decision space by developing a cost optimization model for OARO processes that synthesizes the complex relationships between variables and identifies cost-optimal process design and operation. Cost-based process optimization has been used to assess the design of several desalination technologies including: RO,[28-30] MVC,[13] and multi-effect distillation.[17] The optimization model for an OARO process is inherently more complex than a RO process due to the presence of counter-current sweeps, multiple stages, and make-up, recycle, and purge streams. Additionally, the simplifying assumptions commonly used in RO modeling, including ideal solution, no salt flux across the membrane, no pressure drop across the module, and constant solution density, can introduce substantial errors in OARO processes.[31] Finally, the OARO process is more significantly affected by external and internal concentration polarization than RO, leading to a decrease in the effective driving force that must be accounted for in the optimization model.

This work presents the first comprehensive assessment of the optimal process configurations of the OARO process, the economic feasibility of the OARO process, and the value of improved membrane and process operating parameters in reducing OARO process costs. We use a nonlinear optimization model to identify cost-optimal OARO process designs and operating parameters. Cost optimality is a more relevant metric than energy optimality for processes with high capital costs. We apply this model to explore the performance and economic viability of

OARO processes over a range of inlet feed salinities and water recoveries, while providing additional details for three diverse case studies on environmentally relevant brines. Finally, we leverage the model to extract generalizable guidelines for low cost design and operation of the OARO process, assess the sensitivity of cost to key process parameters, and provide direction for future research on OARO processes.

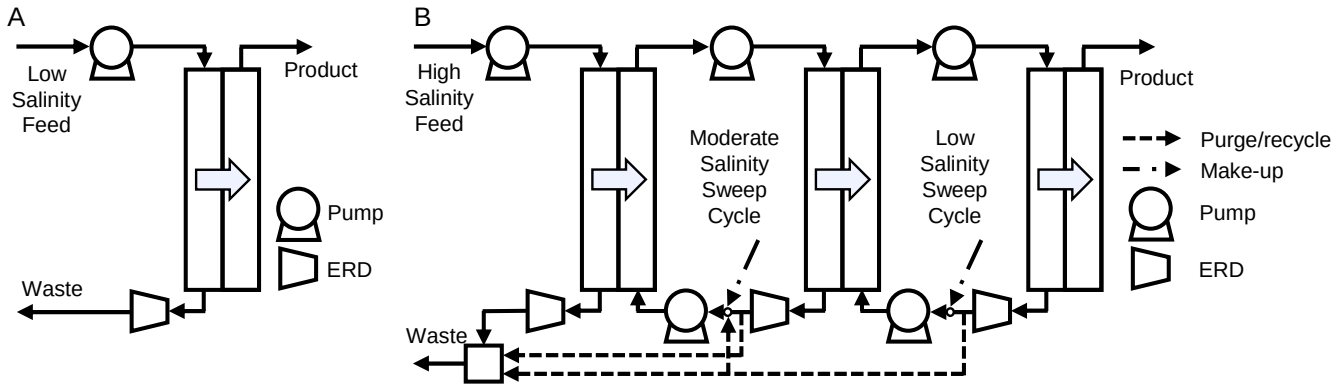

Figure 4.2. *Process diagram of A) a reverse osmosis system and B) an osmotically assisted reverse osmosis (OARO) system. The energy recovery device (ERD) is a pressure exchanger that reduces the demand on the high-pressure feed pumps by recovering energy from the concentrated feed outlets from each stage. The make-up, purge, and recycle streams are necessary for operating the system at steady state because the rate of salt permeation is not equal for each stage.*

4.3 Methods

Modeling osmotically assisted reverse osmosis

Conventional models for membrane based processes describe water flux as a function of the combined hydraulic and osmotic pressure differences across a semi-permeable membrane

(Eq. 4.1), while salt flux is described by the solute concentration difference across the membrane (Eq. 4.2).

$$Jw = A\ (\Delta P - \Delta\pi) \tag{4.1}$$

$$Js = B\ \Delta C \tag{4.2}$$

Here, Jw is the water flux [m^3/m^2-s], A is the water permeability coefficient [m/Pa-s], $\Delta P = (P_f - P_s)$ is the hydraulic pressure difference [Pa], $\Delta\pi = (\pi_f - \pi_s)$ is the osmotic pressure difference [Pa], Js is the salt flux [kg/m^2-s], B is the salt permeability coefficient [m/s], and $\Delta C_m = (C_f - C_s)$ is the concentration difference across the membrane [g/L]. The osmotic pressure is a function of the solute concentration and is detailed in Supplementary Information (SI) Section S.1.

In both Equation 1 and 2, the osmotic pressure and solute concentration differences are evaluated at the membrane interface. The concentration at the membrane interface can be approximated by correcting the bulk concentration of the feed or sweep streams to account for internal and external concentration polarization (Eq. 4.3 and 4.4).

$$Cm_f = Cb_f \exp\left(\frac{Jw}{k_f}\right) - \frac{Js}{Jw}\left[\exp\left(\frac{Jw}{k_f}\right) - 1\right] \tag{4.3}$$

$$Cm_s = Cb_s \exp\left(-Jw\left[\frac{S}{D} + \frac{1}{k_s}\right]\right) + \frac{Js}{Jw}\left[1 - \exp\left(-Jw\left[\frac{S}{D} + \frac{1}{k_s}\right]\right)\right] \tag{4.4}$$

Where Cm_f and Cm_s are the concentrations at the membrane interface [g/L], Cb_f and Cb_s are the concentrations in the bulk fluid [g/L], k_f is the feed-side mass transfer coefficient [m/s], S is the membrane structural parameter [m], D is the solute diffusion coefficient [m/s^2], and k_s is the sweep-side mass transfer coefficient [m/s]. The derivations of Equation 3 and 4 are provided in Supplementary Information (SI) Section S.2 and are similar to the PRO and FO formulations previously described in the literature.[31-33]

OARO cost optimization model

We develop a non-linear optimization model to minimize the cost of the OARO process. This model accounts for all key design and operating variables, including the flowrate of the make-up, purge, and recycle streams and the membrane area (including length and width dimensions), inlet and outlet hydraulic pressure, and inlet and outlet flowrates and concentrations for the feed and sweep of each stage. These variables are optimized subject to mass balance and process performance constraints, which are provided in SI Section S.3. As in our other work,[31] we model each stage with a finite difference approach in which the state variables (flowrate, concentration in the bulk fluid and at the membrane interface, hydraulic pressure, osmotic pressure, water flux, and salt flux) are calculated at nodes along the membrane stage (SI Figure S3).

We formulate the optimization model on a mass basis (i.e. mass flowrate and mass fraction), rather than a volumetric basis (i.e. volumetric flowrate and concentration), to reduce the number of bilinear terms. For example, the overall mass balance equation at each node is linear on a mass basis but would include bilinear terms on a volumetric basis (i.e. volumetric flowrate times density). Further details relating mass fraction, concentration, and fluid properties (i.e. density, viscosity, and osmotic pressure) are presented in SI Section S.1. In addition, our optimization model implements the following assumptions to formulate and specify the OARO process:

- The solute is NaCl and the non-ideal solution osmotic pressure matches experimental results.[34]

- The OARO membrane is asymmetric with the porous support on the sweep-side.
- The length and width dimensions for each membrane stage represent the configuration of the multiple membrane modules (i.e. number in parallel and series) that comprise the stage.
- The feed and sweep-side friction factor and Sherwood number can be estimated from correlations developed from simulated channels with mesh spacers.[35] These parameters are used to determine the pressure drop across the stage and the mass transfer coefficients as shown in SI Section S.3.
- The properties of the OARO and RO membrane (i.e. A, B, S), membrane module (i.e. channel height), fluid (i.e. diffusion coefficient), and equipment performance (i.e. pump efficiency and pressure exchanger efficiency) are specified parameters and are not dependent on operating conditions such as applied hydraulic pressure, salt concentration, and flowrate.
- The outlet diluted sweep is at atmospheric pressure (1 bar) and the outlet reconcentrated sweep is reduced to atmospheric pressure in the pressure exchanger.
- For the RO stage, the permeate side has no pressure drop (constant pressure of 1 bar along the stage) and negligible concentration polarization.
- Recycling only occurs from a sweep cycle to the preceding cycle, as shown in Figure 4.2B (i.e. a recycle stream occurs from sweep cycle 2 to sweep cycle 1).

Process and financial parameters

The process and financial parameters are presented in Table 4.1. The parameters were sourced from the peer-reviewed literature, with the following adaptations: 1) the OARO membrane water and salt permeability coefficient are assumed to be similar to those for a CTA membrane tested in PRO conditions rather than in RO conditions,[36] 2) the OARO structural parameter is conservatively assumed to be twice the value for the same CTA membrane,[36] 3) the OARO membrane unit cost (including the membrane element and module) is conservatively estimated at $\$50/m^2$. We use water and salt permeability coefficients from PRO because the process configuration more closely mimics OARO processes. However, we double the membrane structural parameter for OARO membranes because the OARO process operates at a higher hydraulic pressure and will thus require additional structural support. Finally, we assume that the OARO membrane module cost is significantly greater than RO because of the requirements imposed by counter flow operation. As a result, we estimate that OARO membrane unit costs will be more similar to those for pressure retarded osmosis (PRO) and forward osmosis (FO). We present the sensitivity of the OARO process costs to each of these parameters in the results section.

The OARO process costs are comprised of capital and operating costs. We determine the capital costs of the equipment sized in the optimization model (i.e. membrane units, pumps, and pressure exchangers) and we multiply the equipment costs by a practical investment factor of 1.6 to account for the indirect capital (e.g. piping, tanks, and control systems), siting, and installation costs. We assume the practical investment factor for the OARO process is larger than the 1.4 value for RO desalination plants because OARO is an emerging technology.[37] We also assume the capitalization factor is 10% instead of 8% for RO desalination plants because OARO systems are likely to be deployed in small scale distributed systems.[29, 37] We consider the following

operating costs: electricity, saline make-up, membrane replacement, maintenance, labor, and chemicals. The electricity, saline make-up, and membrane replacement costs are based on the total energy demand from the pumps, saline make-up demand, and initial membrane area, while the maintenance, labor, and chemical costs are estimated with factors based on the initial capital investment, as reported in Table 4.1. We exclude pretreatment costs because the OARO process is designed for high salinity brines that span a wide range of pretreatment needs.[38] We use the annualized capital costs, annual operating costs, and annual water production to estimate the unit water costs ($/m^3 of product water).

Table 4.1. *Process and financial parameters for cost optimization model.* [a]*The structural parameter is double the value of the cited literature.* [b]*The pressure exchanger cost is a non-linear function presented in SI Section S.3.4.* [c]*The practical investment factor is assumed to be 1.6 rather than 1.4 in the cited literature for RO desalination because OARO is an emerging technology.* [d]*The capitalization factor is assumed to be 10% rather than the 8% for RO desalination plants because OARO is likely to be deployed on a smaller scale. These conservative assumptions increase the estimated cost of the OARO process.*

Process parameters	Value	Unit	Source
OARO water permeability coefficient	1.0E-12	m/(Pa-s)	[36]
OARO salt permeability coefficient	8.0E-8	m/s	[36]
OARO maximum feed-side pressure	65	bar	[assumed]
OARO structural parameter	1200[a]	μm	[36]
RO water permeability coefficient	4.2E-12	m/(Pa-s)	[29]
RO salt permeability coefficient	3.5E-8	m/s	[29]
RO maximum feed-side pressure	85	bar	[29]
Pump efficiency	0.75	-	[29, 39]
Pressure exchanger efficiency	0.90	-	[29]
Maximum product water concentration	500	ppm	[40]
Financial parameters	**Value**	**Unit**	**Source**
OARO membrane unit cost	50	$/m^2	[assumed]
RO membrane unit cost	30	$/m^2	[29]
Pump cost	53	$/(m^{3}bar/h)	[37]
Pressure exchanger cost	non-linear function[b]	$/(m^3/h)	[29]
Electricity cost	0.07	$/kWh	[average of 29, 37]
Saturated saline make-up cost	0.025	$/kg	[estimated]
Load factor	90	%	[39]
Practical investment factor	1.6[c]	total investment/equipment cost	[37]
Capitalization factor	10[d]	% of initial investment/year	[29, 37]
Membrane replacement factor	15	% of initial membrane area/year	[39]
Maintenance & labor factor	2	% of initial investment/year	[estimated from 30, 39]
Chemical factor	1	% of initial investment/year	[estimated from 29-30]

Case study specifications

We perform a detailed analysis of the optimal OARO configurations for three case studies representing diverse OARO applications in RO brine concentration and oil and gas wastewater management where MVC is currently the state-of-the-art technology: 1) initial feed of 75 g/L TDS with 50% water recovery, 2) initial feed of 75 g/L TDS with 70% water recovery, and 3) initial feed of 125 g/L TDS with 40% water recovery. For all three cases, the feed flowrate is assumed to be 19.5 m^3/h, which is similar to the flowrate of several MVC systems deployed for oil and gas wastewater treatment.[41]

Solving the optimization model

We solve the optimization model given process and financial parameters (Table 4.1) and a specified initial feed concentration, water recovery, and number of stages. The optimal number of stages for a given initial feed concentration and water recovery is determined by solving the model for a varying number of stages (up to 7). We solve the cost optimization model using GAMS 24.5.6/CONOPT3.[42] We observe that this local optimization solver sufficiently explores the decision space. Specifically, we observe that the solver identifies the same solution for a give scenario with multiple initial guesses and the trends in the optimal design and operation are smooth across a wide range of salinities and water recoveries.

4.4 Results and Discussion

We apply the OARO process optimization model to assess the cost-optimal OARO design configurations and operating conditions for three high salinity brine desalination cases relevant to environmental process streams. OARO design configurations include the number of stages, the dimensions of each membrane stage, and the selection of make-up, purge, and recycle streams, while the OARO operating conditions include the make-up, purge, and recycle

flowrates, as well as the inlet and outlet flowrates, concentrations, and hydraulic pressures for the feed and sweep in each stage. The model size varies based on the number of stages, M, but is approximately equal to 250xM variables and constraints. This leads to average solution times of one and two seconds for the 3 and 5 stage configurations, respectively, when using an Intel i7 CPU 2.6 GHz processor with 8 GB of memory.

Optimal OARO process cost and design for the three case studies

Figure 4.3A provides the cost estimates for the three high-salinity brine desalination cases. The unit water costs were \$2.7, 5.7, and 6.6 per m^3 of product water for case 1, 2, and 3, respectively. Figure 4.3B provides the normalized cost of 4 components: membrane cost (initial membrane unit capital cost and membrane replacement cost), other capital costs (pumps, energy recovery devices, and indirect capital costs), electricity cost, and other operating costs (maintenance, labor, and chemical costs).

Membrane costs are the largest component of the total costs, accounting for 41-53% of total costs, while electricity costs account for 13-23% of the total costs. The contribution of each component to the total cost for the OARO process contrasts with those for a typical RO process in which the electricity costs account for 30-40% of total costs and membrane costs account for only 15-25%.[43] The relative contribution of the membrane costs are larger for the OARO process because: 1) there are multiple membrane stages, 2) OARO stages have water fluxes 4-10 times lower than typical RO stages (1-5 LMH vs 10-20 LMH), and 3) OARO membrane unit costs are expected to be significantly higher than current commercialized spiral wound RO modules. Quantifying the relative contributions of capital and operational costs provides insight into high impact opportunities for future cost reduction.

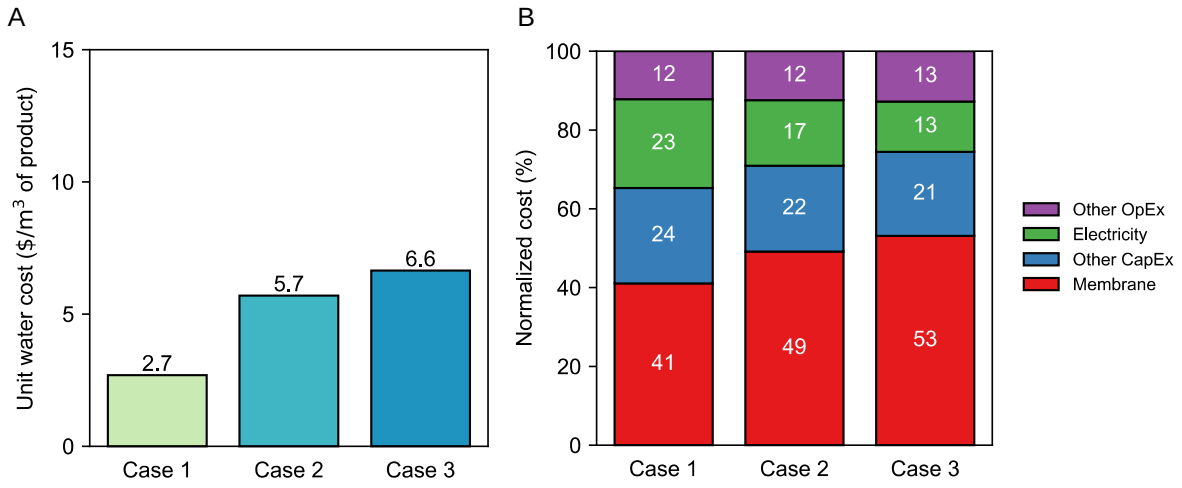

Figure 4.3. *Cost-optimal unit water costs (A) and normalized component costs (B) for the three high salinity brine desalination cases: 1) 75 g/L TDS with 50% recovery, 2) 75 g/L TDS with 70% recovery, and 3) 125 g/L with 40% recovery. Component costs include: membrane costs (membrane capital and replacement costs); other capital expenses (capital costs of pumps, pressure exchanger, and indirect capital); electricity costs; and other operating expenses (chemicals, maintenance, and labor). Comparisons to MVC and RO costs are presented in Figure 4.1.*

Figure 4.4 illustrates the cost-optimal operating conditions for the three OARO cases. The optimal number of stages were 3, 5, and 4 for Case 1, 2, and 3, respectively. Figure 4.4A presents the cost-optimal OARO concentration and flowrate profile of the initial feed, concentrated waste, sweep cycles, and product water. While the salinity of successive sweep streams in an OARO process will always decrease until RO can deliver the desired water recovery, there is a decrease in the difference between the sweep inlet and outlet for successive OARO stages. Similarly, cost-optimal OARO operating conditions decrease the feed and sweep flow rates with each successive OARO stage (Figure 4.4B). A lower inlet sweep flowrate

enables a higher inlet sweep concentration, which increases the average net driving force and water flux in the stage. This also has the effect of decreasing total membrane area in the stage, a significant driver of OARO system cost. However, sequentially lowering the sweep flowrate between stages requires higher water recovery from the later OARO stages. Optimal OARO operating conditions favor higher sweep flowrates in the initial stages of the OARO process, where the membranes are exposed to higher salinities and concentration polarization has a more negative effect on water recovery and process performance.

For all three cases, we observe that the optimal inlet feed pressure for the OARO and RO stages is the maximum allowable pressure of 65 and 85 bar, respectively (Figure 4.4C). We also observe that the optimal membrane area decreases by 25-45% for each successive OARO stage and that the RO stage has at least 85% less area than the first OARO stage (Figure 4.4D). The membrane area can be reduced in later stages because lower salinities are less impacted by concentration polarization and, thus, exhibit higher water flux.

In SI Section S.4, we present additional details on the case studies, including: the optimal make-up, recycle, purge flowrates; average water and salt flux for each stage; membrane stage dimensions (i.e. length and width); average feed-side and sweep-side Reynolds numbers and pressure drop for each stage. For all three cases, we observe that cost-optimal operation does not use make-up streams and only purges from the first sweep cycle. We further observe that for cost-optimal operation the average recycle rate between sweep cycles ranged from 8-14% of re-concentrated sweep flowrate and that the overall purge rate ranged from 6-11% of first stage permeate flowrate (SI Figure S9). The average feed-side and sweep-side Reynolds numbers ranged from 150-300 in OARO stages and 600-900 for the RO stage, while the feed-side and sweep-side pressure drop ranged from 0.5-2.6 bar for each stage (SI Figure S8).

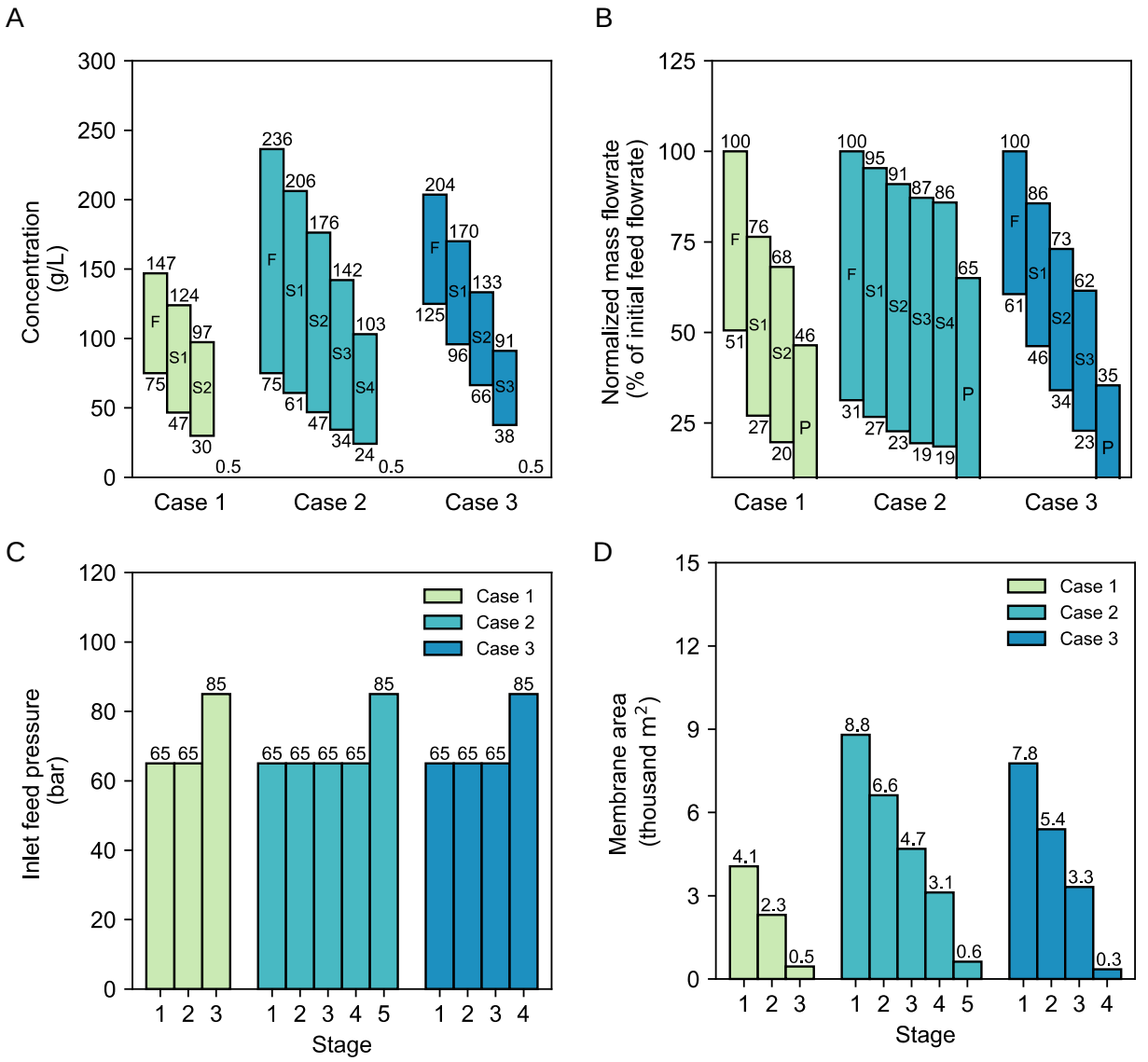

Figure 4.4. *Cost-optimal (A) concentration profile, (B) flowrate profile, (C) inlet feed pressure, and (D) membrane area for the three high-salinity brine desalination cases: 1) 75 g/L TDS with 50% recovery, 75 g/L TDS with 70% recovery, and 125 g/L with 40% recovery. The cost-optimal number of stages are 3, 5, and 4 for the three cases, respectively (noted in C-D). The concentration and flowrate profiles are denoted for the feed (F) and sweep cycles (SX), where X denotes the sweep cycle number. The product water concentration is the final bar for each case. The flowrates are normalized by the inlet feed mass flowrate in the first stage (20.5, 20.5, and*

21.1 Mg/h for each case, respectively. These are based on the assumed volumetric flowrate of 19.5 m^3/h and the density of the feed).

Effect of initial feed concentration and water recovery on optimal process design, cost, and energy consumption

Figure 4.5 presents the optimal number of stages, cost, and energy consumption for initial feed concentrations ranging from 25 to 150 g/L TDS and water recoveries ranging from 30 to 75%. At low initial feed concentrations (up to 50 g/L) and water recoveries up to 70%, a single RO stage can be used at a cost less than \$1/m^3. While a single RO stage can achieve a water recovery up to 50% for a 50 g/L feed at a cost of ~\$0.6/m^3, the resulting product water exceeds the 500 ppm specification. Because the present model formulation does not consider the possibility of a 2 RO stages in series, it identifies the cost-optimal configuration to be a single OARO stage followed by an RO stage for scenarios with an initial feed concentration of 50 g/L and water recoveries between 40-50%.

As the initial feed concentration and water recovery increase, the number of stages, unit water costs, and energy consumption increase. Generally, we observe that the cost-optimal number of OARO stages is the fewest number that can achieve the desired treatment specifications (Figure 4.5A). In some cases, the cost-optimal number of stages is the fewest number plus one. In these cases, the additional stage increases the average water flux in the OARO stages by decreasing the necessary reduction in successive sweep concentration per stage. This higher water flux reduces the total membrane area and costs by enough to overcome the additional costs associated with another stage (i.e. additional pump and pressure exchanger and increased electricity consumption).

Like the number of stages, the cost of the OARO process increases with both the initial feed salinity and water recovery (Figure 4.5B). Over the span of water treatment specifications, we observe a wide range of \$1.2 to \$15 per m^3 of desalinated product water for the OARO process. Literature-based cost estimates of the MVC process suggests that OARO will be cost competitive at less than \$6 per m^3 of product water (Figure 4.1). The OARO process meets or exceeds this target for initial feed salinities up to 125 g/L TDS and a range of water recoveries.

OARO process energy consumption is primarily a function of the number of stages (Figure 4.5C). The energy consumption is dependent on the number of stages because more than 90% of the energy loss in the system is associated with the pressure drop along the membrane stage and the water permeate moving from high to low pressure across the membrane stage. We observe that the OARO process energy consumption ranges from 5-20 kWh per m^3 of product water. This OARO process energy consumption range can be narrowed to 5-12 kWh per m^3 for economically viable conditions, which is less than the MVC energy consumption range of 10-30 kWh per m^3 of product water.[2, 16]

While the energy consumption of the OARO process could be reduced by decreasing the applied hydraulic pressure and the Reynolds number, these changes decrease the water flux and increase the unit water cost. In SI Section S.5, we use a multi-objective optimization technique to develop the relationship between optimal cost and energy consumption (SI Figure S10). We find that energy consumption reductions of 10-20% from the cost optimal solution will increase the costs by 12-15%. SI Section S.5 also contains additional discussion on the limitations of an energy optimization approach, specifically, that the solutions are trivial because the optimized decision variables equal their arbitrarily established bounds.

Additional details and trends on optimal design variables (i.e. average membrane area decrease between successive stages, average flowrate decrease between successive stages, average recycle rate between sweep cycles, and overall purge rate) for all scenarios covering feed concentrations from 25 – 150 g/L and water recoveries of 30-75% are provided in SI Section S.6.

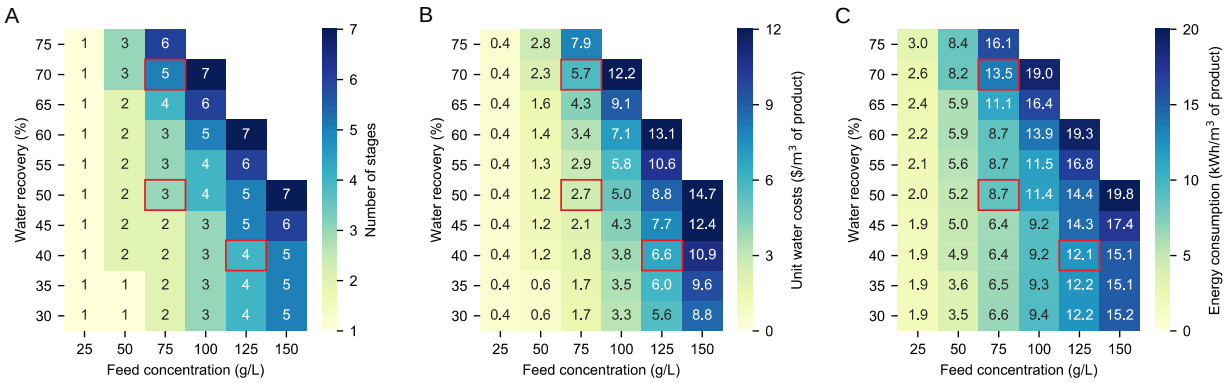

Figure 4.5. *Cost-optimal design configurations and associated performance metrics for OARO/RO membrane-based desalination processes: A) number of stages, B) unit water costs, C) energy use. The three high-salinity brine desalination cases are denoted with a red box. Instances in which there is only a single stage (1) indicate the performance of the RO process only.*

Cost sensitivity of OARO process designs

The optimal OARO configurations and product water costs reported in the previous sections are dependent on the assumed cost parameters reported in Table 4.1. The majority of OARO process components are identical to RO components (e.g. pumps, pressure exchangers, and piping), suggesting lower cost uncertainty and less potential for cost declines. In contrast, the OARO process requires substantially different membrane properties and module geometries than

traditional RO systems. While we accounted for these differences by using conservative cost estimates for membrane components, we did not account for any future cost savings on the membrane modules that might result from research and manufacturing experience with OARO.

We assess the sensitivity of OARO process costs for four key membrane parameters: membrane water permeability coefficient, membrane structural parameter, maximum inlet feed pressure, and membrane unit price. The cost sensitivity of OARO to other parameters, including salt permeability coefficient; channel height; mass transfer coefficient; friction factor; membrane replacement rate; capitalization factor; practical investment factor; maintenance, labor, and chemical cost factors; equipment capital costs; and electricity costs is provided in SI Section S.7.

Increases in the water permeability coefficient, A, decrease the unit water costs for the OARO process by decreasing the required membrane area. When A is doubled from 1E-12 to 2E-12 m/(Pa-s), we observe a modest decrease of 6-9% in the unit water costs for the three cases (Figure 4.6A). This suggests that, despite our earlier observation that membranes account for a significant fraction of OARO costs, designing membranes with improved permeability is unlikely to yield significant cost savings for OARO processes. An increase in permeability has a small effect on the OARO process cost because the water flux in the OARO process is more strongly limited by concentration polarization than the bulk driving force. This finding is consistent with other studies that report limited value in increasing membrane permeability.[1, 44]

In contrast, decreasing the structural parameter, S, yields significant decreases in the unit water costs for OARO. As S is halved from 1200 to 600 μm, we observe a decrease of 15-26% in the unit water costs for the three cases (Figure 4.6B). This difference in the relative impact of A and S parameters on OARO costs highlights the degree to which internal concentration

polarization limits OARO performance and suggests that future research should prioritize lowering the membrane structural parameter over increasing the water permeability coefficient.

Of course, a decreased structural parameter of the membrane support often comes at the expense of high membrane burst pressures, which would have negative effects for recovery in OARO stages. When the maximum inlet feed pressure is decreased from 65 to 55 bar, for example, we observe a 22-38% increase in the unit water costs for the three cases (Figure 4.6C). Conversely, when the maximum inlet feed pressure is increased from 65 to 85 bar, we observe a 35-38% decrease in the unit water costs. While the structural parameter and maximum applied hydraulic pressure are likely to be correlated, we are unaware of studies that quantitatively describe this relationship across a range of membrane chemistries. Thus, our current model varies these parameters independently.

Finally, we consider the effects of potential reductions in OARO membrane costs associated with widespread deployment of OARO systems. If the cost of the membrane decreases from \$50 to \$30 per m^2, the average RO membrane cost reported in the literature (Table 4.1), we observe a 23-30% decrease in the unit water costs for the three cases (Figure 4.6D).

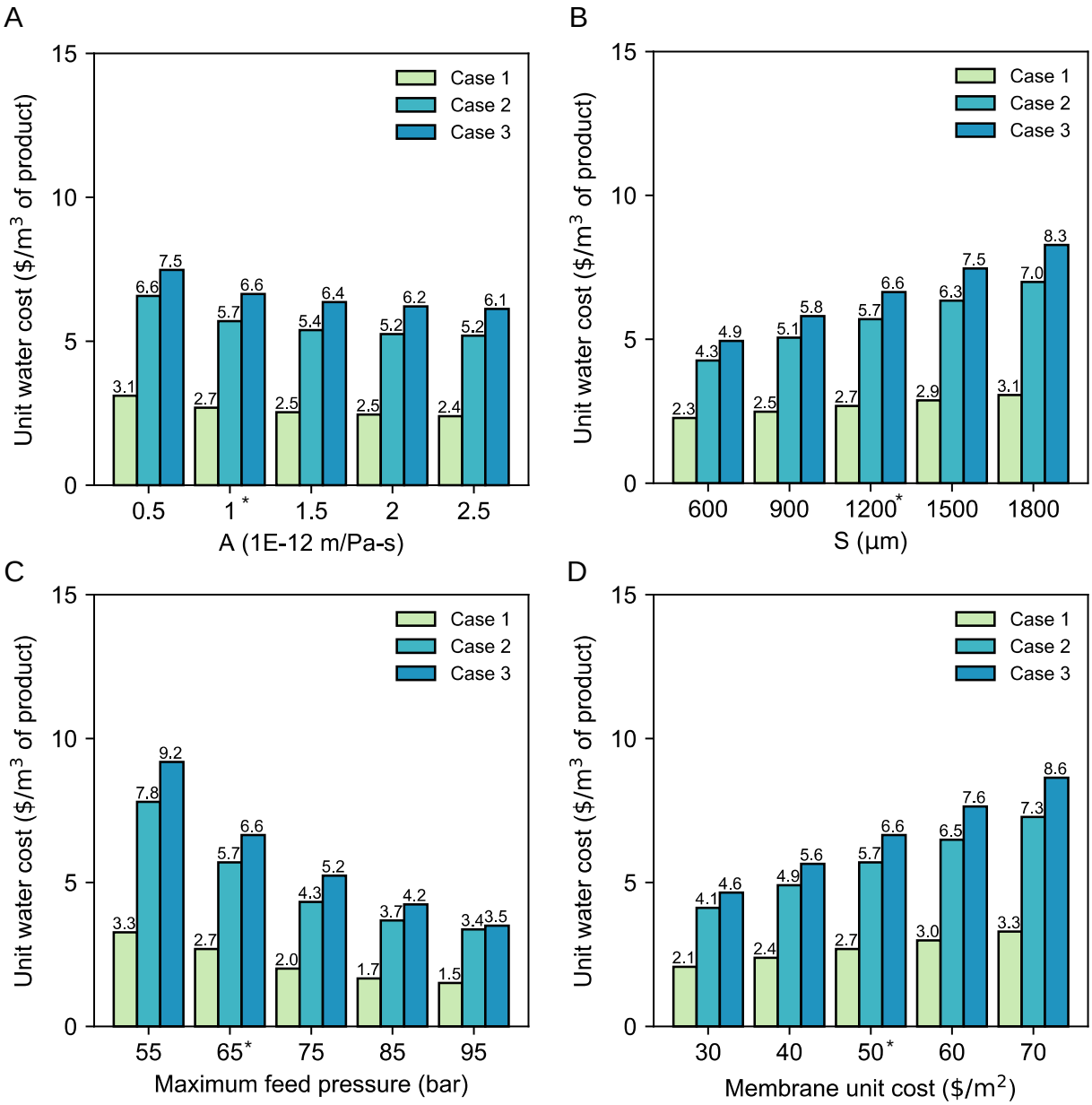

Figure 4.6. *OARO cost sensitivity for A) water permeability coefficient, A; B) structural parameter, S; C) maximum inlet feed pressure, D) OARO membrane unit cost. The baseline value used in modeling each of the cases is marked with an asterisk.*

4.5 Conclusions

The OARO process may lower the cost and energy consumption of high salinity brine management for select feedwater concentrations and water recoveries. This work is the first to comprehensively assess the costs of the OARO process and report cost-optimal design and operation. We identify the inlet feed salinities (up to 125 g/L) and water recoveries (up to 70%) where the OARO process has the potential to be economically feasible given current membrane performance.

In addition to reporting on the cost-competitiveness with respect to other technologies, we observe consistent trends in cost-optimal OARO design and operation. Generally, cost-optimal OARO processes should be configured with as few stages as possible, no saline make-up streams, purge from the first sweep cycle, and successively decreasing stage membrane area and sweep flowrate. These processes should be operated as close as possible to the burst pressure of the membrane. Future research to reduce OARO process costs should focus on reducing membrane unit costs while increasing membrane burst pressure and decreasing membrane structural parameter.

Finally, we demonstrate that energy optimality is an insufficient condition for evaluating membrane-based water treatment processes. Energy optimal module configurations permit unrealistically large membrane areas that are unlikely to be cost effective as a treatment technology. By evaluating cost-optimal design configurations and developing a Pareto frontier for cost and energy tradeoffs, we provide a more realistic assessment of the utility of the emerging OARO water treatment process.

Supporting Information

The additional supporting information for this chapter is included in Appendix C. The supporting information contains details for 1) solution properties; 2) interfacial membrane concentration; 3) optimization model formulation; 4) additional details on the case studies, 5) tradeoffs between energy consumption and cost, 6) key design and operational variables for the OARO process, 7) additional sensitivity analyses.

4.6 Acknowledgements

We would like to thank Jason Arena and Madison Wenzlick for their parallel efforts on assessing OARO membrane properties and MVC processes, respectively. This work was funded via the U.S. Department of Energy's National Energy Technology Laboratory under the Crosscutting Technologies Division and via NSF CBET-1554117. Support for T.V.B. was provided by appointment to the National Energy Technology Laboratory Research Participation Program, sponsored by the U.S. Department of Energy and administered by the Oak Ridge Institute for Science and Education. T.V.B. was also supported by the ARCS Foundation Fellowship.

4.7 References

1. Elimelech, M.; Phillip, W. A., The Future of Seawater Desalination: Energy, Technology, and the Environment. *Science* **2011,** *333* (6043), 712.

2. Shaffer, D. L.; Arias Chavez, L. H.; Ben-Sasson, M.; Romero-Vargas Castrillon, S.; Yip, N. Y.; Elimelech, M., Desalination and reuse of high-salinity shale gas produced water: drivers, technologies, and future directions. *Environ Sci Technol* **2013,** *47* (17), 9569-83.

3. Barbier, E., Geothermal energy technology and current status: an overview. *Renewable and Sustainable Energy Reviews* **2002,** *6* (1), 3-65.

4. Buscheck, T. A.; Sun, Y.; Chen, M.; Hao, Y.; Wolery, T. J.; Bourcier, W. L.; Court, B.; Celia, M. A.; Julio Friedmann, S.; Aines, R. D., Active CO2 reservoir management for carbon storage: Analysis of operational strategies to relieve pressure buildup and improve injectivity. *International Journal of Greenhouse Gas Control* **2012,** *6*, 230-245.

5. Arena, J. T.; Jain, J. C.; Lopano, C. L.; Hakala, J. A.; Bartholomew, T. V.; Mauter, M. S.; Siefert, N. S., Management and dewatering of brines extracted from geologic carbon storage sites. *International Journal of Greenhouse Gas Control* **2017,** *63*, 194-214.

6. Veil, J. A. *U.S. Produced Water Volumes and Management Practices in 2012*; Ground Water Protection Council: Oklahoma City, Oklahoma, 2015.

7. Fritzmann, C.; Löwenberg, J.; Wintgens, T.; Melin, T., State-of-the-art of reverse osmosis desalination. *Desalination* **2007,** *216* (1), 1-76.

8. Mauter, M. S.; Palmer, V. R., Expert Elicitation of Trends in Marcellus Oil and Gas Wastewater Management. *J Environ Eng* **2014,** *140* (5), B4014004.

9. Behrer, A. P.; Mauter, M. S., Allocating Damage Compensation in a Federalist System: Lessons from Spatially Resolved Air Emissions in the Marcellus. *Environmental Science & Technology* **2017,** *51* (7), 3600-3608.

10. Ellsworth, W. L., Injection-Induced Earthquakes. *Science* **2013,** *341* (6142).

11. Yang, L.; Grossmann, I. E.; Mauter, M. S.; Dilmore, R. M., Investment optimization model for freshwater acquisition and wastewater handling in shale gas production. *Aiche J* **2015,** *61* (6), 1770-1782.

12. Bartholomew, T. V.; Mauter, M. S., Multiobjective Optimization Model for Minimizing Cost and Environmental Impact in Shale Gas Water and Wastewater Management. *Acs Sustain Chem Eng* **2016,** *4* (7), 3728-3735.

13. Onishi, V. C.; Carrero-Parreño, A.; Reyes-Labarta, J. A.; Fraga, E. S.; Caballero, J. A., Desalination of shale gas produced water: A rigorous design approach for zero-liquid discharge evaporation systems. *Journal of Cleaner Production* **2017,** *140*, 1399-1414.

14. Salih, H. H.; Li, J.; Kaplan, R.; Dastgheib, S. A., Life cycle assessment of treatment and handling options for a highly saline brine extracted from a potential CO2 storage site. *Water Research* **2017,** *122* (Supplement C), 419-430.

15. Gao, J.; You, F., Optimal design and operations of supply chain networks for water management in shale gas production: MILFP model and algorithms for the water-energy nexus. *Aiche J* **2015,** *61* (4), 1184-1208.

16. Thiel, G. P.; Tow, E. W.; Banchik, L. D.; Chung, H. W.; Lienhard V, J. H., Energy consumption in desalinating produced water from shale oil and gas extraction. *Desalination* **2015,** *366*, 94-112.

17. Onishi, V. C.; Carrero-Parreño, A.; Reyes-Labarta, J. A.; Ruiz-Femenia, R.; Salcedo-Díaz, R.; Fraga, E. S.; Caballero, J. A., Shale gas flowback water desalination: Single vs multiple-effect evaporation with vapor recompression cycle and thermal integration. *Desalination* **2017,** *404*, 230-248.

18. Veza, J., Mechanical vapour compression desalination plants — A case study. *Desalination* **1995,** *101* (1), 1-10.

19. Jamil, M. A.; Zubair, S. M., On thermoeconomic analysis of a single-effect mechanical vapor compression desalination system. *Desalination* **2017,** *420*, 292-307.

20. Al-Sahali, M.; Ettouney, H., Developments in thermal desalination processes: Design, energy, and costing aspects. *Desalination* **2007,** *214* (1), 227-240.

21. Wenzlick, M.; Siefert, N.; Hakala, A., Tailoring Treated Brines for Reuse Scenarios. In *SPE/AAPG/SEG Unconventional Resources Technology Conference*, Unconventional Resources Technology Conference: Houston, Texas, USA, 2018.

22. Bartholomew, T. V.; Mey, L.; Arena, J. T.; Siefert, N. S.; Mauter, M. S., Osmotically assisted reverse osmosis for high salinity brine treatment. *Desalination* **2017,** *421*, 3-11.

23. Arena, J. T.; Bartholomew, T. V.; Mauter, M. S.; Siefert, N. S. In *Dewatering of High Salinity Brines by Osmotically Assisted Reverse Osmosis*, 2017 AWWA-AMTA Membrane Technology Conference and Exposition, Long beach, CA, USA, February 13-17, 2017; Long beach, CA, USA, 2017.

24. Chen, X.; Yip, N. Y., Unlocking High-Salinity Desalination with Cascading Osmotically Mediated Reverse Osmosis: Energy and Operating Pressure Analysis. *Environmental Science & Technology* **2018,** *52* (4), 2242-2250.

25. Kim, J.; Kim, D. I.; Hong, S., Analysis of an osmotically-enhanced dewatering process for the treatment of highly saline (waste)waters. *Journal of Membrane Science* **2018,** *548,* 685-693.

26. Osipi, S. R.; Secchi, A. R.; Borges, C. P., Cost assessment and retro-techno-economic analysis of desalination technologies in onshore produced water treatment. *Desalination* **2018,** *430,* 107-119.

27. Kim, J.; Kim, J.; Kim, J.; Hong, S., Osmotically enhanced dewatering-reverse osmosis (OED-RO) hybrid system: Implications for shale gas produced water treatment. *Journal of Membrane Science* **2018,** *554,* 282-290.

28. Marcovecchio, M. G.; Aguirre, P. A.; Scenna, N. J., Global optimal design of reverse osmosis networks for seawater desalination: modeling and algorithm. *Desalination* **2005,** *184* (1), 259-271.

29. Lu, Y.-Y.; Hu, Y.-D.; Zhang, X.-L.; Wu, L.-Y.; Liu, Q.-Z., Optimum design of reverse osmosis system under different feed concentration and product specification. *Journal of Membrane Science* **2007,** *287* (2), 219-229.

30. Vince, F.; Marechal, F.; Aoustin, E.; Bréant, P., Multi-objective optimization of RO desalination plants. *Desalination* **2008,** *222* (1), 96-118.

31. Bartholomew, T. V.; Mauter, M. S. Computational Framework for Modeling Membrane Processes without Process and Solution Property Simplifications. *J. Membr. Sci.* **2019**, *573*, 682–693.

32. Yip, N. Y.; Tiraferri, A.; Phillip, W. A.; Schiffman, J. D.; Hoover, L. A.; Kim, Y. C.; Elimelech, M., Thin-Film Composite Pressure Retarded Osmosis Membranes for Sustainable

Power Generation from Salinity Gradients. *Environmental Science & Technology* **2011,** *45* (10), 4360-4369.

33. Bui, N.-N.; Arena, J. T.; McCutcheon, J. R., Proper accounting of mass transfer resistances in forward osmosis: Improving the accuracy of model predictions of structural parameter. *Journal of Membrane Science* **2015,** *492*, 289-302.

34. Scatchard, G.; Hamer, W. J.; Wood, S. E., Isotonic Solutions. I. The Chemical Potential of Water in Aqueous Solutions of Sodium Chloride, Potassium Chloride, Sulfuric Acid, Sucrose, Urea and Glycerol at 25°1. *Journal of the American Chemical Society* **1938,** *60* (12), 3061-3070.

35. Guillen, G.; Hoek, E. M. V., Modeling the impacts of feed spacer geometry on reverse osmosis and nanofiltration processes. *Chemical Engineering Journal* **2009,** *149* (1), 221-231.

36. She, Q.; Jin, X.; Tang, C. Y., Osmotic power production from salinity gradient resource by pressure retarded osmosis: Effects of operating conditions and reverse solute diffusion. *Journal of Membrane Science* **2012,** *401–402*, 262-273.

37. Malek, A.; Hawlader, M. N. A.; Ho, J. C., Design and economics of RO seawater desalination. *Desalination* **1996,** *105* (3), 245-261.

38. Fakhru'l-Razi, A.; Pendashteh, A.; Abdullah, L. C.; Biak, D. R. A.; Madaeni, S. S.; Abidin, Z. Z., Review of technologies for oil and gas produced water treatment. *Journal of Hazardous Materials* **2009,** *170* (2), 530-551.

39. Park, C.; Park, P.-K.; Mane, P. P.; Hyung, H.; Gandhi, V.; Kim, S.-H.; Kim, J.-H., Stochastic cost estimation approach for full-scale reverse osmosis desalination plants. *Journal of Membrane Science* **2010,** *364* (1), 52-64.

40. Agency, U. S. E. P. *National Primary Drinking Water Regulations*; 2009.

41. Xu, P.; Stoll, Z.; Mengistu, G.; Cath, T.; Drewes, J. *Technical Assessment of Produced Water Treatment Technologies*; RPSEA Project 11122-53; Colorado School of Mines, New Mexico State University: 2016.

42. Drud, A. S., CONOPT—A Large-Scale GRG Code. *ORSA Journal on Computing* **1994,** *6* (2), 207-216.

43. Rao, P.; Sheaffer, P.; Morrow, W.; Brueske, S.; Dollinger, C.; Price, K.; Sarker, P.; Ward, N.; Cresko, J. *Volume 1: Survey of Available Information in Support of the Energy-Water Bandwidth Study of Desalination Systems*; LBNL - 1006424; Lawrence Berkeley National Laboratory: 2016.

44. Park, H. B.; Kamcev, J.; Robeson, L. M.; Elimelech, M.; Freeman, B. D., Maximizing the right stuff: The trade-off between membrane permeability and selectivity. *Science* **2017,** *356* (6343).

5.0 COST OPTIMIZATION OF GAP MEMBRANE DISTILLATION

5.1 Abstract

While membrane distillation (MD) is considered a promising technology for high salinity brine dewatering, there is great uncertainty in how this process would perform at scale. Some of this uncertainty stems from the difficulty of determining how the process should be designed and operated across a range of feed salinities and water recoveries. This work develops optimization models to determine the cost optimal design and operation of single stage gap membrane distillation. The presented models cover the key decision space of gap MD including the gap type (air, permeate, conductive), system configuration (pass-through or looping), equipment sizes (membrane, heater, chiller, and heat exchanger units), and operating conditions (flow rates, temperatures, and heating and cooling duties). We estimate that the levelized cost of water (LCOW) of gap MD ranges between \$4 and 10 per m^3 for feed salinity of 25 to 200 g/L and water recoveries of 30 to 75%, which may be cost competitive for dewatering high salinity brines in some applications. We find several generalizable trends and guidelines for system operation, including: the largest component of the LCOW is the heating cost; the LCOW is a strong function of brine salinity; and conductive gap designs minimize system costs.

5.2 Introduction

Membrane distillation (MD) is a thermally driven separation process that drives water transport across a membrane through a temperature and vapor pressure gradient. This process can be used to desalinate or dewater brines to produce freshwater and concentrated waste. MD is considered to be a promising desalination technology because it has several advantages over the other common desalination technologies. MD can concentrate brines to near the saturation limit

(~310 g/L TDS or 26 weight % for a pure NaCl brine), whereas reverse osmosis (RO) can only concentrate brines up to 70-85 g/L TDS.[1-2] MD also has advantages over evaporative processes like multi-effect distillation (MED) and multi-stage flash distillation (MSF) that can concentrate brines to a similar level. As a membrane-based process MD can be more modular and have a smaller footprint than MED and MSF.[1] Additionally since MD can be operated at a temperature below the boiling point of water, it can be driven with lower quality or waste heat sources.[1] However, unlike RO, MED, and MSF, MD has not been deployed commercially.

MD has not been deployed at scale because the technoeconomic feasibility of the process is currently unknown. While numerous experimental studies have demonstrated the separation performance of MD at the bench-scale,[3-4] there is relatively high uncertainty in how the MD process should be designed and operated to have practical water recoveries of greater than 30% at scale. The MD process can be designed with many kinds of modules including direct contact, gap, sweeping gas, and vacuum, as well as many system configurations including pass through, looping, and cascading multistage.[1, 5] Across and within these different designs, the estimated performance and cost are highly variable and the levelized cost of water spans two orders of magnitude from $0.25 to 25 per m^3.[6-11] The objective of this work is to provide a comprehensive cost assessment of single stage gap MD through using a detailed cost optimization model.

Assessing the technoeconomic viability of single stage gap MD is challenging because it spans a complex decision space that includes a range of design and operating variables including the type of gap (i.e. air, permeate, or conductive), the system configuration (i.e. pass through, looping), the equipment sizes (i.e. membrane area, heat exchanger surface area), and the operating conditions (i.e. flowrates, temperatures, and heating and cooling duties). In conventional process-based technoeconomic assessments, these variables are specified in order

to determine the process performance and cost.[7-10] The values of these design and operating variables are specified heuristically by the modeler, precluding explicit consideration of the complex tradeoffs between water recovery, energy efficiency, capital costs, and operating costs.

While reducing the decision space by explicitly specifying equipment size, water recovery, or recycle ratio does not substantially impact the energy consumption of MD processes,[5, 12-16] these design decisions can have very large impacts on MD cost. The MD decision space is highly dependent on both capital and operating costs,[7-10] and accounting for these tradeoffs with multiple degrees of freedom is most appropriately handled with optimization modeling approaches.

Several studies have demonstrated the benefits of using cost optimization modeling to assess the performance and cost of dewatering technologies, including RO,[17] osmotically assisted reverse osmosis,[18] MED,[19] mechanical vapor compression,[20] and MD.[11, 21] The most significant advantage of this approach is that it avoids the arbitrary specification of the process design and operating variables. Instead, it determines the cost optimal values of a technology based only on the performance and economic parameters of various components (e.g., membrane permeability and cost). Further, this approach enables modelers to determine the LCOW over a full range of technology applications, in this case a range of feed salinities and water recoveries.[17-18]

This work presents a comprehensive assessment of the key membrane and system performance metrics of gap MD, including average water flux, thermal efficiency, GOR, and LCOW. In this work, we develop a cost optimization model that contains detailed relationships for mass and heat transfer in the membrane module and spans the other process units for system design and operation. We use this model to assess the economic viability of gap MD by determining the optimal LCOW across a range of feed salinities and water recoveries. We further

leverage the model to extract generalizable guidelines for low cost design and operation and assess the cost sensitivity of key parameters to prioritize future research.

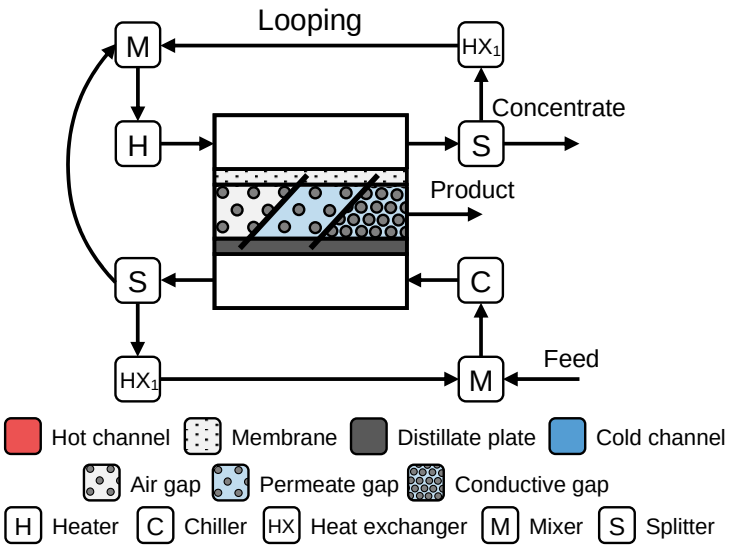

Figure 5.1. *Schematic of single stage membrane distillation gap with multiple gap types (air, permeate, and conductive). In this configuration, the single heat exchanger heats up the hot-side stream and cools down the cold-side stream.*

5.3 Methods

Modeling gap membrane distillation

The dewatering performance of membrane distillation is controlled by mass and heat transfer. At the stage-scale, the governing set of mass and energy balance equations are shown in 5.1-5.7.

$$\frac{1}{W}\frac{dM_h}{dz} = -Jw \tag{5.1}$$

$$\frac{d[M_h X_h]}{dz} = 0 \tag{5.2}$$

$$\frac{1}{W}\frac{dM_p}{dz} = Jw \tag{5.3}$$

$$\frac{1}{W}\frac{dM_c}{dz} = 0 \tag{5.4}$$

$$\frac{1}{W}\frac{d[M_h\,\widehat{H}_l(X_h,T_h)]}{dz} = -Jw\,\widehat{H}_l(X_{hm},T_{hm}) - q_h \tag{5.5}$$

$$\frac{1}{W}\frac{d[M_p\,\widehat{H}_l(X_p,T_p)]}{dz} = Jw\,\widehat{H}_l(0,T_{mg}) + q_{g1} - q_d \tag{5.6}$$

$$\frac{1}{W}\frac{d[M_c\,\widehat{H}_l(X_c,T_c)]}{dz} = q_c \tag{5.7}$$

Where M, X, and T are the state variables mass flowrate [kg/s], salt mass fraction [unitless], and temperature [K] for the hot (h), permeate (p), and cold (c) streams along the length of the stage. z is the dimension along the membrane stage [m] with the direction along the stream flow. In this work, we only consider counterflow operation, so z is in opposing directions for the hot and cold streams. W is the width of the membrane stage [m], Jw is the mass-based water flux [kg/m^2 s], and $\widehat{H}_l(X,T)$ is the specific enthalpy of the liquid [kJ/kg] as a function of salt mass fraction and temperature that is assessed for the bulk hot, permeate, and cold stream, as well as the hot-side membrane interface (hm) and gap-side membrane interface (mg). The equations include several heat fluxes [kW/m^2]: q_h is the heat flux from the hot bulk to the membrane, q_{g1} is the heat flux from the membrane to the gap, q_d is the heat flux through the distillate plate, and q_c is the heat flux from the distillate plate to the cold bulk. Additional details on these variables and their relationships are included in SI Section S1-S3.

Water and heat flux in membrane distillation are generally described by equations 5.8-5.9.

$$Jw = \frac{B}{\delta_m} \Delta Vp \quad (5.8)$$

$$q_{cond} = \frac{\alpha}{\delta} \Delta T \quad (5.9)$$

$$q_{conv} = h \Delta T \quad (5.10)$$

Where B is the water permeability coefficient [kg/m s Pa], δ_m is the thickness of the membrane [m], and ΔVp is the vapor pressure difference across the membrane [Pa]. The conductive and convective heat flux are noted with $cond$ and $conv$, respectively, and are determined from the thermal conductivity [kW/m K], α, material thickness [m], δ, and the convective heat transfer coefficient [kW/m^2 K], h. The conductive heat transfer occurs across the membrane, gap, and distillate plate, while the convective heat transfer occurs in the hot and cold channels.

The gained output ratio (GOR), energy recovery, and levelized cost of water (LCOW) are key performance metrics of the MD system and are determined in equations 5.11-5.13. While both the GOR and energy recovery metrics describe the energy efficiency of the MD process and are strongly related, they are distinct and cannot be directly calculated from one other. The GOR is the ratio of energy required for evaporating the product water to the heat energy input and is generally used as the energy consumption metric for thermal dewatering processes; the energy recovery quantifies the fraction of the energy that passes through the membrane that is reused.

$$GOR = \frac{M_p \hat{H}_{vap}(X_f, T_f)}{Q_{htr}} \quad (5.11)$$

$$ER = 1 - \frac{Q_{htr}}{\Delta E_h} \quad (5.12)$$

$$LCOW = \frac{AOC}{AWP} \quad (5.13)$$

Where GOR is the gained output ratio [unitless], ER is the energy recovery [unitless], and $LCOW$ is the levelized cost of water [\$/m^3]. $\widehat{H}_{vap}$ is the specific heat of vaporization as a function of the salt mass fraction and temperature [kJ/kg] and is assessed at the conditions of the feed (f). Q_{htr} is the heat duty of the heater [kW], ΔE_h is the decrease in energy for the hot stream from the inlet to the outlet of the membrane stage [kW], AOC is the annual operating costs [\$/year] (including annualized capital costs), and AWP is the annual water production [m^3/year].

Additional modeling details such as solving the system of governing equations and relationships for solution properties, cost estimation, other process units, and concentration and temperature polarization in the membrane unit are provided in SI Section S2 and S3.

Gap membrane distillation cost optimization model

We develop non-linear programming models to minimize the LCOW for different gap MD processes. Our models encompass the main decision variables, including the gap type (air, permeate, and conductive), the system configuration (pass through or looping), the equipment sizes (membrane area, heat exchanger surface area), and operating conditions (flow rates, temperatures, and heating and cooling duties). The discrete variables are assessed by comparing the solutions of models with different parameters and formulations. Specifically, the gap types have different thermal conductivities and location of condensation and the system configurations use different stream flows and process units (Figure 5.1). The continuous variables are optimized for each simulation, which must specify a feed salinity, a water recovery, and the process and financial parameters included in Table 5.1.

The optimization models are a system of equations that consist of mass and energy balances, process unit relationships, and financial calculations, the entirety of which are provided

in SI Section S3. We model the governing differential equations for the membrane unit with a finite difference approximation. In the membrane unit, we consider pressure drop, temperature polarization, and concentration polarization by determining local friction factors and heat and mass transfer coefficients. We model the NaCl solution properties (i.e. density, viscosity, solute diffusivity, thermal conductivity, enthalpy, heat of vaporization, and vapor pressure) as a function of temperature and salinity.[22] We estimate the pressure drop in the membrane module to estimate the pumping electricity use. We determine the heat duty in the heat exchangers (including the heater and chiller) with a log mean temperature difference model and an assumed overall heat transfer coefficient (shown in Table 5.1). Lastly, we predict the LCOW by determining the capital and operating cost of the gap MD system.

We make the following assumptions to formulate and fully specify the optimization models for the gap MD system:

- The MD system is well insulated and there is no heat loss to the surroundings
- The MD system can operate at a maximum temperature of 90°C without significant degradation of materials
- The configuration of multiple membrane modules in series and parallel can be represented by continuous length and width variables for the membrane stage
- The gap fluid is relatively stagnant and has negligible convective heat transfer
- The resistance to water flux in the air gap is negligible and ignored because the relative water vapor transport rate is two orders of magnitude higher in the air gap than the membrane (when considering typical membrane permeability, air-water diffusivity, and trans membrane and gap thickness and temperature difference)

- The vapor pressure of the saline solution can be estimated with the ideal solution assumption
- Friction, mass, and heat transfer coefficients can be accurately represented with relationships derived from simulated channels with mesh spacers, as shown in SI Section S3.[23]
- The cooling water temperature increases from 20 to 25°C across the chiller
- The heating provided per unit mass of steam equals the heat of vaporization

Process and financial parameters

The process and financial parameters for the gap MD system are presented in Table 5.1. The process parameters include membrane, module, and process unit properties and constants. Across all gap types, the module design is the same with a height of 2 mm for the hot and cold channels, a height of 1 mm for the gap channel, and a 0.1 mm thick membrane and distillate plate. The thermal conductivities of the membrane and titanium distillate plate are assumed to be 0.05 and 20 [W/m K]. The thermal conductivities of the air, permeate, and conductive gap are 0.2, 0.6, and 10 [W/m K], respectively. As described in Swaminathan et. al. 2018, the assumed thermal conductivity of the air gap accounts for the spacer that supports the channel.[24] The auxiliary unit parameters include an assumed pump efficiency of 75% and overall heat transfer coefficients for the heater of 2 [kW/m^2 K] (liquid to condensing gas heat exchanger) and 1 [kW/m^2 K] of the heat exchanger and chiller (liquid to liquid heat exchangers) as shown in Table 5.1.

The financial parameters are used to estimate the capital, operating, and levelized cost of water for the MD system. We determine the total capital cost by directly estimating the

equipment cost of the membrane, heat exchanger, heater, and chiller units and multiplying these equipment costs by the total investment factor (assumed to be 2) to account for indirect capital, installation, and siting. We estimate the operating cost by directly accounting for membrane replacement, electricity demand for pumping, steam demand for heating, and cooling water demand for chilling and by indirectly estimating the maintenance, labor, and chemical cost with a factor. The assumed factors and costs of these components are provided in Table 5.1 and further details on the cost estimation are included in SI section S3.

Table 5.1. *Process and financial parameters for gap MD*

Process parameters		Value	Unit	Source
Membrane	Water permeability	1.5e-10	kg/m s Pa	assumed
	Thermal conductivity	0.05	W/m K	assumed
	Thickness	100	μm	assumed
Gap	Thermal conductivity - air	0.2	W/m K	[24]
	Thermal conductivity - permeate	0.6	W/m K	[24]
	Thermal conductivity - conductive	10	W/m K	[24]
	Height	1	mm	[24]
Distillate plate	Thermal conductivity	20	W/m K	[25]
	Thickness	100	μm	assumed
Channel	Height	2	mm	assumed
	Mesh void space	90	%	assumed
	Hydraulic diameter	2.57	mm	calculated
Temperatures	Maximum	90	°C	assumed
	Heating source	100	°C	assumed
	Cooling source	20	°C	assumed
Process units	Heat exchanger overall heat transfer coeff.	1	kW/m^2 K	[26]
	Heater overall heat transfer coeff.	2	kW/m^2 K	[26]
	Chiller overall heat transfer coeff.	1	kW/m^2 K	[26]
	Pump efficiency	75	%	[18]
Financial parameters				
Capital costs	Membrane	100	$/m^2	[7, 9]
	Heat exchanger/heater/chiller	100	$/m^2	[11]
	Total investment factor	2	unitless	assumed
Operating costs	Electricity	0.07	$/kWh	[9, 18]
	Cooling water	12	$/kW-year	[11]
	Steam for heater	9	$/tonne	[7, 27]

	Maint., labor, and chemical factor	3	%/year	[18]
	Membrane replacement rate	20	%/year	[9]
Other	Load factor	85	%	[9, 18]
	Capital annualization factor	10	%/year	[9, 11, 18]

Case study parameters

We highlight a single case study that dewaters a 75 g/L feed salinity with 50% water recovery to provide additional details and compare the three investigated gap types. This case represents the dewatering of reverse osmosis concentrate, a common high salinity brine dewatering application.

Implementing and solving the optimization models

We implement the optimization models in Python with the Pyomo software package. The pass-through and looping configurations have roughly 62 + 47N variables and constraints, where N is the number of nodes (fixed at 50 in this work ~ 2400 variables). We solve the models using GAMS 27.1.0/CONOPT 4 and, similarly to the work in chapter 4, we find that the local solver sufficiently explores the decision space.[28]

5.4 Results and discussion

This work uses optimization models to assess the cost optimal performance of gap membrane distillation. We consider three different gap types (i.e. air, permeate, and conductive) and two different system configurations (pass-through and looping). The models identify the cost optimal design and operation including the equipment sizes, looping flow rates, and heating and chilling duties. We leverage the models to compare the optimal LCOW for a case study for the different gap types, estimate the LCOW across a wide range of feed salinities and water

recoveries, extract generalizable guidelines for low cost design and operation, and identify the most cost sensitive parameters.

The models are solved across all conditions in less than 2 s with an Intel i7 CPU 2.6 GHz processor with 8 GB of memory. Consistent with other literature, we find that the pass-through configuration cannot achieve water recoveries greater than 10%.[1, 5] Since this low water recovery is not practically useful for dewatering applications, we only present results for the looping configuration with water recoveries of at least 30% in the body of this manuscript. Additional details on the results of the pass-through configuration at low recoveries are included in SI Section S5.

Case study cost optimal design and operation for the three gap types

The cost optimal performance and financial metrics for the three gap types at the case study conditions (75 g/L TDS feed with 50% water recovery) are reported in Table 5.2. We find that gap types with lower thermal conductivities result in lower water flux and thermal efficiency, where the air, permeate, and conductive gap types have cost optimal average water flux of 3.3, 4.3, 6.9 kg/m^2-h and average thermal efficiency of 53, 60, and 66%, respectively. This decrease in performance occurs because lower gap conductivities have reduced heat transfer across the gap and consequently a smaller temperature and vapor pressure difference across the membrane. Although a lower gap conductivity has the benefit of reducing the conductive heat loss, the thermal efficiency decreases because the water flux is reduced by a greater amount. SI Figure S4 shows the water flux and thermal efficiency as a function of the bulk temperature difference for the three gap types.

We find that cost optimal operations of gap types with lower thermal conductivity have higher average bulk temperature differences. While a higher average bulk temperature difference increases the water flux and thermal efficiency for that gap type, it also increases the heating and cooling demand and reduces the amount of energy that can be recovered in the heat exchanger (i.e. decreases the temperature difference between the cold and hot side outlets). These energy penalties are reflected in the cost optimal GOR of 1.2, 1.5, and 2.4 and energy recovery of 60, 65, and 76% for the air, permeate, and conductive gaps (Table 5.2).

Since gap types with lower thermal conductivities have lower water flux and energy efficiency, they also have higher financial costs. The optimal LCOW for the air, permeate, and conductive gap are \$11.7, \$9.6, and \$6.2 per m^3 of product water for the case study conditions (Table 5.2). The operating costs make up between 82-86% of the total LCOW for the three gap types. The operating costs include membrane replacement, electricity, steam, cooling water, maintenance, labor, and chemicals. Within these components, we find the steam cost contributes to more than 70% of the operating costs and 50% of the total LCOW. This dominant heating cost is consistent with other MD cost estimates.[9-11] The capital costs make up less than 20% of the total LCOW and they include the equipment cost for the membrane, heater, chiller, and heat exchanger units, as well as the estimated indirect capital costs (e.g. auxiliary equipment, siting, installation). Table 5.2 provides further details on the components of the LCOW.

Table 5.2. *Cost optimal performance and financial metrics for the three gap configurations at the case study condition of 75 g/L TDS feed and 50% water recovery. Note: the operating and capital cost sum up to the LCOW and all cost components (i.e. membrane, heater, chiller heat exchanger, recirculation, and other) sum up to the LCOW. These cost component include both the associated operating and capital cost.*

		Air	Permeate	Conductive
Performance metrics	Average water flux [kg/m^2-h]	3.32	4.28	6.86
	Average thermal efficiency [%]	52.5	59.6	65.7
	Average bulk temperature difference [C]	17.9	16.7	11.6
	Gained output ratio [unitless]	1.18	1.49	2.39
	Energy recovery [%]	59.7	64.9	75.6
Financial metrics	Levelized cost of water [$/m^3]	11.73	9.60	6.24
	Operating cost [$/m3]	10.05	8.09	5.13
	Capital cost [$/m3]	1.68	1.51	1.11
	Membrane [$/m3]	1.21	0.94	0.59
	Heater [$/m3]	7.70	6.13	3.82
	Chiller [$/m3]	0.89	0.74	0.45
	Heat exchanger [$/m3]	0.32	0.32	0.29
	Recirculation [$/m3]	0.26	0.26	0.21
	Other [$/m3]	1.34	1.21	0.89

The cost optimal design and operating variables for the three gap types at the case study conditions are reported in Table 5.3. Across all gap types, the cost optimal surface area for the membrane and heat exchanger are similar, while the chiller and heater have less area. The chiller has roughly 5 times greater area than the heater because the approach temperature and log mean temperature difference are significantly greater for the heater. The heater has a relatively high approach temperature of 10°C because the condensing steam has a temperature of 100°C and the maximum allowed temperature for the hot side is 90°C (all cost optimal solutions operate at this maximum temperature), whereas there is no similar constraint for the minimum temperature of the cold side.

The optimal design and operation of the gap types further explain the performance and financial metrics presented in Table 5.2. Generally, the lower the thermal conductivity of the gap, the greater the cost optimal membrane area, looping flow rates, and heating and cooling duties (Table 5.3). Although, increasing looping flow rates and heating and cooling duties directly increases the average bulk temperature difference and the water flux, they also increase the energy use and decrease the potential energy recovery. These complex tradeoffs associated with water flux, energy use, and energy recovery involve all design and operating variables and necessitate the use of a cost optimization model to balance the capital and operating costs.

Figure 5.2A provides additional details on the cost optimal state variables (i.e. mass flow rate, salt mass fraction, and temperature) of conductive gap MD at the case study conditions. Figure 5.2B presents the temperature along the membrane stage. While the bulk temperature difference stays similar along the module, the water flux decreases significantly with the absolute temperature on the hot side because vapor pressure is a nonlinear function of temperature.

Table 5.3*. Cost optimal design and operating variables for the three gap configurations at the case study condition of 75 g/L TDS feed and 50% water recovery.*

		Air	Permeate	Conductive
Design variables	Membrane area [m^2]	504	391	244
	Heater area [m^2]	25	20	14
	Chiller area [m^2]	116	130	73
	Heat exchanger area [m^2]	399	400	360
Operating variables	Hot side looping flow rate [kg/s]	11.83	9.57	7.85
	Cold side looping flow rate [kg/s]	9.64	8.83	7.19
	Heater duty [kW]	894	711	443
	Chiller duty [kW]	831	662	405
	Heat exchanger duty [kW]	1116	1105	1139
	Heater approach temp. [C]	10.0	10.0	10.0
	Chiller approach temp. [C]	2.1	1.3	2.6
	Heat exchanger approach temp. [C]	1.4	2.7	3.0

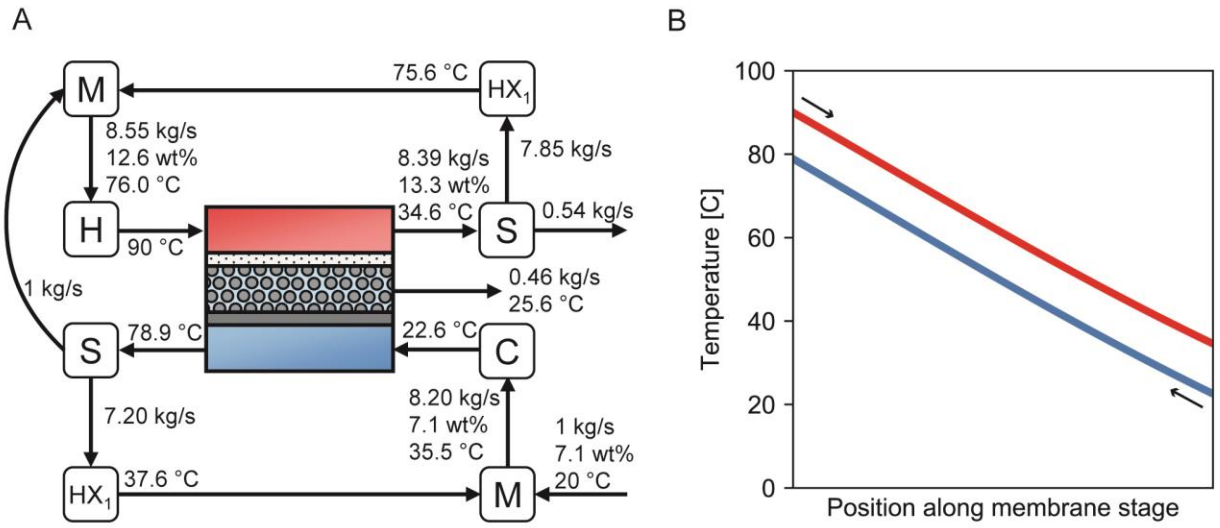

Figure 5.2*. Case study cost optimal state variables (mass flow rate, salt mass fraction, and temperature) for conductive gap MD (A) and temperature and water flux profile along the membrane stage (B).*

Effect of feed salinity and water recovery on cost optimal gap membrane distillation

Figure 5.3A presents the optimal LCOW of conductive gap MD for feed concentrations of 25 to 200 g/L and 30 to 75% water recovery. We observe that the LCOW increases with feed salinity and water recovery and ranges from $4 to 10 per m^3. The LCOW is a strong function of feed salinity and water recovery because a higher salinity decreases the water vapor pressure of the solution and, consequently, the water flux and thermal efficiency of the membrane stage.

Although several studies describe the decreasing performance of MD with increasing salinity,[10-11, 24, 29] many studies generally state that the process is insensitive to salinity.[3, 30] This misconception arises from assuming that the reduction in MD performance will match the absolute vapor pressure decrease of roughly 10-25% for the high salinity cases. However, the vapor pressure difference across the membrane is the driving potential in MD, which is greatly impacted by the vapor pressure only being depressed on the hot side of the membrane and not on

the gap side of the membrane. Therefore, increases in salinity can retard the driving force of MD by more than 10-25% and greatly reduce the water flux and thermal efficiency of the membrane. SI Figure S4 shows the water flux and thermal efficiency of gap MD as a function of salinity and bulk temperature difference.

While the LCOW of gap MD presented in Figure 5.3A is not cost competitive with reverse osmosis at low salinities (< \$1 per m^3), they may be cost competitive for dewatering brines greater than 75 g/L TDS. Generally, literature-based LCOW for high salinity brine dewatering ranges from \$4 to 12 per m^3 and these MD estimates lie in that range.[18-20] Notably, there are a limited number of cost estimates for high salinity brine dewatering, so the cost competitiveness of gap MD is uncertain.

Figure 5.3 also provides cost optimal design and operating conditions for conductive gap MD across the same broad range of feed salinities and water recoveries. We observe that optimal gap MD has higher average bulk temperature differences and looping flow rates for higher feed salinities and water recoveries (Figure 5.3B and 5.3C). Operating at these higher average bulk temperature differences and looping flow rates helps offset the expected decrease in water flux and thermal efficiency for the increasing salinity.

SI Figure S5 presents the average water flux (5.5-8 kg/m^2h), average thermal efficiency (55-78%), GOR (1.2-4.7), and energy recovery (65-85%) across the same range of feed salinities and water recoveries. Expectedly, increasing the feed salinity and water recovery decreases the thermal efficiency, GOR, and energy recovery. Non-intuitively, cost optimal operation has higher average water flux with increasing feed salinity and water recovery. This finding suggests that the cost optimal increase in average bulk temperature difference more than offsets the vapor pressure depression of the higher salt content. While part of the cost reduction from increasing

the average bulk temperature difference and water flux is attributed to reduced membrane costs, the primary cost reduction is in boosting the thermal efficiency and reducing energy costs.

Figure 5.3D presents the optimal heat exchanger to membrane area ratio. This key design ratio increases with feed salinity and water recovery and ranges between 0.9 and 2.0 across all scenarios. Even though the high salinity cases have relatively large heat exchanger areas, they still have relatively low energy recoveries of 65-70% (SI Figure S5D). These low energy recoveries illustrate the limits of recovering energy and the diminishing returns of increasing heat exchanger areas and decreasing approach temperatures.

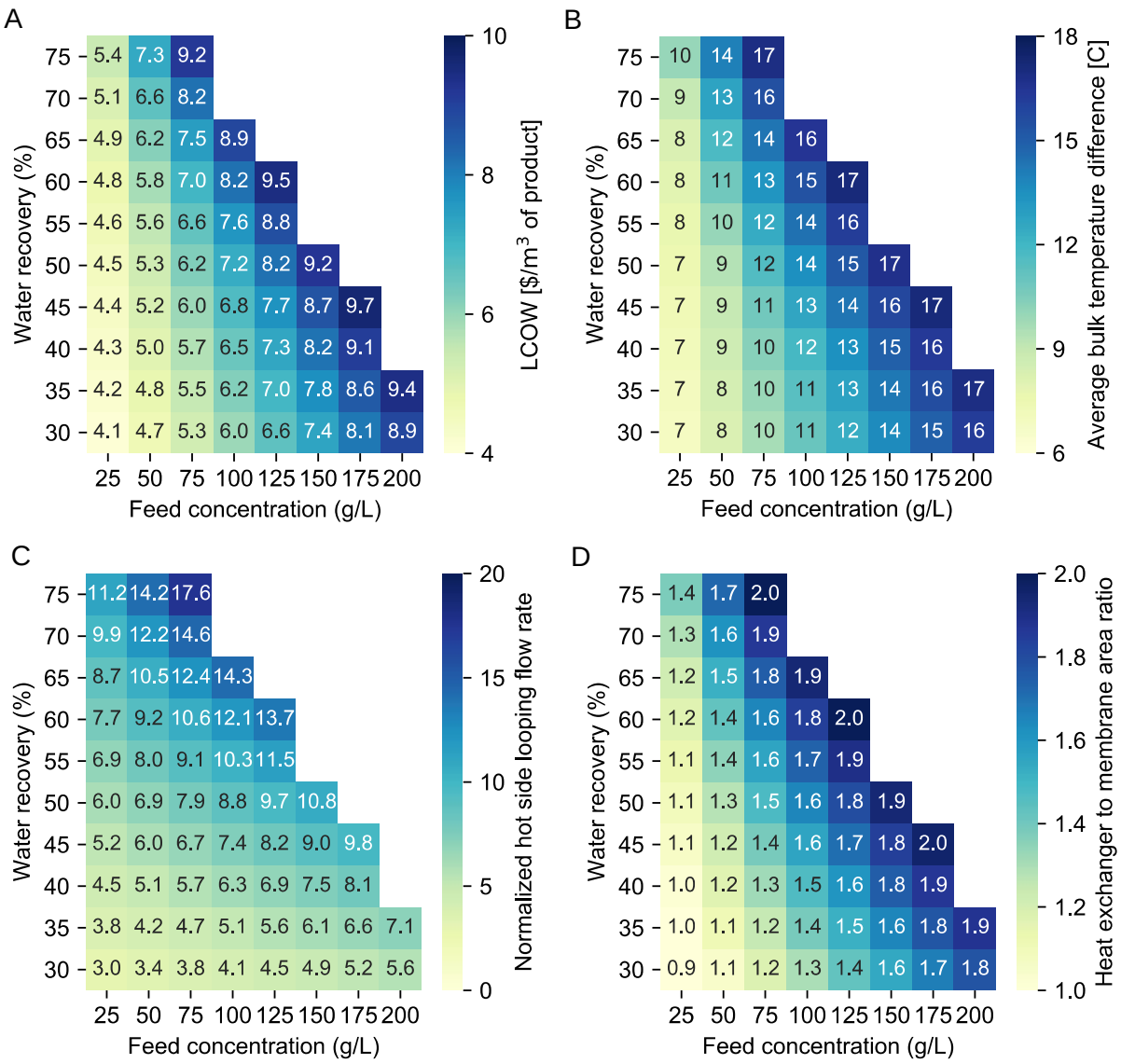

Figure 5.3. *Optimal LCOW (A), average bulk temperature difference (B), normalized hot side looping flow rate (C), and heat exchanger to membrane area ratio (D) for conductive gap MD. The looping flow rate is normalized to the feed flow rate of 1 kg/s.*

Cost sensitivity of process and financial parameters

The results in the previous sections are based on the assumed process and financial parameters presented in Table 5.1. Figure 5.4 shows the LCOW sensitivity of four key parameters: the membrane permeability, the membrane thermal conductivity, the steam cost, and

the maximum temperature of the MD system. The cost sensitivity of gap MD with other parameters, including convective heat transfer coefficient, friction factor, membrane thickness, and membrane module cost is provided in SI Section S6.

Increasing the water permeability of the membrane decreases the cost by decreasing the required membrane area and increasing the thermal efficiency of the membrane. Our sensitivity covers the broad range of possible permeability values including the theoretical upper bound of 2.5E-10 kg/m-s-Pa.[31] We find that even if a membrane had this maximum permeability, the LCOW would only decrease by 10% from our base case (Figure 5.4A). Further, our selected permeability of 1.5E-10 kg/m-s-Pa is generally considered optimistic; if the permeability was three times lower at 0.5E-10 kg/m-s-Pa the LCOW would increase by 60%.

Decreasing the membrane thermal conductivity decreases the cost by decreasing the conductive heat transfer in the membrane and increasing the thermal efficiency of the membrane. As the membrane thermal conductivity decreases from 0.05 to 0.03 W/m-K, the LCOW decreases by 15% (Figure 5.4B). However, this low thermal conductivity of 0.03 W/m-K is likely unachievable for membrane materials because it is equivalent to the conductivity of polystyrene (Styrofoam) and only 20% greater than the conductivity of air.[32] If the thermal conductivity of the membrane is increased to 0.07 W/m-K, the LCOW would increase by 20%.

Since the heating cost is the largest component of the LCOW, the most cost sensitive financial parameter is the cost of the steam. As the cost of steam decreases from $9 to $5 per tonne (45% decrease), the LCOW decreases by 30% (Figure 5.4C). While this LCOW decrease is significant, steam production is a mature process and unlikely to see substantial cost reductions. A commonly discussed way to reduce the cost of MD is to lower steam demand by

utilizing waste heat.[1, 6, 9] However, the source of the waste heat and cost of utilizing it are not clear and out of the scope of this work.

MD is commonly referred to as a low temperature thermal process because it can dewater brines at a temperature less than the boiling point. This attribute is beneficial because it means lower quality energy sources, potentially waste heat, can be used to drive the water treatment. Notably, there is little quantitative discussion of the expected drop in performance and increase in cost when operating at lower temperatures. In our work, we found that cost optimal MD always operated at 90 °C, the maximum temperature allowed. As the maximum temperature allowed decreases from 90 to 75 °C, the LCOW increases 30% (Figure 5.4D). This significant increase in cost suggests that economically feasible MD may require high temperatures.

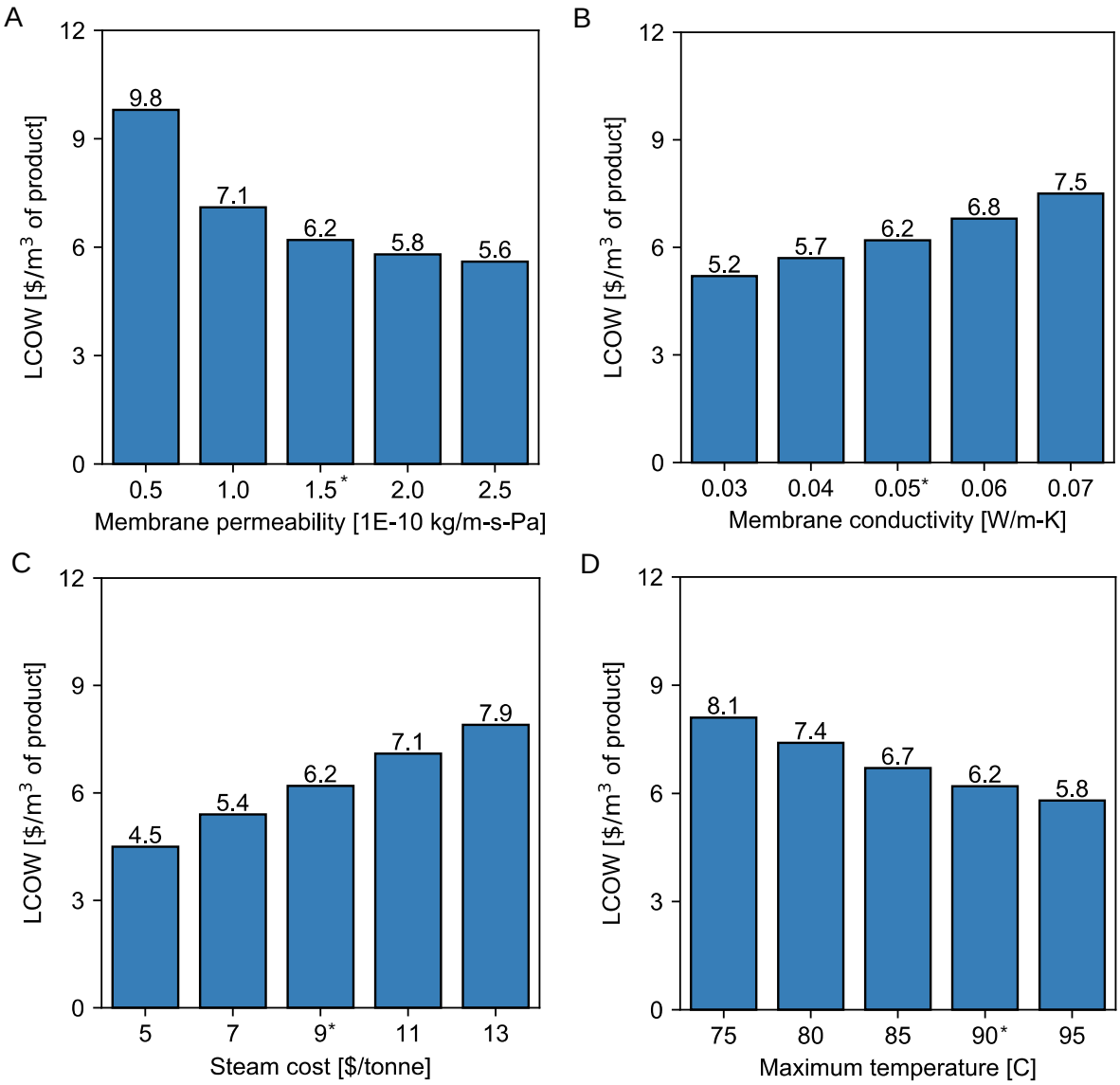

Figure 5.4. *Cost sensitivity for membrane water permeability (A), membrane thermal conductivity (B), price of steam (C), maximum temperature allowed (D) for conductive gap MD. The asterisks denote the base case value assumed in Table 5.1.*

5.5 Conclusions

The cost estimates for MD presented in this work suggest it is not cost competitive for treating low salinity brines, but it may be cost competitive for dewatering brines with greater than 75 g/L TDS. While there are several studies that have developed MD optimization models,

none have included the level of detail of this work. Our models span two configurations (pass-through and looping), three gap types, and several key decision variables (i.e. equipment sizes, flow rates, heating and cooling duties, approach temperatures). Additionally, our models include detailed modeling of solution properties as a function of salinity and temperature, local friction factors and mass and heat transfer coefficients, and direct and indirect cost estimates.

While the absolute performance and financial metrics presented in this work are dependent on the assumed parameters, we observe generalizable trends and guidelines for low cost design and operation of gap MD. These trends include: 1) operating and heating costs make up the majority of the LCOW and 2) increases in feed salinity and water recovery greatly increase the energy consumption and LCOW. Guidelines for low cost design and operation include: 1) design the gap with high thermal conductivity; 2) design the system with a relatively large heat exchanger (same order of magnitude as membrane area); 3) operate at the maximum allowable temperature; 4) operate the heat exchangers at relatively low approach temperatures of less than 5°C; and 5) operate at higher average bulk temperature differences and water flux for higher salinities.

We also provide estimates on how improvements to process and financial parameters could decrease the LCOW of gap MD. While membrane improvements such as increasing water permeability and thermal conductivity could modestly decrease the LCOW, deep reductions would necessitate a significantly cheaper heating source.

Finally, this work emphasizes the importance of using a cost optimization model to assess the technoeconomic feasibility of emerging technologies. An optimization model can address the complex tradeoffs between capital and operating costs without making arbitrary assumptions on

key design and operating variables and it can help expand the analysis beyond a single case study to the full dewatering space.

5.6 Acknowledgements

This work was funded via the U.S. Department of Energy's National Energy Technology Laboratory under the Crosscutting Technologies Division and via NSF CBET-1554117. Support for T.V.B. was provided by appointment to the National Energy Technology Laboratory Research Participation Program, sponsored by the U.S. Department of Energy and administered by the Oak Ridge Institute for Science and Education.

5.7 References

1. Deshmukh, A.; Boo, C.; Karanikola, V.; Lin, S.; Straub, A. P.; Tong, T.; Warsinger, D. M.; Elimelech, M., Membrane distillation at the water-energy nexus: limits, opportunities, and challenges. *Energy & Environmental Science* **2018,** *11* (5), 1177-1196.

2. Shaffer, D. L.; Arias Chavez, L. H.; Ben-Sasson, M.; Romero-Vargas Castrillon, S.; Yip, N. Y.; Elimelech, M., Desalination and reuse of high-salinity shale gas produced water: drivers, technologies, and future directions. *Environ Sci Technol* **2013,** *47* (17), 9569-83.

3. Hickenbottom, K. L.; Cath, T. Y., Sustainable operation of membrane distillation for enhancement of mineral recovery from hypersaline solutions. *Journal of Membrane Science* **2014,** *454*, 426-435.

4. Khayet, M.; Cojocaru, C.; Baroudi, A., Modeling and optimization of sweeping gas membrane distillation. *Desalination* **2012,** *287*, 159-166.

5. He, F.; Gilron, J.; Sirkar, K. K., High water recovery in direct contact membrane distillation using a series of cascades. *Desalination* **2013,** *323*, 48-54.

6. Thomas, N.; Mavukkandy, M. O.; Loutatidou, S.; Arafat, H. A., Membrane distillation research & implementation: Lessons from the past five decades. *Separation and Purification Technology* **2017,** *189*, 108-127.

7. Al-Obaidani, S.; Curcio, E.; Macedonio, F.; Di Profio, G.; Al-Hinai, H.; Drioli, E., Potential of membrane distillation in seawater desalination: Thermal efficiency, sensitivity study and cost estimation. *Journal of Membrane Science* **2008,** *323* (1), 85-98.

8. Ali, A.; Quist-Jensen, C. A.; Macedonio, F.; Drioli, E., Optimization of module length for continuous direct contact membrane distillation process. *Chemical Engineering and Processing: Process Intensification* **2016,** *110*, 188-200.

9. Tavakkoli, S.; Lokare, O. R.; Vidic, R. D.; Khanna, V., A techno-economic assessment of membrane distillation for treatment of Marcellus shale produced water. *Desalination* **2017,** *416*, 24-34.

10. Schwantes, R.; Chavan, K.; Winter, D.; Felsmann, C.; Pfafferott, J., Techno-economic comparison of membrane distillation and MVC in a zero liquid discharge application. *Desalination* **2018,** *428*, 50-68.

11. Carrero-Parreño, A.; Onishi, V. C.; Ruiz-Femenia, R.; Salcedo-Díaz, R.; Caballero, J. A.; Reyes-Labarta, J. A., Optimization of multistage membrane distillation system for treating shale gas produced water. *Desalination* **2019,** *460*, 15-27.

12. Ruiz-Aguirre, A.; Andrés-Mañas, J. A.; Fernández-Sevilla, J. M.; Zaragoza, G., Modeling and optimization of a commercial permeate gap spiral wound membrane distillation module for seawater desalination. *Desalination* **2017,** *419*, 160-168.

13. Lokare, O. R.; Tavakkoli, S.; Khanna, V.; Vidic, R. D., Importance of feed recirculation for the overall energy consumption in membrane distillation systems. *Desalination* **2018,** *428,* 250-254.

14. Cheng, D.; Gong, W.; Li, N., Response surface modeling and optimization of direct contact membrane distillation for water desalination. *Desalination* **2016,** *394,* 108-122.

15. Ali, A.; Tsai, J.-H.; Tung, K.-L.; Drioli, E.; Macedonio, F., Designing and optimization of continuous direct contact membrane distillation process. *Desalination* **2018,** *426,* 97-107.

16. Long, R.; Lai, X.; Liu, Z.; Liu, W., Direct contact membrane distillation system for waste heat recovery: Modelling and multi-objective optimization. *Energy* **2018,** *148,* 1060-1068.

17. Lu, Y.-Y.; Hu, Y.-D.; Zhang, X.-L.; Wu, L.-Y.; Liu, Q.-Z., Optimum design of reverse osmosis system under different feed concentration and product specification. *Journal of Membrane Science* **2007,** *287* (2), 219-229.

18. Bartholomew, T. V.; Siefert, N. S.; Mauter, M. S., Cost Optimization of Osmotically Assisted Reverse Osmosis. *Environmental Science & Technology* **2018,** *52* (20), 11813-11821.

19. Onishi, V. C.; Carrero-Parreño, A.; Reyes-Labarta, J. A.; Ruiz-Femenia, R.; Salcedo-Díaz, R.; Fraga, E. S.; Caballero, J. A., Shale gas flowback water desalination: Single vs multiple-effect evaporation with vapor recompression cycle and thermal integration. *Desalination* **2017,** *404,* 230-248.

20. Onishi, V. C.; Carrero-Parreño, A.; Reyes-Labarta, J. A.; Fraga, E. S.; Caballero, J. A., Desalination of shale gas produced water: A rigorous design approach for zero-liquid discharge evaporation systems. *Journal of Cleaner Production* **2017,** *140,* 1399-1414.

21. González-Bravo, R.; Nápoles-Rivera, F.; Ponce-Ortega, J. M.; Nyapathi, M.; Elsayed, N.; El-Halwagi, M. M., Synthesis of optimal thermal membrane distillation networks. *Aiche J* **2015,** *61* (2), 448-463.

22. Sharqawy, M. H.; Lienhard, J. H.; Zubair, S. M., Thermophysical properties of seawater: a review of existing correlations and data. *Desalination and Water Treatment* **2010,** *16* (1-3), 354-380.

23. Guillen, G.; Hoek, E. M. V., Modeling the impacts of feed spacer geometry on reverse osmosis and nanofiltration processes. *Chemical Engineering Journal* **2009,** *149* (1), 221-231.

24. Swaminathan, J.; Chung, H. W.; Warsinger, D. M.; Lienhard V, J. H., Energy efficiency of membrane distillation up to high salinity: Evaluating critical system size and optimal membrane thickness. *Applied Energy* **2018,** *211*, 715-734.

25. Engineering Toolbox Thermal Conductivity of Metals, Metallic Elements and Alloys. https://www.engineeringtoolbox.com/thermal-conductivity-metals-d_858.html (accessed August 15th 2019).

26. The Engineering ToolBox Heat Exchanger Heat Transfer Coefficients. https://www.engineeringtoolbox.com/heat-transfer-coefficients-exchangers-d_450.html (accessed August 15 2019).

27. Gingerich, D. B.; Mauter, M. S., Retrofitting the Regulated Power Plant: Optimizing Energy Allocation to Electricity Generation, Water Treatment, and Carbon Capture Processes at Coal-Fired Generating Facilities. *Acs Sustain Chem Eng* **2018,** *6* (2), 2694-2703.

28. Drud, A. S., CONOPT—A Large-Scale GRG Code. *ORSA Journal on Computing* **1994,** *6* (2), 207-216.

29. Winter, D.; Koschikowski, J.; Wieghaus, M., Desalination using membrane distillation: Experimental studies on full scale spiral wound modules. *Journal of Membrane Science* **2011,** *375* (1), 104-112.

30. Choi, Y.; Naidu, G.; Nghiem, L. D.; Lee, S.; Vigneswaran, S., Membrane distillation crystallization for brine mining and zero liquid discharge: opportunities, challenges, and recent progress. *Environmental Science: Water Research & Technology* **2019,** *5* (7), 1202-1221.

31. Leitch, M. E.; Lowry, G. V.; Mauter, M. S., Characterizing convective heat transfer coefficients in membrane distillation cassettes. *Journal of Membrane Science* **2017,** *538*, 108-121.

32. Engineering Toolbox Thermal Conductivity of common Materials and Gases. https://www.engineeringtoolbox.com/thermal-conductivity-d_429.html (accessed August 15th 2019).

6.0 MULTI-OBJECTIVE OPTIMIZATION MODEL FOR MINIMIZING COST AND ENVIRONMENTAL IMPACT IN SHALE GAS WATER AND WASTEWATER MANAGEMENT

6.1 Abstract

Unconventional resource extraction from shale plays involves complex operations for water and wastewater management. These water management operations are expensive for companies and emit significant quantities of criteria air pollutants and greenhouse gases that impact human health and the environment (HHE). We present a multi-objective mixed integer linear programming (MILP) framework for assessing the tradeoffs between financial cost and HHE costs for shale gas water acquisition, transport, storage, and treatment under realistic scheduling, operational, and regulatory constraints. We formulate objective functions to identify water management strategies that minimize financial cost, minimize HHE cost, and minimize combined financial and HHE costs. The model was applied to a 14 wellpad case study that is representative of shale gas extraction in the Marcellus Play. We observe significant variation in the financial and HHE costs under different objective functions and regulatory scenarios.

6.2 Introduction

Water and wastewater management at unconventional oil and gas sites is costly. It is costly to firms responsible for acquiring, transporting, storing, treating, and disposing of water. It is costly to society when these activities contribute to environmental emissions,[1] roadway wear,[2] and vehicular accidents.[3] And it is costly to the efficacy of and public trust in the regulatory system when water management-related externalities are not minimized.[4,5] To date, operators and policy makers lack appropriate frameworks for assessing tradeoffs between the financial costs of shale gas water management and the associated human health and

environmental (HHE) impacts. This study assesses those tradeoffs through a multi-objective optimization model that investigates eight distinct water management strategies.

A number of previous studies have quantified the financial costs of water management for shale gas producers. Yang et al. developed mixed integer linear programming (MILP) and mixed integer nonlinear programming (MINLP) investment optimization and scheduling models for minimizing the financial costs of freshwater acquisition, water network optimization, and wastewater management.[6-8] Gao et al. developed mixed integer linear fractional programing (MINFP) models with the objective of minimizing freshwater consumption per unit of profit, as well as a stochastic mixed-integer linear fractional programming (SMILFP) model to optimize the levelized cost of energy generated from shale gas.[9,10]

Similarly, there has been considerable work on quantifying the HHE externalities of shale gas production. While the majority of studies have focused on the lifecycle greenhouse gas emissions associated with the transition from coal to natural gas-based electricity generation,[11,12] there are a few studies focusing specifically on the greenhouse gas emissions of the well development process.[13-15] One study quantifies the greenhouse gas emissions of water and wastewater management activities using an economic input-output life cycle assessment approach,[16] while another quantified criteria air pollutants from shale gas development,[17] and a third evaluated the life cycle impacts of specific wastewater treatment technologies.[18]
One of the limitations with previous criteria air emission studies has been the inability to compare alternative water management scenarios and estimate their costs to shale gas operators. Additionally, most studies quantifying air emissions avoid expressing HHE impacts in terms of their end effects on morbidity, mortality, visibility, or agricultural production. In not assessing

the marginal damages of air emissions, it is more difficult for companies and policy makers to assess tradeoffs implicit in cost-effective policy and decision-making.

The present work extends this past work by presenting the first systematic analysis of the tradeoffs in costs and HHE impacts associated with various water management strategies. We develop an MILP investment optimization model that includes scheduling constraints to quantify the private and public costs of various water management strategies. We also assess the tradeoffs associated with potential regulatory or policy changes that might influence company decisions around water and wastewater management. Finally, we present a case study for the Marcellus Play, and discuss limitations in data availability that constrains the extension of this analysis to other plays or case studies.

6.3 Methods

The problem of determining a bi-objective optimal shale gas water management scheme considering both the privately held costs of wastewater management and the publically borne costs of air emission damages can be addressed as a mixed-integer linear programming (MILP) model. The proposed model is an extension and modification of previously published work by Yang et al. (2015);[7] the revised formulation allows for greater flexibility in freshwater and wastewater transportation and wastewater storage, and incorporates functionality to assess the HHE impacts for a set of midpoint indicators associated with water management activity.[19] This model uses a two-step approach: first the hydraulic fracturing schedule is determined by maximizing profit; second a bi-objective model is used to develop a Pareto frontier for the set fracturing schedule.

The proposed model formulates this bi-objective optimization problem within a defined time horizon. The model assumes the geospatial locations of freshwater sources, impoundments, wellpads, central treatment facilities, and disposal wells. Freshwater demand, wastewater production, and gas production are model inputs. The main decision variables are the hydraulic fracturing schedule, the relative amount of freshwater and wastewater use, the mode of freshwater and wastewater transportation, the method of wastewater handling, and the volume and duration of fresh and wastewater storage.

A long-term time horizon is considered and the schedule is formulated through a discrete-time model. The subsequent case study presents a model with a time horizon of 3 years, discretized into 156 weeks. The weekly discretization was chosen because a week represents the time for a frac crew to transition between wellpads and to begin fracturing. Considering a long-term time horizon is essential for capturing the steep decline curves of both shale gas and wastewater production over the two to three years following well stimulation. Additionally, overall gas and wastewater productivity can vary greatly between wellpads, and natural gas prices change seasonally. Therefore, the fracturing schedule has an effect on the revenue of gas sales and costs of wastewater management.

The proposed superstructure is shown in Figure 6.1A and includes: 1) a set of freshwater sources (o), 2) a set of impoundments (p), 3) a set of well pads (s), 4) a set of central treatment facilities (q), 5) a set of disposal wells (d), and 6) the permissible modes of water transport, including water pipelines, water trucking, or some combination of both. In addition to the activities shown in the superstructure, wastewater can be treated on each wellpad and stored in wastewater tanks on both the wellpads and the impoundment sites.

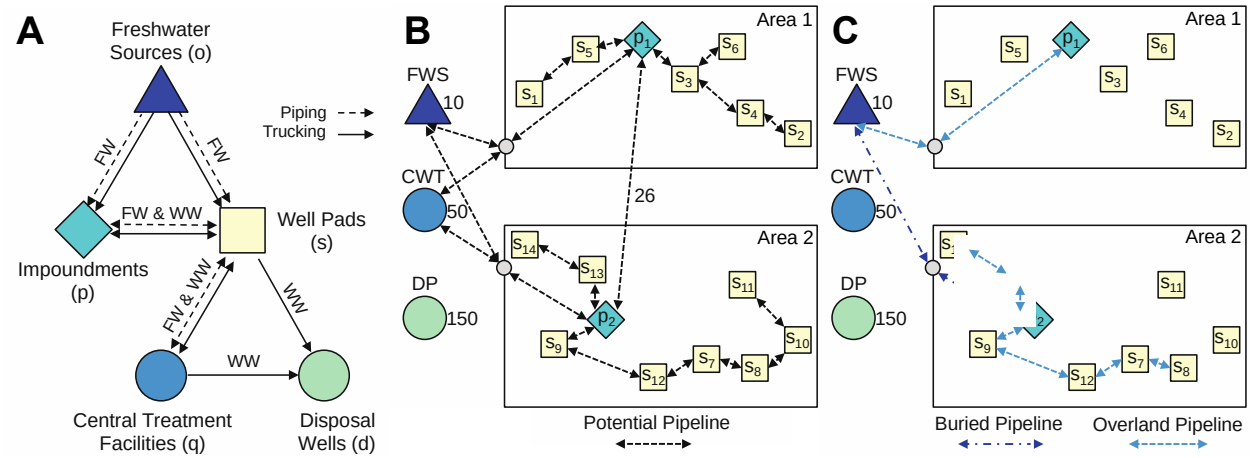

Figure 6.1. *A) Simplified superstructure of shale gas freshwater (FW) and wastewater (WW) management. B) Case study supply chain network including 14 wellpads (s) and 2 impoundments (p) in two areas, a freshwater source (FWS), a central treatment facility (CWT), and a disposal well (DP). The potential fresh and wastewater pipelines are shown in the dotted lines. The numbers next to the pipes are their distances. C) The buried (permanent) and overland (temporary, leased) pipelines for the cost-optimal water management scenario.*

The hydraulic fracturing process uses a blend of water, proppant, and chemicals, titled a "frac fluid", to fracture sub-surface formations and stimulate hydrocarbon production. The volume of frac fluid correlates to the subsurface geology, the type of fracture (e.g. slick-water, gel, crosslinked gel), and the length of the frac stage, among other variables. Assuming these factors to be constant across wellpads in the model, we model the volume of frac fluid as a linear function of the number of frac stages. We assume that both fresh and wastewater can be used to satisfy the frac fluid demand, so long as the total dissolved solids concentration of the blended solution is below 50,000 ppm Total Dissolved Solids (TDS).[7] The proposed model assumes an equivalent formulation that sets the ratio of freshwater to wastewater blending to satisfy the TDS limits.

Freshwater can be acquired from interruptible and uninterruptible sources. Interruptible sources include small ponds, lakes, and rivers whose allowable withdrawal rates vary by season. Uninterruptible sources include large rivers or bodies of freshwater that have no withdrawal rate limits. The proposed model assumes all freshwater sources are uninterruptible; for a demonstration of a model with interruptible sources refer to Linlin et al. (2015).[7] The freshwater can be transported either by pipeline or truck from the source to impoundments for storage and to wellpads for immediate use.

After well stimulation, flowback and produced waters return to the surface as wastewater containing constituents traced to both the composition of the frac fluid and the pore water. Wastewater is transported and disposed of in Class II injection wells, treated onsite for reuse in subsequent well stimulations, or transported to a central treatment facility for recycle or discharge. The balance of these water management options depends upon cost, including both transport and treatment or disposal costs, location, water quality, and the availability of fresh water. The present model considers only cost, location, and water quality.

Onsite treatment occurs on the wellpad and typically removes suspended solids, which allows the wastewater to be reused in frac fluid. Central treatment occurs at a central treatment facility, typically tens of miles away, and produces a purified water stream and concentrated wastewater stream. The purified water stream can be discharged to a river or recycled for additional hydraulic fracturing. The concentrated wastewater stream, the volume of which is determined by treatment technology and recovery rate, must be trucked to a Class II disposal well.

In practice, the cost of water and wastewater management is often determined by the transportation costs to and from the wellpad. Water may be transported via overland pipelines,

buried pipelines or trucks, while wastewater may be transported via buried pipelines or trucks. The proposed model allows overland pipeline to be leased in discrete time intervals that are longer than the weekly time discretization, e.g. yearly or quarterly. The model also assumes separate pipelines for freshwater and wastewater and assumes that wastewater is treated onsite prior to piping. Generally, buried pipelines are associated with high capital costs, low operational costs, low environmental emissions, and low operational versatility. On the other hand, trucking is highly versatile, has low capital costs, but has high operational costs and air emissions per unit of water transport.

Another significant fraction of the costs for water and wastewater management at shale gas sites is water storage. This model assumes freshwater, frac fluid, and wastewater are stored in freshwater impoundments, frac tanks, and wastewater tanks, respectively. The storage volume of freshwater impoundments is on the order of hundreds of thousands of barrels, while the storage volume of frac and wastewater tanks is typically on the order of hundreds of barrels. The location of the freshwater impoundment is predetermined, while the storage volume is determined by the maximum weekly withdrawal from the impoundment over the course of the three year time horizon. Frac tanks are located on wellpads and their storage volume is predetermined. Wastewater storage tanks may be placed at either wellpads or impoundments, and the total wastewater storage volume fluctuates depending on demand.

Water and wastewater management is a significant fraction of the cost of drilling a shale gas well. The activities associated with water transport and treatment are also significant sources of atmospheric emissions of air pollutants, including NH_3, NO_x, $PM_{2.5}$, SO_2, volatile organic compounds (VOCs), and greenhouse gas emissions measured in CO_2 equivalents (CO_2e). We estimate direct and indirect air emissions associated with each water management activity and

estimate the marginal HHE costs using the AP2 model.[20] Direct emissions include emissions associated with a specific activity, such as the emissions from trucks transporting wastewater. Indirect emissions include the emissions due to material manufacture and transport, as well as demand created in other industries. Direct emissions were estimated for trucking and central treatment activities, while the other direct and all indirect emissions are estimated using economic input-output life cycle analysis that estimates emissions based on the economic sector and cost of the activity (SI Section 2).

The main assumptions have been discussed and are as follows:

1. The locations of the freshwater sources, impoundments, wellpads, central treatment facilities, and disposal and transportation paths are predetermined.
2. The gas and wastewater production as a function of time of each well is known.
3. All wells in each wellpad must be fractured and completed before the frac crew can move onto another wellpad.
4. The frac crew maintains the same fracturing rate, independent of the specific wellpads.
5. All freshwater sources are uninterruptible.
6. Freshwater can be transported via truck and buried (purchased) and overland (leased) pipelines
7. Freshwater is stored in centralized impoundments, and the minimum capacity of the impoundment is the largest weekly withdrawal from the impoundment over the time horizon
8. Wastewater use in frac fluid is limited by the TDS, modeled as a ratio of freshwater to wastewater blending.
9. Wastewater can be handled in three ways: onsite treatment, central treatment, disposal in Class II injection wells

10. Wastewater can be transported via truck or buried pipelines, and it must be treated onsite before it can be piped or stored.
11. Wastewater can be stored in wastewater tanks on wellpads and freshwater impoundment locations
12. Onsite treated wastewater can be reused for hydraulic fracturing.
13. Centrally treated wastewater has a TDS of zero and can either be discharged or recycled for hydraulic fracturing.

Model formulation

The proposed water management MILP model is composed of scheduling constraints, mass balance constraints, capacity constraints, pipeline constraints, financial constraints, and HHE constraints. Refer to the SI Section 1 for the detailed model formulation.

The objective is to either 1) maximize profit, 2) minimize the financial costs of water management, 3) minimize the HHE costs of water management, or 4) minimize the combined financial and HHE costs of water management under the following groups of constraints provided in SI Section 1.

Scheduling constraints S1-S2

Mass balance constraints S3-S14

Capacity constraints S15-S18

Pipeline constraints S19-S24

Financial constraints S25-S37

Human Health and Environmental constraints S38-S44

The scheduling constraints ensure that all of the wellpad stages are fracked, only one wellpad is fractured at a time, a wellpad is only fractured when available, and there is adequate time allowed for frac crews to transition to another wellpad. The mass balance constraints ensure that the frac fluid demand is met and describe the relationship of the inputs and outputs of fresh and wastewater throughout the supply chain network. The capacity constraints describe the limits on the transport and storage of fresh and wastewater. The pipeline constraints ensure a feasible pipeline setup. The financial constraints calculate the revenue from natural gas sales and the costs associated with the water management activities. The considered costs include freshwater withdrawal, storage, transportation, and wastewater treatment and disposal. The freshwater withdrawal costs were based on the amount of withdrawn water. Freshwater impoundments and frac tank costs were based on their capacity. Wastewater storage costs were based on the volume and storage time of the wastewater. The operating costs of trucking and piping were based on volume of water and transport distance. The capital costs of pipelines were based on the distance of the pipeline. The wastewater handling costs of onsite treatment, central treatment, and disposal are based on the amount of wastewater. The HHE constraints determine the HHE costs associated with water management activities and are further described in the following section.

Human health and environmental impact assessment

We estimate the direct and indirect air emissions of the criteria air pollutants, NH_3, NO_x, $PM_{2.5}$, SO_2, and VOC, and greenhouse gas emissions in units of CO_2 equivalents for each water management activity: storage, onsite treatment, central treatment, disposal, piping, and trucking. Direct emissions include the emissions directly associated with the activity, while indirect

emissions include the emissions associated with the material manufacture, transport, and installation, and demand created in other industries.

We estimate direct emissions for water trucking and central treatment processes. Direct emission estimates from water trucking are adapted from Behrer and Mauter,[21] and reflect the mean of MOVES, Simapro, and NREL estimates for emissions per mile. Direct emissions from central treatment are estimated through the electricity use of mechanical vapor recompression (MVC)[22] and the associated emissions from electricity production was estimated from the EIA and EPA eGRID and NEI databases.[23-25] The paucity of direct emissions data precludes inclusion of direct emission estimates from other well development activities.

For all activities, we estimate indirect emissions using economic input-output life cycle analysis that estimates industry average emissions based on the economic sector and cost of the activity. Cost estimates are obtained from Yang et al.,[7] or from sources documented in SI Section 3. Additional information on calculating emission coefficients is provided in SI Section 2.

We estimate the HHE damages associated with additional air emissions using the AP2 model.[20] Briefly, AP2 combines atmospheric dispersion models with epidemiological models to estimate the additional morbidity, mortality, and environmental damages (e.g. visibility, timber production, agricultural productivity) associated with a marginal increase in air emissions in a given county. We apply a value of a statistical life (VSL) of $8.5 million USD (2015 dollars) to estimate air emission damages. This generic model assumes marginal damage estimates at the state level using a simple mean of marginal damage estimates across PA's 67 counties. More detailed spatial information on the locations of each activity would allow more accurate estimates of marginal damages. The resulting HHE cost for NH_3, NO_x, $PM_{2.5}$, SO_2, and VOC are

$131, 5.5, 118, 44.5, 11.3 thousand ($2015) per metric ton (Table S6). Additional details on input parameters for the AP2 model are provided in SI section 3.

Environmental damages from unconventional water management activities affect air, water, and soil media. The costs associated with the greenhouse gas emissions were estimated by the U.S. Government Interagency Working Group on Social Cost of Carbon as $41.0/metric ton, assuming a discount rate of 3% and $2015.[26] Environmental risks associated with source water drawdown, habitat fragmentation, ecosystem impacts, chemical release, and soil erosion are not quantitatively modeled or monetized in the present study.[27-29]

Scenarios

We model several scenarios for financial cost optimization reflecting historical, current, or proposed water management practices. The eight scenarios include: no wastewater piping, no wastewater trucking between wellpads and impoundments, no wastewater storage, no freshwater piping, no freshwater trucking, no central treatment, no direct disposal, and no reuse as described further in Table 6.1.

Table 6.1. *Descriptions of the eight regulatory scenarios.*

Scenario	Label	Details
SC 1	no wastewater piping	Prohibits wastewater from being piped, so it must be trucked
SC 2	no local wastewater trucking	Prohibits wastewater from being trucking between impoundments and wellpads, wastewater may still be trucked to disposal
SC 3	no wastewater storage	Prohibits the use of wastewater tanks, forcing wastewater to be treated onsite and used within the week or sent to central treatment and disposal
SC 4	no freshwater piping	Prohibits freshwater from being piped, so it must be trucked
SC 5	no freshwater trucking	Prohibits freshwater from being trucked, so it must be piped
SC 6	no central treatment	Prohibits central treatment and requires all non-reused wastewater to be trucked directly to disposal
SC 7	no direct disposal	Requires all wastewater to be reused onsite or sent to central treatment
SC 8	no reuse	Prohibits the use of wastewater in frac fluid

Case study

We test our model on a case study with time horizon of three years comprising 14 wellpads (s1, s2,… s14) and two impoundments (p1, p2) split across two areas, a freshwater source (o1) that is 10 miles away from each impoundment, one central treatment facility (q1) 50 miles from each wellpad area, and a disposal well (d1) that is 150 miles away from each wellpad area (Figure 6.1B). The relatively far distances from the wellpads and impoundments to central treatment facilities and a disposal well, is typical for the Marcellus play, and allows the distances to be modeled as constant.[30] The permitted fresh and wastewater pipeline connections are shown in Figure 6.1B, and there are two potential types of piping, buried (c1) and overland (c2, c3, … c13). The overland piping is assumed to be leased quarterly and for modeling purposes the 12 quarters each have their own index c. Freshwater trucking is permitted between the sources, impoundments, wellpads, and central treatment facility (for purified stream recycle).

Wastewater trucking is permitted between wellpads, impoundments, the central treatment facility, and the disposal well. Frac fluid use, gas production, and wastewater production varies between the wellpads. The frac fluid use of each wellpad is shown in Figure 6.2. The non-financial and financial parameters, wellpad availability, gas production, and wastewater production are provided in SI section 4.

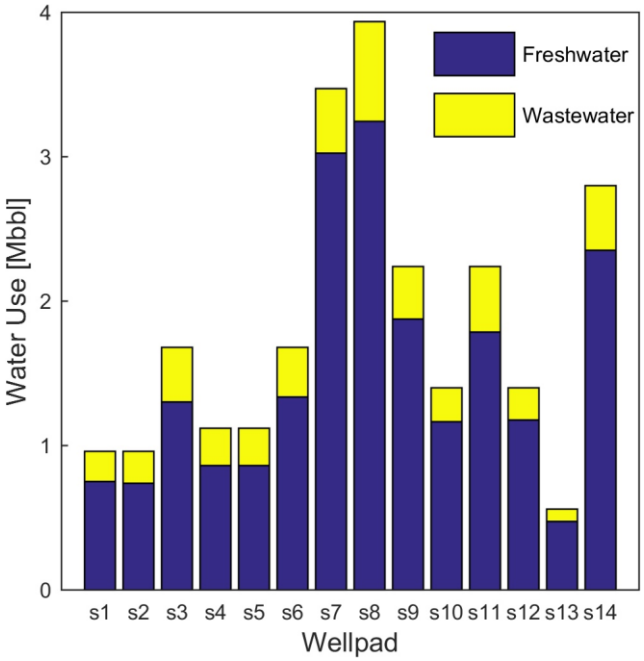

Figure 6.2*. Frac fluid use for the 14 wellpads in the case study, including the financial cost optimal frac fluid blend of fresh (blue) and wastewater (yellow).*

6.4 Results and Discussion

Current investment optimization models for shale gas water and wastewater management do not quantify the externalities of water management processes and lack insight into the tradeoffs between the publically and privately borne costs. This model provides the first quantitative platform for assessing the tradeoffs between the financial and human health and

environmental (HHE) impacts. This model uses a two-step approach, first the hydraulic fracturing schedule is determined by maximizing profit, second a bi-objective model is used to develop a Pareto frontier for the set fracturing schedule. In models that do not adopt a two-step approach, the financial and HHE costs are minimized by extending the hydraulic fracturing schedule such that the HHE externalities are pushed beyond the set period of analysis.

Optimization performance

The case study MILP model consists of 48459 constraints, 210165 continuous variables, and 1748 binary variables. The profit maximization objective model is solved to an optimality gap of 0.1% using GAMS 24.5.6/CPLEX 12.6.2 on an Intel i7 CPU 2.93GHz processor with 12GB memory in about 15 hours. After the optimal schedule was determined and set, the MILP model was solved to the optimal solution (no optimality gap) in about 30 minutes for the following objectives: financial cost minimization, HHE cost minimization, and combined financial and HHE cost minimization.

Case Study Results

We apply this investment and HHE optimization model to the case study, and the output includes a well pad fracturing schedule that accommodates leasing constraints, an optimal water management plan, and a detailed assessment of financial and HHE costs. As described above, we run the model in two phases. First, we run the model to identify the optimal hydraulic fracturing schedule for maximizing profits (revenue minus financial water management costs). The resulting frac schedule suggests that wellpads should be fractured as quickly as possible in order to produce the highest revenue within the time horizon and is shown in SI section 4. The frac schedule does not change under different water management scenarios because the revenues of well development significantly exceed the costs of water management. In the second phase,

this hydraulic fracturing schedule is fixed and transitioned to a minimization model for determining optimal water management strategies under financial, HHE, and combined financial and HHE costs.

Financial Cost Minimization

The financial cost optimal water management case for the 14 wellpad case study provides total revenues of $1.2 billion, water and wastewater management costs of $36.4 million, and HHE costs of $10.9 million (Figure 6.1C and Table 6.2). This financially optimal scenario was characterized by the following attributes: 1) freshwater was both piped and trucked from the source to the impoundments; 2) freshwater was both piped and trucked from impoundments to the wellpads; 3) all wastewater was transported by truck; 4) 94% of wastewater was treated onsite and reused; 5) the remaining 6% of the wastewater was sent to CWT facilities for eventual discharge and disposal; and 6) water is not recycled from CWT facilities. In total, 25.6 million barrels of frac fluid was needed to fracture the wellpads, and the overall composition of the frac fluid was 82% freshwater and 18% wastewater. Despite reuse of wastewater with TDS concentrations as high as 300,000 ppm, the salinity of the blended frac fluid never exceeded 50,000 ppm TDS. The freshwater piping arrangement for the financial cost optimal solution is presented in Figure 6.1C and on a bbl-mile basis, 77% of the freshwater was transported via pipeline and 23% was transported via truck. The pipeline leasing periods and further details on the water management are provided in SI Section 5.

Table 6.2. *Costs of water and wastewater management activities for the three investigated objectives: minimize financial costs, combined financial and HHE costs, and HHE costs.*

Cost Category	Cost for each Objective (M)		
	Financial optimal	**Financial + HHE optimal**	**HHE optimal**
Revenue	$1,181	$1,181	$1,181
Freshwater withdrawal costs	$4.2	$4.2	$4.2
Fresh and wastewater storage costs	$4.3	$5.1	$5.1
Onsite wastewater treatment cost	$13.9	$13.9	$14.0
Central wastewater treatment costs	$1.6	$1.6	$1.3
Wastewater disposal costs	$0.1	$0.1	$0.1
Fresh and wastewater piping costs	$6.9	$7.3	$11.1
Fresh and wastewater trucking costs	$5.5	$4.5	$2.2
Total financial water management costs	**$36.4**	**$36.6**	**$38.0**
Total human health and environmental costs	**$10.9**	**$10.3**	**$9.9**

The HHE costs of the financial cost optimal water management scenario are estimated by first quantifying the air emissions associated with water management activities and then estimating the HHE costs associated with these emissions via the AP2 model and prevailing estimates for the social cost of carbon. This case study does not quantify or monetize human health or environmental damages associated with freshwater drawdown, water emissions, chemical spills, soil erosion, habitat destruction, or any other non-air emission damages. Net air emissions by water management activity and quantity of pollutant (Figure 6.3A) or associated HHE cost (Figure 6.3B) suggest that the externalized costs of water management are significant with respect to the financial costs incurred by the companies (Table 6.2). More than 60% of the total cost of emissions is attributed to fresh and wastewater transportation, with trucking activities incurring higher HHE costs on both an absolute and per mile basis than piping. The non-transport activities with the highest net HHE costs were onsite treatment and storage. Although CO_2e emissions are associated with the largest damage estimates, criteria air pollutant

emissions NO_x, $PM_{2.5}$, SO_2, and VOCs each contribute more than 10% to the total damage estimates.

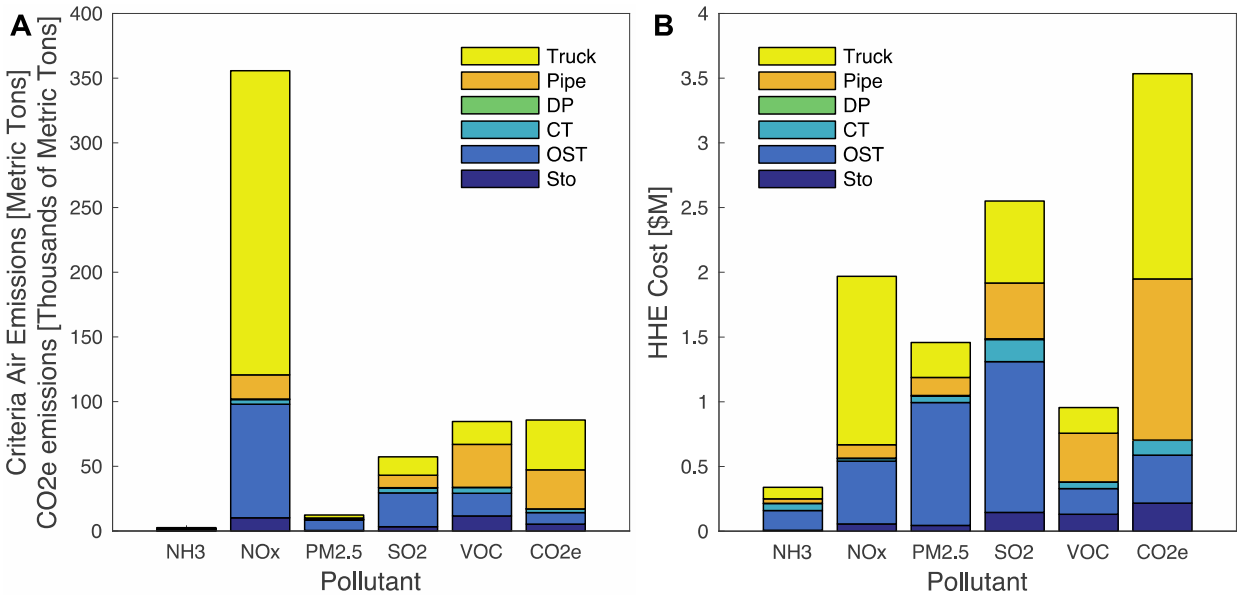

Figure 6.3. *Financial cost optimal water management air emissions and associated human health and environmental (HHE) costs for each pollutant. The water management activity abbreviations are DP for disposal, CT for central treatment, OST for onsite treatment, and Sto for storage.*

Water Management Scenarios

Previous work has documented the significant variation in water management strategies by company, as well as the variation in water management regulation across shale plays and political boundaries.[5] The selected scenarios explore the decision space with respect to the minimum financial costs incurred by companies and the associated HHE damages experienced by downwind communities. Across the eight scenarios, the financial costs of water and wastewater management ranged from $36.4 to 65.1 million and the HHE costs ranged from $10.9 to 27.2 million (Figure 6.4A). We observe a positive correlation between financial costs and HHE costs across the eight scenarios, with the exception of the no freshwater trucking

scenario (SC 5). The tradeoff between the financial cost optimal and the no freshwater trucking scenario is a financial cost increase of $2.1 million and a HHE cost decrease of $0.7 million. This finding demonstrates that further investment in freshwater pipelines in order to reduce trucking emissions may result in lower HHE costs. The no reuse scenario (SC 8) had drastically higher financial and HHE cost of all the scenarios, thereby emphasizing the importance of maximizing waster reuse to lower financial and HHE costs. Further details of the scenarios are included in the SI Section 5.

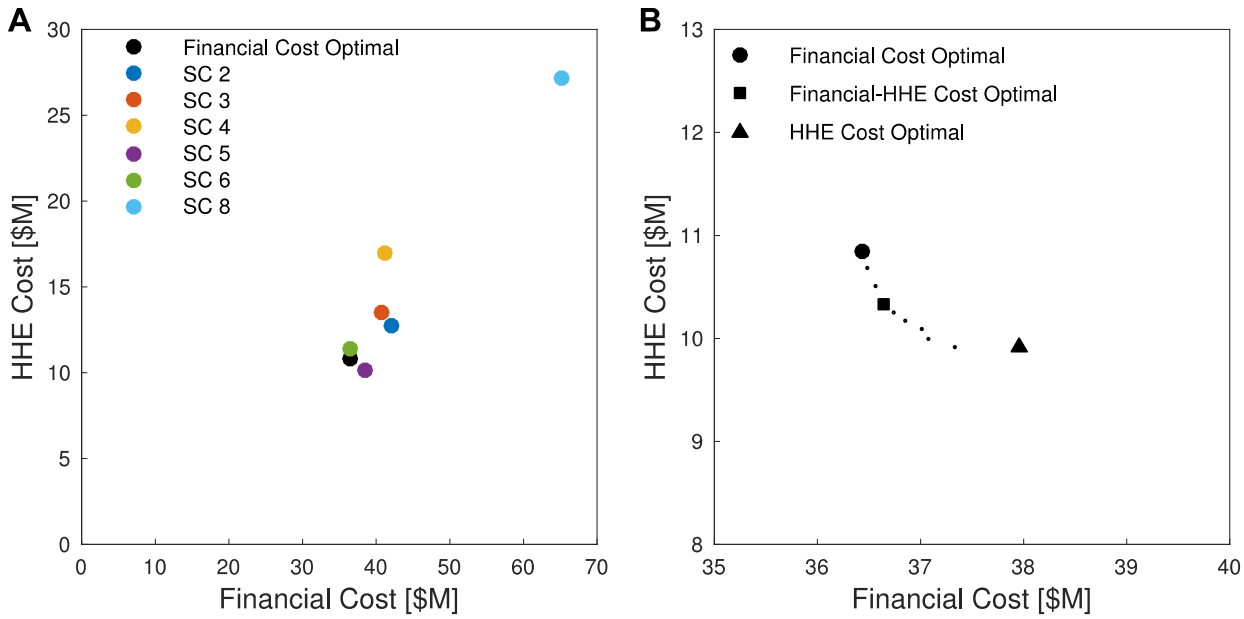

Figure 6.4. *A) Financial and HHE costs associated with air emissions for the financial cost-optimal solution and the constrained scenarios. Scenarios are labeled as follows: SC 1) No wastewater piping (equivalent to financial cost optimal solution), SC 2) No wastewater trucking between wellpads, SC 3) No wastewater storage, SC 4) No freshwater piping, SC 5) No freshwater trucking, SC 6) No central treatment, SC 7) No direct disposal to Class II injection wells (equivalent to financial cost optimal solution), and SC 8) No wastewater reuse. B) Financial and human health and environmental (HHE) costs associated with air emissions for*

the financial cost optimal, HHE cost optimal, and combined financial and HHE cost optimal solutions.

Human Health and Environmental Cost Minimization

Optimal water management strategies that lower HHE costs can be identified by including the HHE costs in the objective function. In addition to the financial cost minimization, two other objectives were investigated: the minimization of HHE costs and the minimization of combined financial and HHE costs. The three investigated objectives can be viewed as private cost minimization, public cost minimization, and combined private and public cost minimization. The financial and HHE costs of each objective is shown in Table 6.2 and the resulting Pareto frontier is shown in Figure 6.4B. Relative to the cost optimal solution, the HHE optimal water management solution increased financial costs by $1.6 million and reduced HHE costs by $1.0 million through a 91% decrease in freshwater trucking, a 30% increase in freshwater piping, a 40% increase in wastewater storage, and 1% more wastewater reuse. The financial and HHE cost optimal water management solution increased financial costs by $0.2 million and reduced HHE costs by $0.6 million through a 29% decrease in freshwater trucking and a 8% increase in freshwater piping, with no other significant changes. For further detail on the differences in water management strategies refer to SI Section 5.

6.5 Conclusions

Unconventional natural gas extraction differs from conventional well development in the intensity of the extraction process and the comparatively short duration of the gas production. As such, it is often likened to on-demand manufacturing processes where cost competitiveness is

determined by process and scheduling optimality. With short to mid-term projections for natural gas prices remaining at historic lows, companies are prioritizing cost-optimal well development.[31]

Water and wastewater management is a significant contributor to the costs of unconventional well development. Over the past five years, many companies have reduced the costs of freshwater acquisition and wastewater disposal by increasing the percentage of wastewater reused in subsequent well stimulations.[30] On the other hand, minimizing operations costs may be associated with increased HHE costs. Companies may avoid implementation of costly emissions control technologies, delay upgrades of capital intensive equipment, reduce the number of employees, or adopt lower cost treatment methods. While regulations are typically designed to curb externalization of HHE costs in scenarios where there is an inverse relationship between operational and HHE costs, there is significant uncertainty around which water management practices minimize HHE damages.

This work presents a framework for companies, regulators, and policy makers to evaluate alignment between financial and HHE cost minimization for common water management scenarios in unconventional well development. For the Marcellus case study, we observe significant variation in the financial costs and HHE damages across water management scenarios, with the bulk of HHE costs embedded in water transport. Financial costs and HHE costs are positively correlated for most cases, though this is partly a function of the large dependence on EIO-LCA impact assessment. The notable exception is the scenario that limits freshwater trucking and forces companies to internalize the air emission externalities of water trucking. More detailed, process-level assessment of the variation in costs and HHE damages

across companies and regions would further clarify the need for regulatory intervention to prevent externalization of operational costs.

Finally, this work suggests that air emission externalities of criteria pollutants are significant with respect to both the financial costs of water management and the climate change externalities of CO_2 emissions. Previous work has focused almost exclusively on the greenhouse gas emissions of unconventional well development operations, but this work demonstrates that the other air pollutants account for a large portion of the total environmental damages.

Supporting Information

The additional supporting information for this chapter is included in Appendix E. 1) model formulation, 2) emission coefficient estimation, 3) description of the AP2 model, 4) case study details, 5) additional case study results.

6.6 Acknowledgments

This material is based upon work supported by the Sloan Foundation, the Environmental Defense Fund, EQT Energy Seed Funds administered by the Scott Institute for Energy Innovation at Carnegie Mellon University, and the U.S. Department of Energy Faculty Scholars Program through the Oak Ridge Associated Universities (ORAU Program) sponsored by the National Energy Technology Laboratory (NETL).

Additionally, this work was completed as part of the NETL research portfolio on onshore unconventional resources. The authors wish to acknowledge Robert Dilmore (Geologic & Environmental Systems Directorate of the Research & Innovation Center at the U.S. Department

of Energy's NETL), Roy Long (NETL Strategic Center for Natural Gas and Oil) and Elena Melchert (DOE Office of Fossil Energy) for programmatic guidance, direction, and support.

Finally, T.V.B was supported in part through an appointment to the National Energy Technology Professional Internship Program, sponsored by the U.S. Department of Energy and administered by the Oak Ridge Institute for Science and Education, through the James Sprauge Presidential Fellowship, and through the ARCS Foundation Fellowship.

6.7 References

(1) Litovitz, A.; Curtright, A.; Abramzon, S.; Burger, N.; Samaras, C. Estimation of regional air-quality damages from Marcellus Shale natural gas extraction in Pennsylvania. *Environmental Research Letters* **2013,** *8* (1), 014017.

(2) Abramzon, S.; Samaras, C.; Curtright, A.; Litovitz, A.; Burger, N. Estimating the Consumptive Use Costs of Shale Natural Gas Extraction on Pennsylvania Roadways. *Journal of Infrastructure Systems* **2014,** *20* (3).

(3) Graham, J.; Irving, J.; Tang, X.; Sellers, S.; Crisp, J.; Horwitz, D.; Muehlenbachs, L.; Krupnick, A.; Carey, D. Increased traffic accident rates associated with shale gas drilling in Pennsylvania. *Accident Analysis and Prevention* **2015,** *74*, 203.

(4) Mauter, M. S.; Alvarez, P. J. J.; Burton, G. A.; Cafaro, D. C.; Chen, W.; Gregory, K. B.; Jiang, G.; Li, Q.; Pittock, J.; Reible, D.et al. Regional variation in water-related impacts of shale gas development and implications for emerging international plays. *Environmental Science & Technology* **2014**, DOI:10.1021/es405432k 10.1021/es405432k.

(5) Mauter, M. S.; Palmer, V. R.; Tang, Y.; Behrer, A. P. The Next Frontier in United States Shale Gas and Tight Oil Extraction: Strategic Reduction of Environmental Impacts. Belfer Center, Harvard Kennedy School **2013**.

(6) Yang, L.; Grossmann, I. E.; Manno, J. Optimization Models for Shale Gas Water Management. *Aiche J* **2014,** *60* (10), 3490.

(7) Yang, L.; Grossmann, I. E.; Mauter, M. S.; Dilmore, R. M. Investment optimization model for freshwater acquisition and wastewater handling in shale gas production. *Aiche J* **2015,** *61* (6), 1770.

(8) Yang, L.; Salcedo-Diaz, R.; Grossmann, I. E. Water Network Optimization with Wastewater Regeneration Models. *Industrial & Engineering Chemistry Research* **2014,** *53* (45), 17680.

(9) Gao, J.; You, F. Deciphering and handling uncertainty in shale gas supply chain design and optimization: Novel modeling framework and computationally efficient solution algorithm. *Aiche J* **2015,** *61* (11), 3739.

(10) Gao, J.; You, F. Optimal Design and Operations of Supply Chain Networks for Water Management in Shale Gas Production: MILFP Model and Algorithms for the Water-Energy Nexus. *Aiche J* **2015,** *61* (4), 1184.

(11) Burnham, A.; Han, J.; Clark, C. E.; Wang, M.; Dunn, J. B.; Palou-Rivera, I. Life-cycle greenhouse gas emissions of shale gas, natural gas, coal, and petroleum. *Environ Sci Technol* **2012,** *46* (2), 619.

(12) Venkatesh, A.; Jaramillo, P.; Griffin, W. M.; Matthews, H. S. Uncertainty in Life Cycle Greenhouse Gas Emissions from United States Natural Gas End-Uses and its Effects on Policy. *Environmental Science & Technology* **2011,** *45* (19), 8182.

(13) Dale, A. T.; Khanna, V.; Vidic, R. D.; Bilec, M. M. Process based life-cycle assessment of natural gas from the Marcellus Shale. *Environ Sci Technol* **2013,** *47* (10), 5459.

(14) Jiang, M.; Griffin, W. M.; Hendrickson, C.; Jaramillo, P.; VanBriesen, J.; Venkatesh, A. Life cycle greenhouse gas emissions of Marcellus shale gas. *Environmental Research Letters* **2011,** *6* (3).

(15) Laurenzi, I. J.; Jersey, G. R. Life Cycle Greenhouse Gas Emissions and Freshwater Consumption of Marcellus Shale Gas. *Environmental Science & Technology* **2013,** *47* (9), 4896.

(16) Jiang, M.; Hendrickson, C. T.; VanBriesen, J. M. Life Cycle Water Consumption and Wastewater Generation Impacts of a Marcellus Shale Gas Well. *Environmental Science & Technology* **2014,** *48* (3), 1911.

(17) Pekney, N. J.; Veloski, G.; Reeder, M.; Tamilia, J.; Rupp, E.; Wetzel, A. Measurement of atmospheric pollutants associated with oil and natural gas exploration and production activity in Pennsylvania's Allegheny National Forest. *Journal of the Air & Waste Management Association* **2014,** *64* (9), 1062.

(18) Coday, B. D.; Miller-Robbie, L.; Beaudry, E. G.; Munakata-Marr, J.; Cath, T. Y. Life cycle and economic assessments of engineered osmosis and osmotic dilution for desalination of Haynesville shale pit water. *Desalination* **2015,** *369*, 188.

(19) Matthews, H. S., Hendrickson, C. T., Matthews, D. H., *Life Cycle Assessment: Quantitative Approaches for Decisions That Matter*, **2015**. http://www.lcatextbook.com (Accessed Oct 22, 2015)

(20) Muller, N. Z.; Mendelsohn, R.; Nordhaus, W. Environmental Accounting for Pollution in the United States Economy. *American Economic Review* **2011,** *101* (5), 1649.

(21) Behrer, A.; Mauter, M. S. Allocating Damage Compensation in a Federalist System: Lessons from Spatially Resolved Air Emissions in the Marcellus. *In review* **2015**.

(22) Al-Karaghouli, A.; Kazmerski, L. L. Energy consumption and water production cost of conventional and renewable-energy-powered desalination processes. *Renewable and Sustainable Energy Reviews* **2013,** *24*, 343.

(23) U.S. Energy Information Administration, Net Generation by State by Type of Producer by Energy Source **2015**. https://www.eia.gov/electricity/data/state/ (Accessed Jan 7, 2016)

(24) U.S. Environmental Protection Agency, The 2011 National Emissions Inventory **2015**. http://www3.epa.gov/ttnchie1/net/2011inventory.html (Accessed Jan 7, 2016)

(25) U.S. Environmental Protection Agency. eGRID2012 Summary Tables **2015**. http://www.epa.gov/energy/egrid-2012-summary-tables. (Accessed Jan 7, 2016)

(26) Interagency Working Group on Social Cost of Carbon, Technical Support Document: - Technical Update of the Social Cost of Carbon for Regulatory Impact Analysis - Under Executive Order 12866. United States Government **2015**.

(27) Torres, L.; Yadav, O. P.; Khan, E. A review on risk assessment techniques for hydraulic fracturing water and produced water management implemented in onshore unconventional oil and gas production. *Science of the Total Environment* **2016,** *539*, 478.

(28) Small, M. J.; Stern, P. C.; Bomberg, E.; Christopherson, S. M.; Goldstein, B. D.; Israel, A. L.; Jackson, R. B.; Krupnick, A.; Mauter, M. S.; Nash, J.et al. Risks and Risk Governance in Unconventional Shale Gas Development. *Environmental Science & Technology* **2014,** *48* (15), 8289.

(29) Mauter, M. S.; Alvarez, P. J. J.; Burton, A.; Cafaro, D. C.; Chen, W.; Gregory, K. B.; Jiang, G. B.; Li, Q. L.; Pittock, J.; Reible, D.et al. Regional Variation in Water-Related Impacts of Shale Gas Development and Implications for Emerging International Plays. *Environmental Science & Technology* **2014,** *48* (15), 8298.

(30) Mauter, M. S.; Palmer, V. R. Expert Elicitation of Trends in Marcellus Oil and Gas Wastewater Management. *J Environ Eng* **2014,** *140* (5).

(31) U.S. Energy Information Administration, Short-Term Energy Outlook **2016**. https://www.eia.gov/forecasts/steo/report/natgas.cfm (Accessed Feb 2, 2016)

7.0 ENERGY AND CO_2 EMISSIONS PENALTIES OF GEOLOGIC CARBON STORAGE BRINE MANAGEMENT

7.1 Abstract

Safe and cost-effective geologic carbon storage will require active CO_2 reservoir management, including brine extraction to minimize subsurface pressure accumulation. While past simulation and experimental efforts have estimated brine extraction volumes, there has been very little work assessing the energy or emissions penalties of managing and disposing of this brine. We estimate energy and CO_2 emission penalties of extracted brine management on a per tonne of CO_2 stored basis by spatially integrating CO_2 emissions from U.S. coal-fired electric generating units, CO_2 storage reservoirs, and brine salinity datasets under several carbon and water management scenarios. We estimate a median energy penalty of 4.4 - 35 kWh/tonne CO_2 stored, suggesting that brine management will be the largest post-capture and compression energy sink in the carbon storage process. These estimates of energy demand for brine management are useful for evaluating end-uses for treated brine, assessing the cost of CO_2 storage at the reservoir level, and optimizing national CO_2 transport and storage infrastructure.

7.2 Introduction

Limiting global temperature increase depends critically on developing realistic carbon budgets and designing cost-effective technology portfolios to support deep decarbonization. Most of these technology portfolios assign a large role for carbon capture and geologic storage from electric power generators and other stationary sources,[1] but the techno-economic feasibility and risk profile of large scale geologic carbon storage (GCS) remains highly uncertain. This uncertainty is both aleatory and epistemic, stemming from heterogeneity among and within the diverse saline reservoirs where carbon is likely to be stored, as well as from uncertainty about the relationships between reservoir capacity, the rate of carbon injection, subsurface pressure

accumulation, earthquake risk, and the effectiveness of active CO_2 reservoir management (ACRM).[2-4] While the extraction of brine from the saturated pore space of saline reservoirs in ACRM is expected to increase reservoir storage capacity and minimize earthquake risk, ACRM also imposes water management costs and energy penalties that will vary with brine composition. Finally, there is uncertainty about the lifecycle cost and energy penalties of source-to-sink carbon capture and geological storage.

Clarifying the optimal role for GCS in decarbonization portfolios will require that we reduce this uncertainty through additional empirical research, as well as through incorporation of high resolution, site-specific data within systems-level integrated assessment models. Past technical and economic assessments of GCS and ACRM have necessarily focused on case studies characterizing the physics of the subsurface[5-7] and on developing generic process-based cost estimates.[8-12] There has been substantially less work integrating reservoir characteristics within carbon and brine management models to develop probabilistic ranges for diverse management scenarios. Doing so is critical to focusing future research and informing infrastructure investments.

The present work characterizes the expected distribution of energy and CO_2 emission penalties associated with GCS brine management at U.S. reservoirs as a function of carbon transport, reservoir management, and brine treatment decisions. While two recent case studies have estimated the energy consumption of brine management and treatment in the Mt. Simon formation using a single treatment technology and brine composition,[13-14] similarly detailed assessments have not been published for other reservoirs or brine compositions. Furthermore, the only nationwide assessment of GCS brine management[15] is restricted to assessing low salinity GCS brines (<40 g/L TDS) and associated treatment technologies. Performing a

comprehensive nationwide assessment of brine management energy and emission penalties requires consideration of the spatial distribution of brine salinities within and between reservoirs, the treatment technologies relevant to managing brines of differing composition, the relative CO_2 injection rates and brine withdrawal volumes at each reservoir, and the tradeoffs between the energy intensity of brine treatment and water recovery. As noted above, this nationwide assessment is critical to informing infrastructure investments for both carbon transport and brine management networks.

Here, we estimate the energy and CO_2 emission penalties of GCS brine management on a per tonne of CO_2 stored basis by spatially integrating CO_2 emission sources, CO_2 storage reservoirs, and brine salinity datasets. We use stochastic simulation to develop a distribution of energy and emission penalties that reflect the variability and uncertainty in extracted brine volume, salinity, treatment, and disposal across 77 U.S. saline reservoirs and three distinct brine management scenarios. Our analysis covers eighty-five percent of U.S. saline reservoir GCS capacity, providing the type of reservoir specific information and national level coverage that will be critical to GCS assessment.

7.2 Results and discussion

Salinity of GCS brines

Saline reservoirs are expected to provide 95% of total U.S. CO_2 storage capacity.[16] We obtained location data and storage capacity for all 178 saline onshore saline reservoirs in the lower 48 states from the National Carbon Sequestration Database and Geographical Information System (NATCARB) v1502.[17] We then use the USGS produced water database v2.2 to estimate the brine salinity medians and distributions for the 105 NATCARB reservoirs with ten or more reported brine samples, which comprise 85% of estimated total U.S. GCS capacity.[18] If the

median brine salinity of a reservoir is less than 10 g/L TDS, we exclude that reservoir from our analysis because it would be considered an underground source of drinking water by the U.S. Environmental Protection Agency and operators would be required to obtain a waiver for CO_2 injection. Excluding the low salinity reservoirs reduces our analysis to 77 NATCARB reservoirs and 64% of the estimated total U.S. GCS capacity (Figure 7.1A, 7.1B).

Saline brine composition is highly variable both between and within reservoirs. The median average salinity for the 77 reservoirs is 72 g/L total dissolved solids (TDS), or roughly double the concentration of seawater, with more than half of U.S. CO_2 storage capacity expected to be saturated with brines of greater than 110 g/L TDS (Figure 7.1B). Intra-reservoir salinity variability has a 35-120% coefficient of variation (10^{th} and 90^{th} percentile, Table 7.1) and is demonstrated for select reservoirs in Figure 7.1B. This variability underscores the importance of treating brine salinity probabilistically during individual reservoir analysis and of utilizing reservoir-specific brine salinity distributions when assessing brine management strategies nationally.

Table 7.1. *Salinity statistics for U.S. saline reservoirs. This study assesses reservoirs with a median salinity greater than 10 TDS g/L and 10 or more USGS produced water samples. The table provides the 10^{th}, 50^{th}, 90^{th} percentile reservoir of the number of samples, average salinity, standard deviation, and coefficient of variation.*

Reservoir percentile	10th	50th	90th
Number of samples	17	104	980
Average salinity (TDS g/L)	17	72	166
Coefficient of variation (%)	35	73	118

Even under aggressive scenarios for carbon capture and storage, GCS capacity far exceeds economically recoverable carbon emissions from stationary sources over the next 50 years of anticipated U.S. fossil energy generation.[17] Thus, the actual salinity of extracted brine will depend on the reservoirs selected for CO_2 storage, their proximity to CO_2 sources, and their sequestration costs. In this work, we constrain our analysis to focus on the energy and emission penalties of brine treatment associated with storing carbon from coal fired electricity generation units (EGUs) because they are the largest point sources of CO_2,[19] the most cost-effective targets for carbon capture,[20] and, with the exception of CA, their geographic distribution is generally representative of CO_2 point sources.[17] We obtain location and CO_2 emissions data for coal fired EGUs from the Emissions & Generation Resource Integrated Database (eGRID2012) (Figure 7.1A).[19]

The CO_2 emissions from EGUs are assigned to CO_2 storage reservoirs using three different reservoir selection cases. In the first case, EGUs are assigned to the reservoir with the lowest median salinity within a 500 mile radius. Case 1 (lowest salinity) prioritizes reducing brine management costs by targeting a lower salinity extracted brine. In the second, the EGUs are assigned to the closest and shallowest reservoir. Case 2 (closest) prioritizes reducing CO_2 sequestration costs by limiting CO_2 transport distance and injection depth. Finally, in the third case, EGUs distribute their CO_2 to the capacity weighted average of all reservoirs within 500 miles. Case 3 (weighted) represents a future scenario in which CO_2 sequestration is widespread and supported by interconnected pipeline infrastructure.

For each case, we estimate the distribution of extracted brine salinity associated with storing the annual CO_2 emissions from each coal-fired EGU using generation data from 2012.

We then sum these distributions to obtain the cumulative distribution of extracted brine salinity across all U.S. EGUs (Figure 7.1C).

Reservoir selection has a significant impact on extracted brine salinity, with the lowest salinity reservoir selection case yielding extracted brine salinities that average 50 and 70 g/L TDS lower than for the closest and weighted cases. This lowest salinity case is only realistic if brine treatment costs dominate the overall carbon storage costs, which is inconsistent with past estimates of GCS costs.[12] We focus the subsequent analysis on Case 3 (weighted average of all reservoirs within 500 miles) because it represents widespread GCS adoption and does not rely on the balance of highly uncertain projected CO_2 storage and brine management costs.

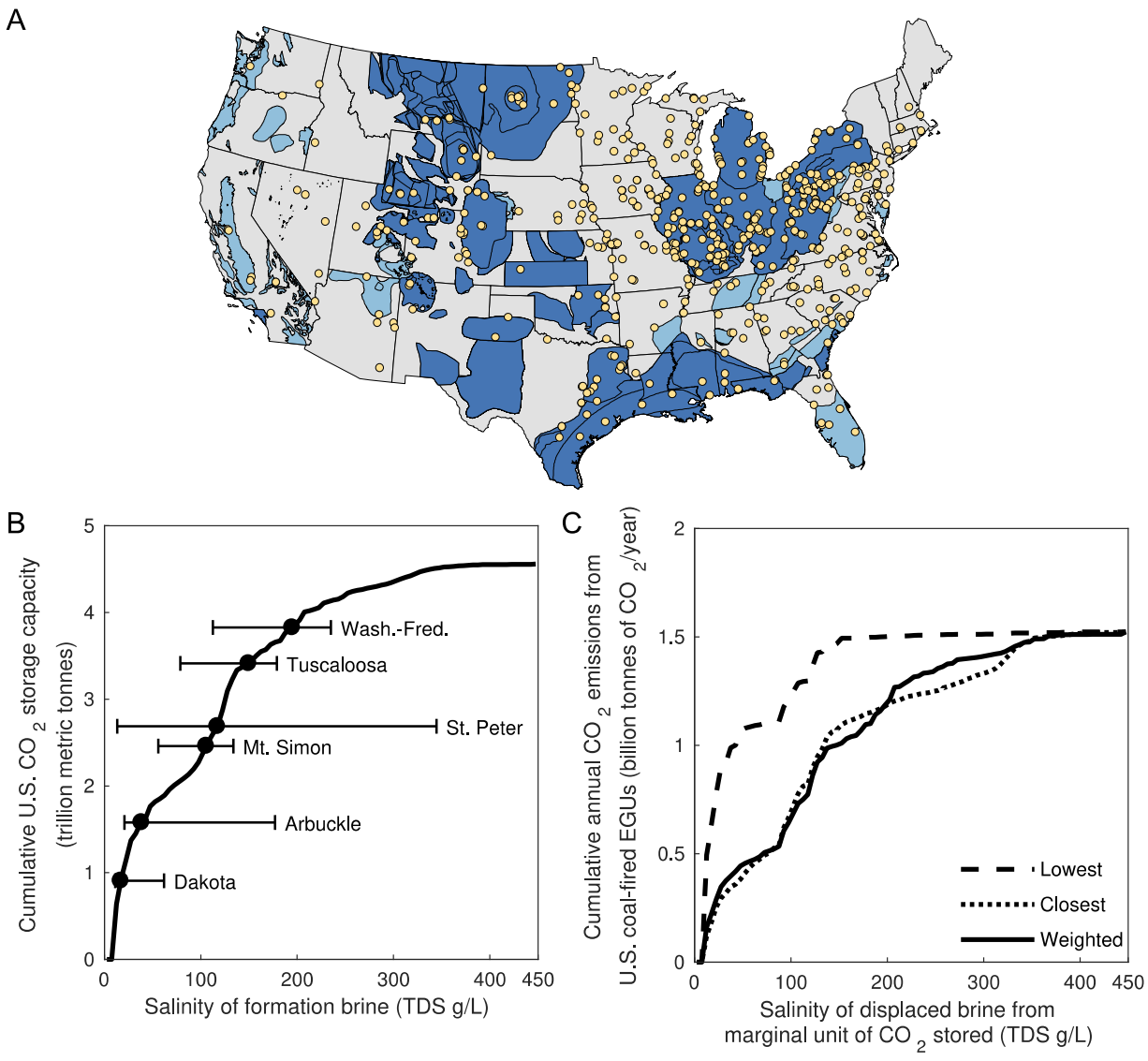

Figure 7.1. *Geologic Carbon Storage Brine Characteristics of U.S. Saline Reservoirs A) U.S. saline reservoirs (dark and light blue) and coal fired EGUs (yellow). The location and storage capacity of these 198 saline reservoirs was obtained from the NATCARB.*[17] *The dark blue reservoirs have at least 10 brine samples included in the USGS produced water database and a median salinity greater than 10 g/L TDS,*[18] *whereas the light blue reservoirs have less than 10 reported brine samples or a median salinity less than 10 g/L TDS and have been excluded from this analysis. The location of the coal fired EGUs was obtained from the eGRID 2012 database.*[19] *B) Salinity of formation brine with cumulative U.S. CO_2 storage capacity for U.S.*

reservoirs with salinity data meeting our analysis criteria. The points and error bars represent the median and 10th-90th percentile salinity distribution for select saline reservoirs: Arbuckle, Mt. Simon, St. Peter, Tuscaloosa, and Washita-Fredericksburg (Wash.-Fred.). These saline reservoirs have been identified as high potential GCS reservoirs by the NATCARB regional partnerships because they have high permeability, high storage capacity, low estimated storage costs, and low risk of CO_2 leakage.[47-49] C) Salinity of displaced brine with cumulative annual CO_2 emissions from coal fired EGUs for three reservoir selection cases: lowest median salinity reservoir within 500 miles of the EGU; closest and shallowest reservoir to the EGU; and storage capacity weighted average of all reservoirs within 500 miles of the EGU.

Technologies for GCS brine concentration and disposal

Environmental, geological, and technological factors constrain management and disposal options for high salinity GCS brines. Even moderate levels of clean brine discharge to the environment are associated with significant declines in water quality, a loss of freshwater biodiversity, and the potential for disinfection byproduct formation in drinking water treatment plants downstream.[21] As a result, most states mandate that inland brines be desalinated for beneficial reuse or disposed of via underground injection into high porosity geological formations. Though deep well injection remains a low cost disposal option in many parts of the country, past reliance on high volume wastewater injection for oil and gas produced water disposal has been linked to increased earthquake frequency in the U.S. and has led to significant public backlash against injection in some regions.[22-24] The annual production of GCS brines from coal fired EGUs alone would represent approximately one third of all U.S. oil and gas wastewater produced in 2012 (details in the methods section), but with significantly fewer

opportunities for on-site reuse of saline brines than in oil and gas.[8, 25] These volumes suggest that deep well injection is likely to face feasibility constraints as a stand-alone brine management technology.

An alternative approach is to desalinate extracted brines to yield a freshwater stream and a concentrated stream that is then crystallized or injected. Treating higher salinity brines is costlier and more energy intensive; the thermodynamic minimum work required to double the concentration of a 20 g/L brine is roughly double that required for a 10 g/L brine. There are also technological barriers to realizing energy efficient brine concentration. State of the art reverse osmosis (RO) membrane separation processes have exceedingly low recovery rates, are economically uncompetitive for treating brines above 45 g/L TDS, and are completely ineffective above 75 g/L TDS.[26] Instead, less efficient thermal separation processes, such as mechanical vapor recompression (MVC), are typically deployed to treat high salinity feeds and concentrate from RO.[27]

We assess the energy intensity and CO_2 emissions penalty of extracted GCS brine disposal under four brine management scenarios: 1) no reuse, in which all extracted brine is injected in a disposal well; 2) low reuse, in which low salinity extracted brine (< 45 g/L) is treated with RO, while RO concentrate and high salinity brine is injected; 3) medium reuse, in which brines with < 250 g/L TDS are treated using a combination of RO and MVC, while the concentrate and any high salinity brine (> 250 g/L) is injected; and 4) maximum reuse, in which all extracted brine is treated with a combination of RO, MVC, and crystallization. This fourth case eliminates injection entirely.

The total estimated energy consumption for each brine management scenario also incorporates energy consumption embedded in the brine extraction, pretreatment, transport, and wastewater disposal steps (Eq. 7.1).

$$EC_k(S) = \hat{E}_e + \sum_i \left(VF_i\ \hat{E}_i + y_i\ \hat{E}_{i,p}\right) + \hat{E}_t \sum_j \left(VF_j\ D_j\right) + VF_d\ \hat{E}_d\ \forall k \quad (7.1)$$

Here, EC is the energy consumption [kWh/m^3 of extracted brine] for each brine management case k and is a function of salinity, S [TDS g/L]; $\hat{E}$ is the specific energy consumption [kWh/m^3 of extracted or treated or disposed water or kWh/(m^3-mile-of transported water)] for extraction (e), treatment technology (i), pretreatment (p), disposal (d), and transportation (t); VF is the volume fraction [m^3 of treated, transported, or disposed water/m^3 of extracted brine] for each treatment technology i (i.e. reverse osmosis, MVC, and crystallization), transportation segment j (i.e. extraction to treatment, treatment to reuse, and treatment to disposal), and disposal d; y_i is a binary variable noting whether the treatment technology is used; and D is the transportation distance [miles] for each transportation segment. The volume fractions are a function of salinity and are determined by the treatment specifications of each brine management case and the specific energy consumption for each activity is based on literature values as outlined in the methods section.

For all cases, we observe higher energy penalties for brine management cases with decreased injection well disposal and higher beneficial reuse (Figure 7.2A). The energy penalties associated with brine and concentrate treatment exceed the estimated energy benefits of reduced transport and disposal options, even for the low salinity brine cases. Note that these estimates assume that beneficial reuse occurs in regions that are otherwise unconstrained by water supply. If inland desalination of GCS brines were displacing inland desalination of other brackish water sources, the optimal brine management approach would be determined by

comparing the energy consumption per unit of treated water (Figure 7.2B) to locally available alternatives.

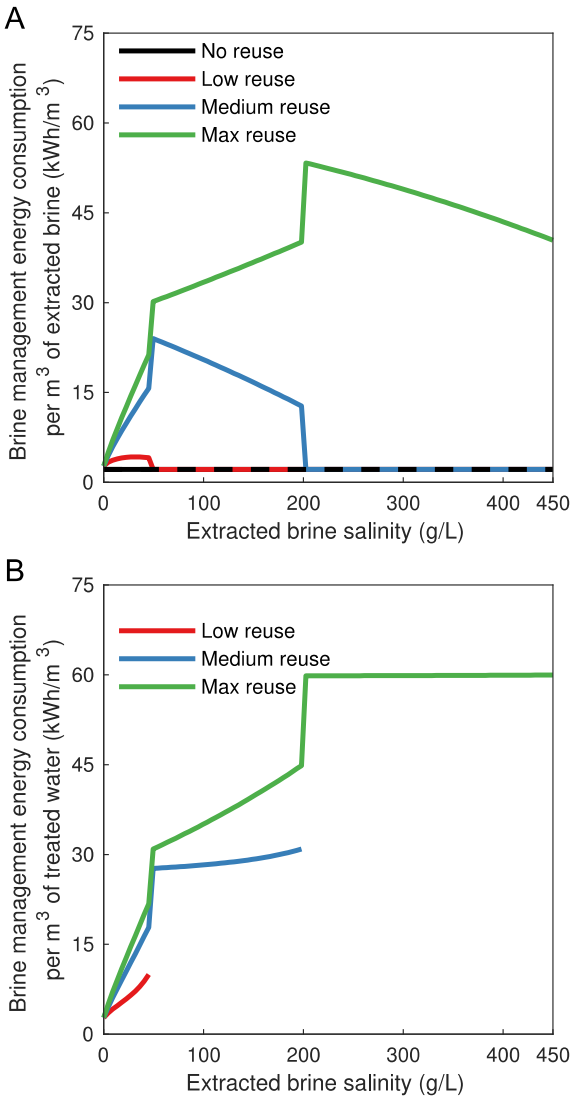

Figure 7.2. *Estimated Energy Consumption of Geologic Carbon Storage Brine Management Energy consumption of GCS brine management on an A) extracted volume and B) treated volume basis. Energy consumption is estimated for the four management cases: 1) no reuse, 2) low reuse, 3) medium reuse, 4) maximum reuse and incorporates the energy embedded in transporting, treating, and disposing of the brine concentrate via deep well injection. For each*

case, we use the mid-point of the ranges for transport distance, treatment efficiency, and disposal wellhead pressure presented in the methods section.

Brine management energy and emission penalty

We estimate the energy penalty of managing GCS brine from U.S. reservoirs by integrating spatially resolved extracted brine salinity, brine management energy consumption, and CO_2 sequestration parameters (Eq. 7.2).

$$EP_k = EC_k(S) * \frac{BE}{\rho_{CO_2}} \quad (7.2)$$

Here EP is the energy penalty [kWh/tonne of CO_2 stored] for each brine management case (k), $EC(S)$ is the energy consumption [kWh/m^3 of extracted brine] as a function of salinity (Eq. 7.1), BE is the brine extraction ratio [m^3 of extracted brine/m^3 of CO_2 stored], and ρ_{CO_2} is the density of supercritical CO_2 [tonne of CO_2/m^3 of CO_2] in the storage reservoir. We convert the energy penalty to an emission penalty by multiplying by the 2016 national average carbon intensity of electricity [453 g CO_2/kWh].[28] While the national average may underestimate the current carbon intensity of electricity in regions with a high number of coal-fired EGUs, when carbon capture and sequestration is adopted the carbon intensity will decrease and converge toward this national average. We also convert the energy penalty to a parasitic loss at the power plant by multiplying by a power plant carbon capture intensity of 0.001 tonne of captured CO_2/net kWh generated as estimated by the Integrated Environmental Control Model (IECM).[29]

We use the median salinity of the extracted brine salinity distribution for each coal-fired EGU to estimate the energy penalty deterministically (Figure 7.3A). The median energy and emission penalties for the extracted brine management cases range from 4.3 - 37 kWh and 1.9 - 17 kg of CO_2 emitted per tonne of CO_2 stored. We observe less than a 5% difference between

the 25th and 75th percentile of brine management energy penalties for each case. We attribute this narrow range to the low variation in the median salinity between each coal fired EGU for the weighted average CO_2 reservoir selection case. Note that this deterministic calculation does not account for intra-formation salinity variability or uncertainty in sequestration and brine management processes.

To address these shortcomings, we augment our deterministic analysis with a Monte Carlo simulation (Figure 7.3B). This approach allows us to stochastically estimate the energy and emission penalty for the extracted brine salinity distribution (Figure 7.1C, weighted) and the range of treatment technology energy demands, brine extraction ratios, and CO_2 densities detailed in the methods section. The median energy and emission penalties for the Monte Carlo simulation range from 4.4 to 35 kWh and 2.0 to 16 kg of CO_2 emitted per tonne of CO_2 stored, respectively. These estimates suggest that brine management will impose the largest post-capture and compression energy penalty on a per-tonne of CO_2 basis, up to an order of magnitude greater than carbon transport.[30]

As expected, brine management with higher reuse results in higher energy and emission penalties. The average percentage of water reuse for the no, low, medium, and maximum reuse are: 0%, 20%, 63%, 93%, respectively. The low reuse case has a similar energy penalty to the no reuse case because most extracted brine is above the treatment salinity threshold for this case and is injected for disposal. Water reuse in the low reuse case is limited by the salinity limits for RO, which demonstrates the importance of the evaporative treatment technologies MVC and crystallization for realizing the high reuse cases. The maximum reuse case does not obtain 100% water reuse because the crystallized solids contain an assumed 10% water content.

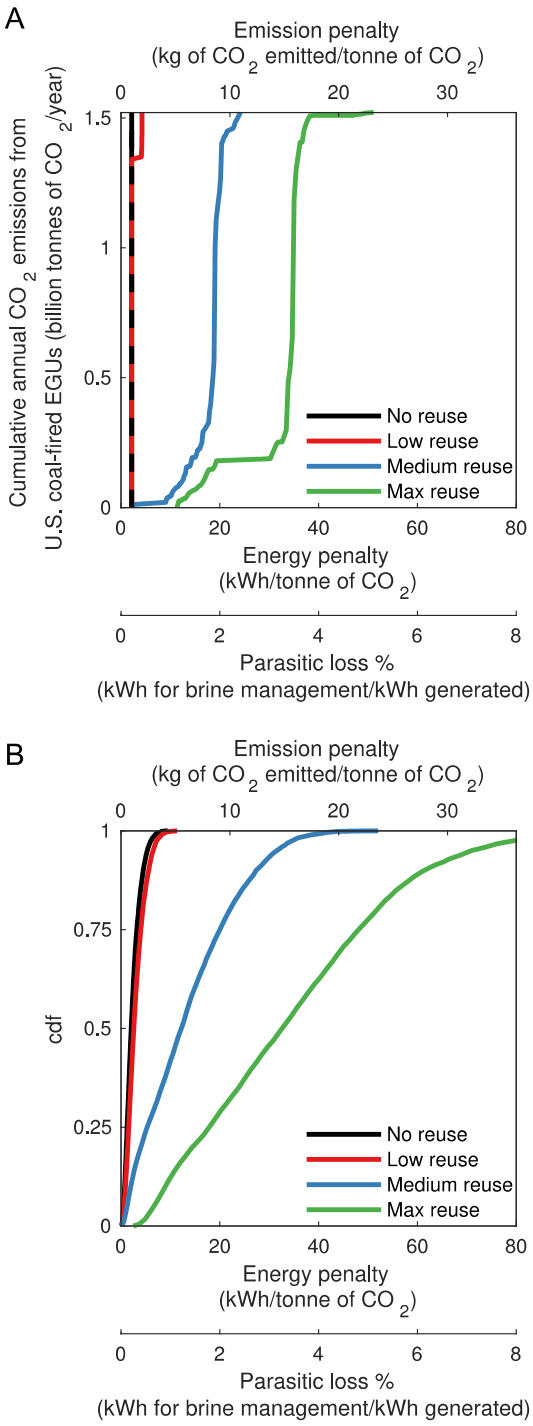

Figure 7.3. *Brine management energy and emission penalties for four brine management cases: 1) no reuse, 2) low reuse, 3) medium reuse, 4) maximum reuse. A) Deterministic energy and emission penalty for all U.S. coal-fired EGUs using median values for brine salinity and*

management. The salinity for each reservoir is assumed to equal the median from the capacity weighted CO_2 storage case. The deterministic values for the energy consumption parameters values are the bisection of the ranges presented in the methods section. B) Stochastic energy and emission penalty estimated from a Monte Carlo simulation that accounts for the distribution of brine salinity within reservoirs and the uncertainty in brine management parameters as described in the methods section.

Implications of brine management energy intensity for GCS planning

There is a narrowing window in which infrastructure investments can mitigate the most severe impacts of climate change. Proposed responses include increasing energy efficiency, renewable electricity generation, low carbon fuels, and carbon capture and geologic disposal.[31] Regardless of whether this carbon capture occurs by retrofitting existing power plants,[32] combusting alternative fuels,[33] building new facilities that utilize alternative power cycles,[34] capturing carbon at a distributed set of industrial sources,[35] or performing direct air capture,[36-37] the post-capture management process is likely to share several common elements. First, widespread deployment of CO_2 capture suggests that the volume of captured carbon will exceed practical end use applications and will require transport and storage in geologic formations. Second, these transport and storage functions will impose cost and energy penalties above and beyond those cited for carbon capture processes. And third, minimizing these cost and energy penalties will require spatially resolved accounting of the tradeoffs between transportation, storage, and produced brine treatment. The present work quantifies the expected salinity distribution of brines from potential carbon storage reservoirs, delineates management options for these brines, and estimates the energy intensity of managing these brines. In so doing, we

contribute the first spatially resolved assessment of energy and emissions tradeoffs between brine management strategies.

While the carbon capture and compression processes are likely to incur energy penalties an order of magnitude greater than those of brine management, our study demonstrates the potential for wide variation in the energy intensity of brine management across different saline reservoirs, reservoir management protocols, and brine disposal practices. For reference, post-combustion carbon capture and compression at a conventional coal fired EGU is expected to decrease the net thermal efficiency from 30-45% to 25-35%, which is roughly equivalent to a 30% parasitic loss for the EGU.[20, 38] If electricity to manage and dispose of the brines generated via ACRM were sourced from a coal fired EGU, the electricity demand would be expected to impose an additional parasitic loss of 0.3-8%, assuming a brine management energy penalty of 3-80 kWh per tonne of CO_2 stored.

7.3 Conclusions

We find that GCS brine management will impose the largest post-capture and compression energy penalty on a per-tonne of CO_2 basis, up to an order of magnitude greater than carbon transport. This work suggests that the energy penalty of brine management can be reduced by prioritizing storage in low salinity reservoirs, minimizing the brine extraction ratio, and limiting the extent of brine recovery. Unfortunately, each of these management strategies imposes their own tradeoffs. Lower salinity reservoirs have limited storage capacity and their spatial distribution may impose higher transportation-related cost and energy penalties. Minimizing the brine extraction ratio will limit reservoir storage capacity and decrease the safe rate of CO_2 injection. Finally, restricting the use of evaporative technologies for brine concentration and freshwater recovery will also increase the volume of brine disposal via deep

well injection and will limit beneficial reuse. Evaluating these tradeoffs within the context of a complete carbon capture utilization and storage infrastructure system will be critical to maximizing CO_2 emission mitigation, minimizing financial costs, and limiting environmental externalities.

7.4 Methods

Saline reservoir location, capacity, and salinity

Saline reservoir location and capacity data were obtained from the NATCARB database.[17] We down-selected the saline reservoirs to include only those within the 48 contiguous states, yielding 178 unique reservoirs. These reservoirs were matched with brine water quality samples from the USGS produced water database.[18] We developed an empirical distribution of reservoir brine salinity using samples collected from a depth of greater than 2500 feet and a salinity of greater than 10 g/L to ensure sufficient pressure for supercritical CO_2 storage and prevent disruption of potential brackish water drinking water sources.[8] The names, capacity, and salinity statistics for each saline reservoir are included in Supplementary Information Section S1.

CO_2 storage cases

We used ArcGIS 10.3 to construct the three reservoir selection cases that pair coal-fired EGU with saline storage reservoirs. The first case identifies the single reservoir with the lowest median salinity within 500 miles of the EGU. This 500 mile distance roughly represents the maximum transport distance in current large-scale CO_2 pipeline networks.[39] The second identifies the single reservoir that is closest and then shallowest to the coal-fired EGU. For these two cases, the extracted brine salinity distribution for each coal-fired EGU is represented by the

empirical salinity distribution for the selected reservoir. The third case weights the contribution of all saline reservoirs within 500 miles by their respective storage capacity.

Comparison of extracted brine volumes from GCS to oil and gas wastewater

The potential extracted brine volume from GCS depends on the stored CO_2 volume and the brine extraction ratio. Annual CO_2 emissions for U.S. coal-fired EGUs was 1.5 billion metric tonnes in 2012.[19] If these EGUs are retrofitted to capture 90% of CO_2 without additional coal combustion to offset the energy consumption of carbon capture, then the annual stored CO_2 volume would be 1.35 billion metric tonnes. If the stored CO_2 density is 650 kg per m^3 and the brine extraction ratio is 0.5 m^3 of extracted brine per m^3 of stored CO_2, the annual volume of extracted brine would be 1 billion m^3. This potential annual volume of extracted brine represents approximately 30 to 40% of the 2.4 to 3.3 billion m^3 wastewater produced by the oil and gas industry in 2012.[25]

Brine management cases and energy consumption

We consider four brine management cases: no reuse, low reuse, medium reuse, and maximum reuse. We estimate the energy consumption of brine management for each case by multiplying the energy intensity of extraction, pretreatment, treatment, transport, and disposal by the respective volume fractions for each specified brine management case (Eq. 7.1).

The specific energy consumption of brine extraction, disposal, and transport is based on pump energy demand. We assume a head loss of 100 m for extraction and injection.[40] In addition to overcoming the head loss, the injection pump must increase the brine pressure to the wellhead gauge pressure. We assume that the range of 0-2.8 MPa wellhead pressure for the Class II disposal wells in Oklahoma are representative for future GCS brine disposal.[41] We also assume that the brine will be transported via pipeline, the head loss ranges from 5-50 m per 1000

m, and the transportation distances range from 0-10, 10-50, 0-50 miles for extraction to treatment, treatment to beneficial use, and treatment to disposal, respectively (further details in SI Section 3). For all pump energy calculations, we assume an isothermal pump efficiency of 80% and a motor efficiency of 85%.[42]

For the no reuse case, all extracted brine is transported to the disposal well (same distance as treatment to disposal) and injected without pretreatment.

For each treatment case, we assume a fixed value of either 0.5 kWh/m^3 for RO or 0.05 kWh/m^3 of extracted brine for MVC/crystallization, respectively.[26, 43] Since pretreatment energy consumption is relatively low, we only consider a fixed value.

For the low reuse case, extracted brine with salinity < 45 g/L is concentrated to 75 g/L via RO. This concentrated waste and all other extracted brine > 45 g/L is disposed of via injection. The energy consumption of RO is estimated using the theoretical minimum work of separation and an assumed 40-50% second law efficiency (ratio of minimum work of separation to actual electrical energy input).[44] We estimate the theoretical minimum work of separation with Gibbs free energy calculations obtained from the NRTL method in AspenPlus for a pure NaCl solution. A NaCl solution is an appropriate approximation of the extracted brine composition because, on average, NaCl comprises 90% of the TDS for the saline reservoirs studied in this work. Refer to the SI section 1 for the median brine composition data for each saline reservoir.

For the medium reuse case, extracted brine with salinity < 250 g/L is treated with RO (same specifications as the low reuse case) and/or MVC to 310 g/L (NaCl saturation). MVC consumes between 20-30 kWh per m^3 of treated water when concentrating a NaCl brine to saturation.[27]

For the maximum reuse case, the extracted brine is treated with RO (same specifications as low reuse), MVC (same specifications as medium reuse), and crystallization. We assume the crystallizer consumes between 50-65 kWh per m^3 of treated water and generates desalinated water and solid waste that is 10% water by weight.[45]

Energy and emission penalty

The energy penalty was estimated as a function of brine salinity, stored CO_2 density, brine extraction ratio, and brine management energy consumption. The brine salinity was represented by the distribution of extracted brine salinity for the capacity weighted CO_2 storage case (Figure 7.1C). We considered a range of stored CO_2 density and brine extraction ratio based on literature values. The CO_2 density ranged from 550 to 750 kg per m^3 of CO_2.[46] The brine extraction ratio ranged from 0.3 to 1 m^3 of extracted brine per m^3 of injected CO_2.[4, 6] The brine management energy consumption as a function of salinity is presented in Figure 7.2 and the preceding methods section provides the specific energy consumption of the activities and the treatment specifications for the brine management cases.

We deterministically estimated the energy penalty of GCS brine management for each coal-fired EGUs with the median value or midpoint of the ranges for the extracted brine salinity, CO_2 density (650 kg/m^3), brine extraction ratio (0.65), disposal wellhead pressure (1.4 MPa), transport distances (5, 30, and 25 miles), RO treatment efficiency (45%), MVC energy consumption (25 kWh/m^3), and crystallization energy consumption (57.5 kWh/m^3). To reflect the uncertainty in sequestration and brine management processes, we performed a Monte Carlo simulation to stochastically estimate the energy penalty. The brine salinity distribution was developed in the CO_2 storage case, while all other parameters, except for CO_2 density, were modeled with a uniform distribution with the upper and lower bound defined by the stated range.

The CO_2 density was modeled with a triangular distribution because the range was defined by extreme cases.[46] The emission penalty and the parasitic loss at the power plant were estimated based on conversions with the national average carbon intensity of electricity and the power plant carbon capture intensity, as discussed in the brine management energy and emission section of the manuscript.

Supporting Information

The additional supporting information for this chapter is included in Appendix F.

7.5 Acknowledgements

We would like to thank Nicholas Siefert for thoughtful advice in sourcing data for this work. This work was funded by NSF CBET-1554117 and the ARCS Foundation Fellowship. T.V.B. is currently supported by the National Energy Technology Laboratory Research Participation Program, sponsored by the U.S. Department of Energy and administered by the Oak Ridge Institute for Science and Education.

7.6 References

1. International Energy Agency *Technology Roadmap: Carbon capture and storage*; International Energy Agency: Paris, France, 2013.

2. Buscheck, T. A.; Sun, Y.; Chen, M.; Hao, Y.; Wolery, T. J.; Bourcier, W. L.; Court, B.; Celia, M. A.; Julio Friedmann, S.; Aines, R. D., Active CO2 reservoir management for carbon storage: Analysis of operational strategies to relieve pressure buildup and improve injectivity. *International Journal of Greenhouse Gas Control* **2012,** *6*, 230-245.

3. Birkholzer, J. T.; Cihan, A.; Zhou, Q., Impact-driven pressure management via targeted brine extraction—Conceptual studies of CO2 storage in saline formations. *International Journal of Greenhouse Gas Control* **2012,** *7*, 168-180.

4. Cihan, A.; Birkholzer, J. T.; Bianchi, M., Optimal well placement and brine extraction for pressure management during CO2 sequestration. *International Journal of Greenhouse Gas Control* **2015,** *42*, 175-187.

5. Bergmo, P. E. S.; Grimstad, A.-A.; Lindeberg, E., Simultaneous CO2 injection and water production to optimise aquifer storage capacity. *International Journal of Greenhouse Gas Control* **2011,** *5* (3), 555-564.

6. Heath, J. E.; McKenna, S. A.; Dewers, T. A.; Roach, J. D.; Kobos, P. H., Multiwell CO2 Injectivity: Impact of Boundary Conditions and Brine Extraction on Geologic CO2 Storage Efficiency and Pressure Buildup. *Environmental Science & Technology* **2014,** *48* (2), 1067-1074.

7. Ziemkiewicz, P.; Stauffer, P. H.; Sullivan-Graham, J.; Chu, S. P.; Bourcier, W. L.; Buscheck, T. A.; Carr, T.; Donovan, J.; Jiao, Z.; Lin, L.; Song, L.; Wagoner, J. L., Opportunities for increasing CO2 storage in deep, saline formations by active reservoir management and

treatment of extracted formation water: Case study at the GreenGen IGCC facility, Tianjin, PR China. *International Journal of Greenhouse Gas Control* **2016,** *54*, 538-556.

8. Harto, C. B.; Veil, J. A. *Management of Water Extracted from Carbon Sequestration Projects*; Argonne National Laboratory: Chicago, Illinois, 2011.

9. Middleton, R. S.; Keating, G. N.; Stauffer, P. H.; Jordan, A. B.; Viswanathan, H. S.; Kang, Q. J.; Carey, J. W.; Mulkey, M. L.; Sullivan, E. J.; Chu, S. P.; Esposito, R.; Meckel, T. A., The cross-scale science of CO2 capture and storage: from pore scale to regional scale. *Energy & Environmental Science* **2012,** *5* (6), 7328-7345.

10. Breunig, H. M.; Birkholzer, J. T.; Borgia, A.; Oldenburg, C. M.; Price, P. N.; McKone, T. E., Regional evaluation of brine management for geologic carbon sequestration. *International Journal of Greenhouse Gas Control* **2013,** *14*, 39-48.

11. Sullivan, E. J.; Chu, S.; Stauffer, P. H.; Middleton, R. S.; Pawar, R. J., A method and cost model for treatment of water extracted during geologic CO2 storage. *International Journal of Greenhouse Gas Control* **2013,** *12*, 372-381.

12. Roach, J. D.; Heath, J. E.; Kobos, P. H.; Klise, G. T., System-level benefits of extracting and treating saline water from geologic formations during national-scale carbon capture and storage. *International Journal of Greenhouse Gas Control* **2014,** *25*, 186-197.

13. Kaplan, R.; Mamrosh, D.; Salih, H. H.; Dastgheib, S. A., Assessment of desalination technologies for treatment of a highly saline brine from a potential CO2 storage site. *Desalination* **2017,** *404*, 87-101.

14. Salih, H. H.; Li, J.; Kaplan, R.; Dastgheib, S. A., Life cycle assessment of treatment and handling options for a highly saline brine extracted from a potential CO2 storage site. *Water Research* **2017,** *122* (Supplement C), 419-430.

15. Klise, G. T.; Roach, J. D.; Kobos, P. H.; Heath, J. E.; Gutierrez, K. A., The cost of meeting increased cooling-water demands for CO2 capture and storage utilizing non-traditional waters from geologic saline formations. *Hydrogeology Journal* **2013,** *21* (3), 587-604.

16. NETL *Carbon Storage Atlas - Fifth Edition*; U.S. Department of Energy: 2015.

17. NETL, National Carbon Sequestration Database and Geographic Information System (NATCARB). v1502 ed.; Energy, U. S. D. o., Ed. 2015.

18. Blondes, M.; Gans, K.; Engle, M.; Kharaka, Y.; Reidy, M.; Saraswathula, V.; Thordsen, J.; Rowan, E.; Morrissey, E., U.S. Geological Survey National Produced Waters Geochemical Database v2.2. 2016.

19. Emissions & Generation Resource Integrated Database (eGRID2012). Agency, U. S. E. P., Ed. 2015.

20. Zhai, H.; Ou, Y.; Rubin, E. S., Opportunities for Decarbonizing Existing U.S. Coal-Fired Power Plants via CO2 Capture, Utilization and Storage. *Environmental Science & Technology* **2015,** *49* (13), 7571-7579.

21. Mauter, M. S.; Alvarez, P. J. J.; Burton, A.; Cafaro, D. C.; Chen, W.; Gregory, K. B.; Jiang, G.; Li, Q.; Pittock, J.; Reible, D.; Schnoor, J. L., Regional Variation in Water-Related Impacts of Shale Gas Development and Implications for Emerging International Plays. *Environmental Science & Technology* **2014,** *48* (15), 8298-8306.

22. Ellsworth, W. L., Injection-Induced Earthquakes. *Science* **2013,** *341* (6142).

23. Mark, A. H.; Zui Chih, L., Marcellus Shale Development and the Susquehanna River: An Exploratory Analysis of Cross-Sector Attitudes on Natural Gas Hydraulic Fracturing. *Organization & Environment* **2014,** *27* (1), 25-42.

24. Jacquet Jeffrey, B.; Stedman Richard, C., Perceived Impacts from Wind Farm and Natural Gas Development in Northern Pennsylvania. *Rural Sociology* **2013,** *78* (4), 450-472.

25. Veil, J. A. *U.S. Produced Water Volumes and Management Practices in 2012*; Ground Water Protection Council: Oklahoma City, Oklahoma, 2015.

26. Fritzmann, C.; Löwenberg, J.; Wintgens, T.; Melin, T., State-of-the-art of reverse osmosis desalination. *Desalination* **2007,** *216* (1), 1-76.

27. Thiel, G. P.; Tow, E. W.; Banchik, L. D.; Chung, H. W.; Lienhard V, J. H., Energy consumption in desalinating produced water from shale oil and gas extraction. *Desalination* **2015,** *366*, 94-112.

28. Samaras, C.; Azevedo, I.; Schivley, G.; Goldstein, A.; Zhai, H.; Matthews, H. S.; Kumar, Y.; Gandhi, S. Power Sector Carbon Index. https://www.emissionsindex.org (accessed August).

29. Rubin, E. S.; Haibo, Z.; Kietzke, K.; Mantripragada, H., Integrated Envrionmental Control Model (IECM), Version 9.5. Carnegie Mellon University: 2017.

30. Knoope, M. M. J.; Ramírez, A.; Faaij, A. P. C., A state-of-the-art review of techno-economic models predicting the costs of CO2 pipeline transport. *International Journal of Greenhouse Gas Control* **2013,** *16*, 241-270.

31. Millar, R. J.; Fuglestvedt, J. S.; Friedlingstein, P.; Rogelj, J.; Grubb, M. J.; Matthews, H. D.; Skeie, R. B.; Forster, P. M.; Frame, D. J.; Allen, M. R., Emission budgets and pathways consistent with limiting warming to 1.5 °C. *Nature Geoscience* **2017,** *10*, 741.

32. Reiner, D. M., Learning through a portfolio of carbon capture and storage demonstration projects. *Nature Energy* **2016,** *1*, 15011.

33. Heck, V.; Gerten, D.; Lucht, W.; Popp, A., Biomass-based negative emissions difficult to reconcile with planetary boundaries. *Nature Climate Change* **2018,** *8* (2), 151-155.

34. Allam, R. J.; Topham, A. Integrated air separation plant - integrated gasification combined cycle power generator. 5081845, January 21, 1992.

35. Leeson, D.; Mac Dowell, N.; Shah, N.; Petit, C.; Fennell, P. S., A Techno-economic analysis and systematic review of carbon capture and storage (CCS) applied to the iron and steel, cement, oil refining and pulp and paper industries, as well as other high purity sources. *International Journal of Greenhouse Gas Control* **2017,** *61*, 71-84.

36. Sanz-Pérez, E. S.; Murdock, C. R.; Didas, S. A.; Jones, C. W., Direct Capture of CO2 from Ambient Air. *Chemical Reviews* **2016,** *116* (19), 11840-11876.

37. Keith, D. W.; Holmes, G.; St. Angelo, D.; Heidel, K., A Process for Capturing CO₂ from the Atmosphere. *Joule* **2018,** *2* (8), 1573-1594.

38. Goto, K.; Yogo, K.; Higashii, T., A review of efficiency penalty in a coal-fired power plant with post-combustion CO2 capture. *Applied Energy* **2013,** *111* (Supplement C), 710-720.

39. Middleton, R. S.; Clarens, A. F.; Liu, X.; Bielicki, J. M.; Levine, J. S., CO2 Deserts: Implications of Existing CO2 Supply Limitations for Carbon Management. *Environmental Science & Technology* **2014,** *48* (19), 11713-11720.

40. Trautz, R. *Phase II Field Demonstration at Plant Smith Generating Station: Assessment of Opportunities for Optimal Reservoir Pressure Control, Plume Management and Produced Water Strategies.*; DE-FE0026140; Electric Power Research Institute: Palo Alto, CA, 2016.

41. Murray, K. *Class II Underground Injection Control Well Data for 2010-2013 by Geologic Zones of Completion, Oklahoma*; OF1-2014; Oklahoma Geological Survey: Norman, OK, 2014.

42. Kobos, P. H.; Krumhansl, J. L.; Dewers, T. A.; Cappelle, M. A.; Heath, J. E.; Dwyer, B. P.; Borns, D. J.; McNemar, A. *Study of the Use of Deep Saline Formations for Combined*

Thermoelectric Power Plant Water Needs and Carbon Sequestration at a Regional-Scale: Phase II Report; SAND2010-8073P; National Energy Technology Laboratory: 2010.

43. Gingerich, D. B.; Mauter, M. S., Air Emissions Damages from Municipal Drinking Water Treatment Under Current and Proposed Regulatory Standards. *Environmental Science & Technology* **2017,** *51* (18), 10299-10306.

44. Elimelech, M.; Phillip, W. A., The Future of Seawater Desalination: Energy, Technology, and the Environment. *Science* **2011,** *333* (6043), 712.

45. Mickley, M. *Survey of High-Recovery and Zero Liquid Discharge Technologies for Water Utilities*; WateReuse Foundation: Alexandria, Virginia, 2008.

46. Stauffer, P. H.; Viswanathan, H. S.; Pawar, R. J.; Guthrie, G. D., A System Model for Geologic Sequestration of Carbon Dioxide. *Environmental Science & Technology* **2009,** *43* (3), 565-570.

47. McPherson, B. *Southwest Regional Partnership on Carbon Sequestration Final Report*; Socorro, New Mexico, 2006.

48. Battelle *The Midwest Regional Carbon Sequestration Partnership Phase I Final Report*; DE-FC26-03NT41981; Columbus, Ohio, 2005.

49. Finley, R. *An Assessment of Geological Carbon Sequestration Options in the Illinois Basin: Final Report*; DE-FC26-03NT41994; Illinois State Geological Survey: 2005.

8.0 SUMMARY AND CONCLUSIONS

8.1 Overview

This thesis sought to provide insight into high salinity brine dewatering and management by addressing two questions: 1) What dewatering technologies are most cost effective across a broad range of brine salinities and water recoveries? and 2) What impact would dewatering strategies have on the overall cost and environmental impact of high salinity brine management? While developing a consensus on these questions will take a large collective research effort and will be context dependent, this thesis demonstrated that optimization modeling is a powerful tool to assess the technoeconomic feasibility of emerging dewatering technologies and brine management strategies.

This thesis was organized across three research objectives that span different scales of brine dewatering and management. The objectives were as follows:

1. At the module-scale, develop models for membrane-based technologies that accurately predict the separation performance for high salinity brines
2. At the process-scale, develop cost optimization models that determine the technoeconomic feasibility of emerging membrane-based brine dewatering processes
3. At the network-scale, develop network-scale supply chain optimization models and spatially resolved analyses that identify low cost and environmental impact brine management strategies across the U.S.

Addressing high salinity brine dewatering and management at these three scales helped overcome the barriers associated with assessing the technoeconomic feasibility described in chapter 1, including: developing models that accurately predict performance, specifying the

design and operation without experience or heuristics, and handling the high uncertainty in parameters.

At the module-scale, this thesis developed highly detailed models for hydraulic (RO, OARO), osmotic (FO), and vapor pressure (MD) driven membrane-based technologies. These models were more detailed than previous models in the literature because they did not make several common process and solution property simplifications. Despite these additional details, the models were often solved in less than two seconds with highly efficient solvers (i.e. CONOPT). While this work at the module-scale was primarily emphasized in chapter 2, these models were the basis for modeling the separation performance for chapters 3 through 5. Some key findings of the module-scale work include quantifying the expected error of common simplifications for hydraulic and osmotic membrane processes in chapter 2 and demonstrating the strong effects salinity has on the performance of membrane distillation in chapter 5.

At the process-scale, this thesis used cost optimization models to determine the technoeconomic feasibility of OARO (chapter 4) and gap MD (chapter 5). Specifically, the models were used to determine the levelized cost of water across the full dewatering space (broad range of feed salinities and water recoveries), extract generalizable guidelines for low cost design and operation, and identify the most cost sensitive parameters to prioritize future research. Generally, this work found that OARO and gap MD may be cost competitive with mechanical vapor compression, the predominant high salinity brine dewatering technology.

At the network-scale, this thesis used a supply chain optimization model and spatially resolved data analysis to investigate brine management strategies for shale gas wastewater in chapter 6 and geologic carbon storage (GCS) in chapter 7. Generally, the results of this work emphasized that brine dewatering is a critical component of brine management. In chapter 6, the

financial cost optimal and human health and environmental cost optimal strategies preferred brine dewatering over transporting the wastewater far distances for disposal. In chapter 7, the chosen brine dewatering strategy (low, medium, and high reuse) dominated the energy consumption of brine management for GCS. Further, it was found that the energy consumption of brine management is likely an order of magnitude greater than the other carbon storage activities, suggesting that it should be the key consideration when designing and operating carbon storage networks.

8.2 Recommendations for future work

There are three recommendations for future work on understanding high salinity brine dewatering and management.

The first recommendation for future work is to simulate the performance of dewatering technologies for brines with dissolved solids other than NaCl. Throughout this thesis all simulated brines were assumed to be only composed of NaCl. This simplification was made because the solution properties of NaCl brines are well established. However, most high salinity brine applications have waters with many other components (e.g. K^+, Mg^{2+}, Ca^{2+}, Br^-, SO_4^{2-}). Many of these additional components can greatly affect the solution properties of the brine, most notably the water vapor pressure, and increase scale formation, which is a detrimental phenomenon for many dewatering technologies. Understanding the effects of these multicomponent brines on the performance of the dewatering technologies will be critical because they will need to treat these waters when deployed in the field.

The second recommendation is to assess the benefit of using multiple dewatering technologies to achieve a desired separation. For example, it may reduce the cost of

concentrating a brine to near saturation if a dewatering train uses OARO or MD to concentrate to 200 g/L TDS and then uses MVC to concentrate to near saturation. An initial assessment of combining multiple dewatering technologies could be achieved by leveraging the simulated LCOW as a function of salinity and water recovery for each technology (e.g. Figure 4.5 for OARO and Figure 5.3 for gap MD). It would be beneficial to complete similar analyses for the other major high salinity dewatering technologies including: MSF, MED, MVC, and direct contact/vacuum/sweeping gas MD. Additionally, since some of these technologies could benefit from integration with other technologies (i.e. recycle loops, heat exchanger network), it would be worthwhile to expand the process-scale models to consider multiple technologies directly.

The third recommendation for future work is to incorporate more detailed modeling on dewatering processes with network-level brine management optimization models. Generally, these network-level models have only considered coarse modeling of dewatering processes, such as having a fixed water recovery and unit cost. These types of formulations provide no or little insight into the optimal extent of brine dewatering, which is a critical consideration for brine management. One way to address this shortcoming is to incorporate dewatering models that relate brine salinity, water recovery, and cost. While the detailed process models presented in chapter 4 and 5 will likely be too computationally demanding for a network-level optimization problem, tractable metamodels could be created from regressions on the simulated results of the detailed process models.

APPENDIX A: SUPPORTING INFORMATION FOR CHAPTER 2 - COMPUTATIONAL FRAMEWORK FOR MODELING MEMBRANE PROCESSES WITHOUT PROCESS AND SOLUTION PROPERTY SIMPLIFICATIONS

Supporting Information Summary:
The supporting information contains details for 1) solution properties; 2) concentration polarization relationships; 3) hydraulic diameter calculation, 4) model scaling, bounding, and initializing, 5) additional FO and PRO cases.

This supporting information is 17 pages long and contains 6 figures (Fig. S1-S6), 1 Table (Table S1), and 13 equations (Eq. S1-S18).

S.1) Solution properties

The solution properties used in our model include: osmotic pressure, density, viscosity, and diffusivity of the solute. All four properties are a function of solution concentration and temperature. We model the properties solely as a function of concentration because we assume the temperature is constant at 25° C. In this section, we present the solution property relationships that were developed from regressions of tabulated solution properties.

We calculate the osmotic pressure as a function of concentration with Eq. S1 (Eq. 3 in the main manuscript). Typically, the solution is assumed to be ideal by setting the osmotic coefficient (ϕ) to one. With the ideal solution assumption, the osmotic pressure calculation becomes linear with concentration. When we account for a non-ideal solution, the osmotic coefficient is a function of concentration and the osmotic pressure calculation becomes nonlinear. We determine the osmotic coefficient function by fitting a quadratic function to tabulated osmotic coefficient data from Scatchard et al. 1938 and Pitzer et al. 1984 as shown in Eq. S2 (R-squared greater than 0.99) and Fig S1A.[1-2] Using this osmotic coefficient relationship (Eq. S2), we plot the osmotic pressure as a function of concentration in Fig S1B.

$$\pi = f_{\pi}(C) = i\, f_{\phi}(C)\, C\, \frac{1}{MW}\, R\, T \tag{S1}$$

$$\phi = f_{\phi}(C) = 3.14E\text{-}6\ \mathrm{C}^2\ + 2.13E\text{-}4\ \mathrm{C}\ + 0.917 \tag{S2}$$

Where π is the osmotic pressure [bar], i is the number of dissociating ions [-], f_{ϕ} is the osmotic coefficient [-] as a function of solute concentration, C is the solute concentration [g/L], MW is the molecular weight [g/mol], R is the gas constant [8.314E-2 L-bar/mol-K], and T is the temperature [K].

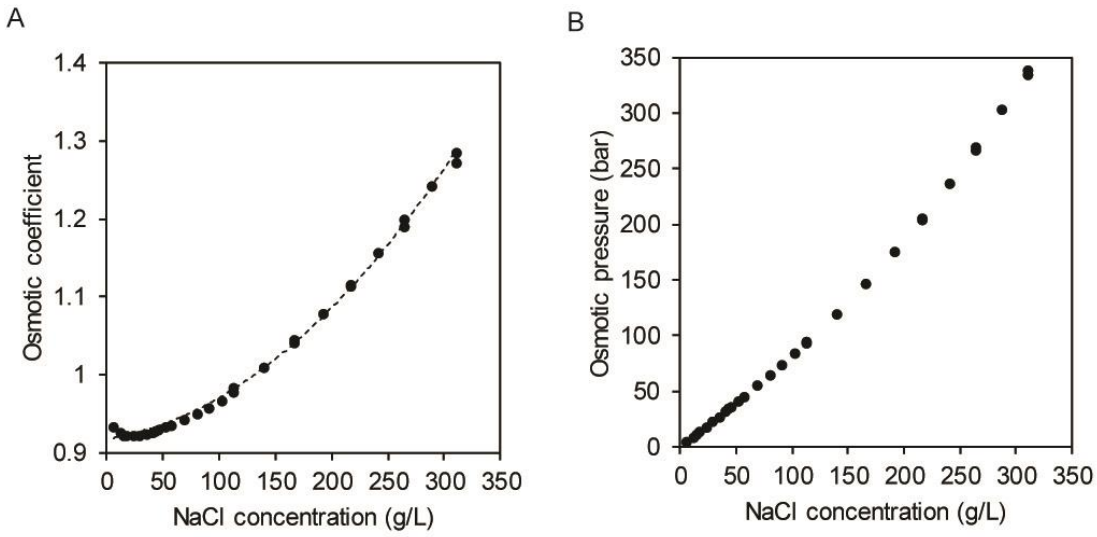

Figure S1. *NaCl solution osmotic coefficient (A) and osmotic pressure (B). The dashed line is the quadratic fit for the osmotic coefficient (Eq. S2).*

In Figure S2, we present solution density, viscosity, and diffusivity data from Pitzer et al. 1984, International critical tables, and Lobo 1983, respectively.[2-4] The linear fit of the density and viscosity is shown in Eq. S3 and S4 (R-squared greater than 0.999). The fourth order fit of the diffusivity is shown in Eq. S5 (R-squared of 0.970). These relationships are based on mass fraction instead of concentration. The conversion between mass fraction and concentration is presented in the main manuscript with Eq. 7.

$$\rho = 756\,X + 995 \tag{S3}$$

$$\mu = 2.15E\text{-}3\,X + 9.80E\text{-}4 \tag{S4}$$

$$D = 153\,X^4 - 122\,X^3 + 30.1\,X^2 - 2.00\,X + 1.51 \tag{S5}$$

Where ρ is the density [g/L or kg/m^3], X is the solution NaCl mass fraction [%], μ is the dynamic viscosity [Pa-s], and D is the diffusivity [1E-9 m^2/s].

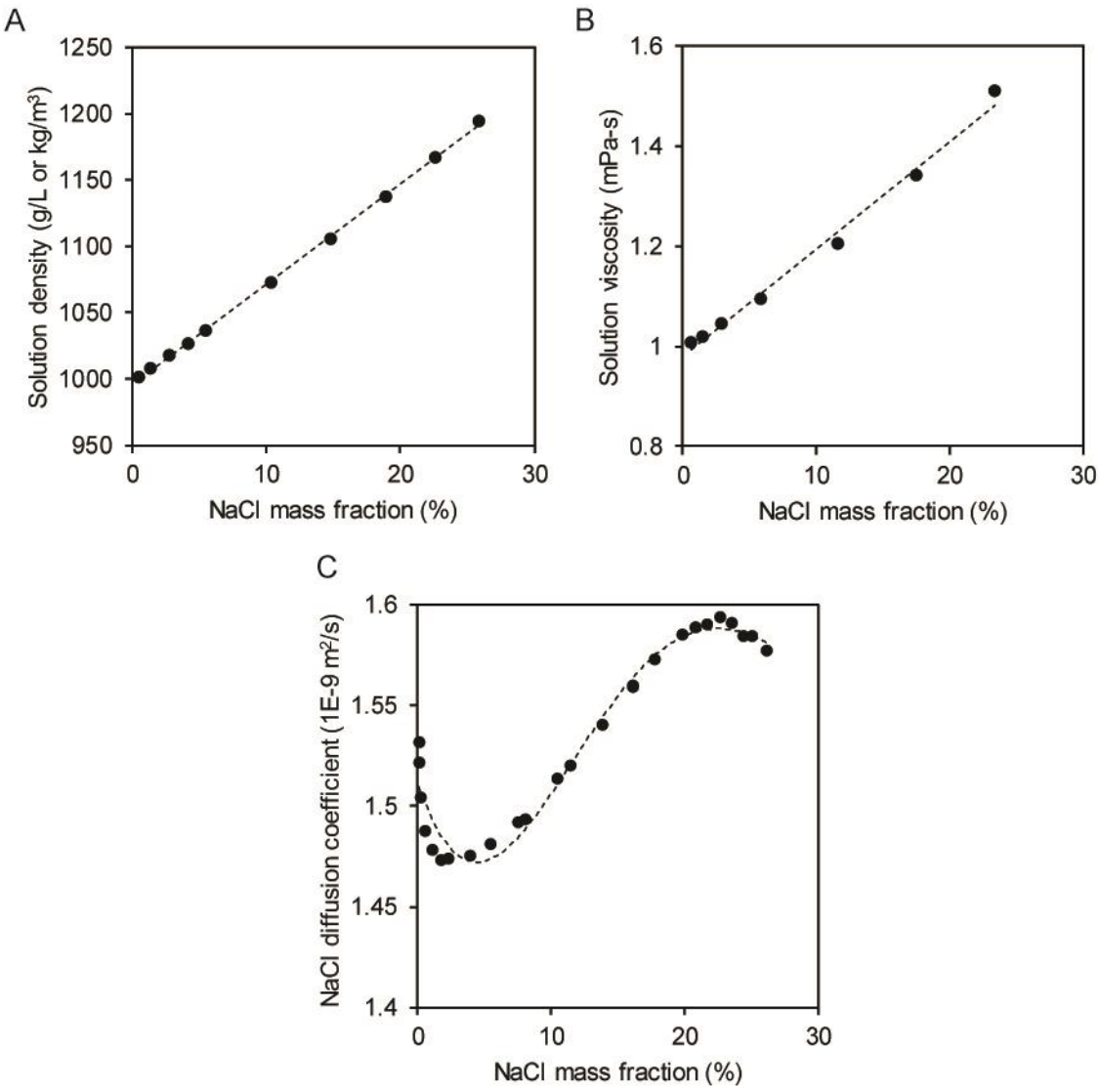

Figure S2. *NaCl solution density (A), viscosity (B), and diffusivity (C). The dashed line is the fit for each property (Eq S3-S5).*

S.2) Concentration polarization relationships

Concentration polarization relationships can be derived by accounting for diffusive and convective transport of the solute and using film theory and the steady state assumption. In Figure S3, we present a schematic of the membrane stage cross section that notes the direction of water and salt flux and the locations of boundary layers and porous support.

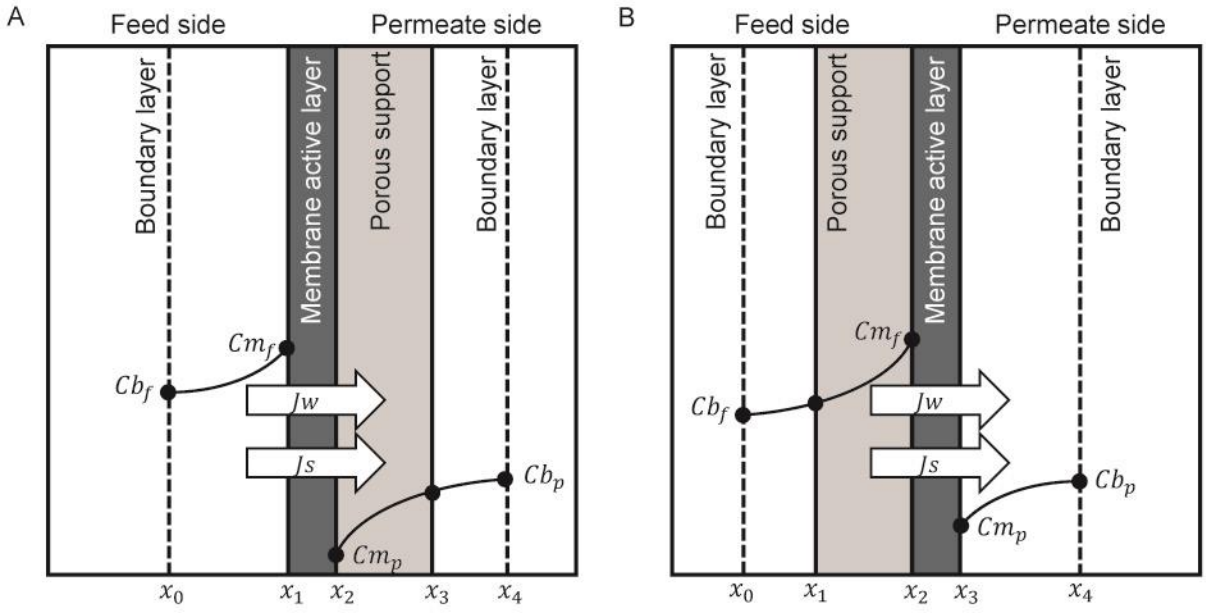

Figure S3. Schematic of the membrane stage cross-section with the porous support on the permeate (A) and feed (B) side. In our work, we assume the porous support is on the permeate side for RO, OARO, and FO and vice versa for PRO. The defined direction of the water (Jw) and salt (Js) flux are noted with arrows. Since the permeate side concentration is greater than the feed side for FO and PRO, the salt flux is negative (as described in the manuscript). The x index denotes key regions in the membrane cross section.

The following derivation for the membrane processes closely follows the work by Yip et al. 2011, Bui et al. 2015, and Bartholomew et al. 2018.[5-7] The governing equation that balances salt flux through the membrane and convective and diffusive transport is Eq. S6.

$$Js = -D^* \frac{dC}{dx} + Jw\ C \tag{S6}$$

Where Js and Jw are the salt flux [kg/m^2 s] and water flux [m^3/m^2 s], D^* is the diffusion coefficient of the solute [m^2/s], C is the solute concentration [kg/m^3], and x is the spatial dimension [m]. Note that the diffusion coefficient, D^*, varies based on the region. The effective diffusion coefficient in the porous support, D^s, is related to the diffusion coefficient of the solute by $D^s = \frac{D\varepsilon}{\tau}$. Where ε is the porosity and τ is the tortuosity of the porous support.

To determine the feed side relationship, we separate the variables and integrate Eq. S6 from the bulk to the membrane interface. For RO, OARO, and FO there is no feed side porous support and we obtain Eq. S7a. For PRO with a feed side porous support, we obtain Eq. S7b. The integration of Eq. S7a and S7b is shown in Eq. S8a and S8b. After solving for the feed side interfacial membrane concentration (Cm_f) and substituting the feed side boundary layer thickness, δ_f, for $x_1 - x_0$, and the porous support thickness, t, for $x_2 - x_1$, we obtain equation S9a and S9b. We further substitute the feed side mass transfer coefficient, k_f, for D/δ_f and the structural parameter, S, for $t\ \tau/\epsilon$ and obtain equation S10a and S10b, which are Eq. 8a and 8b in the main manuscript.

$$\int_{Cb_f}^{Cm_f} \frac{dC}{Jw\ C - Js} = \int_{x_0}^{x_1} \frac{1}{D}\ dx \tag{S7a}$$

$$\frac{1}{\mathrm{Jw}} \ln\left(\frac{Jw\ Cm_f - Js}{Jw\ Cb_f - Js}\right) = \frac{(x_1 - x_0)}{D} \tag{S8a}$$

$$Cm_f = Cb_f \exp\left(Jw\frac{\delta_f}{D}\right) - \frac{Js}{Jw}\left(\exp\left(Jw\frac{\delta_f}{D}\right) - 1\right) \quad \text{(S9a)}$$

$$Cm_f = Cb_f \exp\left(\frac{Jw}{k_f}\right) - \frac{Js}{Jw}\left(\exp\left(\frac{Jw}{k_f}\right) - 1\right) \quad \text{(S10a)}$$

$$\int_{Cb_f}^{Cm_f} \frac{dC}{Jw\,C - Js} = \int_{x_0}^{x_1} \frac{1}{D}\,dx + \int_{x_1}^{x_2} \frac{1}{D^s}\,dx \quad \text{(S7b)}$$

$$\frac{1}{\mathrm{Jw}} \ln\left(\frac{Jw\,Cm_f - Js}{Jw\,Cb_f - Js}\right) = \frac{(x_1 - x_0)}{D} + \frac{(x_2 - x_1)}{D^s} \quad \text{(S8b)}$$

$$Cm_f = Cb_f \exp\left(Jw\left[\frac{\delta_f}{D} + \frac{t}{D^s}\right]\right) - \frac{Js}{Jw}\left(\exp\left(Jw\left[\frac{\delta_f}{D} + \frac{t}{D^s}\right]\right) - 1\right) \quad \text{(S9b)}$$

$$Cm_f = Cb_f \exp\left(Jw\left[\frac{1}{k_f} + \frac{S}{D}\right]\right) - \frac{Js}{Jw}\left(\exp\left(Jw\left[\frac{1}{k_f} + \frac{S}{D}\right]\right) - 1\right) \quad \text{(S10b)}$$

We determine the permeate side relationship with the same method as the feed side. We separate the variables and integrate Eq. S6 from the membrane interface to the bulk (Eq. S11a and S11b). Note that Eq. S6 is integrated starting from the membrane interface, as opposed to the bulk, because the direction of dimension x is the same as the water flux. After solving for the concentration at the membrane interface and making similar substitutions as the feed side, we obtain Eq. S14a and S14b, which are the same as Eq. 9a and 9b in the main manuscript.

$$\int_{Cm_p}^{Cb_p} \frac{dC}{Jw\,C - Js} = \int_{x_2}^{x_3} \frac{1}{D^s}\,dx + \int_{x_3}^{x_4} \frac{1}{D}\,dx \quad \text{(S11a)}$$

$$\frac{1}{\mathrm{Jw}} \ln\left(\frac{Jw\,Cb_p - Js}{Jw\,Cm_p - Js}\right) = \frac{(x_3 - x_2)}{D^s} + \frac{(x_4 - x_3)}{D} \quad \text{(S12a)}$$

$$Cm_p = Cb_p \exp\left(\text{-}Jw\left(\frac{t}{D^s} + \frac{\delta_s}{D}\right)\right) - \frac{Js}{Jw}\left(\exp\left(\text{-}Jw\left(\frac{t}{D^s} + \frac{\delta_s}{D}\right)\right) - 1\right) \quad \text{(S13a)}$$

$$Cm_p = Cb_p \exp\left(\text{-}Jw\left(\frac{S}{D} + \frac{1}{k_p}\right)\right) + \frac{Js}{Jw}\left(1 - \exp\left(\text{-}Jw\left(\frac{S}{D} + \frac{1}{k_p}\right)\right)\right) \quad \text{(S14a)}$$

$$\int_{Cm_p}^{Cb_p} \frac{dC}{Jw\ C - Js} = \int_{x_3}^{x_4} \frac{1}{D^s}\ dx \tag{S11b}$$

$$\frac{1}{\mathrm{Jw}} \ln\left(\frac{Jw\ Cb_p - Js}{Jw\ Cm_p - Js}\right) = \frac{(x_4 - x_3)}{D} \tag{S12b}$$

$$Cm_p = Cb_p \exp\left(\text{-}Jw \frac{\delta_s}{D}\right) - \frac{Js}{Jw}\left(\exp\left(\text{-}Jw \frac{\delta_s}{D}\right) - 1\right) \tag{S13b}$$

$$Cm_p = Cb_p \exp\left(\frac{\text{-}Jw}{k_p}\right) + \frac{Js}{Jw}\left(1 - \exp\left(\frac{\text{-}Jw}{k_p}\right)\right) \tag{S14b}$$

S.3) Hydraulic diameter calculation

The hydraulic diameter is an important parameter used in the Reynolds number, mass transfer coefficient, and pressure drop relationships. We determine the hydraulic diameter from the specified channel dimensions and mesh configuration.

We use the same mesh configuration assumed in Guillen and Hoek 2009, which is the study that developed the Sherwood number and friction factor correlations used in our model.[8] Guillen and Hoek represented the mesh with isolated filaments that are separated by a specified distance and are perpendicular to the bulk flow, as shown in Figure S4. For this configuration, the hydraulic diameter is determined with Eq. S15.

$$d_h = \frac{4\,(flow\ area)}{(wetted\ surface)} = \frac{4\left(l_f\,h_c - A_f\right)}{2\,l_f + P_f} \tag{S15}$$

Where d_h is the hydraulic diameter [m], l_f is the center to center distance between filaments [m], h_c is the channel height [m], A_f is the cross-sectional area of the filament [m^2], and P_f is the perimeter of the filament.

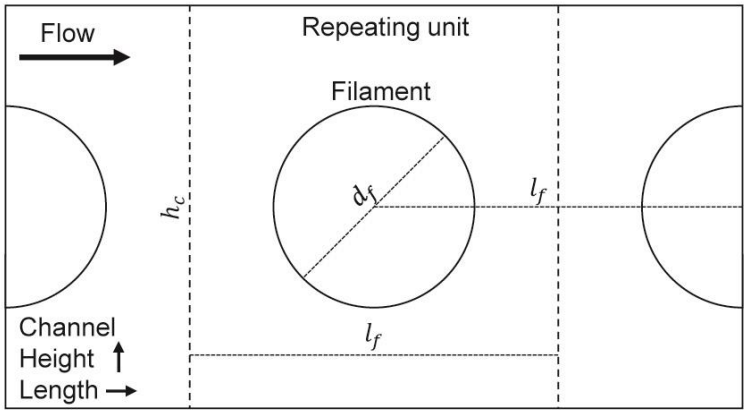

Figure S4. *Channel and mesh configuration. Key dimensions such as height of channel (h_c), diameter of filament (d_f), and center to center distance between filaments (l_f) are noted.*

To determine the hydraulic diameter, we need to make some assumptions regarding the mesh in the channel. We assume the filament shape is circular and channel height to diameter of filament ratio is 0.5 because those were the base case assumptions considered in Guillen and Hoek. We also fix the distance between filaments so that the void space of the mesh is 97%. We assume the void space is 97% because it is the average void space for the two center to center distance between filaments (l_f) considered in Guillen and Hoek 2009. With these assumptions, the hydraulic diameter is determined with Eq. S16-S18 for a channel height of 1 mm (RO case) and 2 mm (OARO, FO, PRO cases) as 1.73 mm and 3.46 mm, respectively.

$$d_f = 0.5\, h_c \tag{S16}$$

$$l_f = \frac{\pi\, {d_f}^2}{4\, h_c(1-\varepsilon)} \tag{S17}$$

$$d_h = \frac{4\left(l_f\, h_c - \frac{\pi}{4}\, {d_f}^2\right)}{2\, l_f + \pi\, d_f} \tag{S18}$$

Where d_f is the diameter of the filament [m] and ε is the void space of the mesh.

S.4) Model scaling, bounding, and initializing

Scaling, bounding, and initializing variables allows the solver to reliably and efficiently find the single feasible solution. This section describes our assumptions regarding the variable scale, bounds, and initial values.

We rescale some variables as follows:

- Water (Jw) and salt (Js) flux in units of LMH and g/m^2-h, respectively
- Pressure loss per unit length (PL) in units of Pa/m
- Mass transfer coefficients (k) in units of mm/h

We assume the following bounds:

- Average water flux, Jw_{avg}, lower and upper bound are 0.1 and 20 LMH, respectively. Since RO has significantly higher water flux, we adjust the bounds for that process to 0.5 and 50 LMH, respectively. Local water flux, Jw, lower and upper bound are determined from the average water flux by dividing by 5 and multiplying by 1.5
- Average and local salt flux, Js_{avg} and Js, lower and upper bound are 0 and 50 g/m^2-h
- Reynolds number, Re, lower and upper bound are 100 and 2000
- Schmidt number, Sc, lower and upper bound are 600 and 1000
- Pressure loss per unit length, PL, lower and upper bound are 0 and 30 kPa/m
- Salt recovery, SR, lower and upper bound are 0 and 0.2

Other bounds can be estimated with mass balance or other relationships from the case study specifications (e.g. inlet concentration, flowrate, and water recovery for the state variables bounds) or previous bounds (e.g. Reynolds, Schmidt, and diffusion coefficient bounds for the mass transfer coefficient bounds).

For the initial values, we found that we only need to supply an initial guess for the average water flux for CONOPT to converge to the feasible solution. Our initial guess for the average water flux was 30 LMH for RO and 2 LMH for OARO, FO, and PRO. We also applied this guess to the local water flux.

S.5) Additional FO and PRO Cases

The FO and PRO case studies presented in the main manuscript have a nearly flat water flux profile, which results in a small difference between the two simplified inlet-outlet models. Here we adjust two specifications for each process to create steeper water flux profiles. For both processes, we adjust the permeate side flowrate fraction. We then also adjust the permeate side inlet concentration for FO and the permeate side inlet hydraulic pressure for PRO so that the average water flux is within 5% of the case presented in the main manuscript. The adjusted specifications for these cases are provided in Table S1.

Table S1. *Parameter specifications for two additional FO cases.*

	FO-2	FO-3	PRO-2	PRO-3
Inlet specifications				
Permeate side mass flowrate fraction [-]	0.25 ± 5%	0.5 ± 5%	0.4 ± 5%	0.6 ± 5%
Permeate side inlet concentration [g/L]	205 ± 5%	145 ± 5%	35 ± 5%	35 ± 5%
Permeate side inlet pressure [bar]	NS	NS	11 ± 5%	15 ± 5%

The water flux profile for the additional FO and PRO cases are presented in Fig. S5. While the local water flux varies across the membrane stage by more than 30% for the cases, the shape of the water flux profiles are substantially different. For case FO-2, the local water flux increases from the feed inlet to the feed outlet and is nonlinear. Conversely, for case FO-3, the local water flux decreases from the feed inlet to the feed outlet and is nearly linear. For case PRO-2, the local water flux increases from the feed inlet to the feed outlet and is nonlinear. For case PRO-3, the local water flux decreases from the feed inlet to the feed outlet and is more linear. The profiles are different because the case specifications affect where the lowest driving

force occurs. For example, in FO, a low inlet draw flowrate with a high concentration (case FO-2), the lowest driving force occurs at the feed inlet, where for a high inlet draw flowrate with a low concentration (case FO-3), the lowest driving force occurs at the feed outlet.

The average water flux for the additional FO and PRO cases are presented in Fig. S6. The mean formulations with the lowest average water flux error differ for each case for both processes. The arithmetic mean formulation has the lowest error for the cases with the more linear water flux profiles (FO-3 and PRO-3), where the log and geometric mean formulations have the lowest error for cases with the more non-linear water flux profiles (FO-2 and PRO-2). We observe less than a 5% absolute difference in the average water flux error between the different mean formulations for three of the cases (FO-2, FO-3, PRO-3) and a slightly larger spread up to 10% for case PRO-2. We also find that all three mean formulations overestimate the average water flux for case FO-2 by roughly 5%, which suggests other means that more heavily weight the lower water flux (e.g. harmonic mean) would have a smaller error for this specific case.

The most accurate mean for FO and PRO inlet-outlet modeling can be selected if the shape of the water flux profile is predicted. However, the main benefit of inlet-outlet modeling is the reduced computational demand from not determining the profile of variables along the membrane stage. Therefore, practical application of inlet-outlet modeling for FO and PRO processes will have uncertain accuracy implications.

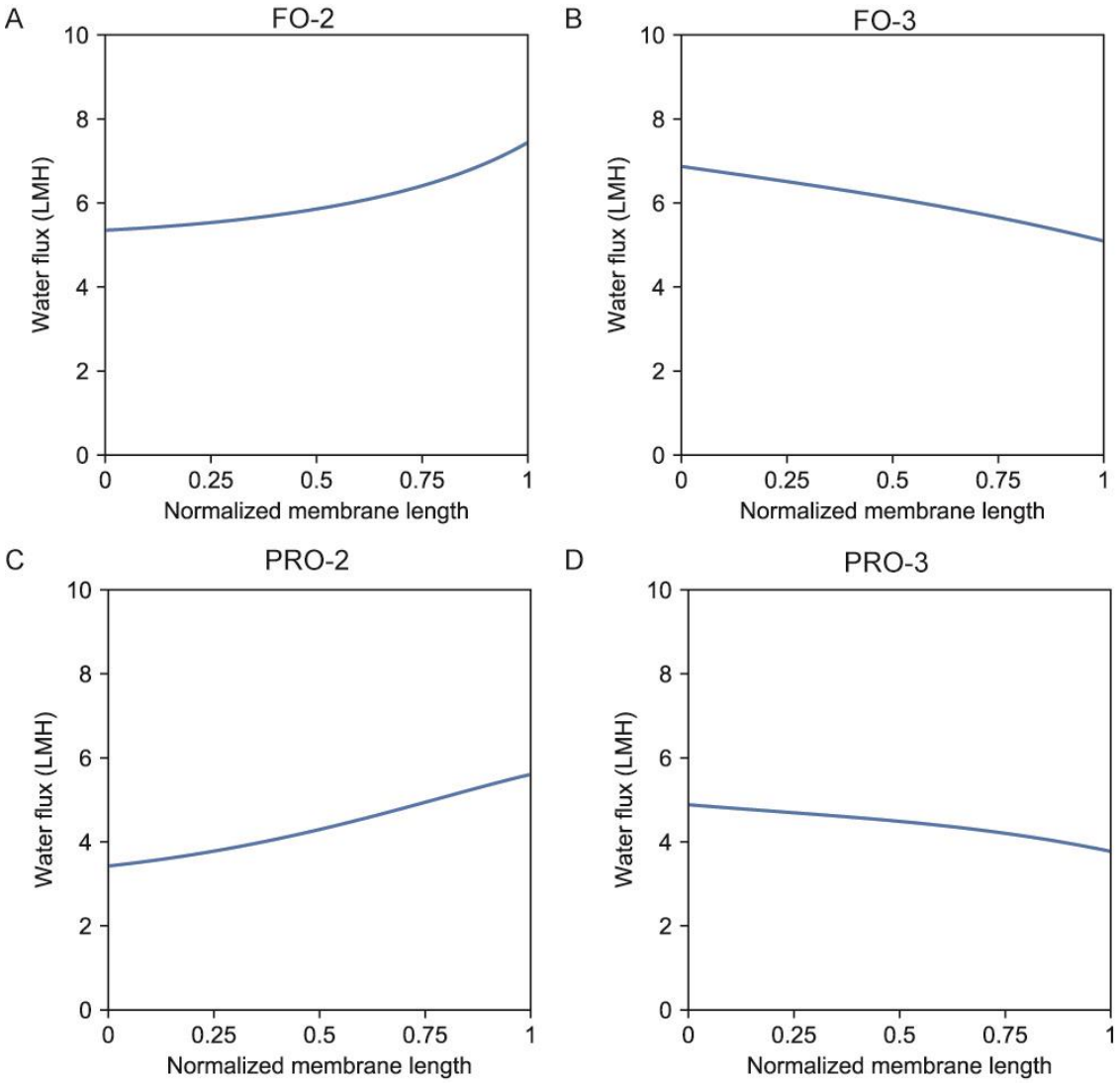

Figure S5. *Water flux profiles for A) FO-2, B) FO-3, C) PRO-2, D) PRO-3 cases. Each profile is the solution of the 100 node finite difference model. The specifications for each case are noted in Table 1 in the main manuscript and Table S1.*

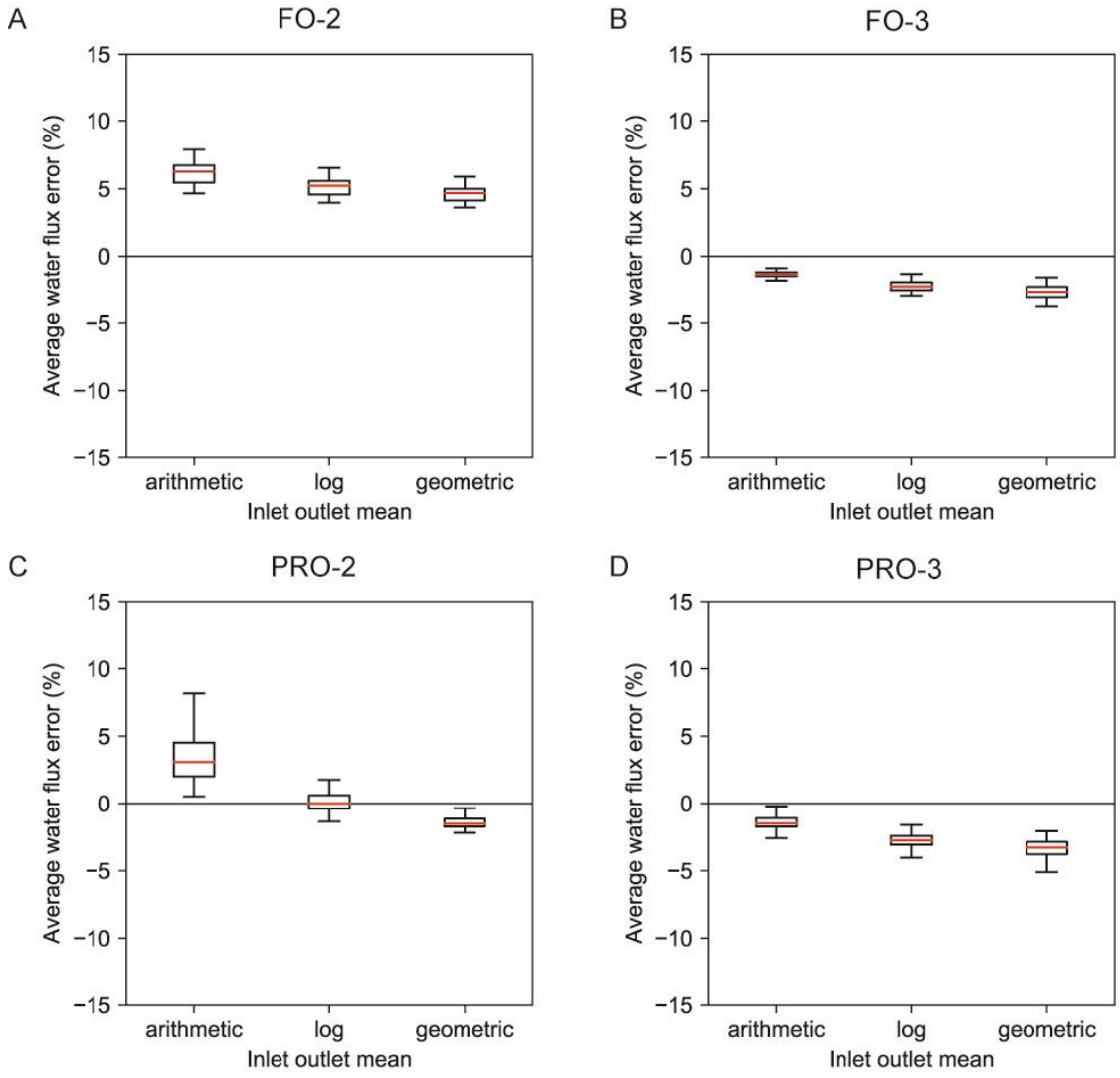

Figure S6. *Accuracy of the inlet-outlet model formulations relative to the 100 node model for A) FO-2, B) FO-3, C) PRO-2, and D) PRO-3. The distribution of the water flux errors was developed using a Monte Carlo simulation that varied the specified parameters by ±5%, as noted in Table 1 in the main manuscript and Table S1.*

References

1. Scatchard, G.; Hamer, W. J.; Wood, S. E., Isotonic Solutions. I. The Chemical Potential of Water in Aqueous Solutions of Sodium Chloride, Potassium Chloride, Sulfuric Acid, Sucrose, Urea and Glycerol at 25°1. *Journal of the American Chemical Society* **1938,** *60* (12), 3061-3070.

2. Pitzer, K. S.; Peiper, J. C.; Busey, R. H., Thermodynamic Properties of Aqueous Sodium Chloride Solutions. *Journal of Physical and Chemical Reference Data* **1984,** *13* (1), 1-102.

3. Washburn, E. W., International Critical Tables of Numerical Data, Physics, Chemistry and Technology (1st Electronic Edition). Knovel.

4. Lobo, V. M. M., Mutual diffusion coefficients in aqueous electrolyte solutions (Technical Report). In *Pure and Applied Chemistry*, 1993; Vol. 65, p 2613.

5. Yip, N. Y.; Tiraferri, A.; Phillip, W. A.; Schiffman, J. D.; Hoover, L. A.; Kim, Y. C.; Elimelech, M., Thin-Film Composite Pressure Retarded Osmosis Membranes for Sustainable Power Generation from Salinity Gradients. *Environmental Science & Technology* **2011,** *45* (10), 4360-4369.

6. Bui, N.-N.; Arena, J. T.; McCutcheon, J. R., Proper accounting of mass transfer resistances in forward osmosis: Improving the accuracy of model predictions of structural parameter. *Journal of Membrane Science* **2015,** *492*, 289-302.

7. Bartholomew, T. V.; Siefert, N. S.; Mauter, M. S., Cost Optimization of Osmotically Assisted Reverse Osmosis. *Environmental Science & Technology* **2018,** *52* (20), 11813-11821.

8. Guillen, G.; Hoek, E. M. V., Modeling the impacts of feed spacer geometry on reverse osmosis and nanofiltration processes. *Chemical Engineering Journal* **2009,** *149* (1), 221-231.

APPENDIX B: SUPPORTING INFORMATION FOR CHAPTER 3 - OSMOTICALLY ASSISTED REVERSE OSMOSIS MODEL FOR TREATING HIGH SALINITY BRINES

Supporting Information Summary:
The supporting information contains details for 1) osmotic pressure calculations; 2) discrete element single module model; 3) multi-module model; 4) base case concentration profile along the first OARO module; 5) determining salt rejection; 6) pressure drop effects.

This supporting information is 19 pages long and contains 9 figures (Fig. S1-S9), and 14 equations (Eq. S1-S13).

1. Osmotic pressure calculations

The osmotic pressure was calculated by Eq. (1).

$$\pi = i\phi CRT \quad (1)$$

Where π is the osmotic pressure, i is the number of dissociating species (2 for sodium chloride), ϕ is the osmotic coefficient, C is the concentration of the solute, R is the gas constant, and T is the temperature.

In our model, we assumed the only solute within both the feed and sweep was sodium chloride (NaCl). We obtained the concentration dependent osmotic coefficient for NaCl from Scatchard et al.[1] Since the dissociation of NaCl results in two ions the NaCl molar concentration was multiplied by two to obtain the solute concentration. For all simulations, we assumed that the solutions were at 298 K. Figure S1 presents the osmotic pressure spanning the range of NaCl concentrations investigated in this work.

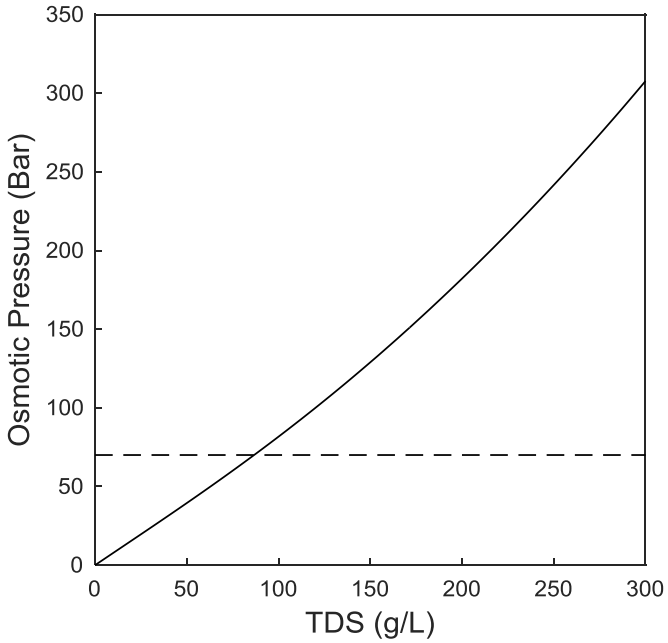

Figure S1*. The osmotic pressure of a sodium chloride solution at 298K as calculated by the Morse equation and the osmotic coefficient from Scatchard et al.*[1] *The dotted line is the assumed membrane burst pressure of 70 bar.*

2. Discrete element single module model

2.1 Discrete model mass balance and water transport

We modeled the flat plate counter-current membrane module as a discrete set of 100 nodes. A visual representation of the nodes is presented in Figure S2. For each node, the inputs are the solution flowrate (Q) and NaCl concentration (C) entering the node (either from a previous node or an initial condition) and an estimated water flux (J_W) and salt flux (J_S). The model then uses mass balance equations (2)-(5), to determine the flowrate and concentration of the solution leaving the node. Since the feed (f) and sweep (s) flows are counter-current, the index of the inlets and outlet of the nodes are different and is reflected in Figure S2 and in Eq. (2), Eq. (3), Eq. (4), and Eq. (5).

Eq. (2) and Eq. (3) calculate the output flowrate and concentration of feed nodes.

$$Q_{f,n} = \frac{Q_{f,n-1}\rho_{f,n-1} - (J_{W,n} + J_{S,n})A_m}{\rho_{f,n}} \quad (2)$$

$$C_{f,n} = \frac{Q_{f,n-1}C_{f,n-1} - J_{S,n}A_m}{Q_{f,n}} \quad (3)$$

Where $Q_{f,n}$ is the feed flowrate $\left(\frac{m^3}{s}\right)$ out of node n, $Q_{f,n-1}$ is the feed flowrate $\left(\frac{m^3}{s}\right)$ into node n, ρ_f is the feed density $\left(\frac{kg}{m^3}\right)$ of the respective nodes, $J_{W,n}$ and $J_{S,n}$ are the water and salt flux $\left(\frac{kg}{m^2 s}\right)$, respectively, in node n, A_m is the membrane area (m^2) of the node, and $C_{f,n}$ is the feed NaCl concentration $\left(\frac{kg}{m^3}\right)$ out of node n.

Eq. (4) and Eq. (5) calculate the output flowrate and concentration of sweep nodes.

$$Q_{s,n} = \frac{Q_{s,n+1}\rho_{s,n+1} + (J_{W,n} + J_{S,n})A_m}{\rho_{s,n}} \quad (4)$$

$$C_{s,n} = \frac{Q_{s,n+1}C_{s,n+1} + J_{S,n}A_m}{Q_{s,n}} \quad (5)$$

Where $Q_{s,n}$ is the sweep flowrate out of node n, $Q_{s,n-1}$ is the sweep flowrate into node n, ρ_s is the sweep density $\left(\frac{kg}{m^3}\right)$.

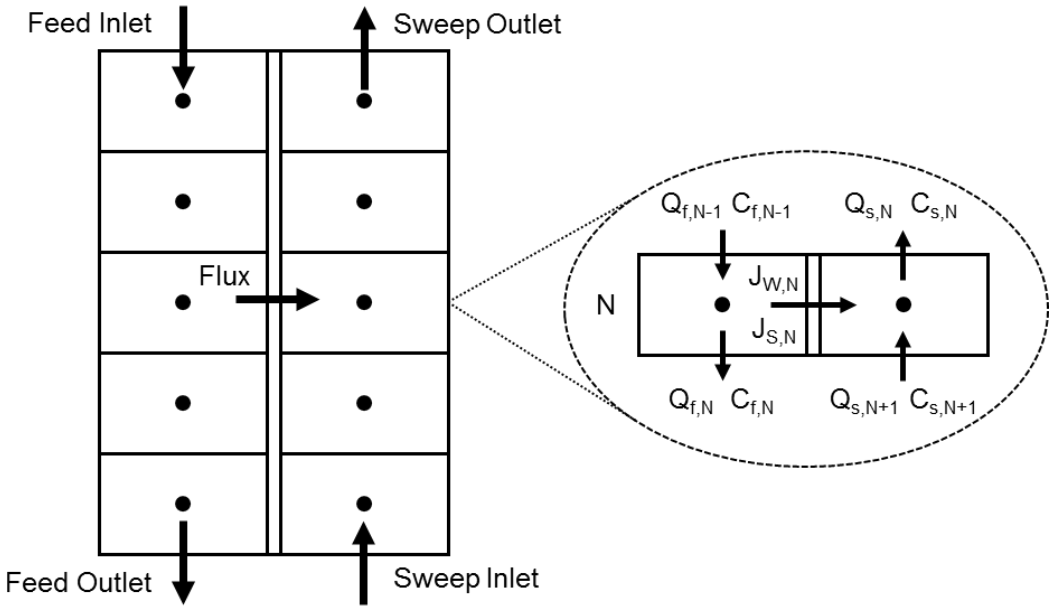

Figure S2. *Discrete node, flow directions, and variables for the flat plate counter-current membrane module. The dots represent the center of each node and the surrounding box is the boundaries. A zoomed in subsection of node N is provided with the relevant flowrates* (Q)*, concentrations* (C)*, water flux* (J_W)*, salt fulx* (J_S) *labeled.*

The water transport is calculated using equation (6).

$$J_w = A\left[\left(P_f - P_s\right) - \left(\pi_{f,m} - \pi_{s,m}\right)\right] \quad (6)$$

Here, J_w is the water flux $\left(\frac{m^3}{m^2\ s}\right)$ from the feed to the sweep, A is the pure water permeability coefficient $\left(\frac{m}{s\ Pa}\right)$, P_f and P_s are the hydraulic pressures (Pa) for the feed and sweep, and $\pi_{f,m}$ and $\pi_{s,m}$ are the osmotic pressure (Pa) at the membrane surface for the feed and sweep. The osmotic pressure of a solution is estimated as a function of solute concentration using equation (1).

The solute concentration at the membrane surface for the feed and sweep can be calculated from equation (7) and (8).{McCutcheon, 2006 #40}

$$C_{f,m} = C_{f,b} \exp\left(\frac{J_w}{k}\right) \quad (7)$$

$$C_{s,m} = C_{s,b} \exp(-J_w K) \quad (8)$$

Where, $C_{f,m}$ and $C_{s,m}$ are the solute concentrations at the membrane surface for the feed and sweep, $C_{f,b}$ and $C_{s,b}$ are the respective bulk solute concentrations of the feed and sweep, k is the feed mass transfer coefficient $\left(\frac{m}{s}\right)$, and K is the solute resistivity for diffusion in the sweep side porous support $\left(\frac{s}{m}\right)$; refer to McCutcheon and Elimelech for further direction in determining these parameters.{McCutcheon, 2006 #40} Note that the equations in McCutcheon and Elimelech refer to osmotic pressure instead of concentration. That relationship is only valid with their assumption that the osmotic pressure is linearly proportional to the concentration, which is not the case for high salinity brines (Figure S1).

If equation (7) and (8) are substituted into equation 6 the water flux can be calculated from the hydraulic pressure and the bulk concentration at each node, as shown in equation (9)

$$J_w = A\left[\left(P_f - P_s\right) - \left(\pi\left(C_{f,b}\exp\left(\frac{J_w}{k}\right)\right) - \pi\left(C_{s,b}\exp(-J_w K)\right)\right)\right] \quad (9)$$

Where the osmotic pressure, π, is a function of the estimated concentration at the membrane surface and can be calculated with equation (1).

The water flux can be calculated at node from the implicit equation (9) with a nonlinear root solver, e.g. fzero in MATLAB. In order to use the solver, intermediate variables such as hydraulic pressure, osmotic pressure, mass transfer coefficient, and solute resistivity for diffusion must be determined for each node. We determine the hydraulic pressure from its position along the membrane because we assume a constant pressure drop of 5 kPa per m of membrane length. The mass transfer coefficient and solute resistivity for diffusion changes along the membrane because the solution density, diffusivity, and viscosity are concentration dependent. The concentration dependent relationships are shown in SI section 2.2.

For the results in the paper, we assume that there is no salt transport across the membrane. This assumption is relaxed in SI section 4 to assess salt rejection.

2.2 Concentration dependent intermediate variables

The NaCl solution density, diffusivity, and viscosity are concentration dependent. We determined the relationships from regressions of data from a literature source or databases.[3,4]

Density: The NaCl solution density is based on data from the International Critical Tables.[3] The data was linearly fit and presented in Figure S3.

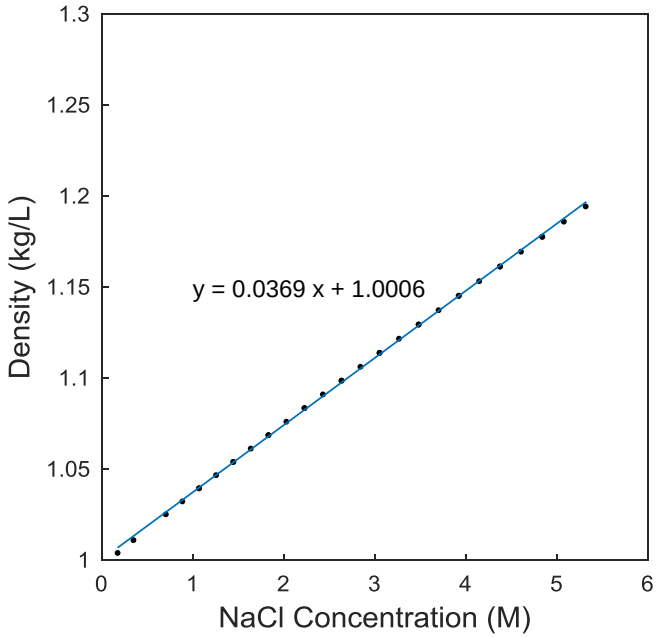

Figure S3*. NaCl solution density versus concentration.*

Diffusivity: The NaCl solution diffusivity is based on data from Lobo (1993).[4] We use a linear fit at low concentrations and a 4th order polynomial fit at moderate and high concentration, which are presented in Figure S4.

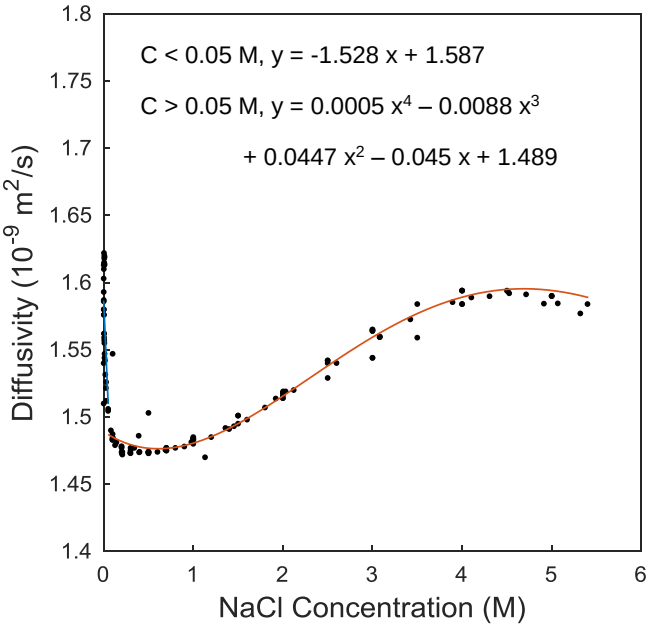

Figure S4*. NaCl solution diffusivity versus concentration.*

Viscosity: The viscosity of NaCl solution is based on data from the international critical table.[3] We apply a linear fit, which is presented in Figure S5.

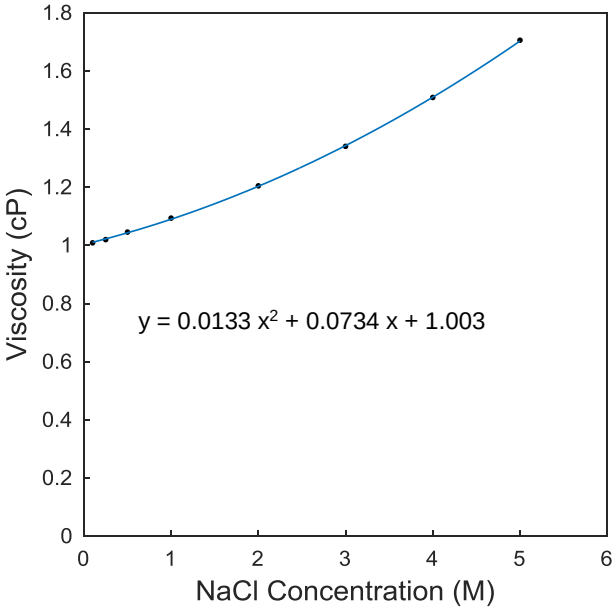

Figure S5*. NaCl solution viscosity versus concentration.*

2.3 Model solution method

We use an iterative approach to solve the counter-current module. The solution steps are presented in Figure S3. The model is solved by guessing a water flux, determining the concentrations with the mass balance equations (2)-(5), calculating the water flux using the concentrations, and then updating the guessed water flux. These steps continue until the guessed and calculated flux is within 0.1% for each node. Since the density is concentration dependent the mass balance equations (2)-(5) become implicit. To avoid the more demanding implicit calculations for the mass balance, the density was assumed to be based on the concentrations of the previous iteration. This assumption has a negligible effect on the results as the density has less than a 0.1% difference between the final iterations.

Initialization: the model is initiated by guessing there is no water flux, $J_{WG,n}$, setting the feed density, $\rho_{f,n}$, based on the feed inlet concentration, setting the sweep density, $\rho_{S,n}$, based on the sweep inlet concentration for all nodes (n).

Iteration: Given a guessed water flux, $J_{WG,n}$, and set density for the feed and sweep, $\rho_{*,n}$, the mass balance calculations can be solved to determine the feed and sweep flowrate, $Q_{*,n}$, and concentration, $C_{*,n}$ for all nodes (n). Given the concentrations the water flux can be calculated, $J_{WC,n}$. Then the relative error between the guessed water flux and calculated water flux is calculated. If the relative error in the water flux is less than 0.1% for each node, then the model is considered solved. If the relative error is greater than 0.1% for each node, then the guessed water flux is updated with equation (10).

$$J^{*}_{WG,n} = \alpha J_{WC,n} + (1-\alpha) J_{WG,n} \quad (10)$$

Where $J^*_{WG,n}$is the updated guessed water flux, $J_{WC,n}$ is the calculated water flux based on the concentrations, $J_{WG,n}$ is the previously guessed water flux, and α is the step size (we use 0.3).

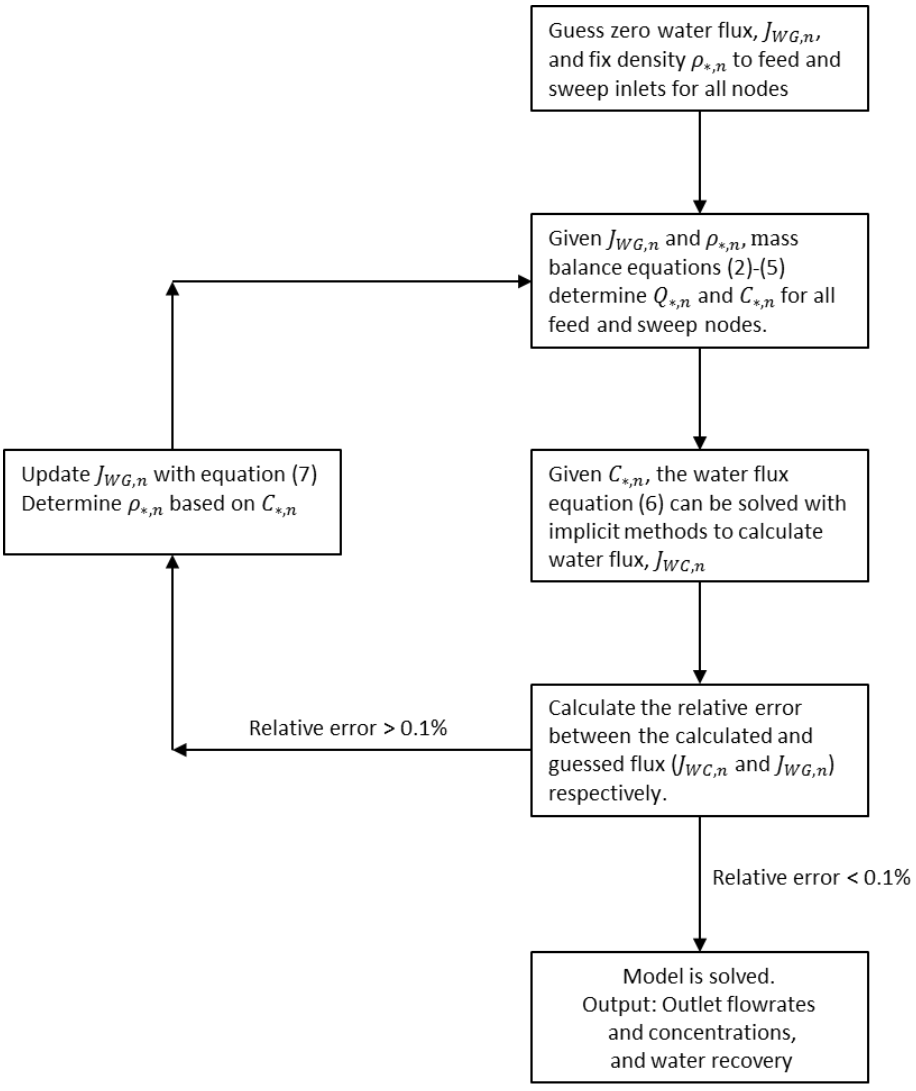

Figure S6. *Solution method for the a single OARO module. The method iterates until the guessed flux, $J_{WG,n}$, agrees within 0.1% with the calculated flux, $J_{WC,n}$. The flowrate, $Q_{*,n}$, concentration, $C_{*,n}$, and density, $\rho_{*,n}$, are determined for the feed and sweep (both denoted as subscript $*$) for all nodes (n).*

3. Multi-module model

The OARO process is typically comprised of multiple OARO modules and one RO module. Each of these modules must have the same water transport across their membranes in order to satisfy our assumption that the process is operating at steady state. Once we define the specifications of the first OARO module and determine its water permeate volume, we must determine what design variables result in the same permeate volume for the successive modules.

The key design variables for the OARO module are: membrane area, module dimensions, feed and sweep inlet pressure, sweep flowrate, and sweep concentration. We assume that all of the design variables, except the sweep concentration, are constant throughout the OARO modules. This simplifying assumption allows there to be one free variable, the sweep concentration, so that the entire OARO process becomes deterministic based on the specifications of the first OARO module. For the final RO unit, the free variable becomes the feed inlet pressure since the RO module does not have a sweep. The method for determining the operation of the entire OARO process is presented in Figure S7.

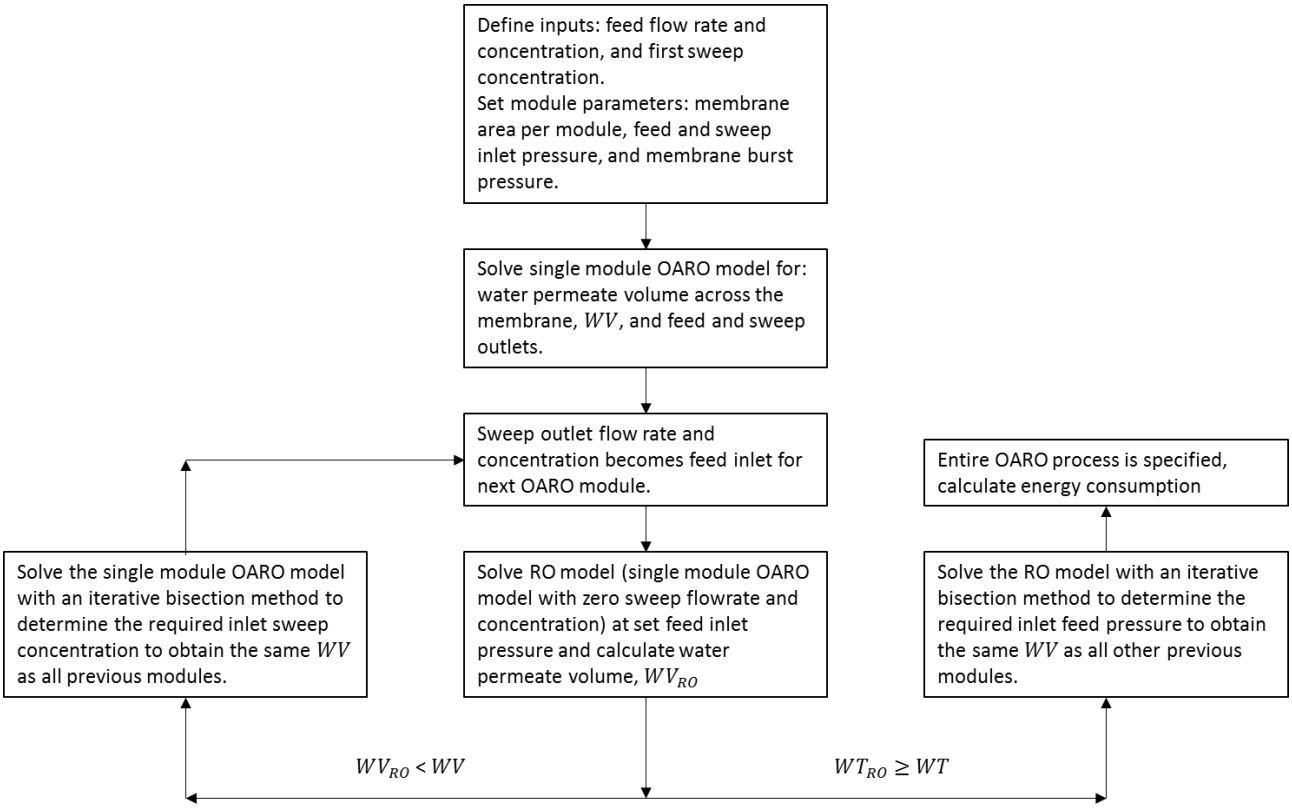

Figure S7. *Method for determining the steady state multi-module configuration of the OARO process. In order to enforce steady state operation, the water permeate volume across the membrane in each module, WV, must be the same.*

We estimate the energy consumption of the OARO process through the energy demand of the high pressure pumps. A pressure exchanger is used for each module in order to recover pressure from the feed outlet to the feed inlet. The relationship between the change in pressure for the feed inlet and feed outlet is provide in equation (11a) and solved for the intermediate feed inlet pressure in equation (11b).

$$Q_{f,in}\left(P_{int} - P_{s,out}\right) = Q_{f,out}\left(P_{f,out} - P_{s,in}\right)\eta_{ex} \tag{11a}$$

$$P_{int} = \frac{Q_{f,out}\left(P_{f,out} - P_{s,in}\right)\eta}{Q_{f,in}} \tag{11b}$$

Where P_{int} is the intermediate feed inlet pressure before the high pressure pump, $Q_{*,*}$ and $P_{*,*}$ are the inlet (in) and outlet (out) flowrate and pressure of the feed (f) and sweep (s), and η_{ex} is the pressure exchanger efficiency, which is assumed to be 96%. Figure S8 provides a diagram of theses variables.

After the intermediate feed inlet pressure is determined, the power demand of the high pressure pump can be calculated with equation (12).

$$PP = \frac{Q_{f,in}\left(P_{f,in} - P_{f,int}\right)}{\eta_{pump}} \quad (12)$$

Where PP is the power demand of the high pressure pump and η_{pump} is the isentropic efficiency of the pump, which is assumed to be 80%. The power demand of the pump can be converted to an energy consumption per unit volume of product water by dividing by the volumetric flowrate of freshwater recovered. The summation of the energy demand for all the pumps is the estimated energy consumption of the OARO process.

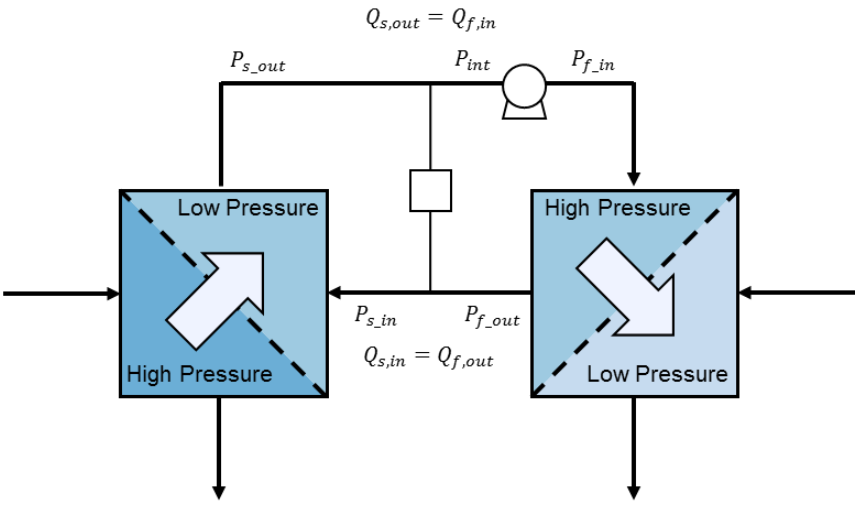

Figure S8. *Pressure and flowrate variables relevant for calculating the energy consumption of the high pressure pumps.*

4. Base case concentration profile along the first OARO module.

The first module of the base case, defined in the paper, has a feed inlet TDS concentration of 125 g/L and a sweep inlet TDS concentration of 175 g/L. The concentration profile across the membrane is presented in Figure S9. While the sweep inlet TDS concentration is greater than the feed inlet, due to the counter-current operation the feed TDS concentration is greater than the sweep along the membrane. Notice that the sweep outlet TDS concentration is 100 g/L, which is below the inlet feed concentration. This decrease in TDS concentration is essential for a series of OARO modules to eventually decrease the TDS concentration enough to effectively use a RO module and produce a freshwater product. If the sweep TDS concentration was greater than the feed TDS concentration, than the module operates like pressure assisted forward osmosis and would require a final separation step like a distillation column, instead of a RO unit.

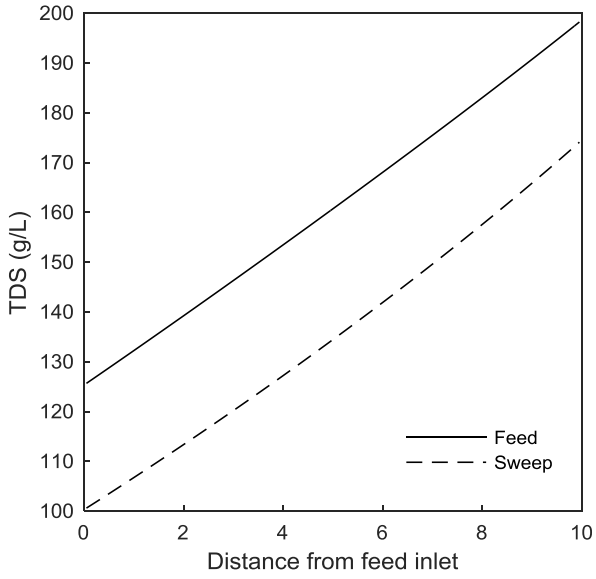

Figure S9. *Concentration profile of the feed and sweep for the first OARO module in the base-case scenario.*

5. Determining salt rejection.

For the results in the paper, we assume that there is no salt flux across the membrane. However, we used equation (13) for a preliminary estimate of salt flux.

$$J_S = B\left[C_f - C_s\right] \tag{13}$$

Where (J_S) is the salt flux $\left(\frac{kg}{m^2\ s}\right)$, B is the salt permeability coefficient $\left(\frac{m}{s}\right)$, and C is the concentration, $\left(\frac{kg}{m^3}\right)$, of the feed (f) and sweep (s). The membrane that we based the water permeability and structural parameter has a salt permeability coefficient of $7.7x10^{-8}$.[5]

When the salt flux was included for the base case, defined in the paper, 1.7% of the mass of salt transported across the membrane. The small amount of salt mass transported across the membrane confirms that the salt rejection is high. Including the salt flux increased the estimated

water transport by about 2%. This small beneficial effect would result in a similar decrease in the energy consumption. However, the water and salt transport across the multiple modules would not be equal, and steady state operation would not be satisfied. The actions required to ensure steady state operation, such as purge streams or addition of saline solutions to the sweep cycles, would offset the benefits associated with increased water transport. The unsteady state operation associated with the salt flux is out of the scope of this preliminary analysis of the OARO process.

6. Pressure drop effects.

The sensitivity of the assumed pressure drop of 5 kPa per meter of module length was investigated. When the pressure drop was tripled to 15 kPa per meter, the base case total water transport changed by less than 0.1% and the energy consumption increased by less than 5%.

References

(1) Scatchard, G.; Hamer, W. J.; Wood, S. E. Isotonic Solutions. I. The Chemical Potential of Water in Aqueous Solutions of Sodium Chloride, Potassium Chloride, Sulfuric Acid, Sucrose, Urea and Glycerol at 25°1. *Journal of the American Chemical Society* **1938,** *60* (12), 3061.

(2) McCutcheon, J. R.; Elimelech, M. Influence of concentrative and dilutive internal concentration polarization on flux behavior in forward osmosis. *Journal of Membrane Science* **2006,** *284* (1–2), 237.

(3) Washburn, E.W., International Critical Tables of Numerical Data, Physics, Chemistry and Technology (1st Electronic Edition). Knovel **2003**. Online version available at http://app.knovel.com/hotlink/toc/id:kpICTNDPC4/international-critical/international-critical

(4) Lobo, V. M., Mutual diffusion coefficients in aqueous electrolyte solutions. *Pure and Applied Chemistry* **1993**, (65) 2613-2640.

(5) She, Q.; Jin, X.; Tang, C. Y. Osmotic power production from salinity gradient resource by pressure retarded osmosis: Effects of operating conditions and reverse solute diffusion. *Journal of Membrane Science* **2012,** *401–402*, 262.

APPENDIX C: SUPPORTING INFORMATION FOR CHAPTER 4 - COST OPTIMIZATION OF OSMOTICALLY ASSISTED REVERSE OSMOSIS

Supporting Information Summary:
The supporting information contains details for 1) solution properties; 2) interfacial membrane concentration; 3) optimization model formulation; 4) additional details on the case studies; 5) tradeoffs between energy consumption and cost; 6) key design and operational variables for the OARO process; 7) additional sensitivity analyses.

This supporting information is 46 pages long and contains 13 figures (Figures S1-S13) and 98 equations (Equations S1-S98).

S.1) Solution properties

The NaCl solution properties used in our model include: diffusivity of the solute, density, viscosity, and osmotic pressure. These solution properties vary based on solution temperature and NaCl concentration. For our work, we assume a constant temperature of 25° C. We also assume the diffusivity of NaCl is 1.5E-9 m^2/s and not dependent on NaCl concentration.[1] This simplification is common in literature because the diffusivity varies by less than 10% between dilute and saturated solutions.[2]

Throughout this section we present the solution property relationships that were developed from regressions of tabulated data, a similar presentation is included in the supplementary information of our other work.[3]

S.1.1) Density

The solution density varies with NaCl mass fraction as shown in Figure S1. We fit density data from the USGS with a linear relationship, shown in equation S1.[4] The resulting regression has an R^2 value greater than 0.99.

$$\rho(X) = 750.6\,X + 995.1 \tag{S1}$$

Where ρ is the density [g/L or kg/m^3] and X is the solution NaCl mass fraction [%].

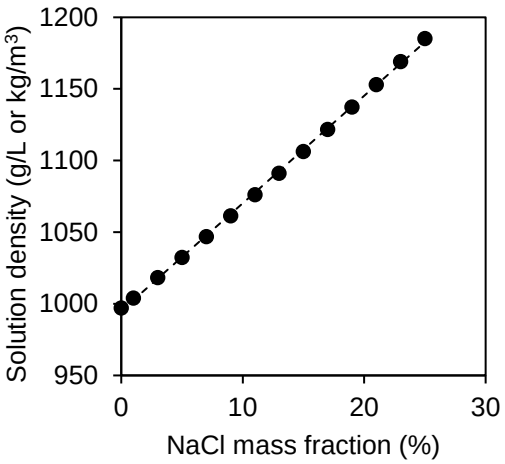

Figure S1. *Density of NaCl solution at 25° C.[4] The dotted line is the linear fit (equation S1).*

The density can be used to relate the NaCl concentration and the NaCl mass fraction as shown in equation S2 and S3.

$$C(X) = \rho(X)\, X = 750.6\, X^2 + 995.1\, X \tag{S2}$$

$$X(C) = positive\ root\ of\ (750.6\, X^2 + 995.1\, X\ - C) \tag{S3}$$

Where C is the NaCl concentration [g/L or kg/m^3] and X is the NaCl mass fraction [%].

S.1.2) Viscosity

We model the viscosity as a function of NaCl mass fraction by fitting data from the international critical tables with a linear relationship, shown in Figure S2 and equation S4.[5]

$$\mu(X) = 2.15E\text{-}5\, X + 9.80E\text{-}4 \tag{S4}$$

Where μ is the dynamic viscosity [Pa-s] and the regression has an R-squared value of 0.99.

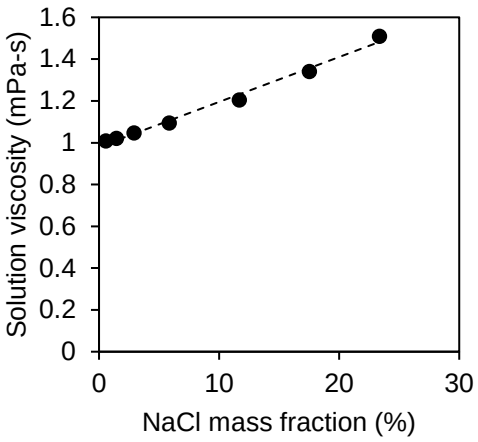

Figure S2*. Dynamic viscosity of NaCl solution at 25° C.*[5] *The dotted line is the linear fit (equation S4).*

S.1.3) Osmotic pressure

The osmotic pressure of a solution can be determined with equation S5.

$$\pi = i\ \phi\ C_M\ R\ T \tag{S5}$$

Where π is the osmotic pressure [bar], i is the number of dissociating ions (2 for NaCl), ϕ is the osmotic coefficient, C_M is the mole-based concentration [moles/L], R is the gas constant [8.314E-2 L bar mol^{-1} K^{-1}], T is the temperature [293.15 K].

When the solution is assumed to be ideal, the osmotic coefficient is 1. We account for non-ideal behavior of NaCl solution by fitting experimental osmotic coefficient data from Scatchard et al. (1938).[6] The osmotic coefficient data and the quadratic fit are shown in Figure S3 and equation S6. The resulting regression has an R-squared value greater than 0.99. Given this osmotic coefficient relationship, we determine the osmotic pressure of the solution with equation S7.

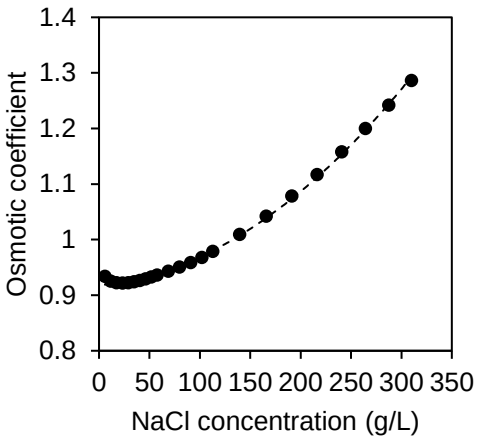

Figure S3. *Osmotic coefficient as a function of NaCl concentration. The dotted line is the quadratic fit (equation S6).*

$$\phi(C) = 3.33E\text{-}6\ \mathrm{C}^2\ + 1.78E\text{-}4\ \mathrm{C}\ + 0.918 \tag{S6}$$

$$\pi(C) = \frac{i\,R\,T}{MW}\ (3.33E\text{-}6\ \mathrm{C}^2\ + 1.78E\text{-}4\ \mathrm{C}\ + 0.918\ )\ \mathrm{C} \tag{S7}$$

Where π is the osmotic pressure [bar], C is the NaCl concentration [g/L], and MW is the molecular weight of NaCl [58.44 g/mol].

S.2) Interfacial membrane concentration

The relationship between the bulk and interfacial membrane concentration can be derived from the convective and diffusive transport and the steady state assumption. The following derivation for OARO concentration polarization closely follows the steps demonstrated for PRO concentration polarization in Yip et al. 2011 and FO concentration polarization in Bui et al 2015.[3, 7-8] Figure S4 includes a depiction of the solute concentration profiles and key variables and regions for the derivation.

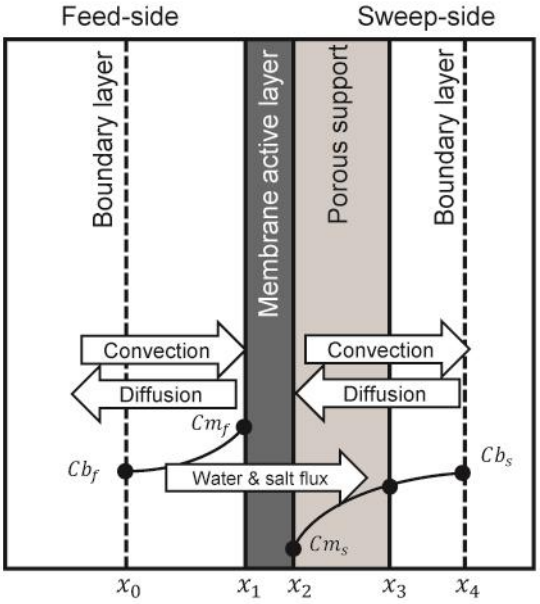

Figure S4. *Illustration of the solute concentration profiles for osmotically assisted reverse osmosis (OARO). The bulk and interfacial membrane concentrations are noted with Cb_f and Cm_f for the feed and Cb_s and Cm_s for the sweep. The x indices denote the key regions in the membrane cross-section. The arrows denote the direction and mode (convection and diffusion) of salt transport in the feed and sweep. The feed-side experiences external concentration polarization, while the sweep-side experiences internal concentration polarization (within the porous support) and external concentration polarization.*

The feed-side external concentration polarization is governed by equation S8.

$$Js = -D\frac{dC}{dx} + Jw\ C \tag{S8}$$

Where Js and Jw are the salt flux [kg/m^2 s] and water flux [m^3/m^2 s], D is the diffusion coefficient of the solute [m^2/s], C is the solute concentration [kg/m^3] that varies spatially with dimension x [m] (direction noted in Fig. S4).

We separate the variables and integrate equation S8 across the feed-side boundary layer, where at the bulk-boundary layer interface, $x = x_0$ and $C = Cb_f$ (the feed-side bulk concentration), and at the membrane interface, $x = x_1$ and $C = Cm_f$ (the feed-side interfacial membrane concentration), as shown in equation S9.

$$\int_{Cb_f}^{Cm_f} \frac{dC}{Jw\ C - Js} = \int_{x_0}^{x_1} \frac{1}{D}\ dx \tag{S9}$$

We integrate equation S9 and obtain equation S10.

$$\frac{1}{\mathrm{Jw}} \ln\left(\frac{Jw\ Cm_f - Js}{Jw\ Cb_f - Js}\right) = \frac{(x_1 - x_0)}{D} \tag{S10}$$

We solve equation S10 for Cm_f and substitute δ_f (the feed-side boundary layer thickness) for $x_1 - x_0$ to obtain equation S11.

$$Cm_f = Cb_f \exp\left(\frac{Jw\ \delta}{D}\right) - \frac{Js}{Jw}\left(\exp\left(\frac{J_w\ \delta}{D}\right) - 1\right) \tag{S11}$$

We further substitute k_f (the feed-side boundary layer mass transfer coefficient) for $\frac{D}{\delta}$ to obtain equation S12. Equation S12 is the same as equation 3 in the main manuscript.

$$Cm_f = Cb_f \exp\left(\frac{Jw}{k_f}\right) - \frac{Js}{Jw}\left(\exp\left(\frac{J_w}{k_f}\right) - 1\right) \tag{S12}$$

The sweep-side internal and external concentration polarization is governed by equation S12. Note that the diffusion coefficient, D^*, varies based on the region. In the porous support, D^s (the effective diffusion coefficient in the porous support) is related to the diffusion coefficient of the solute by $D^s = \frac{D\varepsilon}{\tau}$. Where ε is the porosity and τ is the tortuosity of the porous support.

$$Js = -D^* \frac{dC}{dx} + Jw\ C \tag{S13}$$

Using the same approach as the feed-side, we separate the variables and integrate equation S13 across the porous support and the sweep-side boundary layer. At the sweep-side membrane interface, $x = x_2$ and $C = Cm_s$ (the sweep-side interfacial membrane concentration), and at the sweep-side bulk-boundary layer, $x = x_4$ and $C = Cb_s$ (the sweep-side bulk concentration), as shown in equation S14.

$$\int_{Cm_s}^{Cb_s} \frac{dC}{Jw\ C - Js} = \int_{x_2}^{x_3} \frac{1}{D^s}\ dx + \int_{x_3}^{x_4} \frac{1}{D}\ dx \tag{S14}$$

After integrating equation S14, we obtain equation S15.

$$\frac{1}{\mathrm{Jw}} \ln\left(\frac{Jw\ Cb_s - Js}{Jw\ Cm_s - Js}\right) = \frac{(x_3 - x_2)}{D^s} + \frac{(x_4 - x_3)}{D} \tag{S15}$$

We solve equation S15 for Cm_s and substitute t (the thickness of the porous support) for $x_3 - x_2$ and δ_s (the sweep-side boundary layer thickness) for $x_4 - x_3$ to obtain equation S16.

$$Cm_s = Cb_s \exp\left(-Jw\left(\frac{t}{D^s} + \frac{\delta_s}{D}\right)\right) - \frac{Js}{Jw}\left(\exp\left(-Jw\left(\frac{t}{D^s} + \frac{\delta_s}{D}\right)\right) - 1\right) \tag{S16}$$

We substitute S (the structural parameter) for $\frac{t\,\tau}{\epsilon}$ and k_s (the sweep-side mass transfer coefficient) for D/δ_s to obtain equation S17. Equation S17 is the same as equation 4 in the main manuscript.

$$Cm_s = Cb_s \exp\left(-Jw\left(\frac{S}{D}+\frac{1}{k_s}\right)\right)+\frac{Js}{Jw}\left(1-\exp\left(-Jw\left(\frac{S}{D}+\frac{1}{k_s}\right)\right)\right) \quad \text{(S17)}$$

S.3) Optimization model formulation

We formulate the OARO process as a nonlinear programming (NLP) model with the objective to minimize the unit water costs. The model can be solved for a given feed flow rate, concentration, water recovery, and number of stages. We determine the optimal number of stages through inspection after solving the optimization model with different number of stages for the same specified feed concentration and water recovery.

S.3.1) Modeling the membrane stages

We model the membrane stage with a detailed one-dimensional model that is also described in our other work.[3] This model determines the state (e.g. mass flow rate, salt mass fraction, hydraulic pressure) and process (e.g. water and salt flux) variables across the length of the membrane stage. The model also accounts for concentration polarization, pressure loss from friction, and solution properties as a function of concentration. The model is based on a finite difference approximation of the one-dimensional governing system of differential equations shown in equations S18-S23.

$$\frac{dM_f}{dz} = -(Jw\ \rho w + Js)\ W \tag{S18}$$

$$\frac{d(M_f\ X_f)}{dz} = -Js\ W \tag{S19}$$

$$\frac{dM_s}{dz} = (Jw\ \rho w + Js)\ W \tag{S20}$$

$$\frac{d(M_s\ X_s)}{dz} = Js\ W \tag{S21}$$

$$\frac{dP_f}{dz} = -PL_f \tag{S22}$$

$$\frac{dP_s}{dz} = -PL_s \quad \text{(S23)}$$

Where z is the dimension along the length of the membrane stage [m], M is the mass flow rate [kg/h], X is the salt mass fraction [kg of salt/kg of solution], P is the hydraulic pressure [bar], W is the width of the membrane stage [m], Jw is the water flux [m^3/m^2-h], Js is the salt flux [kg/m^2-h], ρw is the density of water [995 kg/m^3], PL is the pressure loss per unit length [bar/m], and subscript f and s note the feed and sweep side. The direction of z is from the inlet to the outlet on both sides (e.g. M_f is $M_{f,in}$ at z=0 and $M_{f,out}$ at z=L, the length of the membrane stage).

The process variables Jw, Js, and PL are determined as functions of the state variables in equations S24-S26. Throughout the description of this model, functions are noted as $f_x(y_1, y_2, \dots)$, where x is determined from variables y.

$$Jw = f_{Jw}(P_f, P_s, Cm_f, Cm_s) = A\left(\left[P_f - P_s\right] - \left[f_\pi(Cm_f) - f_\pi(Cm_s)\right]\right) \quad \text{(S24)}$$

$$Js = f_{Js}(Cm_f, Cm_s) = B\ (Cm_f - Cm_s) \quad \text{(S25)}$$

$$PL = f_{PL}(M, X, Re, W) = \frac{f_F(Re)\ M^2}{4\ f_\rho(X)\ H^3\ W^2\ \varepsilon^2} \left[\frac{1\ h}{3600\ s}\right]^2 \left[\frac{1\ bar}{1E5\ Pa}\right] \quad \text{(S26)}$$

Where A is the water permeability coefficient [m/h-bar], B is the salt permeability coefficient [m/h], π is the osmotic pressure [bar] and is a function of the concentration at the membrane interface, Cm, (equation S7), F is the friction factor and is a function of the Reynolds number (equation S27), ρ is the solution density [kg/m^3] and is a function of the salt mass fraction (equation S1), H is the channel height [m], ε is the void space of the mesh spacer (assumed to be 75%).

We estimate the friction factor with a correlation developed by Guillen and Hoek (2009) for a mesh filled channel in equation S27.[9] The parameters for F are based on a mesh with a circular cross section and an effective cross-sectional area of 25% (i.e. void space of 75%).

$$F = f_F(Re) = 0.42 + \frac{189.3}{Re} \tag{S27}$$

The mass transfer coefficient, k, [m/h] is determined by equation S28.

$$k = \frac{D\ Sh}{d_h} \tag{S28}$$

Where D is the diffusion coefficient [m^2/h], Sh is the Sherwood number, and d_h is the hydraulic diameter. The Sherwood number is determined from a correlation developed by Guillen and Hoek (2009) in equation S29 and the hydraulic diameter is approximated in equation S30, when $W \gg H$.[9]

$$Sh = 0.46(Re\ Sc)^{0.36} \tag{S29}$$

$$d_h = \frac{2\ W\ H}{W+H} \approx 2H \tag{S30}$$

We substitute equation S28 with equations S29 and S30 to model the mass transfer coefficient as a function of variables in our model, as shown in equation S31.

$$k = f_k(Re, Sc) = \frac{D}{2H}\ 0.46(Re\ Sc)^{0.36} \tag{S31}$$

Finite difference model

We use the finite difference approximation to approximate the governing system of differential equations. This approach discretizes the membrane stage along the length into nodes,

where the state and process variables are evaluated. A schematic of the finite difference approach is shown in Figure S5.

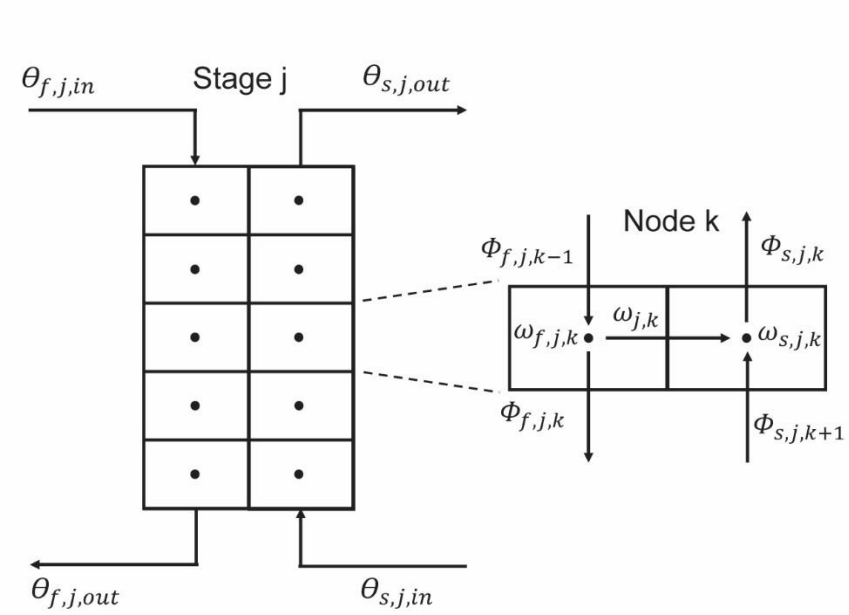

Figure S5. *Finite difference approach to modeling a membrane stage. θ are inlet and outlet stage variables and ϕ are inter-node variables that include: mass flow rate, salt mass fraction, Reynolds number, Schmidt number, and pressure loss per unit length. ω are nodal variables that include: water flux, salt flux, hydraulic pressure, osmotic pressure, bulk concentration, concentration at the membrane interface, and mass transfer coefficient. The variables are indexed by the feed (f) and sweep (s), stage (j), and node (k).*

The finite difference approximation of the governing mass balance (equations S18-S21) is shown in equations S32-S43.

$$M_{f,j,k} = M_{f,j,k-1} - \frac{Amem}{N}\left(Jw_{j,k}\,\rho_w + Js_{j,k}\right) \quad \forall j, \forall k, k \neq k1 \tag{S32}$$

$$M_{f,j,k}X_{f,j,k} = M_{f,j,k-1}X_{f,j,k-1} - \frac{Amem}{N} Js_{j,k} \quad \forall j, \forall k, k \neq k1 \tag{S33}$$

$$M_{f,j,k1} = M_{f,j,in} - \frac{Amem}{N}\left(Jw_{j,k1}\,\rho_w + Js_{j,k1}\right) \quad \forall j \tag{S34}$$

$$M_{f,j,k1}X_{f,j,k1} = M_{f,j,in}X_{f,j,in} - \frac{Amem}{N} Js_{j,k1} \quad \forall j \tag{S35}$$

$$M_{f,j,out} = M_{f,j,kN} \quad \forall j \tag{S36}$$

$$X_{f,j,out} = X_{f,j,kN} \quad \forall j \tag{S37}$$

$$M_{s,j,k} = M_{s,j,k+1} + \frac{Amem}{N}\left(Jw_{j,k}\,\rho_w + Js_{j,k}\right) \quad \forall j, \forall k, k \neq kN \tag{S38}$$

$$M_{s,j,k}X_{s,j,k} = M_{s,j,k+1}X_{s,j,k+1} + \frac{Amem}{N} Js_{j,k} \quad \forall j, \forall k, k \neq kN \tag{S39}$$

$$M_{s,j,kN} = M_{s,j,in} + \frac{Amem}{N}\left(Jw_{j,kN}\,\rho_w + Js_{j,kN}\right) \quad \forall j \tag{S40}$$

$$M_{s,j,kN}X_{s,j,kN} = M_{s,j,in}X_{s,j,in} + \frac{Amem}{N} Js_{j,kN} \quad \forall j \tag{S41}$$

$$M_{s,j,out} = M_{s,j,k1} \quad \forall j \tag{S42}$$

$$X_{s,j,out} = X_{s,j,k1} \quad \forall j \tag{S43}$$

Where $Amem$ is the stage membrane area [m^2], and the state and process variables are noted for stage j in the set of stages J ($j1, j2, \ldots jM$, with M being the number of stages), for node k in the set of nodes K ($k1, k2, \ldots kN$, with N being the number of nodes), and for stage inlet or outlet with in and out, respectively.

The finite difference approximation of the governing pressure drop (equations S22 and S23) are shown in equations S44-S49. Note that since the hydraulic pressure is a nodal variable (ω in figure S5) and the mass flow rate and salt mass fraction are inter-node variables (ϕ in

figure S5), there is a small deviation in the finite difference formulation (e.g. $1/N$ in equation S34 and $1/2N$ in equation S45).

$$P_{f,j,k} = P_{f,j,k-1} - PL_{f,j,k-1}\frac{L}{N} \quad \forall j, \forall k, k \neq k1 \tag{S44}$$

$$P_{f,j,k1} = P_{f,j,in} - PL_{f,j,in}\frac{L}{2N} \quad \forall j \tag{S45}$$

$$P_{f,j,out} = P_{f.j,kN} - PL_{f,j,kN}\frac{L}{2N} \quad \forall j \tag{S46}$$

$$P_{s,j,k} = P_{s,j,k+1} - PL_{s,j,k+1}\frac{L}{N} \quad \forall j, \forall k, k \neq kN \tag{S47}$$

$$P_{s,j,kN} = P_{s,j,in} - PL_{s,j,in}\frac{L}{2N} \quad \forall j \tag{S48}$$

$$P_{s,j,out} = P_{s,j,k1} - PL_{s,j,k1}\frac{L}{2N} \quad \forall j \tag{S49}$$

The nodal variables (ω in Fig. S5), including: water flux, salt flux, osmotic pressure, bulk concentration, concentration at the membrane interface, and mass transfer coefficient are determined in equations S50-S63. As described in the main manuscript, we neglect concentration polarization on the sweep-side (permeate-side) for the RO stage as shown in equation S55. Since we neglect the sweep side concentration polarization for the RO stage, we do not evaluate the sweep mass transfer coefficient for that stage (noted by equations S62 and S63 for all j except jM).

$$Jw_{j,k} = A\left(\left(P_{f,j,k} - P_{s,j,k}\right) - \left(\pi_{f,j,k} - \pi_{s,j,k}\right)\right) \quad \forall j, \forall k \tag{S50}$$

$$Js_{j,k} = B\left(Cm_{f,j,k} - Cm_{s,j,k}\right) \quad \forall j, \forall k \tag{S51}$$

$$\pi_{u,j,k} = f_{\pi}\left(Cm_{u,j,k}\right) \quad \forall u \in (f,s), \forall j, \forall k \tag{S52}$$

$$Cm_{f,j,k} = f_{Cm_f}\left(Cb_{f,j,k}, Jw_{j,k}, k_{f,j,k}\right) \quad \forall j, \forall k \tag{S53}$$

$$Cm_{s,j,k} = f_{Cm_s}\left(Cb_{s,j,k}, Jw_{j,k}, k_{s,j,k}\right) \quad \forall j, j \neq jM, \forall k \tag{S54}$$

$$Cm_{s,jM,k} = Cb_{s,jM,k} \quad \forall k \tag{S55}$$

$$Cb_{f,j,k} = \frac{f_C(X_{f,j,k}) + f_C(X_{f,j,k-1})}{2} \quad \forall j, \forall k, k \neq k1 \tag{S56}$$

$$Cb_{f,j,k1} = \frac{f_C(X_{f,j,in}) + f_C(X_{f,j,k1})}{2} \quad \forall j \tag{S57}$$

$$Cb_{s,j,k} = \frac{f_C(X_{s,j,k}) + f_C(X_{s,j,k+1})}{2} \quad \forall j, \forall k, k \neq kN \tag{S58}$$

$$Cb_{s,j,kN} = \frac{f_C(X_{s,j,in}) + f_C(X_{s,j,kN})}{2} \quad \forall j \tag{S59}$$

$$k_{f,j,k} = \frac{f_k(Re_{f,j,k}, Sc_{f,j,k}) + f_k(Re_{f,j,k-1}, Sc_{f,j,k-1})}{2} \quad \forall j, \forall k, k \neq k1 \tag{S60}$$

$$k_{f,j,k1} = \frac{f_k(Re_{f,j,in}, Sc_{f,j,in}) + f_k(Re_{f,j,k}, Sc_{f,j,k})}{2} \quad \forall j \tag{S61}$$

$$k_{s,j,k} = \frac{f_k(Re_{s,j,k}, Sc_{p,k}) + f_k(Re_{s,j,k+1}, Sc_{s,j,k+1})}{2} \quad \forall j, j \neq jM, \forall k, k \neq kN \tag{S62}$$

$$k_{s,j,kN} = \frac{f_k(Re_{s,j,in}, Sc_{s,j,in}) + f_k(Re_{s,j,kN}, Sc_{s,j,kN})}{2} \quad \forall j, j \neq jM \tag{S63}$$

Where the functions for osmotic pressure (f_π) is equation S7, concentrations at the membrane interface (f_{Cm_f} and f_{Cm_s}) are equations S12 and S17, and concentration from mass fraction (f_C) is equation S2. Note that the bulk concentration (Cb) and mass transfer coefficient (k) are based on the average of their functions evaluated at the adjacent inter-node variables.

The inter-node variables (ϕ in Fig. S5), including: pressure loss per unit length, Reynolds number, and Schmidt number are determined in equations S64-S69. As described in the main

manuscript, we assume there is no sweep pressure drop for the RO stage (equation S66). Additionally, since we assume no sweep concentration polarization for the RO stage, we do not evaluate the Reynolds number for that stage (noted by equation S68 for all j except jM).

$$PL_{f,j,v} = f_{PL}\left(M_{f,j,v}, X_{f,j,v}, Re_{f,j,v}, W\right) \quad \forall j, \forall v \in (K, in) \tag{S64}$$

$$PL_{s,j,v} = f_{PL}\left(M_{s,j,v}, X_{s,j,v}, Re_{s,j,v}, W\right) \quad \forall j, j \neq jM, \forall v \in (K, in) \tag{S65}$$

$$PL_{s,jM,v} = 0 \quad \forall v \in (K, in) \tag{S66}$$

$$Re_{f,j,v} = f_{Re}\left(M_{f,j,v}, X_{f,j,v}, W\right) \quad \forall j, \forall v \in (K, in) \tag{S67}$$

$$Re_{s,j,v} = f_{Re}\left(M_{s,j,v}, X_{s,j,v}, W\right) \quad \forall j, j \neq jM, \forall v \in (K, in) \tag{S68}$$

$$Sc_{u,j,v} = \frac{f_{\mu}\left(X_{u,j,v}\right)}{f_{\rho}\left(X_{u,j,v}\right) D} \quad \forall u \in (f, s), \forall j, \forall v \in (K, in) \tag{S69}$$

Where the functions for viscosity (f_{μ}) and density (f_{ρ}) are equations S4 and S1.

The membrane area of each stage is related to the width and length in equation S70.

$$Amem_j = W_j \, L_j \tag{S70}$$

We also determine the average water and salt flux for each stage with equations S71 and S72.

$$Jw_{avg,j} = \frac{1}{N} \sum_k Jw_{j,k} \quad \forall j \tag{S71}$$

$$Js_{avg,j} = \frac{1}{N} \sum_k Js_{j,k} \quad \forall j \tag{S72}$$

S.3.2) Modeling the OARO process streams

The previous section describes how each membrane stage is modeled, in this section, we describe the relationships that link the stages together. As shown in Figure 2 in the main manuscript, the OARO process is composed of sweep cycles, purge, recycle, and make-up streams. This system is modeled by relating the outlet and inlet streams to each other as follows.

In the OARO process, the inlet feed for each stage is the outlet sweep of the previous stage (except for the first stage) as shown in equations S73 and S74.

$$M_{f,j,in} = M_{s,j-1,out} \quad \forall j, j \neq j1 \tag{S73}$$

$$X_{f,j,in} = X_{s,j-1,out} \quad \forall j, j \neq j1 \tag{S74}$$

Additionally, the outlet feed of each stage is disposed of or recycled to another stage, as shown in equation S75.

$$M_{f,j,out} = Md_j + \sum_{j'} Mr_{j,j'} \quad \forall j \tag{S75}$$

Where Md is the mass flow rate [kg/h] sent to disposal from stage j and Mr is the mass flow rate for recycle from stage j to stage j'. The recycle stream within a sweep cycle is represented with j'=j-1. Note that since this stream is an inherent part of sweep cycle operation, it is not marked as recycle in Figure 2 in the main manuscript. The only other permitted recycle stream is from a sweep cycle to the preceding sweep cycle, which occurs when $j' = j - 2$. All other recycle streams are fixed to zero as shown in SI section S.3.6.

The inlet sweep out each stage is composed of recycle and make-up streams (with the exception of the last stage) as shown in equations S76 and S77. In the last stage (RO), the sweep inlet mass flow rate ($M_{s,jM,in}$) and salt mass fraction ($X_{s,jM,in}$) are fixed to zero.

$$M_{s,j,in} = Ma_j + \sum_{j'} Mr_{j',j} \quad \forall j, j \neq jM \tag{S76}$$

$$M_{s,j,in}\, X_{s,j,in} = Ma_j\, Xa + \sum_{j'} Mr_{j',j}\, X_{f,j',out} \quad \forall j, j \neq jM \tag{S77}$$

Where Ma is the mass flow rate of make-up to stage j and Xa is the salt mass fraction of the make-up (assumed to be saturated solution of NaCl at 0.26).

S.3.3) Modeling the system performance

In this section, we provide the relationships that determine the overall system performance. The annual water production rate, AWP, [m^3/year] is determined in equation S78.

$$AWP = \left(\frac{M_{s,jM,out}}{f_\rho(X_{s,jM,out})}\ LF\ \left[\frac{8760\ h}{year}\right] \right) \tag{S78}$$

Where LF is the load factor [time operated/time in year] (assumed to be 0.9).

The water recovery, Rw, is an important parameter specified for our model and it is related to the model variables by equation S79.

$$Rw = \frac{M_{s,jM,out}\left(1 - Xs_{out,jM}\right)}{M_{f,j1,in}\left(1 - X_{f,j1,in}\right) + \sum_j Ma_j (1 - Xa)} \tag{S79}$$

Where equation S79 can be interpreted as the mass of the product water over the mass of water entering the process. Note that the water recovery is on a mass basis of water, rather than a volumetric basis of solution.

The overall purge rate is a key system variable and is defined as the fraction of disposal mass flow rate from the sweep cycles over the first stage permeate mass flow rate, as shown in equation S80.

$$PR = \frac{\sum_{j \neq j1} Md_j}{M_{f,j1,in} - M_{f,j1,out}} \tag{S80}$$

We estimate the energy consumption of the OARO process by accounting for the power demand of the pumps with equation S81. The pump power is determined in equations S82-S84.

$$EC = \frac{f_\rho(X_{s,jM,out})}{M_{s,jM,out}} \sum_j \left(Pow_{f,j} + Pow_{s,j}\right) \left[\frac{1E5\ Pa}{bar}\right] \left[\frac{1\ kJ}{1000\ J}\right] \left[\frac{1\ h}{3600\ s}\right] \quad \text{(S81)}$$

$$Pow_{f,j} = \frac{\frac{M_{f.j.in}}{f_\rho(X_{f.j.in})}(P_{f,j,in} - P_{s,j-1,out}) - \frac{M_{f,j,out}}{f_\rho(X_{f.j.out})}(P_{f,j,out} - 1)\,\eta_{px}}{\eta_{pmp}} \quad \forall j, j \neq j1 \quad \text{(S82)}$$

$$Pow_{f,j1} = \frac{\frac{M_{f.j1.in}}{f_\rho(X_{f.j1.in})}(P_{f,j,in} - 1) - \frac{M_{f,j1,out}}{f_\rho(X_{f.j1.out})}(P_{f,j1,out} - 1)\,\eta_{px}}{\eta_{pmp}} \quad \text{(S83)}$$

$$Pow_{s,j} = \frac{M_{s,j,in}}{\rho w} \frac{(P_{s,j,in} - 1)}{\eta_{pmp}} \quad \forall j \quad \text{(S84)}$$

Where EC is the energy consumption [kWh/m^3 of product water], Pow is the pump power for the feed and sweep at each stage [m^3-bar/h], η is the efficiency of the pump (pmp) and pressure exchanger (px). This power calculation for the feed pump does not explicitly model the split inlet feed flow rates and the two feed pumps that are required to operate the pressure exchanger; however, this formulation is common in literature and is equivalent for overall power demand, which is the basis of our cost calculations.[10-11]

S.3.4) Modeling process constraints

Two key process constraints include: 1) the product water specification and 2) the maximum inlet feed pressure. Both constraints are shown in equations S85 and S86.

$$X_{s,jM,out} \leq \frac{500}{1E6} \quad \text{(S85)}$$

$$P_{f,j,in} \leq P_{max,f,j} \quad \forall j \quad \text{(S86)}$$

Where the product water mass fraction, $X_{s,jM,out}$, must be less than or equal to 500 ppm and the inlet feed pressure for each stage must be below the maximum feed inlet pressure, $P_{max,f,j}$, for that stage (OARO stage: 65 bar in the base case, RO stage: 85 bar).

S.3.4) Modeling OARO process costs

As described in the main manuscript, we determine the unit water costs of the OARO process by estimating the capital investment and operating costs. To estimate the capital investment, we determine the direct cost of three components (membrane units, pumps, and pressure exchangers) and use factors to account for indirect capital, installation, siting, and engineering costs. We also directly estimate the electricity, saline make-up, and membrane replacement operating costs and indirectly estimate maintenance & labor and chemical operating costs.

The capital costs of the membrane unit, feed and sweep pump, and pressure exchanger are determined in equations S87-S89.

$$CC_{mem,j} = CP_{mem,j} Amem_j \quad \forall j \tag{S87}$$

$$CC_{pmp,u,j} = CP_{pmp,u,j} Pow_{u,j} \quad \forall j, \forall u \in (f, s) \tag{S88}$$

$$CC_{px,j} = 3134.7 \left(\frac{M_{f,j,out}}{f_\rho(X_{f,j,out})} \right)^{0.58} \quad \forall j \tag{S89}$$

Where CC is the capital costs [$] for the membrane unit (mem), pump (pmp), and pressure exchanger (px) and CP is the associated cost parameters that are presented and cited in the main manuscript Table 1.

The total capital investment is a multiple of the total equipment costs, as shown in S90.

$$TCI = F_{TCI} \sum_j \left(CC_{mem,j} + CC_{pmp,f,j} + CC_{pmp,s,j} + CC_{px,j} \right) \quad \text{(S90)}$$

Where TCI is the total capital investment [$] and F_{TCI} is the practical investment factor [$ investment/$ equipment] (assumed to be 1.6 in the base case).

The annual operating costs from electricity, make-up streams, membrane replacement, maintenance & labor, and chemicals are determined in equations S91-S95.

$$OC_{elec} = CP_{elec}\, EC\, AWP \quad \text{(S91)}$$

$$OC_{sal} = CP_{sal}\ \sum_j Ma_j\, LF\ \left[\frac{8760\ h}{year}\right] \quad \text{(S92)}$$

$$OC_{mem} = RR_{mem} \sum_j CC_{mem,j} \quad \text{(S93)}$$

$$OC_{m\&l} = F_{m\&l} TCI \quad \text{(S94)}$$

$$OC_{chem} = F_{chem} TCI \quad \text{(S95)}$$

Where OC is the annual operating cost for electricity ($elec$), make-up steams (sal), membrane replacement (mem), maintenance & labor ($m\&l$), and chemicals ($chem$). The cost parameters (CP), cost factors (F), and rate of membrane replacement (RR_{mem}) are provided in Table 1 in the main manuscript.

The total annual costs and unit water costs are determined in equations S96 and S97.

$$TAC = (OC_{elec} + OC_{sal} + OC_{mem} + OC_{mlc}) + CF * TCI \quad \text{(S96)}$$

$$UWC = \frac{TAC}{AWP} \quad \text{(S97)}$$

Where TAC is the total annual costs [$/year], CF is the capitalization factor [$/$ total capital investment-year] (assumed to be 10% in the base case), UWC is the unit water costs [$/m^3].

S.3.5) Objective function

The objective of our optimization model is to minimize the unit water costs as shown in equation S98.

$$min.\, obj = UWC \tag{S98}$$

S.3.6) Fixing, scaling, initializing, and bounding variables

In this section, we describe the fixed variables in our model and how we scale, initialize, and bound the variables to assist the solver.

Fixed variables

We fix several variables that are defined in the OARO process:

- The inlet feed mass flow rate and mass fraction, $X_{f,j1,in}$, for the first stage ($M_{f,j1,in}$ and $X_{f,j1,in}$) are specified by the case study
- The inlet sweep mass flow rate and mass fraction for the RO stage ($M_{s,jM,in}$ and $X_{s,jM,in}$) are 0
- The inlet, outlet, and nodal sweep pressure for the RO stage ($P_{s,jM,in}$, $P_{s,jM,out}$, $P_{s,jM,k}$) are 1 bar
- There is no make-up stream and no sweep pump for the RO stage (Ma_{jM}, $Pow_{s,jM}$)
- The recycle mass flow rate, $Mr_{j,j'}$, is zero for all combinations of j and j', except when $j = j'$-1 (regular sweep cycle flow) and $j = j'$-2 (inter-sweep cycle flow).

Scaled variables

We rescale several variables, as follows:

- Water (Jw) and salt (Js) flux in units of LMH and g/m^2-h, respectively
- Pressure loss per unit length (PL) in units of Pa/m
- Mass transfer coefficients (k) in units of mm/h

Initialized variables

We initialize the following variables:

- The inlet feed pressure ($P_{f,j,in}$) to the maximum allowed pressure ($P_{max,f,j}$)
- The outlet product water mass fraction ($X_{s,jM,out}$) to the specified constraint (500 ppm)
- The make-up stream mass flow rate (Ma_j) to 0

Bounded variables

The variable bounds are essential for the local solver to initialize and find a feasible solution. We assume the following bounds:

Average water flux: $0.1\ LMH \leq Jwavg_j \leq 10\ LMH\ \forall j \neq jM$. We observe that these assumed average water flux bounds were inactive for all scenarios assessed in this work. Both bounds are multiplied by 4 for the RO stage ($j = jM$).

Water flux: The water flux at the node, $Jw_{j,k}$, can be less than or greater than the average water flux bounds. Therefore, we decrease and increase the average water flux bounds by a factor of 5 and 1.5, respectively, for the water flux at the node bounds. We observe that these bounds were inactive for all assessed scenarios.

Average salt flux: $0 \leq Jsavg_j \leq 50 \frac{g}{m^2\ h}$. We observe that this assumed average salt flux maximum is about 3 times greater than the highest optimal average salt flux for all assessed scenarios.

Salt flux: The salt flux at the node has similar values to the average salt flux because, unlike the water flux, the driving force stays relatively constant across the membrane stage. Therefore, we use the same average salt flux bounds for the salt flux at the node.

Reynolds number: $100 \leq Re \leq 2000$. We set the minimum and maximum Reynolds number for both the feed and sweep side in the laminar regime. We find that the low flow rate streams (feed outlet and sweep inlet), typically, are operated at or near the minimum Reynolds number for the OARO stages.

Purge rate: $0 \leq PR \leq 0.2$. We observe that this assumed maximum purge rate is about twice the highest optimal purge rate for all assessed scenarios.

First sweep to first feed inlet concentration ratio: We assume the minimum and maximum first inlet sweep concentration is within a factor of 3 of the first inlet feed concentration.

RO stage feed inlet and outlet concentration: We assume that the minimum feed inlet and outlet concentration for the RO stage is 10 g/L. These lower bounds are about half the minimum optimal concentrations for all assessed scenarios.

Sweep flow rate: We assume the inlet sweep flow rate is within 15 and 80% of the inlet feed flow rate for each stage. This assumption is a 10% relaxation from 1 minus the minimum and maximum water recovery (30 and 75%) assessed in this work. 1 minus the water recovery is a key metric to assess the sweep to feed mass flow rate ratio because when the ratio equals this

metric, the sweep outlet flow rate will equal the feed inlet flow rate (excluding the small effect of salt permeation). We observe that the lower bound is active in 2 stage processes (1 OARO and 1 RO) at low feed salinities and water recoveries.

Recycle rate: We assume that the maximum recycle rate between two sweep cycles is less than 20% of the maximum sweep cycle flow rate. The maximum sweep cycle flow rate is determined based on the maximum permeate flow rate and the assumed maximum sweep to feed mass flow rate ratio. We observe that this bound is about an order of magnitude higher than any optimal recycle rates between two sweep cycles for all assessed scenarios.

Given the above assumptions, the bounds for all other variables can be determined based on the specified inputs (feed flow rate, feed concentration, and water recovery), solution properties (maximum and minimum of density, viscosity, and osmotic pressure), mass balances (e.g. determining bounds for flow rates and concentrations based on the inlet flow rate and maximum and minimum permeate flows), and OARO operational constraints (e.g. sweep concentration decreases with successive stages).

S.3.7) Notation for optimization model

Parameters:

A – water permeability coefficient [m/h-bar]

B – salt permeability coefficient [m/h]

CF – capitalization factor [$/$ total capital investment-year]

Cp – cost parameters shown in Table 1

D – diffusion coefficient [m^2/h]

d_h - hydraulic diameter [m]

F_{chem} – factor for chemical costs, $ chemical costs/$ initial investment-year

$F_{m\&l}$ – factor for maintenance and labor costs, $ maintenance and labor costs/$ initial investment-year

F_{TCI} – factor for total capital investment, % of direct capital costs

H – height of channel [m]

LF – load factor [%]

RR_{mem} – Rate of membrane replacement [%/year]

S – structural parameter [m]

Xa – make up stream mass fraction [kg salt/kg solution]

ε – void space of the mesh spacer [-]

η_{pmp} – pump efficiency, %

η_{px} – pressure exchanger efficiency, %

Sets:

J – stages (j1, j2, … jM)

K – nodes (k1, k2, … kN)

Variables:

$Amem$ – membrane area [m^2]

AWP – annual water production rate [m^3/year]

Cb – bulk concentration [g/L or kg/m^3]

CC – capital costs [$]

Cm – concentration at the membrane interface [g/L or kg/m^3]

EC – energy consumption [kWh/m^3]

F – friction factor [-]

L – length of membrane stage [m]

Js – salt flux [kg/m^2-h]

Jw – water flux [m^3/h]

k – mass transfer coefficient [m/h]

M – mass flow rate [kg/h]

Md – disposal mass flow rate [kg/h]

Mr – recycle mass flow rate [kg/h]

Ma – make-up mass flow rate [kg/h]

OC – annual operating cost [$/year]

P – hydraulic pressure [bar]

PL – pressure loss per unit length [bar/m]

Pow – pump power [m^3-bar/h]

PR – overall purge rate [purge mass flow rate/first stage permeate mass flow rate]

Re – Reynolds number [-]

Rw – water recovery [water flow rate in product water/water flow rate in initial feed]

Sc – Schmidt number [-]

TAC – total annual costs [$/year]

TCI – total capital investment [$]

UWC – unit water costs [$/kWh]

W – width of membrane stage [m]

X – mass fraction [kg salt/kg of solution]

μ – viscosity [Pa-s]

ρ – density [kg^3/m^3]

π – osmotic pressure [bar]

Function:

$f_x(y_1, y_2, \dots)$ – function that determines variable x from variables y

S.4) Additional details on optimal design and operation for the case studies

The optimal make-up, recycle, purge flow rates for the three high salinity brine treatment cases are presented in figure S.6. For all case studies, we observe no makeup stream in the cost optimal solutions. Additionally, we observe that the only purge stream occurs from the first sweep cycle for the case studies. We also observe that the recycle mass flow rates decrease with successive stages. These three trends occur hold across all assessed scenarios (25-150 g/L feed concentration and 30-75% water recovery).

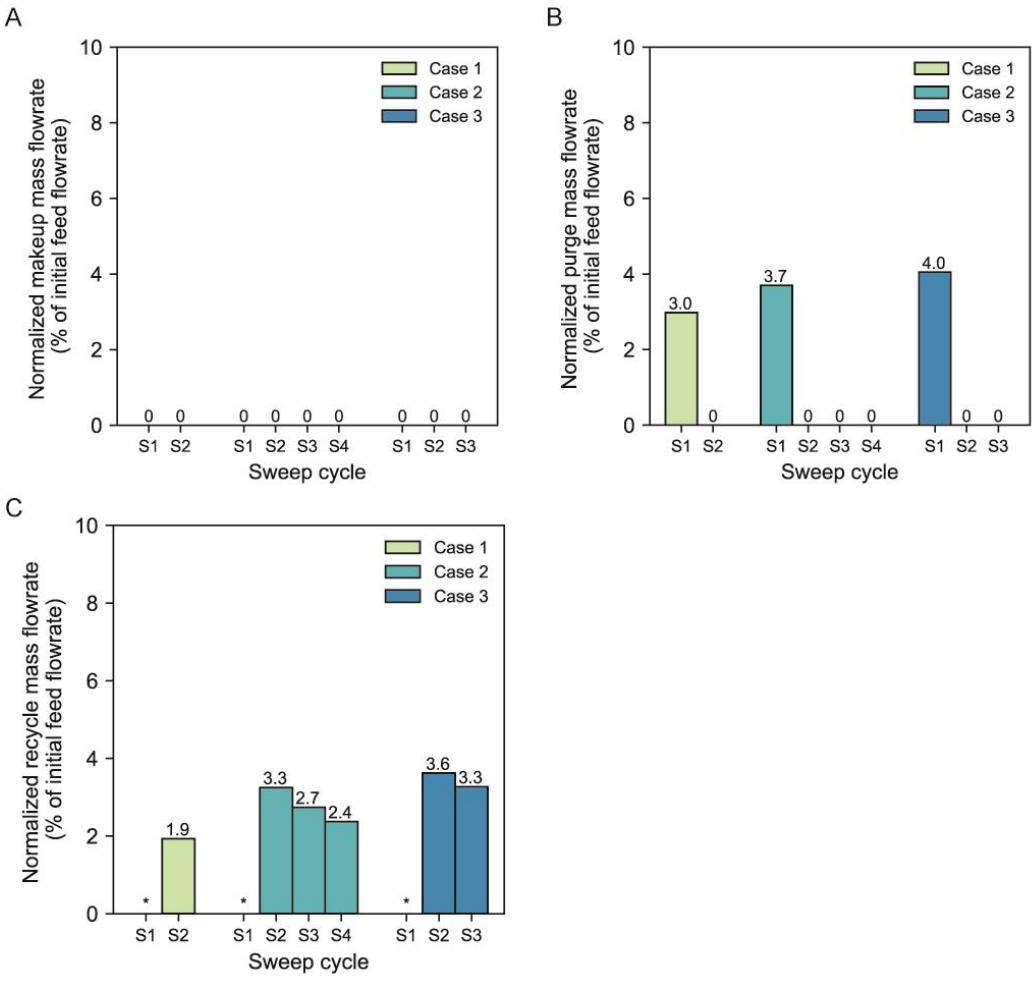

Figure S6. *Cost optimal make-up (A), purge (B), and recycle (C) flow rates for the three high-salinity brine desalination cases: 1) 75 g/L TDS with 50% recovery, 75 g/L TDS with 70%*

recovery, and 125 g/L with 40% recovery. The flow rates are normalized by the inlet feed mass flow rate in the first stage (20.5, 20.5, and 21.1 Mg/h for each case, respectively. These are based on the assumed volumetric flow rate of 19.5 m3/h and the density of the feed). Since recycle only occurs from one sweep cycle to the previous one, the first sweep cycle cannot recycle to another cycle (denoted with the asterisk).

Additional details on membrane stage water and salt flux, dimensions (width and length), flow conditions, and stage pressure drop are shown in Figure S7 and S8. The average water flux increases with successive OARO stages and has a large increase in the RO stage. However, the average salt flux is roughly constant and results in a much greater salt permeation in the early stages due to the much larger membrane areas. This difference in salt permeation requires the purge from the first sweep cycle and dilution via recycle streams from subsequent sweep cycles in order to operate at steady state.

Like the stage membrane area, the width and length of the membrane stage decrease with successive stages. We observe that the optimal membrane width corresponds to feed and sweep average Reynolds numbers below 300 in the OARO stages, while the average Reynolds number can reach as high as 1000 in the RO stages. Optimal Reynolds numbers are low in OARO stages to limit the pressure drop in the stage and obtain a higher net driving force at the end of the stage. This contrasts with RO stages, where the optimal Reynolds number are higher to reduce the feed-side external concentration polarization. The OARO stages do not prioritize the reduction of the feed or sweep-side external concentration because their water flux is more affected by the sweep-side internal concentration polarization that is independent of the flow conditions.

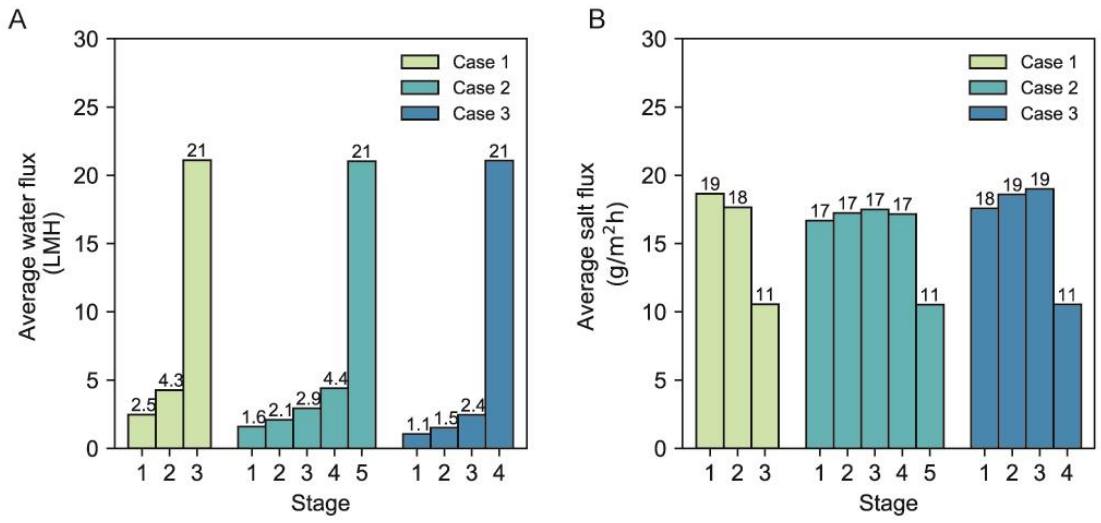

Figure S7. *Cost-optimal water (A) and salt (B) flux for the three high salinity brine desalination cases. LMH stands for L/m^2-h.*

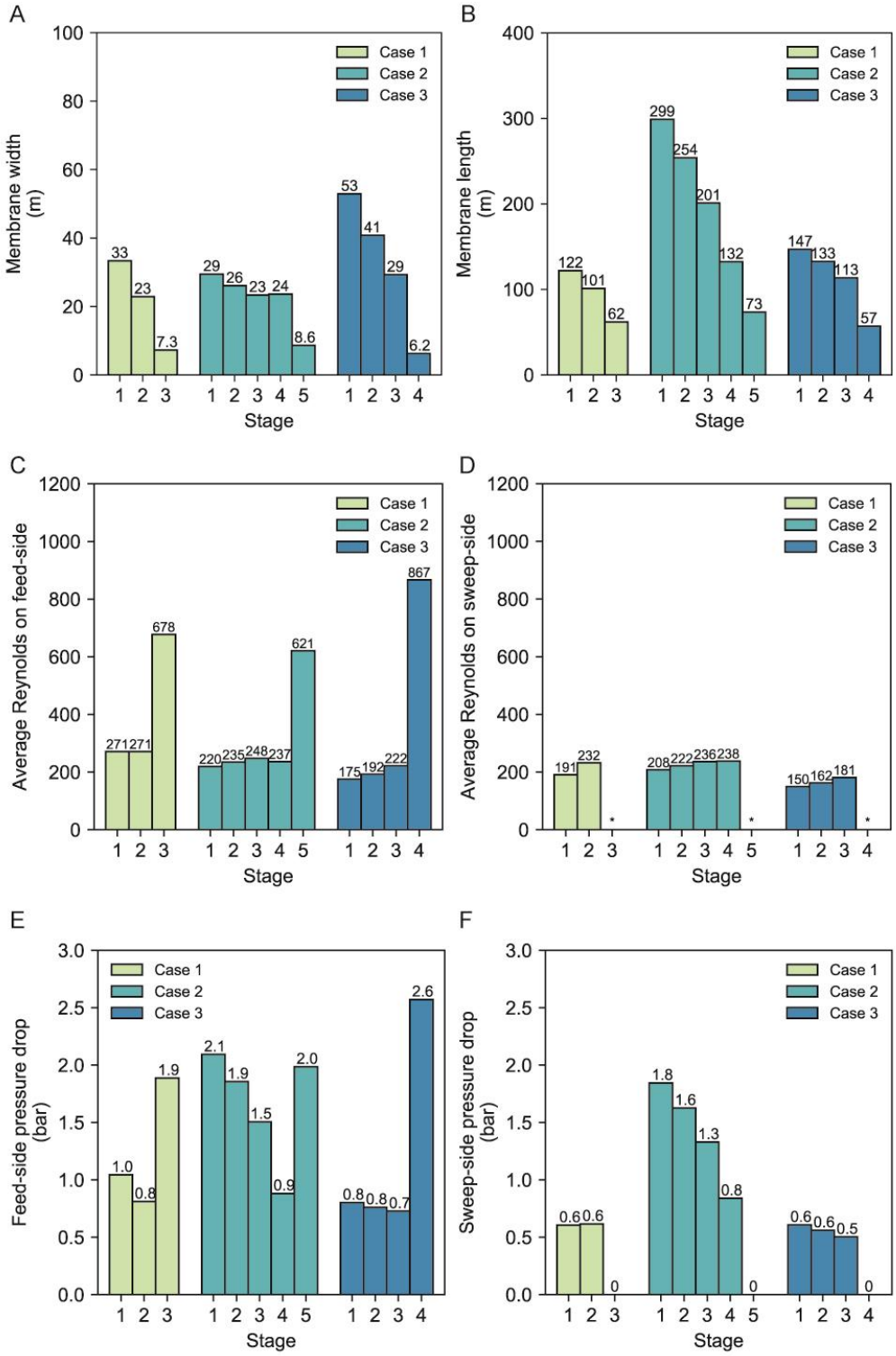

Figure S8. *Cost optimal membrane stage width (A), length (B), average Reynolds number for feed-side (C) and sweep-side (D), and pressure drop for feed-side (E) and sweep-side (F) for the*

three high salinity brine desalination cases. The asterisk denotes the Reynolds number is not determined for the sweep-side (permeate-side) of the RO stage.

S.5) Trade-offs between energy consumption and cost

Throughout our work, we have focused primarily on the unit water costs of the OARO process. While our cost optimization model provides insight into the design and operating conditions that minimize cost, it does not provide much insight into the tradeoffs between other key outcome metrics (e.g. energy consumption and product water quality). In this section, we demonstrate how multi-objective optimization techniques can be used to determine the tradeoffs between energy consumption and unit water costs for the OARO process.

Figure S9 presents the Pareto frontier between energy consumption and unit water cost for the three cases. We developed this Pareto frontier by adding a constraint on the maximum energy consumption and successively decreasing the value. We find that reducing the energy consumption of the cost optimal solution by 10-20% results in a 12-15% increase in costs across the 3 cases. We also observe that further decreases in energy consumption may result in a large increase in cost (>50%).

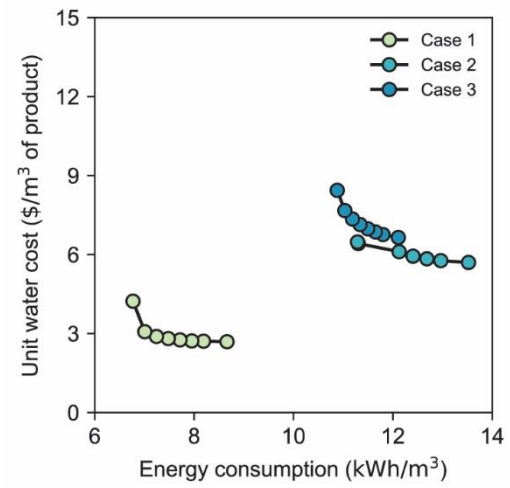

Figure S9. *OARO process cost and energy consumption tradeoffs for the three case studies. The graph provides the Pareto frontier developed by parametrically decreasing the energy consumption from the cost optimal solution (point on the far right).*

The cost of the OARO process can increase significantly for modest decreases in energy consumption because OARO designs and operations with lower energy consumption have much lower water flux and higher membrane area. Figure S10 presents the unit water cost, concentration profile, inlet feed pressure, and membrane area for case 1 Pareto frontier solutions. We observe that decreasing the energy consumption by 20% (8.66 to 7.0 kWh/m^3), increases the unit water costs by 15% (2.69 to 3.08 \$/m^3) for case 1. The reduction in energy consumption was achieved by decreasing the inlet feed pressure in the 2nd and 3rd stage (Figure S10 C), which requires lower dilute sweep concentrations (Figure S10 B) and higher membrane areas (Figure S10 D) in stage 1 and 2.

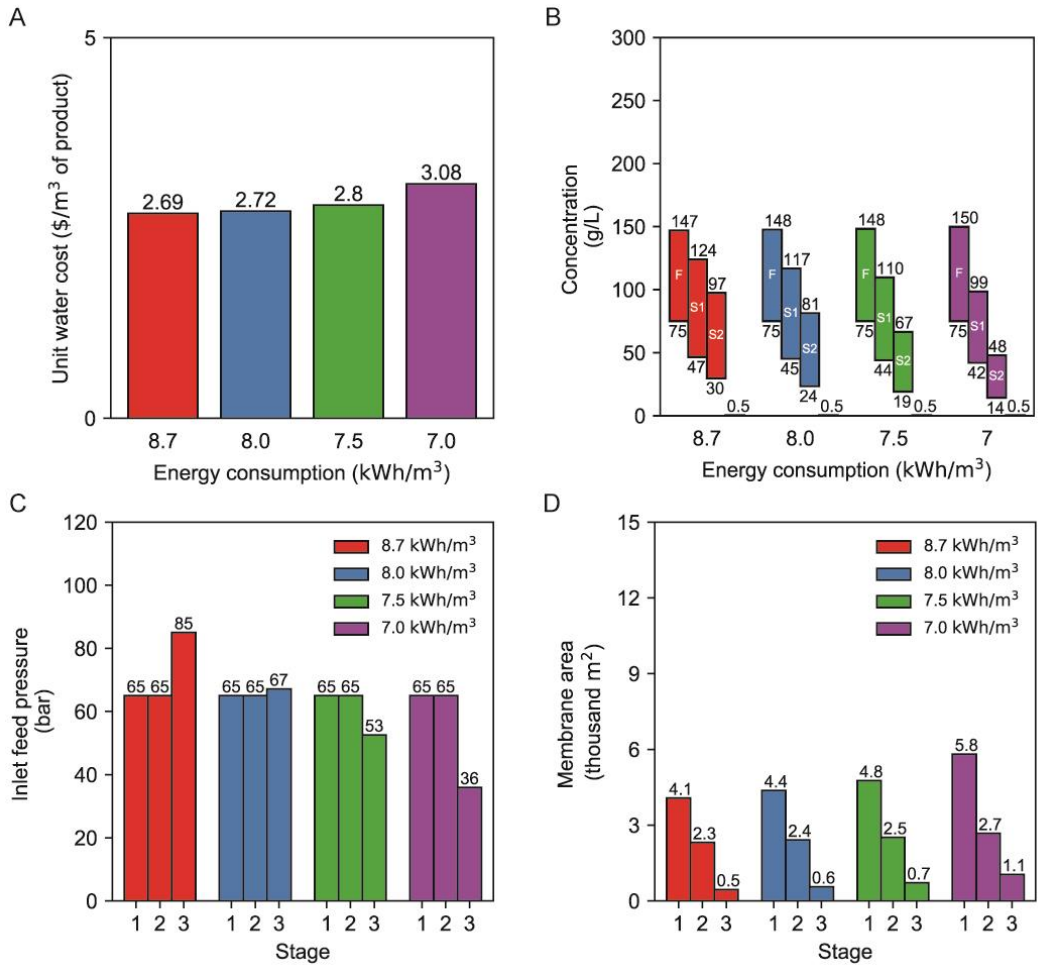

Figure S10. *Cost (A), concentration profile (B), inlet feed pressure (C), and membrane area (D) for case 1 Pareto frontier solutions. The cost optimal solution has an energy consumption of 8.7 kWh/m^3 (red) and the other solutions have a lower energy consumption of 8 kWh/m^3 (blue), 7.5 kWh/m^3 (green), and 7 kWh/m^3 (purple).*

While we can change our optimization model objective to minimize the energy consumption of the OARO process, this approach is not insightful because the solutions are trivial. When the model minimizes energy consumption, the expected variables approach their bounds. For example, the energy optimal solution would minimize the pressure drop in the stage by reducing

the Reynolds number to the lowest allowed (we assumed a lower bound of 100). This decrease in Reynolds number would increase the concentration polarization and decrease the water flux. Additionally, the energy optimal solution would minimize the inlet feed pressure for all stages, which would decrease the water flux to the lowest allowed (generally, the lowest allowed water flux was limited by the mostly unchanged salt flux and the product water quality constraint). Since we could have anticipated these operating conditions without the optimization model and these solutions are solely dependent on the arbitrary bounds, the energy optimal solutions are not valuable. This result is in stark contrast to and further emphasizes the value of the cost optimization approach, which balances complex tradeoffs in design and operating decisions.

S.6) Key design and operational variables for the OARO process

Figure S11 presents the key design variables for cost optimal OARO process configurations, including: average membrane decrease with successive OARO stages, average dilute stream flow rate decrease with successive OARO stages, overall purge rate, and average recycle rate between sweep cycles.

We observe that the overall purge rate generally increases with increasing feed concentration and decreasing water recovery. Conversely, we find that the average recycle rate between sweep cycles generally increases with decreasing feed concentration and increasing water recovery. While there are small local deviations in these trends due to the multitude of competing tradeoffs and the discrete number of stages, the trends describe the optimal design and operating conditions over the wide range of feed concentrations and water recoveries. However, there are two significant exceptions: 1) feed concentration of 75 g/L with 45% water recovery and 2) feed concentration of 100 g/L with 45% water recovery. Both exceptions have a higher overall purge rate and the second exception has a higher average recycle rate than the surrounding conditions. These exceptions deviate from the general trend because their optimal number of stages is near the switch over point for an additional stage. In both cases, their optimal number of stages have relatively low water fluxes of 2.0, 1.3 LMH in the first OARO stage. Since the water flux is low and the salt flux stays roughly constant, these cases have low selectivity in the first stage and require a greater overall purge rate and average recycle rate relative to the surrounding conditions. The average water flux in the first OARO stage for these cases is increased by 15% and 23% with an additional stage and results in a modest increase in the unit water costs of 12 and 5%, respectively. In the additional stage solutions, the overall

purge rate decreases to 6.2 and 7.7% and the average recycle rate decreases to 10.6%, which align with the general trends for those key design variables.

We observe that both the average membrane area decrease and average dilute stream flow rate decrease in successive stages increase with lower feed concentrations and lower water recoveries. The average membrane area decrease in successive OARO stages is inversely correlated with the number of stages, while the average dilute stream flow rate decrease in successive stages is more dependent on the specified water recovery.

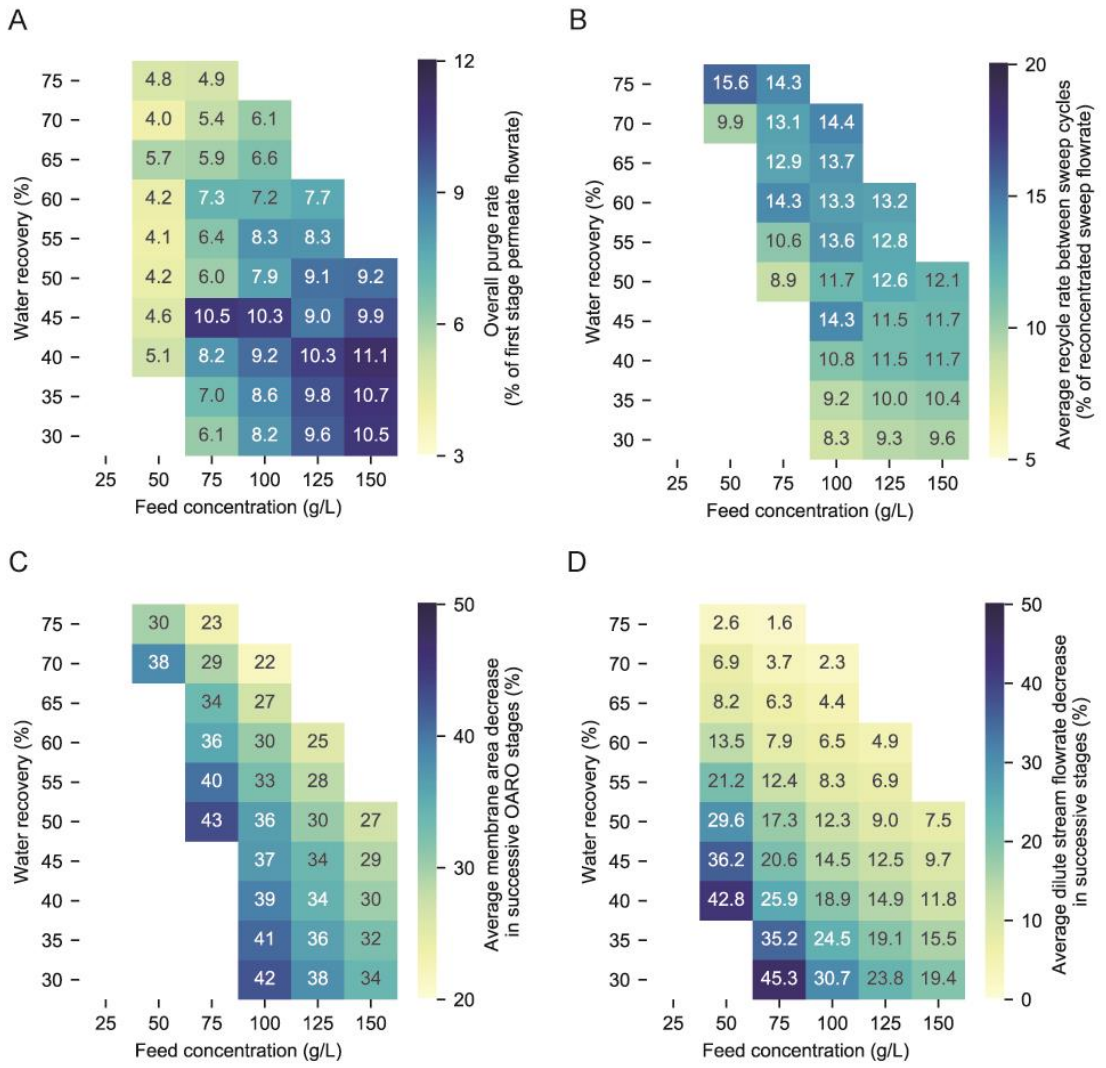

Figure S11. *Key design variables for the cost optimal OARO process: A) overall purge rate, B) average recycle rate between sweep cycles, C) average membrane area decrease in successive OARO stages, D) average dilute stream flow rate decrease in successive stages. Note that each of these metrics require at least an OARO stage and the average membrane area decrease for successive OARO stages and the average recycle rate between sweep cycles require at least two OARO stages.*

S.7) OARO cost sensitivity analysis

The OARO cost sensitivity for select process and financial parameters are shown in Figure S12 and S13.

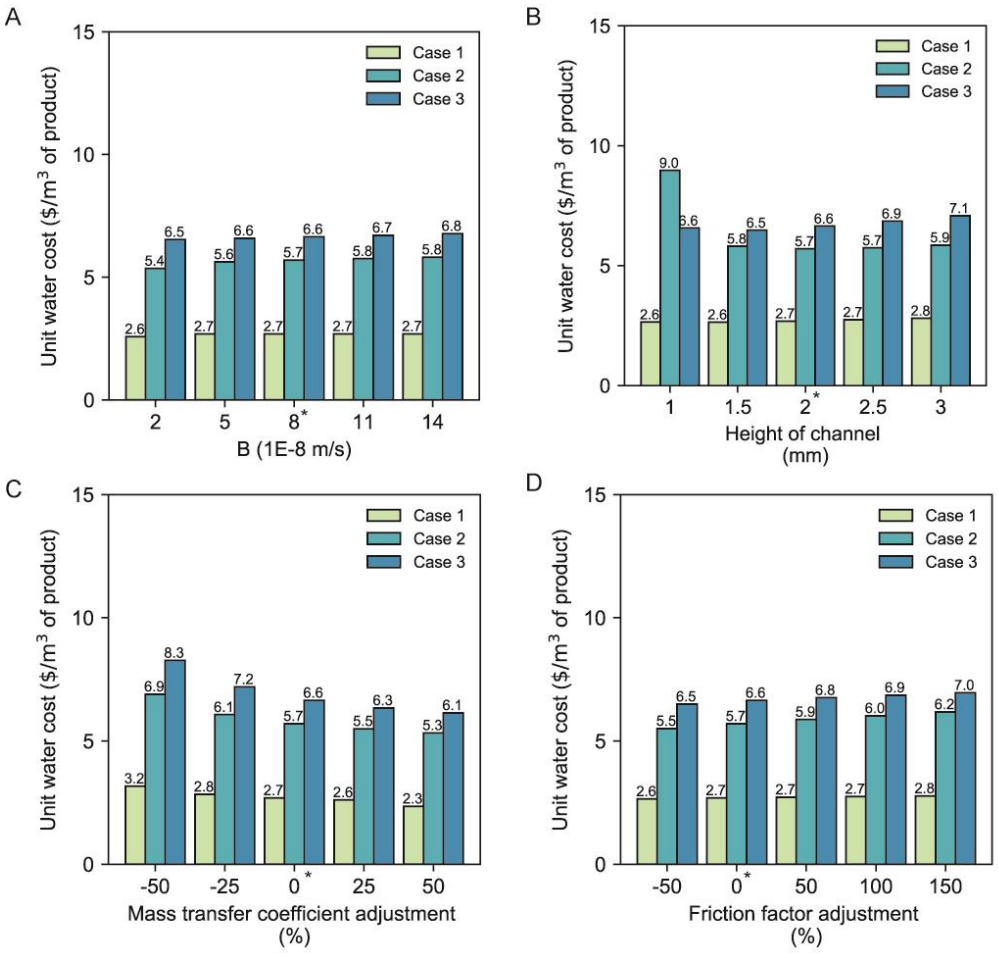

Figure S12. *OARO cost sensitivity for process parameters: A) salt permeability coefficient, B; B) height of channel; C) mass transfer coefficient adjustment; D) friction factor adjustment. For both the mass transfer coefficient and friction factor adjustment, a factor was multiplied to the relationships obtained from literature (equation S63 and S69). Asterisk denotes base case.*

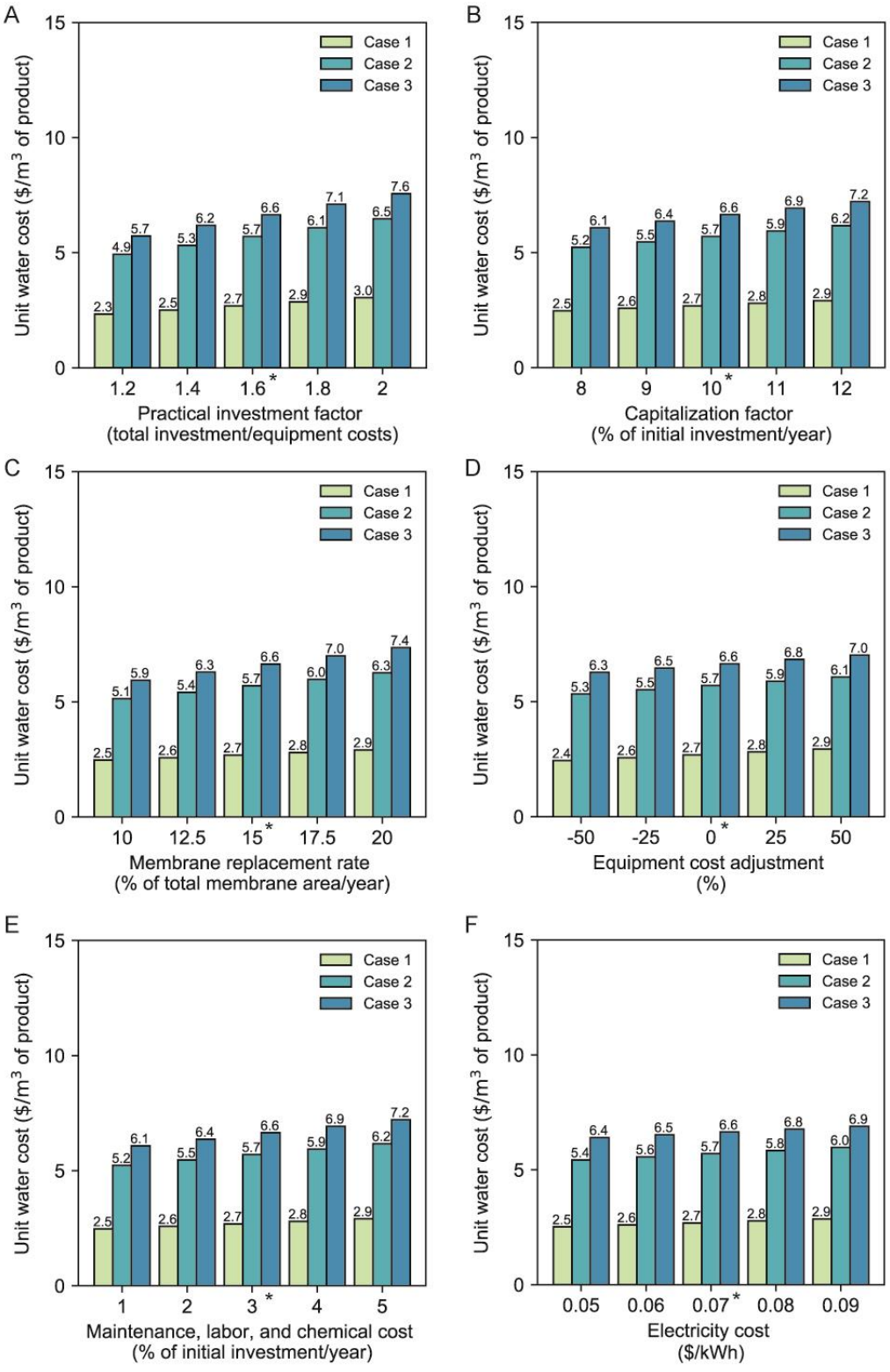

Figure S13. *OARO cost sensitivity for financial parameters: A) practical investment factor, B)*

capitalization factor, C) membrane replacement rate, D) equipment cost adjustment, E) maintenance, labor, and chemical factor, and F) electricity cost. Asterisk denotes base case.

References

1. Straub, A. P.; Yip, N. Y.; Elimelech, M., Raising the Bar: Increased Hydraulic Pressure Allows Unprecedented High Power Densities in Pressure-Retarded Osmosis. *Environmental Science & Technology Letters* **2014,** *1* (1), 55-59.

2. Lobo, V. M. M., Mutual diffusion coefficients in aqueous electrolyte solutions (Technical Report). In *Pure and Applied Chemistry*, 1993; Vol. 65, p 2613.

3. Bartholomew, T. V.; Mauter, M. S., Computational framework for modeling membrane processes without process and solution property simplifcations. *Journal of Membrane Science* **Under Review**.

4. Potter, R. W.; Brown, D. L. *The Volumetric Properties of Aqueous Sodium Chloride Solutions from 0 to 500°C at Pressures up to 2000 Bars Based on a Regression of Available Data in the Literature.*; 76-608267; United States Geological Survey: 1977.

5. Washburn, E. W., International Critical Tables of Numerical Data, Physics, Chemistry and Technology (1st Electronic Edition). Knovel.

6. Scatchard, G.; Hamer, W. J.; Wood, S. E., Isotonic Solutions. I. The Chemical Potential of Water in Aqueous Solutions of Sodium Chloride, Potassium Chloride, Sulfuric Acid, Sucrose, Urea and Glycerol at 25°1. *Journal of the American Chemical Society* **1938,** *60* (12), 3061-3070.

7. Yip, N. Y.; Tiraferri, A.; Phillip, W. A.; Schiffman, J. D.; Hoover, L. A.; Kim, Y. C.; Elimelech, M., Thin-Film Composite Pressure Retarded Osmosis Membranes for Sustainable Power Generation from Salinity Gradients. *Environmental Science & Technology* **2011,** *45* (10), 4360-4369.

8. Bui, N.-N.; Arena, J. T.; McCutcheon, J. R., Proper accounting of mass transfer resistances in forward osmosis: Improving the accuracy of model predictions of structural parameter. *Journal of Membrane Science* **2015,** *492*, 289-302.

9. Guillen, G.; Hoek, E. M. V., Modeling the impacts of feed spacer geometry on reverse osmosis and nanofiltration processes. *Chemical Engineering Journal* **2009,** *149* (1), 221-231.

10. Park, C.; Park, P.-K.; Mane, P. P.; Hyung, H.; Gandhi, V.; Kim, S.-H.; Kim, J.-H., Stochastic cost estimation approach for full-scale reverse osmosis desalination plants. *Journal of Membrane Science* **2010,** *364* (1), 52-64.

11. Vince, F.; Marechal, F.; Aoustin, E.; Bréant, P., Multi-objective optimization of RO desalination plants. *Desalination* **2008,** *222* (1), 96-118.

APPENDIX D: SUPPORTING INFORMATION FOR CHAPTER 5 – COST OPTIMIZATION OF GAP MEMBRANE DISTILLATION

Supporting Information Summary:
The supporting information contains details for 1) solution properties; 2) modeling theory; 3) optimization model; 4) effect of salinity on MD performance, 5) cost optimal outcome metrics for MD, 6) additional sensitivity analysis

This supporting information is 30 pages long and contains 6 figures (Fig. S1-S6), and 137 equations (Eq. S1-S137).

S.1) Solution properties

The NaCl solution properties including density, concentration, viscosity, vapor pressure, thermal conductivity, specific heat of vaporization, and specific enthalpy of liquid are modeled as functions of salt mass fraction and temperature. These functions are sourced from Sharqawy et al. 2010,[1] where the authors compiled a list of functions and provided their applicable salinity and temperature ranges. The equations used in this work are provided in Table S1.

In addition to the previous properties, we consider two properties (i.e. solute diffusivity and specific enthalpy of the vapor) that are modeled as a function of only temperature. We use regression to develop a quadratic equation for NaCl solute diffusivity by fitting data from Fell et al. 1971.[2] The data and the resulting fit are shown in Figure S1. We do not model the diffusivity as a function of salinity because the effect of salinity is orders of magnitude less than the effect of temperature and our previous work shows negligible errors when excluding the salinity effects for other membrane processes.[3] We model the specific enthalpy of vapor as a function of only temperature as shown in Table S1 because there is no salt content in the water vapor.

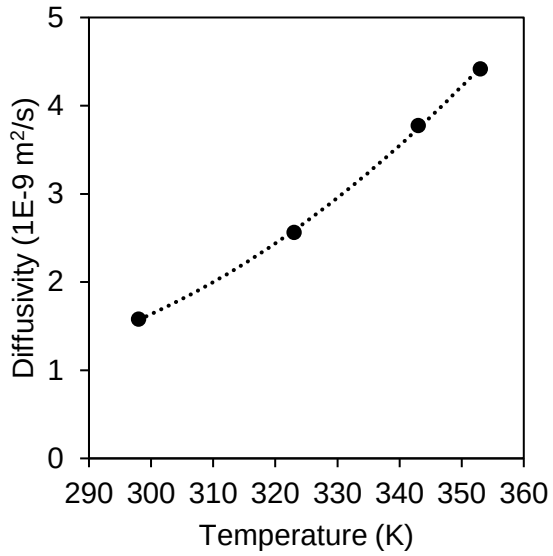

Figure S1. *NaCl diffusivity as a function of temperature. The dots are the average diffusivity for the four temperatures tested in Fell et al. 1971.[2] The dotted line is the quadratic fit with an R-squared value greater than 0.99 and is shown in Table 1.*

Table S1. *Solution property function.*

Variable	Function	Units	Source
Density, ρ	$f_\rho(X,T)$	kg m^{-3}	Eq. 5 in [1]
Concentration, C	$f_C(X,T) = \rho\, X$	kg m^{-3}	
Viscosity, μ	$f_\mu(X,T)$	Pa s	Eq. 22 in [1]
Diffusivity, D	$f_D(T) = A\,T^2 + B\,T + C$ $A = 3.847e\text{-}4$, $B = -0.1984$, $C = 26.54$	1E-9m^{2}s^{-1}	Regression from [2]
Vapor pressure, Vp	$f_{Vp}(X,T)$	Pa	Antoine equation with ideal solution assumption
Thermal conductivity, α	$f_\alpha(X,T)$	W m^{-1} K^{-1}	Eq. 13 in [1]
Specific heat, Cp	$f_{Cp}(X,T)$	kJ kg^{-1} K^{-1}	Eq. 9 in [1]
Specific heat of vaporization, $\widehat{H}_{vap}$	$f_{\widehat{H}_{vap}}(X,T)$	kJ kg^{-1}	Eq. 54 in [1] and ideal solution assumption
Specific enthalpy of liquid, $\widehat{H}_l$	$f_{\widehat{H}_l}(X,T)$	kJ kg^{-1}	Eq. 42 and 55 in [1]
Specific enthalpy of vapor, $\widehat{H}_v$	$f_{\widehat{H}_v}(T) = f_{\widehat{H}_l}(0,T) + f_{\widehat{H}_{vap}}(0,T)$	kJ kg^{-1}	

S.2) Modeling theory

The main manuscript provides equations for the governing mass and energy balance, basic water and heat flux, and process metrics (i.e. GOR, energy recovery, and LCOW). In this section, we provide the full details for modeling the governing differential equations; module conditions; mass and heat transfer; pressure drop; membrane and system metrics; and the heat exchangers (i.e. heater, chiller, and heat exchanger).

Governing differential equations

The governing mass and energy balance are shown in the main manuscript with equations 1-7. Figure S2 provides labels for the points of interest (e.g. hb for hot-side bulk, hm for hot-side membrane interface) and the heat fluxes used in those equations. While most MD models do not consider the nonconstant heat flux across the membrane and gap, we account for it in our model to appropriately account for salinity effects and close energy balances. Additional details on estimating the heat flux is provided in the heat transfer section below.

This system of differential equations is approximated with a finite difference method shown in Figure S3. Using this method, the state variables (i.e. mass flowrate, salt mass fraction, temperature) and process variables (e.g. water flux, heat flux, pressure loss, etc.) are estimated at nodes a long the membrane stage. The implementation of the finite difference method is included in SI Section 3.

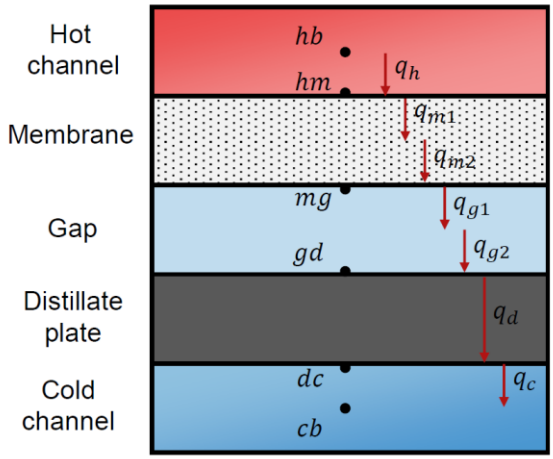

Figure S2. *Labels for points of interest and heat fluxes. Points of interest include: hot-side bulk (hb), hot-side membrane interface (hm), gap-side membrane interface (mg), gap-side distillate plate interface (gd), cold-side distillate plate interface (dc), and cold-side bulk (cb).*

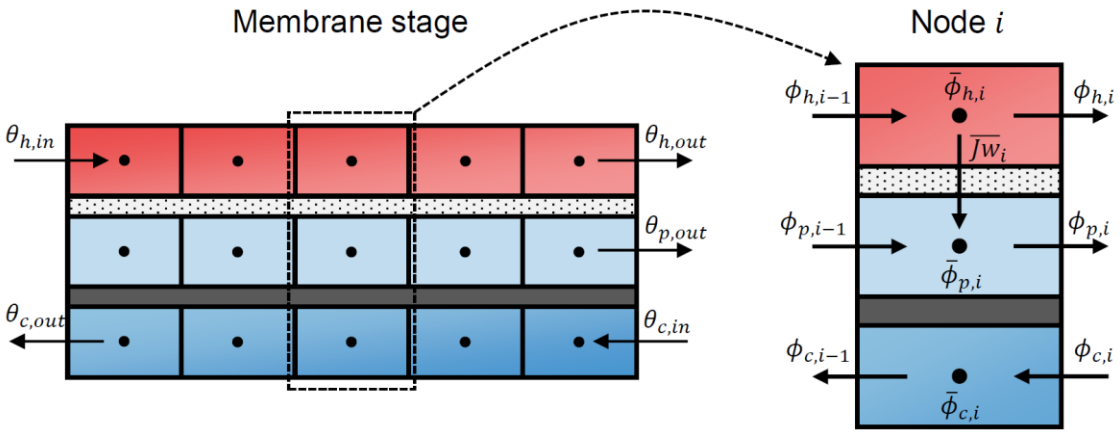

Figure S3. *Finite difference model for the membrane stage. θ are state variables (i.e. mass flowrate, salt mass fraction, and temperature) in and out of the stage for the hot-side (h), cold-side (c), and permeate (p). ϕ are internodal state variables and $\bar{\phi}$ are nodal variables that include both state and process variables (e.g. water flux, heat flux, pressure loss, dimensionless numbers, etc.)*

Module conditions

Many of the process relationships for MD depend on explicitly modeling the conditions in the membrane module. Specifically, the heat and mass transfer relationships are based on the following dimensionless numbers: Reynolds, Schmidt, Prandtl, Sherwood, and Nusselt. These 5 dimensionless numbers are determined with equations S1-5.

$$Re = \frac{\rho\, v\, d_h}{\mu} \quad \text{(S1)}$$

$$Sc = \frac{\mu}{\rho\, D} \quad \text{(S2)}$$

$$Pr = \frac{Cp\, \mu}{\alpha} \quad \text{(S3)}$$

$$Sh = a\, Re^b\, Sc^c \quad \text{(S4)}$$

$$Nu = a\, Re^b\, Pr^c \quad \text{(S5)}$$

Where Re is the Reynolds number, Sc is the Schmidt number, Pr is the Prandtl number, Sh is the Sherwood number, Nu is the Nusselt number, ρ is the density, v is the velocity, d_h is the hydraulic diameter, μ is the dynamic viscosity, D is the solute diffusivity, Cp is the specific heat capacity, α is the thermal conductivity, and a, b, and c are parameters that estimate the Sherwood and Nusselt number. In our work, we use Sherwood and Nusselt number relationships developed by Guillen and Hoek 2009 for mesh filled channels,[4] where a, b, and c are 0.46, 0.36, and 0.36, respectively. The hydraulic diameter of a mesh filled channel with a height of 2 mm, a filament of 1 mm, and void space of 90% is determined to be 2.57 mm as shown in Table 1 of the main manuscript. The equations to calculate the hydraulic diameter are included in the supporting information of our previous work.[3]

Mass transfer

Besides the advective mass transfer in the bulk fluids, there are two other mass transfer phenomena in the MD module. The first is the water flux across the membrane as shown in the main manuscript with equation 8. The second is the salt concentration polarization that arises from the solution flux and rejection of the solute at the membrane interface. The relationship describing the concentration polarization is shown in equation S6.

$$C_{hm} = C_{hb} \exp\left(\frac{Jw}{\rho_w\, k}\right) \tag{S6}$$

Where C is the concentration at the hot-side membrane interface (hm) and hot-side bulk (hb), Jw is the water flux, ρ_w is the density of water, and k is the mass transfer coefficient. The mass transfer coefficient, k, is determined from equation S7.

$$k = \frac{D}{d_h}\, Sh \tag{S7}$$

Heat transfer

The convective and conductive heat fluxes shown in Figure S2 are determined in equations S8-12. Additional relationships that connect the heat fluxes through energy balances at the interfaces are shown in equations S13-S18. This work considers nonconstant heat flux across the membrane (and the gap for air gap) that arises from the energy released as the water flux cools through the mediums as shown in equations S14 and S16b. Equations S15a, S16a, and S17a are for the gap types with condensation on the gap-side membrane interface (permeate and conductive gap) and equations S15b, S16b, and S17b are for the air gap with condensation on the gap-side distillate plate interface.

$$q_h = h_{conv,h}[T_{hb} - T_{hm}] \quad \text{(S8)}$$

$$\frac{1}{2}(q_{m1} + q_{m2}) = \frac{\alpha_m}{\delta_m}\left[T_{hm} - T_{mg}\right] \quad \text{(S9)}$$

$$\frac{1}{2}\left(q_{g1} + q_{g2}\right) = \frac{\alpha_g}{\delta_g}\left[T_{mg} - T_{gd}\right] \quad \text{(S10)}$$

$$q_d = \frac{\alpha_d}{\delta_d}\left[T_{gd} - T_{dc}\right] \quad \text{(S11)}$$

$$q_c = h_{conv,c}[T_{dc} - T_{cb}] \quad \text{(S12)}$$

$$q_h = q_{m1} + Jw\, f_{\hat{H}_{vap}}(X_{hm}, T_{hm}) \quad \text{(S13)}$$

$$q_{m1} + Jw\, f_{\hat{H}_v}(T_{hm}) = q_{m2} + Jw\, f_{\hat{H}_v}\left(T_{mg}\right) \quad \text{(S14)}$$

$$q_{m2} + Jw\, f_{\hat{H}_v}\left(T_{mg}\right) = q_{g1} + Jw\, f_{\hat{H}_l}\left(0, T_{mg}\right) \quad \text{(S15a)}$$

$$q_{m2} = q_{g1} \quad \text{(S15b)}$$

$$q_{g1} = q_{g2} \quad \text{(S16a)}$$

$$q_{g1} + Jw\, f_{\hat{H}_v}\left(T_{mg}\right) = q_{g2} + Jw\, f_{\hat{H}_v}\left(T_{gd}\right) \quad \text{(S16b)}$$

$$q_{g2} = q_d \quad \text{(S17a)}$$

$$q_{g2} + Jw\, f_{\hat{H}_{vap}}\left(0, T_{gd}\right) = q_d \quad \text{(S17b)}$$

$$q_d = q_c \quad \text{(S18)}$$

Where q is the heat flux and T is the temperature with their subscripts noted in Figure S2; h_{conv} is the convective heat transfer coefficient of the cold and hot-side; and α is the thermal conductivity and δ is the thickness of the membrane (m), gap (g), and distillate plate (d).

Pressure drop

We estimate the pressure drop across a membrane stage from friction with equation S19.

$$PD = PL_{avg}\, L \tag{S19}$$

Where PD is the pressure drop, PL_{avg} is the pressure loss per unit length, and L is the length of the membrane stage. The local pressure loss per unit length, PL, is determined in equation S20.

$$PL = \frac{F_f\, \rho\, v^2}{2\, d_h} \tag{S20}$$

Where F_f is the friction factor. We estimate the friction factor for the mesh filled channel using a relationship from Guillen and Hoek 2009,[4] as shown in equation S21.

$$F_f = 0.42 + \frac{189.3}{Re} \tag{S21}$$

Membrane and system metrics

In this section, we provide details on the key membrane and system performance metrics provided in Table 2 in the main manuscript including the average water flux, average thermal efficiency, average bulk temperature difference, GOR, energy recovery, and LCOW.

The basic calculations for water flux, GOR, energy recovery, and LCOW are provided in equations 8 and 11-13 in the main manuscript. The decrease in energy for the hot stream from the inlet to the outlet of membrane stage, ΔE_h, used to calculate the energy recovery, is determined with equations S22-24.

$$\Delta E_h = E_{h,mem,in} - E_{h,mem,out} \tag{S22}$$

$$E_{h,mem,in} = M_{h,mem,in}\, f_{\widehat{H}_l}\left(X_{h,mem,in}, T_{h,mem,in}\right) \tag{S23}$$

$$E_{h,mem,out} = M_{h,mem,out}\, f_{\widehat{H}_l}\left(X_{h,mem,out}, T_{h,mem,out}\right) \qquad \text{(S24)}$$

Where E_h is the energy content in the hot-side stream for the inlet (in) and outlet (out) in the membrane stage (mem).

The membrane thermal efficiency, TE, and bulk temperature difference, BTD, are determined in equations S25 and S26.

$$TE = \frac{Jw\, f_{\widehat{H}_v}(T_{mg})}{Jw\, f_{\widehat{H}_v}(T_{mg}) + q_{m2}} \qquad \text{(S25)}$$

$$BTD = T_{hb} - T_{cb} \qquad \text{(S26)}$$

The water flux, thermal efficiency, and bulk temperature difference are local variables and are determined across membrane stage at each node in the finite difference modeling. Their averages are reported to summarize the membrane and system performance.

Additional details on determining the LCOW are included in the costing section of the optimization model (SI Section S3).

Heat exchanger

As described in the main manuscript, the heat duties in the heat exchangers (including the heater and chiller) are determined with a log mean temperature difference model. The heat duty and log mean temperature difference are determined in equations S27-30. Where the log mean temperature difference is approximated with Chen's approximation in order to avoid the discontinuities within the domain range of the temperature variables.[5-6]

$$Q_{hxr} = U_{hxr}\, \Delta T_{LM}\, Area_{hxr} \qquad \text{(S27)}$$

$$\Delta T_{LM} = \frac{\Delta T_2 - \Delta T_1}{\ln\left(\frac{\Delta T_2}{\Delta T_1}\right)} \approx \left(\Delta T_1 \Delta T_2 \frac{(\Delta T_1 + \Delta T_2)}{2}\right)^{\frac{1}{3}} \quad \text{(S28)}$$

$$\Delta T_1 = T_{h,in} - T_{c,out} \quad \text{(S29)}$$

$$\Delta T_2 = T_{h,out} - T_{c,in} \quad \text{(S30)}$$

Where Q_{hxr} is the heat exchanger duty, U_{hxr} is the overall heat transfer coefficient, ΔT_{LM} is the log mean temperature difference, $Area_{hxr}$ is the heat exchanger surface area, ΔT_1 is the temperature difference on the hot inlet and cold outlet, ΔT_2 is the temperature difference on the hot outlet and cold inlet. The approach temperature (AT) is the minimum of these two differences, as shown in equation S31.

$$AT = \min(\Delta T_1, \Delta T_2) \quad \text{(S31)}$$

S.3) Optimization model

We formulate nonlinear programming models to minimize the LCOW of gap MD. As described in the main manuscript, we form different models for the discrete choices such as gap type. The models have minor modifications between them, which are noted in the equations. The base model is permeate/conductive gap MD with a looping configuration, while the differing equations for air gap is noted with a "b".

System-scale

System mass balance

The mass balance for the cold-side and hot-side mixer are provided in equations S32-S35. In our system configuration the feed combines with the cold-side loop in the cold-side mixer, and the pass-through stream combines with the hot-side loop in the hot-side mixer.

$$M_{c,mix,in} + M_f = M_{c,mix,out} \quad \text{(S32)}$$

$$M_{c,mix,in} X_{c,mix,in} + M_f\, X_f = M_{c,mix,out} X_{c,mix,out} \quad \text{(S33)}$$

$$M_{h,mix,in} + M_{pass} = M_{h,mix,out} \quad \text{(S34)}$$

$$M_{h,mix,in}\, X_{h,mix,in} + M_{pass}\, X_{pass} = M_{h,mix,out}\, X_{h,mix,out} \quad \text{(S35)}$$

Where M is the mass flowrate [kg/s] and X is the salt mass fraction [unitless] and are noted for the hot-side (h), cold-side (c), mixer (mix), feed (f), pass-through ($pass$) and whether it is the inlet (in) or outlet (out) of the process unit.

The mass balance for the cold-side and hot-side splitter (spl) are shown in equations S36-S41. Both splitters form the looping stream for their sides, as well as the pass-through stream for the cold-side and the disposal stream for the hot-side (d).

$$M_{c,spl,in} = M_{c,spl,out} + M_{pass} \quad \text{(S36)}$$

$$X_{c,spl,in} = X_{c,spl,out} \quad \text{(S37)}$$

$$X_{c,spl,in} = X_{pass} \quad \text{(S38)}$$

$$M_{h,spl,in} = M_{h,spl,out} + M_d \quad \text{(S39)}$$

$$X_{h,spl,in} = X_{h,spl,out} \quad \text{(S40)}$$

$$X_{h,spl,in} = X_d \quad \text{(S41)}$$

The overall mass balance for the membrane unit is shown in equations S42-S45. In gap MD, all the mass loss in the hot-side forms the permeate stream (p) and the cold-side does not gain or lose mass. We assume that no salt passes through the membrane.

$$M_{c,mem,in} = M_{c,mem,out} \quad \text{(S42)}$$

$$X_{c,mem,in} = X_{c,mem,out} \quad \text{(S43)}$$

$$M_{h,mem,in} = M_{h,mem,out} + M_p \quad \text{(S44)}$$

$$M_{h,mem,in}\, X_{h,mem,in} = M_{h,mem,out}\, X_{h,mem,out} \quad \text{(S45)}$$

There is no change in mass flowrate for the other process units, including the heat exchanger (hxr), heater (htr), and chiller (chl) as shown in equations S46 and S47.

$$M_{s,u,in} = M_{s,u,out} \quad \forall s \in (h,c), \forall u \in (hxr, htr, chl) \quad \text{(S46)}$$

$$X_{s,u,in} = X_{s,u,out} \quad \forall s \in (h,c), \forall u \in (hxr, htr, chl) \quad \text{(S47)}$$

System energy balance

The energy balance for the cold and hot-side mixer are shown in equations S48 and S49. Where the specific enthalpy of the solution is determined as a function of salt mass fraction and temperature ($f_{\hat{H}_l}$) with additional details provided in Table S1.

$$M_u\, f_{\hat{H}_l}(X_u, T_u) + M_f\, f_{\hat{H}_l}(X_f, T_f) = M_v\, f_{\hat{H}_l}(X_v, T_v)$$

$$u = (c, mix, in)\,, v = (c, mix, out) \quad \text{(S48)}$$

$$M_u\, f_{\hat{H}_l}(X_u, T_u) + M_{pass}\, f_{\hat{H}_l}(X_{pass}, T_{pass}) = M_v\, f_{\hat{H}_l}(X_v, T_v)$$

$$u = (h, mix, in)\,, v = (h, mix, out) \quad \text{(S49)}$$

The energy balance in the cold and hot-side splitter is shown in equations S50-S52. Since we assume there is no heat loss in the MD system, the splitter energy balance reduces to simply equating the temperatures of the inlet and outlet streams.

$$T_{s,spl,in} = T_{s,spl,out} \quad \forall s \in (h, c) \tag{S50}$$

$$T_{c,spl,in} = T_{pass} \tag{S51}$$

$$T_{h,spl,in} = T_d \tag{S52}$$

The energy balance for the membrane unit is provided in equation S53. Note that the subscripts u, v, w, and x are noted in the following line.

$$M_u f_{\hat{H}_l}(X_u, T_u) + M_v f_{\hat{H}_l}(X_v, T_v) = M_w f_{\hat{H}_l}(X_w, T_w) + M_x f_{\hat{H}_l}(X_x, T_x) + M_p f_{\hat{H}_l}(0, T_p)$$

$$u = (c, mem, in)\ , v = (h, mem, in), w = (c, mem, out), x = (h, mem, out) \tag{S53}$$

The energy balance for the heat exchanger, heater, and chiller are provided in equations S54-S57. Where Q is the heating or cooling duty [kW].

$$M_u f_{\hat{H}_l}(X_u, T_u) - Q_{hxr} = M_v f_{\hat{H}_l}(X_v, T_v) \quad u = (c, hxr, in), v = (c, hxr, out) \tag{S54}$$

$$M_u f_{\hat{H}_l}(X_u, T_u) + Q_{hxr} = M_v f_{\hat{H}_l}(X_v, T_v) \quad u = (h, hxr, in), v = (h, hxr, out) \tag{S55}$$

$$M_u f_{\hat{H}_l}(X_u, T_u) + Q_{htr} = M_v f_{\hat{H}_l}(X_v, T_v) \quad u = (h, htr, in), v = (h, htr, out) \tag{S56}$$

$$M_u f_{\hat{H}_l}(X_u, T_u) - Q_{chl} = M_v f_{\hat{H}_l}(X_v, T_v) \quad u = (c, chl, in), v = (c, chl, out) \tag{S57}$$

Heat duties

The heating or cooling duty of the heat exchanger, heater, and chiller are determined in equation S58.

$$Q_u = U_u \, \Delta T_{LM,u} \, Area_u \quad \forall u \in (hxr, htr, chl) \tag{S58}$$

Where U is the overall heat transfer coefficient (provided in table 1 in the main manuscript), ΔT_{LM} is the log mean temperature difference, $Area$ is the surface area of the heat exchanger. Equations S59-S61 determine the log mean temperature difference for the three process units and use Chen's approximation provided in equation S28.

$$\Delta T_{LM,hxr} = f_{\Delta \mathrm{T_{LM}}}\left(T_{c,hxr,in} - T_{h,hxr,out}, T_{c,hxr,out} - T_{h,hxr,in}\right) \quad \text{(S59)}$$

$$\Delta T_{LM,htr} = f_{\Delta \mathrm{T_{LM}}}\left(T_{s} - T_{h,htr,out}, T_{s} - T_{h,htr,in}\right) \quad \text{(S60)}$$

$$\Delta T_{LM,chl} = f_{\Delta \mathrm{T_{LM}}}\left(T_{c,chl,in} - T_{cool,out}, T_{c,chl,out} - T_{cool,in}\right) \quad \text{(S61)}$$

Where T_s is the temperature of the steam assumed to be 100 °C (373 K), and $T_{cool,in}$ and $T_{cool,out}$ is the temperature of the cooling water assumed to be 20 and 25 °C (293 and 298 K), respectively.

The mass flow rate of steam (M_s) is determined in equation S62. We assume that all the steam condenses and that the heat of vaporization provides all of the energy for the heater.

$$Q_{htr} = M_s \, f_{\hat{H}_{vap}}(0{,}373) \quad \text{(S62)}$$

System connections

The mass and energy balances described in the preceeding sections are around individual process units. This section connects the streams together to form the MD system. For the cold-side the connections are as follows: mixer to chiller, chiller to membrane, membrane to splitter, splitter to mixer. For the hot-side the connections are: mixer to heater, heater to membrane, membrane to splitter, splitter to mixer. These connections are enforced for all three state variables (mass flowrate, salt mass fraction, and temperature) with equations S63-S68.

$$Y_{c,mix,out} = Y_{c,chl,in} \quad \forall Y \in (M, X, T) \tag{S63}$$

$$Y_{c,chl,out} = Y_{c,mem,in} \quad \forall Y \in (M, X, T) \tag{S64}$$

$$Y_{h,mix,out} = Y_{h,htr,in} \quad \forall Y \in (M, X, T) \tag{S65}$$

$$Y_{h,htr,out} = Y_{h,mem,in} \quad \forall Y \in (M, X, T) \tag{S66}$$

$$Y_{s,mem,out} = Y_{s,spl,in} \quad \forall Y \in (M, X, T), \forall s \in (h, c) \tag{S67}$$

$$Y_{s,spl,out} = Y_{s,mix,in} \quad \forall Y \in (M, X, T), \forall s \in (h, c) \tag{S68}$$

Membrane stage-scale

As described in SI Section 2, we model the governing equations of the membrane stage with the finite difference method. This method explicitly determines the local variables along the membrane stage at a series of nodes, including mass flowrate, salt mass fraction, temperature, water flux, heat fluxes, pressure loss per unit length, vapor pressure, concentration, and dimensionless numbers. This detailed one-dimensional model accounts for pressure drop, concentration and temperature polarization, and the salinity and temperature dependence of solution properties.

Membrane stage connections

As shown in Figure S3, the finite difference model is based on internodal and nodal variables. There are N number of nodes and the node is noted with subscript i ($i1, i2, \ldots iN$). For inter-nodal variables, the subscript i denotes the variable to the right of node i and the variable to the left of the first node is noted with $i0$. These internodal and nodal variables are connected to the inlet and outlet variables for the membrane unit as shown in equations S69-S74.

$$Y_{h,i0} = Y_{h,mem,in} \quad \forall Y \in (M, X, T) \tag{S69}$$

$$Y_{h,iN} = Y_{h,mem,out} \quad \forall Y \in (M, X, T) \tag{S70}$$

$$Y_{p,i0} = 0 \quad \forall Y \in (M, X) \tag{S71}$$

$$Y_{p,iN} = Y_p \quad \forall Y \in (M, X, T) \tag{S72}$$

$$Y_{c,iN} = Y_{c,mem,in} \quad \forall Y \in (M, X, T) \tag{S73}$$

$$Y_{c,i0} = Y_{c,mem,out} \quad \forall Y \in (M, X, T) \tag{S74}$$

Membrane stage mass balance

The finite difference approximation of the mass balance for the hot-side, permeate, and cold-side (governing equations 1-4 in the main manuscript) are shown in equations S75-S79.

$$M_{h,i-1} = M_{h,i} + \frac{1}{N} Area_{mem} \overline{Jw_i} \quad \forall i, i \neq i0 \tag{S75}$$

$$M_{h,i} X_{h,i} = M_{h,i-1} X_{h,i-1} \quad \forall i, i \neq i0 \tag{S76}$$

$$M_{p,i-1} + \frac{1}{N} Area_{mem} \overline{Jw_i} = M_{p,i} \quad \forall i, i \neq i0 \tag{S77}$$

$$M_{c,i+1} = M_{c,i} \quad \forall i, i \neq iN \tag{S78}$$

$$X_{c,i+1} = X_{c,i} \quad \forall i, i \neq iN \tag{S79}$$

Where $Area_{mem}$ is the membrane area, Jw is the water flux, and N is the number of nodes. The bar above Jw denotes that the variable is a nodal variable.

Membrane stage energy balance

The finite difference approximation of the energy balance for the hot-side, permeate, and cold-side (governing equations 5-7 in the main manuscript) are shown in equations S80-S82. Where the difference in the condensation location for the air gap is corrected in equation S81b.

$$M_{h,i-1} f_{\hat{H}_l}\left(X_{h,i-1}, T_{h,i-1}\right) = M_{h,i} f_{\hat{H}_l}\left(X_{h,i}, T_{h,i}\right) + \frac{1}{N} Area_{mem}\, \overline{Jw_i}\, f_{\hat{H}_l}\left(\bar{X}_{hm,i}, \bar{T}_{hm,i}\right) + \bar{q}_{h,i} \quad \forall i, i \neq i0 \quad \text{(S80)}$$

$$M_{p,i-1} f_{\hat{H}_l}\left(0, T_{p,i-1}\right) + \frac{1}{N} Area_{mem}\, \overline{Jw_i}\, f_{\hat{H}_l}\left(0, \bar{T}_{mg,i}\right) + \bar{q}_{g1,i} = M_{p,i} f_{\hat{H}_l}\left(0, T_{p,i}\right) + \bar{q}_{g2,i} \quad \forall i, i \neq i0 \quad \text{(S81)}$$

$$M_{p,i-1} f_{\hat{H}_l}\left(0, T_{p,i-1}\right) + \frac{1}{N} Area_{mem}\, \overline{Jw_i}\, f_{\hat{H}_v}\left(0, \bar{T}_{gd,i}\right) + \bar{q}_{g2,i} = M_{p,i} f_{\hat{H}_l}\left(0, T_{p,i}\right) + \bar{q}_{d,i} \quad \forall i, i \neq i0 \quad \text{(S81b)}$$

$$M_{h,i+1} f_{\hat{H}_l}\left(X_{h,i+1}, T_{h,i+1}\right) + \bar{q}_{c,i} = M_{h,i} f_{\hat{H}_l}\left(X_{h,i}, T_{h,i}\right) \quad \forall i, i \neq iN \quad \text{(S82)}$$

Membrane mass transfer

The water flux and resulting concentration polarization are enforced in equation S83 and S84.

$$\overline{Jw_i} = B\left(\overline{Vp}_{hm,i} - \overline{Vp}_{mg,i}\right) \quad \forall i, i \neq i0 \quad \text{(S83)}$$

$$\bar{C}_{hm,i} = \bar{C}_{hb,i} \exp\left(\frac{\overline{Jw_i}}{\bar{k}_i}\right) \quad \forall i, i \neq i0 \quad \text{(S84)}$$

Where Vp is the vapor pressure, and C is the solute concentration at the hot-side membrane interface (hm) and bulk (hb) at node i.

Membrane heat transfer

The heat fluxes are determined with equations S85-S89. Where the notation is described in SI Section S2 and figure S2. The energy balance around the membrane and gap are provided in equation S90 and S91. Lastly, the energy balance at the interfaces are provided in equations S92-S95. In all of these relationships, the modifications for the air gap are noted with "b".

$$\bar{q}_{h,i} = \bar{h}_{h,i}\left[\bar{T}_{hb,i} - \bar{T}_{hm,i}\right] \quad \forall i, i \neq i0 \tag{S85}$$

$$\frac{1}{2}\left(\bar{q}_{m1,i} + \bar{q}_{m2,i}\right) = \frac{\alpha_m}{\delta_m}\left[\bar{T}_{hm,i} - \bar{T}_{mg,i}\right] \quad \forall i, i \neq i0 \tag{S86}$$

$$\frac{1}{2}\left(\bar{q}_{g1,i} + \bar{q}_{g2,i}\right) = \frac{\alpha_g}{\delta_g}\left[\bar{T}_{mg,i} - \bar{T}_{gd,i}\right] \quad \forall i, i \neq i0 \tag{S87}$$

$$\bar{q}_d = \frac{\alpha_d}{\delta_d}\left[\bar{T}_{gd,i} - \bar{T}_{dc,i}\right] \quad \forall i, i \neq i0 \tag{S88}$$

$$\bar{q}_c = \bar{h}_{c,i}\left[\bar{T}_{dc,i} - \bar{T}_{cb,i}\right] \quad \forall i, i \neq i0 \tag{S89}$$

$$\bar{q}_{m1,i} + \overline{Jw}_i\, f_{\hat{H}_v}\left(\bar{T}_{hm,i}\right) = \bar{q}_{m2,i} + \overline{Jw}_i\, f_{\hat{H}_v}\left(\bar{T}_{mg,i}\right) \quad \forall i, i \neq i0 \tag{S90}$$

$$\bar{q}_{g1,i} = \bar{q}_{g2,i} \quad \forall i, i \neq i0 \tag{S91}$$

$$\bar{q}_{g1,i} + \overline{Jw}_i\, f_{\hat{H}_v}\left(\bar{T}_{mg}\right) = \bar{q}_{g2,i} + \overline{Jw}_i\, f_{\hat{H}_v}\left(\bar{T}_{gd}\right) \quad \forall i, i \neq i0 \tag{S91b}$$

$$\bar{q}_{h,i} = \bar{q}_{m1,i} + \overline{Jw}_i\, f_{\hat{H}_{vap}}\left(\bar{X}_{hm,i}, \bar{T}_{hm,i}\right) \quad \forall i, i \neq i0 \tag{S92}$$

$$\bar{q}_{m2,i} + \overline{Jw}_i\, f_{\hat{H}_v}\left(\bar{T}_{mg,i}\right) = \bar{q}_{g1,i} + \overline{Jw}_i\, f_{\hat{H}_l}\left(0, \bar{T}_{mg,i}\right) \quad \forall i, i \neq i0 \tag{S93}$$

$$\bar{q}_{m2,i} = \bar{q}_{g1,i} \quad \forall i, i \neq i0 \tag{S93b}$$

$$\bar{q}_{g2,i} = \bar{q}_{d,i} \quad \forall i, i \neq i0 \tag{S94}$$

$$\bar{q}_{g2,i} + \overline{Jw}_i\, f_{\hat{H}_{vap}}\left(0, \bar{T}_{gd,i}\right) = \bar{q}_{d,i} \quad \forall i, i \neq i0 \tag{S94b}$$

$$\bar{q}_{d,i} = \bar{q}_{c,i} \quad \forall i, i \neq i0 \tag{S95}$$

Nodal variables

Several nodal variables are determined with equations S96-S107, including the mass flow rate (M), bulk salt mass fraction (X_{hb}, X_{cb}), bulk fluid temperature (T_{hb}, T_{cb}), membrane interface salt concentration (C_{hm}), membrane interface salt mass fraction (X_{hm}), bulk salt concentration (C_{hb}), vapor pressure (Vp), density (ρ), viscosity (μ), diffusivity (D), thermal conductivitiy (α), and specific heat (Cp). Additional details on the functions used to calculate the solution properties are provided in Table S1.

$$\bar{M}_{s,i} = \frac{1}{2}\left(M_{s,i} + M_{s,i-1}\right) \quad \forall s \in (h,c), \forall i, i \neq i0 \tag{S96}$$

$$\bar{X}_{sb,i} = \frac{1}{2}\left(X_{s,i} + X_{s,i-1}\right) \quad \forall s \in (h,c), \forall i, i \neq i0 \tag{S97}$$

$$\bar{T}_{sb,i} = \frac{1}{2}\left(T_{s,i} + T_{s,i-1}\right) \quad \forall s \in (h,c), \forall i, i \neq i0 \tag{S98}$$

$$\bar{C}_{hm,i} = f_C\left(\bar{X}_{hm,i}\right) \quad \forall i, i \neq i0 \tag{S99}$$

$$\bar{C}_{hb,i} = f_C\left(\bar{X}_{hb,i}\right) \quad \forall i, i \neq i0 \tag{S100}$$

$$\overline{Vp}_{hm,i} = f_{Vp}\left(\bar{X}_{hm,i}, \bar{T}_{hm,i}\right) \quad \forall i, i \neq i0 \tag{S101}$$

$$\overline{Vp}_{mg,i} = f_{Vp}\left(0, \bar{T}_{mg,i}\right) \quad \forall i, i \neq i0 \tag{S102}$$

$$\bar{\rho}_{s,i} = f_\rho\left(\bar{X}_{sb,i}, \bar{T}_{sb,i}\right) \quad \forall s \in (h,c), \forall i, i \neq i0 \tag{S103}$$

$$\bar{\mu}_{s,i} = f_\mu\left(\bar{X}_{sb,i}, \bar{T}_{sb,i}\right) \quad \forall s \in (h,c), \forall i, i \neq i0 \tag{S104}$$

$$\bar{D}_{s,i} = f_D\left(\bar{X}_{sb,i}, \bar{T}_{sb,i}\right) \quad \forall s \in (h,c), \forall i, i \neq i0 \tag{S105}$$

$$\bar{\alpha}_{s,i} = f_{\alpha}\left(\bar{X}_{sb,i}, \bar{T}_{sb,i}\right) \quad \forall s \in (h,c), \forall i, i \neq i0 \tag{S106}$$

$$\overline{Cp}_{s,i} = f_{Cp}\left(\bar{X}_{sb,i}, \bar{T}_{sb,i}\right) \quad \forall s \in (h,c), \forall i, i \neq i0 \tag{S107}$$

The local dimensionless numbers are determined with equations S108-S112. Note the Reynolds number calculation has been rearranged for the variables considered in the model and the Sherwood and Nusselt number calculations are from Guillen and Hoek 2009.[4]

$$\overline{Re}_{s,i} = \frac{\bar{M}_{s,i}\, d_h}{\bar{\mu}_{s,i}\, H\, W\, \varepsilon} \quad \forall s \in (h,c), \forall i, i \neq i0 \tag{S108}$$

$$\overline{Sc}_{s,i} = \frac{\bar{\mu}_{s,i}}{\bar{\rho}_{s,i}\, \bar{D}_{s,i}} \quad \forall s \in (h,c), \forall i, i \neq i0 \tag{S109}$$

$$\overline{Pr}_{s,i} = \frac{\overline{Cp}_{s,i}\, \bar{\mu}_{s,i}}{\bar{\alpha}_{s,i}} \quad \forall s \in (h,c), \forall i, i \neq i0 \tag{S110}$$

$$\overline{Sh}_{s,i} = 0.46\, \overline{Re}_{s,i}^{\,0.36}\, \overline{Sc}_{s,i}^{\,0.36} \quad \forall s \in (h,c), \forall i, i \neq i0 \tag{S111}$$

$$\overline{Nu}_{s,i} = 0.46\, \overline{Re}_{s,i}^{\,0.36}\, \overline{Pr}_{s,i}^{\,0.36} \quad \forall s \in (h,c), \forall i, i \neq i0 \tag{S112}$$

Where H is the height of the channel (2 mm), d_h is the hydraulic diameter (calculated as 2.57 mm), ε is the void space of the channel (assumed to be 90%), and W is the width of the stage.

The mass transfer coefficient (k), convective heat transfer coefficient (h), and pressure loss per unit length (PL) are determined in equations S113-S115. Note that the pressure loss per unit length calculation has been rearranged for the variables considered in the model.

$$\bar{k}_{s,i} = \frac{\bar{D}_{s,i}}{d_h}\, \overline{Sh}_{s,i} \tag{S113}$$

$$\bar{h}_{s,i} = \frac{\bar{\alpha}_{s,i}}{d_h}\, \overline{Nu}_{s,i} \tag{S114}$$

$$\overline{PL}_{s,i} = \frac{f_F(\overline{Re}_{s,i})\overline{M}_{s,i}{}^2}{2\, d_h\, \overline{\rho}_{s,i}\, H^2\, W^2\, \varepsilon^2} \quad \text{(S115)}$$

Membrane stage metrics

The metrics for the membrane stage including local thermal efficiency (TE), average thermal efficiency (TE_{avg}), average water flux (Jw_{avg}), and pressure drop (PD) are calculated in equations S116-S119.

$$\overline{TE}_i = \frac{\overline{Jw}_i\, f_{\hat{H}_v}(T_{mg,i})}{\overline{Jw}_i\, f_{\hat{H}_v}(T_{mg,i}) + q_{m2,i}} \quad \forall i \quad \text{(S116)}$$

$$TE_{avg} = \frac{1}{N}\sum_i \overline{TE}_i \quad \text{(S117)}$$

$$Jw_{avg} = \frac{1}{N}\sum_i \overline{Jw}_i \quad \text{(S118)}$$

$$PD_s = \frac{L}{N}\sum_i \overline{PL}_{s,i} \quad \forall s \in (h,c) \quad \text{(S119)}$$

Where L is the length of the membrane stage.

System metrics

The metrics for the MD system including annual water production (AWP), gained output ratio (GOR), energy recovery (ER), and power of the pump (Pow_{pmp}) are determined in equations S120-S124.

$$AWP = M_p\, LF \left[\frac{3600\ s}{h}\right]\left[\frac{8760\ h}{y}\right] \quad \text{(S120)}$$

$$GOR = \frac{Q_{htr}}{M_p f_{\hat{H}_{vap}}(X_f, T_f)} \quad \text{(S121)}$$

$$ER = 1 - \frac{Q_{htr}}{\Delta E_h} \quad \text{(S122)}$$

$$\Delta E_h = M_{h,mem,in}\, f_{\widehat{H}_l}\left(X_{h,mem,in}, T_{h,mem,in}\right) - M_{h,mem,out}\, f_{\widehat{H}_l}\left(X_{h,mem,out}, T_{h,mem,out}\right) \quad \text{(S123)}$$

$$Pow_{pmp} = \frac{1}{\eta_{pmp}} \frac{M_{h,mem,in}}{f_{\rho}\left(X_{h,mem,in}, T_{h,mem,in}\right)} \sum_s PD_s \quad \text{(S124)}$$

Where LF is the load factor (assumed to be 85%), and η_{pmp} is the pump efficiency (assumed to be 75%).

System constraints

There are two constraints that are imposed on the overall system. The first is the water recovery (Rw) is fixed to a user specified value as shown in equation S125. The second is the maximum temperature of the streams is fixed to a maximum value (90 °C/363 K in the base case), as shown in constraint S126.

$$Rw = \frac{M_p}{M_f\left(1 - X_f\right)} \quad \text{(S125)}$$

$$T_{s,p,u} \leq T_{max} \quad \forall s \in (h,s), \forall p \in (mix, mem, hxr, htr, chl, spl), \forall u \in (in, out) \quad \text{(S126)}$$

Determining costs

As described in the main manuscript, we determine the costs of the MD system by estimating the capital investment and operating cost.

The equipment cost of the membrane, heat exchanger, heater, and chiller units are determined in equations S127 and S128. The total capital cost (includes indirect capital, installation, and siting) is estimated based on the total capital cost factor F_{TCC} as shown in S129. The total capital cost factor is assumed to be 2 and is presented in Table 1 in the main manuscript.

$$CC_{mem} = VC_{mem}\, Area_{mem} \quad \text{(S127)}$$

$$CC_{hxr} = VC_{hxr}(Area_{hxr} + Area_{htr} + Area_{chl}) \quad \text{(S128)}$$

$$TCC = F_{TCC}(CC_{mem} + CC_{hxr}) \quad \text{(S129)}$$

The operating cost for electricity, heating, and chilling demand are determined in equations S130-S132. Where the variable cost (VC) of each component is provided in Table 1 of the main manuscript. The operating cost for membrane replacement is determined in equation S133, where the membrane replacement rate (RR_{mem}) is assumed to be 20% and is provided in Table 1 of the main manuscript.

$$OC_{elec} = VC_{elec} Pow_{pmp}\ LF\ \left[\frac{3600\ s}{h}\right]\left[\frac{8760\ h}{y}\right] \quad \text{(S130)}$$

$$OC_{htr} = VC_{htr}\ M_s\ LF\ \left[\frac{3600\ s}{h}\right]\left[\frac{8760\ h}{y}\right] \quad \text{(S131)}$$

$$OC_{chl} = VC_{chl}\ Q_{chl}\ LF\ \left[\frac{3600\ s}{h}\right]\left[\frac{8760\ h}{y}\right] \quad \text{(S132)}$$

$$OC_{mem} = RR_{mem}\ CC_{mem} \quad \text{(S133)}$$

The operating cost for maintenance, labor, and chemicals is indirectly estimated from the total capital cost with a factor (F_{MLC}), as shown in equation S134. The maintenance, labor, and chemical factor is assumed to be 3% as provided in Table 1 in the main manuscript.

$$OC_{MLC} = F_{MLC}\ TCC \quad \text{(S134)}$$

The total operating cost is the sum of the 5 considered operating costs, as shown in equation S135.

$$TOC = OC_{elec} + OC_{mem} + OC_{htr} + OC_{chl} + OC_{MLC} \quad \text{(S135)}$$

The annualized operating cost (AOC) of the MD system is determined in equation S136. Where F_{CF} is the capital annualization factor and is assumed to be 10% and provided in Table 1 in the main manuscript. The levelized cost of water ($LCOW$) is determined in equation S137 and is the objective of the nonlinear programming model

$$AOC = TOC + F_{CF}\, TCC \tag{S136}$$

$$LCOW = \frac{AOC}{AWP} \tag{S137}$$

S.4) Effect of salinity on membrane distillation performance

Figure S.4.1 presents the local water flux and thermal efficiency for membrane distillation as a function of salinity and bulk temperature difference for air, permeate, and conductive gap. The figure demonstrates the decrease in water flux and thermal efficiency with increasing salinity at the membrane interface.

While lower gap thermal conductivities generally have lower water flux and thermal efficiency for a given bulk temperature difference and salinity, the trend is not always true between the air and permeate gap. At low salinities, air gap has higher water flux and thermal efficiency than permeate gap, despite having a lower thermal conductivity. However, water flux and thermal efficiency have a significantly higher decline with increased salinity for the air gap. We observe this non-intuitive result because not only do the gaps have different thermal conductivities but also the location of the condensation changes (i.e. interface at the distillate plate for air gap and membrane for permeate gap).

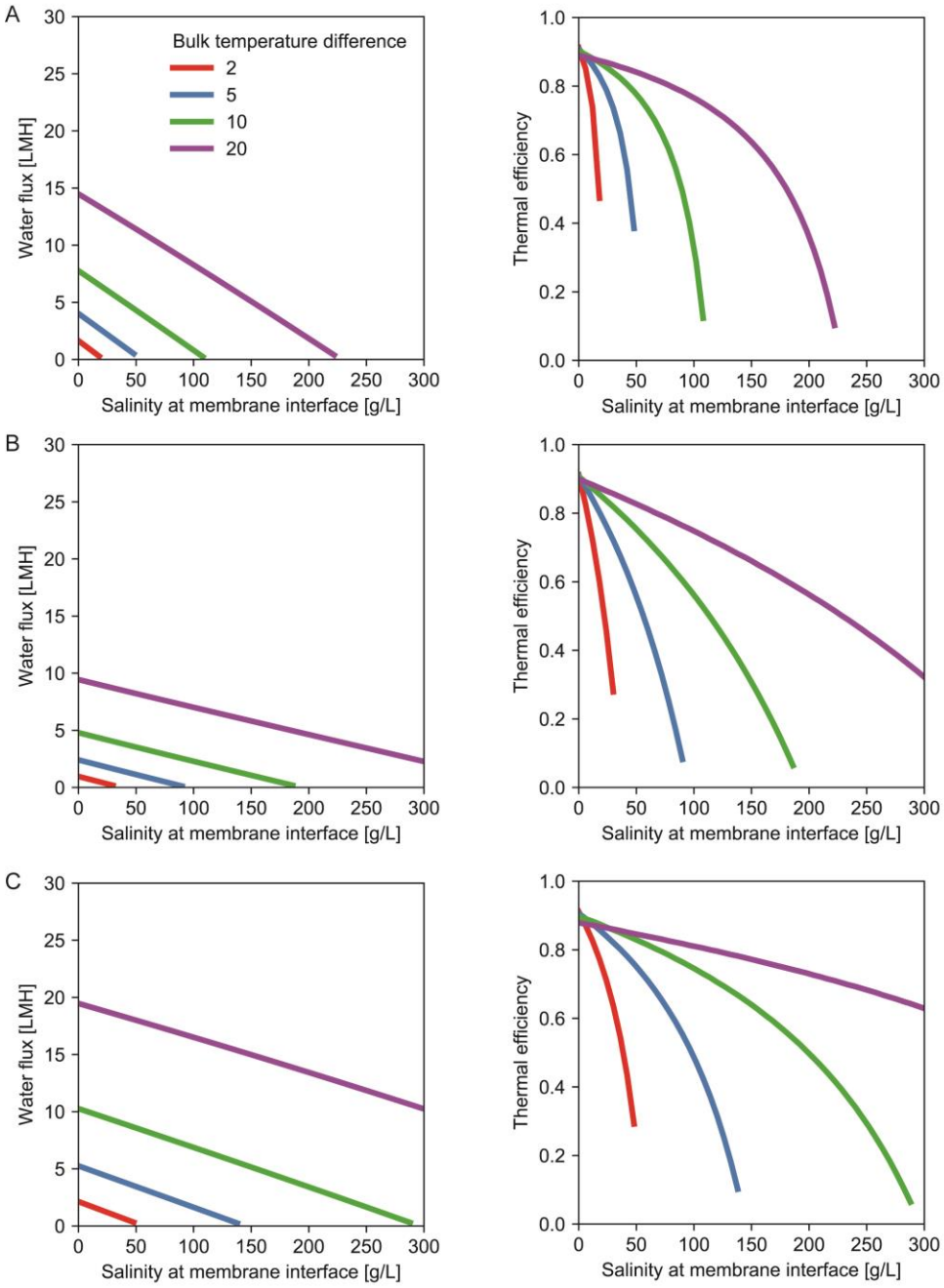

Figure S4. Local water flux and thermal efficiency as a function of salinity and bulk temperature difference for air (A), permeate (B), and conductive gap (C). The temperature of the hot bulk is 70 °C, the heat transfer coefficient for the hot and cold-side are 2 kW/m^2-K, and the thermal conductivities of the air, permeate, and conductive gap are 0.2, 0.6, and 10 W/m-K.

S.5) Outcome metrics for simulated maps

Figure S5 provides the cost optimal outcome metrics for conductive gap MD across the same simulated feed concentrations and water recoveries as presented in the main manuscript.

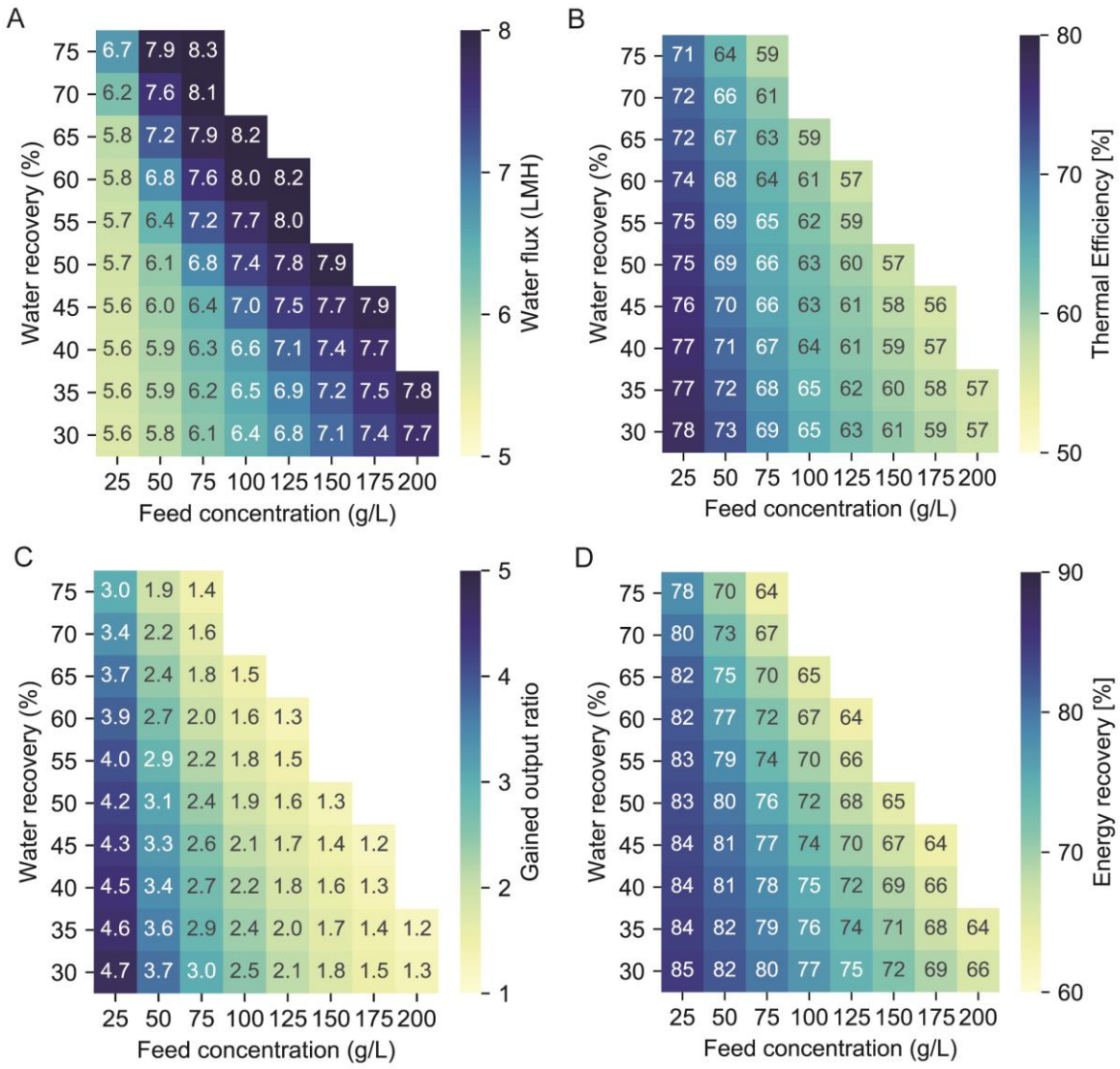

Figure S5. Cost optimal water flux (A), thermal efficiency (B), gained output ratio (C) and energy recovery (D) for conductive gap MD across a range of feed concentrations and water recoveries.

S.5) Additional sensitivity analysis

Figure S6 presents the cost sensitivity for the convective heat transfer coefficient, friction factor, membrane thickness, and module cost.

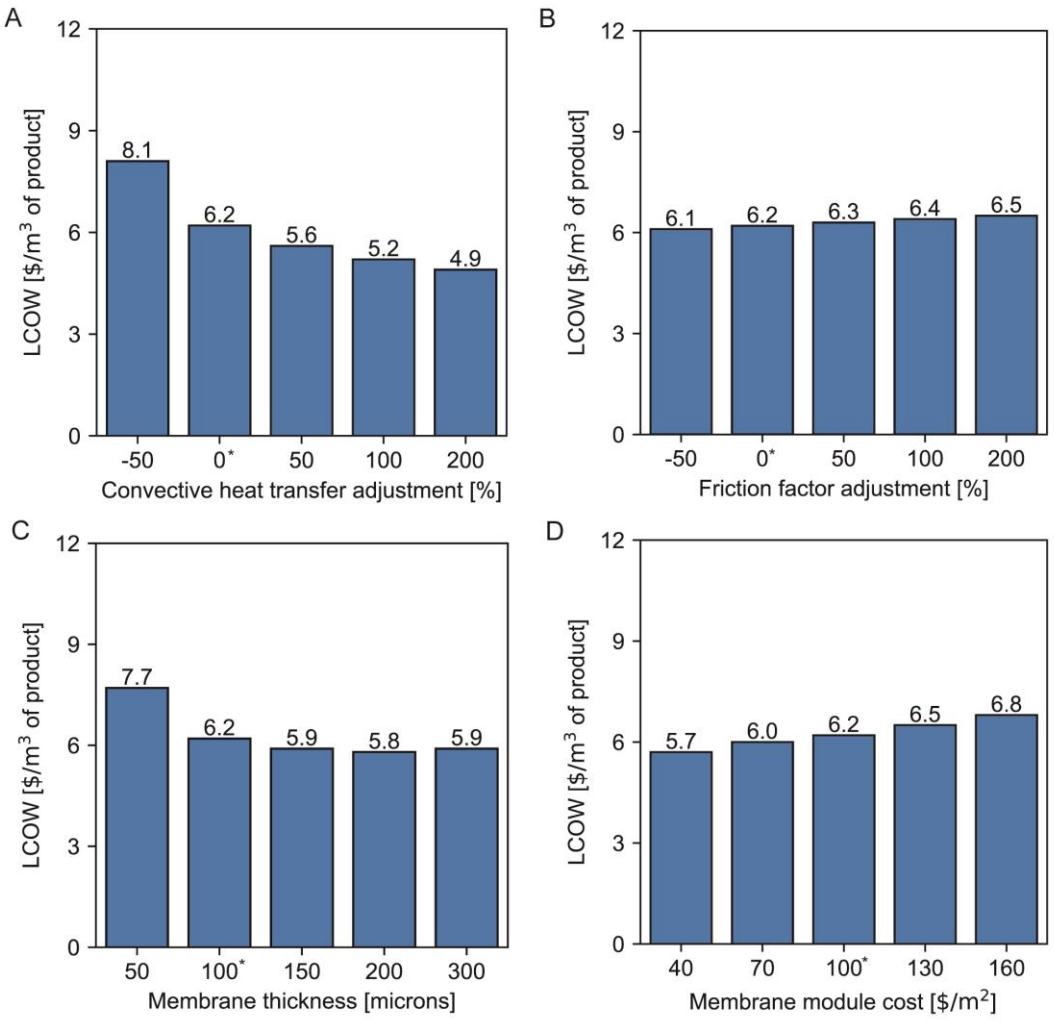

Figure S6. Conductive gap MD cost sensitivity for convective heat transfer coefficient (A), friction factor (B), membrane thickness (C), and membrane module cost (D).

References

1. Sharqawy, M. H.; Lienhard, J. H.; Zubair, S. M., Thermophysical properties of seawater: a review of existing correlations and data. *Desalination and Water Treatment* **2010,** *16* (1-3), 354-380.

2. Fell, C. J. D.; Hutchiso.Hp, Diffusion Coefficients for Sodium and Potassium Chlorides in Water at Elevated Temperatures. *Journal of Chemical and Engineering Data* **1971,** *16* (4), 427-&.

3. Bartholomew, T. V.; Mauter, M. S., Computational framework for modeling membrane processes without process and solution property simplifications. *Journal of Membrane Science* **2019,** *573*, 682-693.

4. Guillen, G.; Hoek, E. M. V., Modeling the impacts of feed spacer geometry on reverse osmosis and nanofiltration processes. *Chemical Engineering Journal* **2009,** *149* (1), 221-231.

5. Chen, J., Comments on improvements on a replacement for the logarithmic mean. *Chemical Engineering Science* **1987,** *42* (10), 2488-2489.

6. Mistry, M.; Misener, R., Optimising heat exchanger network synthesis using convexity properties of the logarithmic mean temperature difference. *Computers & Chemical Engineering* **2016,** *94*, 1-17.

APPENDIX E: SUPPORTING INFORMATION FOR CHAPTER 6 - MULTI-OBJECTIVE OPTIMIZATION MODEL FOR MINIMIZING COST AND ENVIRONMENTAL IMPACT IN SHALE GAS WATER AND WASTEWATER MANAGEMENT

Supporting Information Summary:
The supporting information contains details for 1) model formulation; 2) emission coefficient estimation; 3) AP2 modeling parameters, 4) case study details; 5) additional case study results.

This supporting information is 41 pages long and contains 7 figures (Fig. S1-S7), 6 Tables (Table S1- Table S6), and 55 equations (Eq. S1-S44).

1. Model Formulation

The model is an extension from Yang et al (2015) and uses similar notation and formulation.[1] The revised formulation changes the freshwater and wastewater transportation and wastewater storage and incorporates the HHE impacts associated with the water management activities.

1.1 Hydraulic Fracturing Schedule.

Wellpad s is fractured exactly once at a given date t, and is represented in constraint (1).

$$\sum_t y_{st} = 1 \quad \forall s \tag{1}$$

where y_{st} is a binary variable that indicates the fracturing starting date t for well pad s.

Only one wellpad can be fractured at a time, and the backward aggregation constraint (2) ensures there is no over-lap between wellpad operations.

$$\sum_s \sum_{t'=t-SFL_s-STC+1}^{t} y_{st'} \leq 1 \quad \forall t \tag{2}$$

where SFL_s is the duration of the hydraulic fracturing for wellpad s in weeks. STC is the transition time required to move the frac crew from wellpad s to the next wellpad. When considering wellpad availability, y_{st} was fixed to zero for the unavailable times.

1.2 Water use:

The total weekly frac fluid requirement for wellpad s is shown in the constraint (3).

$$f_{st} = \sum_{t'=t-SFL_s+2}^{t} SDW y_{st'} + \sum_{t'=t-SFL_{sk}+1} SLW_s y_{st'} \quad \forall s, \forall t \tag{3}$$

where f_{st} is a continuous variable that defines the frac fluid use at each wellpad. It is assumed that the weekly number of stages and volume of frac fluid per stage is set, therefore each fracturing week has a constant frac fluid use, represented by SDW. In the last week of fracturing

a wellpad, the remaining stages for the wellpad may be less than the weekly number of stages, SLW_s is the water requirement for the remaining stages.

The frac fluid can be composed of freshwater and wastewater as shown in constraint (4).

$$f_{st} = f_{st}^{FW} + f_{st}^{WW} \quad \forall s, \forall t \tag{4}$$

where f_{st}^{FW} and f_{st}^{WW} are continuous variables for the freshwater and wastewater use at time t and wellpad s, respectively.

The wastewater is assumed to be limited by a percentage of frac fluid, represented by ρ^{WW}, and is represented by constraint (5).

$$\rho^{WW} f_{st} \geq f_{st}^{WW} \quad \forall s, \forall t \tag{5}$$

1.3 Freshwater:

Freshwater can be transported by either pipe or truck. The continuous variable $f_{uu'ct}^{FW,Pipe}$ represents the flow of freshwater transported using pipeline of type c from location u to u' at time t. The set of u represents the locations of all wellpads, sources of freshwater, impoundments, treatment facilities, and disposal wells which are given by the indices s, o, p, q, and d, respectively. The allowable freshwater pipeline connections are known beforehand and is represented by set $DFP_{uu'}$. The continuous variable $f_{uu't}^{FW,Trk}$ represents the flow of freshwater transport using trucks from location u to u' at time t. The allowable freshwater trucking is known beforehand and represented by set $DFT_{uu'}$.

The freshwater balance at each wellpad includes the freshwater piped in and out, trucked in and out, and used on the wellpad and is shown in constraint (6).

$$\sum_{u\in DFP_{us}} \sum_c f_{usct}^{FW,Pipe} + \sum_{u\in DFT_{us}} f_{ust}^{FW,Trk} = f_{st}^{FW} + \sum_{u\in DFP_{su'}} \sum_c f_{su'ct}^{FW,Pipe} + \sum_{u\in DFT_{su'}} f_{su't}^{FW,Trk} \quad \forall s, \forall t \tag{6}$$

The freshwater balance at each impoundment includes the freshwater piped in and out, trucked in and out, and volume change at the impoundment and is shown in constraint (7).

$$\sum_{u\in DFP_{up}} \sum_c f_{upct}^{FW,Pipe} + \sum_{u\in DFT_{up}} f_{upt}^{FW,Trk} + v_{pt-1}^{IP} = \sum_{u\in DFP_{pu'}} \sum_c f_{pu'ct}^{FW,Pipe} + \sum_{u\in DFT_{pu'}} f_{pu't}^{FW,Trk} + v_{pt}^{IP} \quad \forall p, \forall t \tag{7}$$

where the volume stored at impoundments at any time t is represented by the continuous variable v_{pt}^{IP}.

1.4 Wastewater production:

The wastewater flow back for each wellpad is represented by the continuous variable f_{st}^{FB} and is determined in constraint (8).

$$f_{st}^{FB} = \sum_{t''\in t-t'+1} \sum_{t'} SF_{st''}^{FB} y_{st'} \tag{8}$$

where SF_{st}^{FB} is a parameter that indicates flowback flow rate after fracture start date.

1.5 Wastewater handling:

Wastewater can be handled in three ways: onsite treatment, central treatment, or disposal. Onsite treated wastewater occurs on each wellpad, therefore does not require transportation. Centrally treated wastewater requires transportation via wastewater pipelines or trucks to the CWT. However, for wastewater to be piped it must be treated onsite first. Wastewater destined for disposal can only be trucked. Therefore there are three immediate options for wastewater: treated

onsite f_{st}^{OT}, trucked to central treatment, $f_{sqt}^{WW,Trk}$, and trucked to disposal $f_{sdt}^{WW,Trk}$. The wastewater handling is shown in constraint (9).

$$f_{st}^{FB} = f_{st}^{OT} + \sum_q f_{sqt}^{WW,Trk} + \sum_d f_{sdt}^{WW,Trk} \quad \forall s, \forall t \tag{9}$$

Onsite treated wastewater can be either stored, piped, or trucked. The storage and transport methods are directly linked with the wastewater balance on each wellpad shown in constraint (10).

$$f_{st}^{OT} + \sum_{u \in DWP_{us}} \sum_c f_{usct}^{WW,Pipe} + \sum_{u \in DWP_{us}} f_{ust}^{WW,Trk} + v_{st-1}^{WT} = \sum_{u \in DWP_{su'}} \sum_c f_{su'ct}^{WW,Pipe} + \sum_{u \in DWT_{su'}} f_{su't}^{WW,Trk} + v_{st}^{WT} \quad \forall s, \forall t \tag{10}$$

where $f_{uu'ct}^{WW,Pipe}$ and $f_{uu't}^{WW,Trk}$ are the continuous variables for piping and trucking, respectively, with similar notation as the freshwater equivalents. DWP and DWT are the sets of allowable wastewater piping and trucking, respectively. The volume of the wastewater tank is represented by v_{st}^{WT}.

Wastewater can be transported and stored at impoundments. The wastewater balance at each impoundment is shown in constraint (11).

$$\sum_{u \in DWP_{up}} \sum_c f_{upct}^{WW,Pipe} + \sum_{u \in DWP_{up}} f_{upt}^{WW,Trk} + v_{pt-1}^{WT} = \sum_{u \in DWP_{pu'}} \sum_c f_{pu'ct}^{WW,Pipe} + \sum_{u \in DWT_{pu'}} f_{pu't}^{WW,Trk} + v_{pt}^{WT} \quad \forall p, \forall t \tag{11}$$

where the volume of wastewater tank is represented by v_{pt}^{WT}.

The amount of wastewater that is centrally treated is represented by the continuous variable f_{qt}^{CT}. Wastewater can be transported to central treatment by pipeline or truck to central treatment, and the aggregated flow is shown in constraint (11).

$$f_{qt}^{CT} = \sum_{u \in DWT_{uq}} \sum_{c} f_{uqt}^{WW,Trk} + \sum_{u \in DWP_{uq}} \sum_{c} f_{uqct}^{WW,Pipe} \quad \forall t, \forall q \tag{11}$$

Central treatment can produce desalinated water that can be recycled or discharged. f_{qt}^{RCT} is a continuous variable indicating the amount of desalinated water that is recycled, and its use is limited by constraint (12).

$$\eta_q f_{qt}^{CT} \geq f_{qt}^{RCT} \quad \forall t, \forall q \tag{12}$$

where parameter η_q is the recovery of the central treatment.

The recycled desalinated water can be transported by either pipeline or truck and is described by constraint (13).

$$f_{qt}^{RCT} = \sum_{u \in DFP_{qu}} \sum_{c} f_{quct}^{FW,Pipe} + \sum_{u \in DFT_{qu}} f_{qut}^{FW,Trk} \quad \forall t, \forall q \tag{13}$$

The final wastewater handling method is disposal and the amount of wastewater that is disposed of is represented by the continuous variable f_t^{DP}. There are two methods of wastewater disposal, it can be either trucked directly from the wellpad or from the central treatment concentrated waste stream as shown in constraint (14).

$$f_t^{DP} = \sum_{u \in DWT_{ud}} f_{udt}^{WW,Trk} + \sum_{q} \left(1 - \eta_q\right) f_{qt}^{CT} \quad \forall t \tag{14}$$

1.6 Capacity constraints

The capacity constraint for the impoundments is shown in constraint (15).

$$CP_p^{min,IP} \leq l_p^{IP} \leq CP_p^{max,IP} \quad \forall p \tag{15}$$

where the capacity of the impoundment is l_p^{IP}, and the lower and upper capacity limits are $CP_p^{min,IP}$ and $CP_p^{max,IP}$, respectively.

The volume of freshwater in an impoundment is constrained by the impoundment capacity, as shown in constraint (16).

$$v_{pt}^{IP} \leq l_p^{IP} \quad \forall p, \forall t \tag{16}$$

The capacity constraint for the frac tank on each wellpad is shown in constraint (17).

$$l_s^{FT} \geq CP_p^{min,FT} \quad \forall s, \forall t \tag{17}$$

where the capacity of the frac tank is l_s^{FT}, and the minimum capacity limit is $CP_p^{min,FT}$.

It was assumed that wastewater tanks on wellpads cannot be used until fracturing on the wellpad has started. Constraint (18) is a big M constraint to ensure that the volume in wastewater tanks is zero before the start of fracturing, and is relaxed after fracturing has started.

$$v_{st}^{WWT} \leq M \sum_{t'}^{t} y_{st'} \quad \forall s, \forall t \tag{18}$$

1.7 Pipeline constraints.

Pipeline variables $y_{uu'c}^{FW,Pipe}$ and $y_{uu'c}^{WW,Pipe}$ are binary variables that indicate whether pipeline of type c between u and u' is used. Constraints (19) and (20) ensure that the pipelines flow in both directions.

$$y_{uu'c}^{FW,Pipe} = y_{u'uc}^{FW,Pipe} \; \forall uu' \in DFP_{uu'}, \forall c \tag{19}$$

$$y_{uu'c}^{WW,Pipe} = y_{u'uc}^{WW,Pipe} \; \forall uu' \in DWP_{uu'}, \forall c \tag{20}$$

Constraints (21) and (22) ensure that only one type of pipeline is used.

$$\sum_c y_{uu'c}^{FW,Pipe} \leq 1 \;\; \forall uu' \in DFP_{uu'} \tag{21}$$

$$\sum_c y_{uu'c}^{WW,Pipe} \leq 1 \;\; \forall uu' \in DWP_{uu'} \tag{22}$$

Constraints (23) and (24) ensure that the pipeline flow capacities are bounded by the upper flow, UF.

$$f_{uu'ct}^{FW,Pipe} \leq y_{uu'c}^{FW,Pipe} UF \quad \forall uu' \in DFP_{uu'}, \forall c, \forall t \tag{23}$$

$$f_{uu'ct}^{WW,Pipe} \leq y_{uu'c}^{WW,Pipe} UF \quad \forall uu' \in DWP_{uu'}, \forall c, \forall t \tag{24}$$

1.8 Leased pipelines

If one of the pipeline types may be leased then each discrete rental period is represented by a separately indexed c and the associated set is represented by LPC. The t indices associated with the time period for each c of the leased pipelines is represented by set LPT. For example, in the case study there are two piping types: purchased buried pipelines (c1) and leased overland pipelines (c2… c13), where c2-c13 is set LPC. There are 12 c indexes associated with the leased pipeline because the pipeline may be leased quarterly over the 3 year time horizon for a total of 12 time periods. The first quarter leased pipeline (c2) is associated with t indices t1-t13 and is a

part of the set LPT. Constraints (21b) and (22b) replace constraints (21) and (22) to allow for the leasing of a pipeline.

$$\sum_{c' \notin LPC} y_{uu'c'}^{FW,Pipe} + y_{uu'c}^{FW,Pipe} \leq 1 \quad \forall uu' \in DFP_{uu'}, \forall c \in LPC \tag{21b}$$

$$\sum_{c' \notin LPC} y_{uu'c'}^{WW,Pipe} + y_{uu'c}^{WW,Pipe} \leq 1 \quad \forall uu' \in DWP_{uu'}, \forall c \in LPC \tag{22b}$$

Furthermore, a leased pipeline cannot be used during the time period it is not in use, as shown in the additional constraints (23b) and (24b). Note (23) and (24) are still necessary.

$$f_{uu'ct}^{FW,Pipe} \leq 0 \quad \forall uu' \in DFP_{uu'}, \forall ct \notin LPT_{ct} \tag{23b}$$

$$f_{uu'ct}^{WW,Pipe} \leq 0 \quad \forall uu' \in DWP_{uu'}, \forall ct \notin LPT_{ct} \tag{24b}$$

1.9 Financial constraints

Revenue is calculated by constraint (25).

$$Revenue = \sum_s \sum_t P_{st} y_{st} \tag{25}$$

where parameter P_{st} is the revenue of natural gas over the three year time horizon if wellpad s was fractured at date t. This parameter can be calculated from the expected gas production of each wellpad and the sales price of natural gas, both of which are time dependent.

Withdrawal costs include the cost of withdrawing water from the freshwater source and is shown in constraint (26).

$$Cost^{Wdl} = \sum_o \sum_{u' \in DFP_{uu'}} \sum_c \sum_t OC_o^{FW} f_{ou'ct}^{FW,Pipe} + \sum_o \sum_{u' \in DFT_{uu'}} \sum_t OC_o^{FW} f_{ou't}^{FW,Trk} \tag{26}$$

where OC_o^{FW} is the cost of freshwater withdrawal per unit of freshwater.

Freshwater transport includes the cost of pumping water, capital cost of pipelines, and costs of trucking and is shown in constraint (27) and (28). The pumping cost coefficient, OC^{Pipe}, is based on amount of pumped water, pipe capital cost coefficient, IC_c^{Pipe}, is based on pipe distance (note IC_c^{Pipe} can account for leased pipelines), and the trucking cost coefficient, OC^{Trk}, is based on the amount and distance of the trucked water.

$$Cost^{FW,Pipe} = \sum_u \sum_{u' \in DFP_{uu'}} \sum_c \sum_t OC^{Pipe} f_{uu'ct}^{FW,Pipe} Dist_{uu'} +$$

$$\sum_u \sum_{u' \in DFP_{uu'}} \sum_c IC_c^{Pipe} y_{uu'c}^{FW,Pipe} \frac{1}{2} Dist_{uu'} \quad (27)$$

$$Cost^{FW,Trk} = \sum_u \sum_{u' \in DFT_{uu'}} \sum_t OC^{Trk} f_{uu't}^{FW,Trk} Dist_{uu'} \quad (28)$$

Wastewater transport includes the cost of pumping water, capital cost of pipelines, and costs of trucking and is shown in constraints (29) and (30). The pumping cost coefficient, OC^{Pipe}, is based on amount of pumped water, the pipe capital cost coefficient, IC_c^{Pipe}, is based on pipeline distance, and the trucking cost coefficient, OC^{Trk}, is based on the amount and distance of trucked water.

$$Cost^{WW,Pipe} = \sum_u \sum_{u' \in DWP_{uu'}} \sum_c \sum_t OC^{Pipe} f_{uu'ct}^{WW,Pipe} Dist_{uu'} +$$

$$\sum_u \sum_{u' \in DWP_{uu'}} \sum_c IC^{Pipe} y_{uu'c}^{FW,Pipe} \frac{1}{2} Dist_{uu'} \quad (29)$$

$$Cost^{WW,Trk} = \sum_u \sum_{u' \in DWT_{uu'}} \sum_t OC^{Trk} f_{uu't}^{WW,Trk} Dist_{uu'} +$$

$$\sum_q \sum_d \sum_t OC^{Trk} f_{tq}^{CT} (1 - \eta_q) Dis_{qd} \quad (30)$$

Impoundment costs, $Cost^{IP}$, include a base capital cost, $IC^{IP,Base}$, and an incremental cost, $C^{IP,Inc}$, based on capacity as shown in constraint (31).

$$Cost^{IP} = \sum_p IC^{IP,Base} + IC^{IP,Inc} l_p^{IP} \quad (31)$$

Frac tank costs, $Cost^{FT}$, include costs of frac tanks on each wellpad, and is estimated by a frac tank cost coefficient, IC^{FT}, based on frac tank capacity as shown in constraint (32).

$$Cost^{FT} = \sum_s IC^{FT} l_s^{FT} \quad (32)$$

Wastewater tanks costs, $Cost^{WWT}$, include costs for both wellpads and impoundments, and is estimated by a wastewater tank cost coefficient, IC^{WWT}, based on wastewater volume and time stored as shown in constraint (33).

$$Cost^{WWT} = \sum_s \sum_t IC^{WWT} v_{st}^{WWT} + \sum_p \sum_t IC^{WWT} v_{pt}^{WWT} \quad (33)$$

Onsite treatment costs, $Cost^{OT}$, are estimated by an onsite treatment cost coefficient, OC^{OT}, based on the amount of onsite treatment as shown in constraint (34).

$$Cost^{OT} = \sum_s \sum_t OC^{OT} f_{st}^{OT} \quad (34)$$

Central treatment costs, $Cost^{CT}$, are estimated by an central treatment cost coefficient, OC^{CT}, based on the amount of central treatment as shown in constraint (35).

$$Cost^{CT} = \sum_q \sum_t OC_q^{CT} f_{qt}^{CT} \quad (35)$$

Disposal costs, $Cost^{DP}$, are estimated by disposal cost coefficient, OC^{DP}, base on the amount of disposal as shown in constraint (36).

$$Cost^{DP} = \sum_t OC^{DP} f_t^{DP} \quad (36)$$

The total cost, $Cost^{total}$, is shown in constraint (37)

$$Cost^{total} = (Cost^{Wdl} + Cost^{FW,Pipe} + Cost^{FW,Trk} + Cost^{WW,Pipe} + Cost^{WW,Trk} + Cost^{IP} + Cost^{WWT} + Cost^{OT} + Cost^{CT}) \quad (37)$$

1.10 Environmental constraints

The air emissions of NH_3, NO_x, $PM_{2.5}$, SO_2, VOC, CO_2e were estimated for the modeled water management shale gas activities. Emission coefficients, m_e, where subscript e represents the set of pollutatnts, were used to relate the main decision variable of each activity to the associated air emissions and the calculations are shown below. Refer to SI section 2, for the emission coefficients used in the case study.

The emissions from fresh and wastewater storage, M_e^{Sto}, includes freshwater impoundments, frac tanks, and wastewater tanks on wellpads and impoundments as shown in constraint (38).

$$M_e^{Sto} = \sum_p m_e^{Sto,IP} l_p^{IP} + \sum_s m^{Sto,FT} l_s^{FT} + \sum_s \sum_t m_e^{Sto,WWT} v_s^{WWT} + \sum_p \sum_t m_e^{Sto,WWT} v_p^{WWT} \quad \forall e \ (38)$$

where the emission coefficient for freshwater impoundments, $m_e^{Sto,IP}$, is based on capacity. The emission coefficient for frac tank storage, $m_e^{Sto,FT}$, is based on capacity. The emission coefficient for wastewater storage, $m_e^{Sto,WWT}$, is based on volume and storage time.

Constraint (38) relates the storage emissions to the main decision variables, which is the consistent format throughout the environmental constraint section. However, since all of the emission coefficients are estimated through EIO-LCA and the capacity of freshwater impoundments is not proportional to the costs, the impoundment emission coefficient, $m_e^{Sto,IP}$, cannot be determined. Therefore the application of constraint (38) takes on the form of (38b),

where the EIO emission coefficient, $m_e^{Sto,EIO}$, relates the cost of the impoundments to the associated emissions.

$$M_e^{Sto} = m_e^{Sto,EIO} Cost^{IP} + \sum_s m^{Sto,FT} l_s^{FT} + \sum_s \sum_t m_e^{Sto,WWT} v_s^{WWT} +$$

$$\sum_p \sum_t m_e^{Sto,WWT} v_p^{WWT} \quad \forall e \qquad (38b)$$

The emissions from fresh and wastewater piping, M_e^{Pipe}, includes emissions due to building and operating the pipeline, as shown in constraint (39).

$$M_e^{Pipe} = + \sum_u \sum_{u'} \sum_c m_e^{PipeC} (y_{uu'c}^{FW,Pipe} + y_{uu'c}^{WW,Pipe}) \frac{1}{2} Dist_{uu'} +$$

$$\sum_u \sum_{u'} \sum_c \sum_t m_e^{PipeO} (f_{uu'ct}^{FW,Pipe} + f_{uu'ct}^{WW,Pipe}) Dist_{uu'} \quad \forall e \qquad (39)$$

where the emission coefficient for building the pipeline, m_e^{PipeC}, is based on pipeline distance. The emission coefficient for operating the pipeline, m_e^{PipeC}, is based on the amount of water and the distance transported.

The emissions from fresh and wastewater trucking, M_e^{Trk}, are estimated by the trucking air emission coefficient, m_e^{Trk}, based on the amount of water and distance transported as shown in constraint (40).

$$M_e^{Trk} = \sum_u \sum_{u'} \sum_t m_e^{Trk} (f_{uu't}^{FW,Trk} + f_{uu't}^{WW,Trk}) Dis_{uu'} + \sum_d \sum_q \sum_t m_e^{Trk} f_{qt}^{CT} (1 - \eta) Dis_{qd} \quad \forall e \ (40)$$

The emissions from onsite treatment, M_e^{OT}, are estimated by the onsite treatment air emission coefficient, m_e^{OT}, based on the amount of wastewater treated onsite as shown in constraint (41).

$$M_e^{OT} = \sum_s \sum_t m_e^{OT} f_{st}^{OT} \quad \forall e \qquad (41)$$

The emissions from central treatment, M_e^{CT}, are estimated by the central treatment air emission coefficient, m_e^{CT}, based on the amount of wastewater treated centrally as shown in constraint (42).

$$M_e^{CT} = \sum_q \sum_t m_e^{CT} f_{qt}^{CT} \quad \forall e \tag{42}$$

The emissions from disposal, M_e^{DP}, are estimated by the disposal air emission coefficient, m_e^{DP}, based on the amount of disposed water as shown in constraint (43).

$$M_e^{DP} = \sum_t m_e^{DP} f_t^{DP} \quad \forall e \tag{43}$$

The human health and environmental (HHE) damages associated with the air emissions, $Cost^{HHE}$, are determined as shown in constraint (44).

$$Cost^{HHE} = \sum_e CE_e (M_e^{sto} + M_e^{Pipe} + M_e^{Trk} + M_e^{OT} + M_e^{CT} + M_e^{DP}) \tag{44}$$

where CE_e is the HHE damage coefficient for pollutant e, as shown in Table 1 in the article.

1.11 Objective

The scheduling problem objective was to maximize the difference between the revenue from gas sales and the water management costs.

$$max. objective \; = \; Revenue - \; Cost^{total}$$

Once the above schedule was determined and set, three other objectives were used.

Financial Cost optimization: $min. objective = Cost^{total}$

HHE cost optimization: $min. objective = Cost^{HHE}$

Financial and HHE cost optimization: $min. objective = Cost^{total} + Cost^{HHE}$

2. Emission Coefficient Estimation

The direct and indirect air emissions of NH_3, NO_x, $PM_{2.5}$, SO_2, VOC, CO_2e were investigated for the modeled water management shale gas activities: storage, onsite treatment, central treatment, disposal, piping, and trucking. The direct emissions from trucking and central treatment were estimated. The other direct and all indirect emissions are estimated using economic input-output life cycle analysis that estimate emissions based on the economic sector and cost of the activity. In general, the economic sectors chosen for each activity was based on the work by Jiang et al.[2]

2.1 Trucking

The direct emissions associated with trucking, $m_e^{Trk,Dir}$, were estimated using the U.S. Environmental Protection Agency's Motor Vehicle Emissions Simulator (MOVES), the SIMAPRO LCA calculator, and NREL's emission calculator. Beher and Mauter (2015) provided parameter inputs for all three tools in the article's supplementary information and the results are summarized in the table T2.[3] Both Simapro and NREL base estimates on the weight of the vehicle, so an empty and full tanker resulted in different emissions. A full tanker was assumed to hold 120 bbl of water. Additionally, it is assumed that the transport of fresh and wastewater requires a round trip with one leg being full and the other being empty. Therefore, the average of the empty and full truck load emission coefficient for Simapro and NREL was used. There are some gaps of pollutant estimates: all three tools did not estimate NH_3, Simapro did not estimate VOCs, and NREL did not estimate $PM_{2.5}$ and CO_2e. In order to estimate these emissions, ratios from the EIO-LCA US 2002 model were used.[4] For $1 million of activity in the "Truck Transportation" the sector's emissions was 8.2, 0.023, 8.6, 0.43, 0.18, 0.92, 990 metric tons.[4] The NH_3 emissions were estimated by taking the mean of the NH_3 estimates from the ratios of the other emissions as shown in equation (1).

$$m_b = \frac{1}{n}\sum_a \frac{M_b^{eio}}{M_a^{eio}} m_a \quad (1)$$

where m_b is the estimated emission coefficient for pollutant b. The subscript a references the pollutants in which the emission coefficient, m_a, is already determined and n is the number of pollutants in set a. M_b^{eio} and M_a^{eio} are the EIO-LCA emissions associated with the pollutant for $1 million in activity.

Simapro's VOC emission were also estimated by equation (1). NREL's PM2.5 emissions were estimated by using the ratio between PM2.5 and PM10 emissions. NREL's CH_4 and CO_2 emission coefficients were converted into CO_2e through using the 100 year global warming potential of 34 for CH_4 and adding it to the estimated CO_2 emission coefficient.[5]

The three emission coefficients from the tools are in units of mass of pollutant per total distance traveled $[\frac{g}{mile}]$ and were converted to units of mass of pollutant per amount of water per distance traveled $[\frac{g}{mile-bbl}]$ by dividing the tool's emission coefficient by the 120 bbl capacity of the truck and multiplying by 2 to account for the round trip. The $m_e^{Trk,Dir}$ for MOVES, Simapro, and NREL are shown in table S1, and the average of the three is determined to be direct emission estimate, $m_e^{Trk,Dir}$.

The indirect emissions associated with trucking, $m_e^{Trk,Ind}$, were estimated with EIO-LCA through equation (2) and (3).

$$m_e^{Trk,Ind,EIO} = m_e^{Trk,Tot,EIO} - m_e^{Trk,Dir,EIO} \quad (2)$$

where $m_e^{Trk,Ind,EIO}$ is the indirect emission from the "Truck Transportation" sector in units of $\left[\frac{Tonne}{\$M}\right]$. The $m_e^{Trk,Tot,EIO}$ and $m_e^{Dir,EIO}$ are the total and direct emission from the "Truck

transportation" sector in units of $\left[\frac{Tonne}{\$M}\right]$, which are both readily available from the EIO-LCA tool.[4] The indirect emissions for $1 million of activity was 0.023, 2.3, 0.12, 9.72, 0.53, and 410 metric tons for NH_3, NO_x, $PM_{2.5}$, SO_2, VOC, CO_2e, respectively.

$$m_e^{Ind} = m_e^{Ind,EIO} * Cost\ Coefficient \quad (3)$$

where m_e^{Ind} is the trucking indirect emissions for in units of $\left[\frac{g}{bbl-mile}\right]$ and is shown in Table S1. The trucking $Cost\ Coefficient$ is 0.053 $\left[\frac{\$}{bbl-mile}\right]$.

Combining the indirect and the direct emissions results in the total emissions, m_e^{Trk}, as shown in Table S1.

Table S1. *Trucking emission coefficients.*

	units	NH_3	NO_x	$PM_{2.5}$	SO_2	VOC	CO_2e
MOVES	$\frac{g}{mile}$	no est	8.1E-03	3.7E-04	2.3E-05	3.7E-04	1.2E+00
$m_e^{Trk,Dir,MOVES}$	$\frac{g}{mile-bbl}$	3.9E-04	2.2E-01	9.9E-03	6.2E-04	9.9E-03	3.2E+01
NREL	$\frac{g}{mile}$	no est	2.3E-01	7.0E-04	7.6E-03	1.1E-02	3.5E+01
$m_e^{Trk,Dir,NREL}$	$\frac{g}{mile-bbl}$	1.3E-02	6.2E+00	1.9E-02	2.0E-01	3.0E-01	9.3E+02
SimaPro	$\frac{g}{mile}$	no est	4.1E-05	6.4E-04	3.3E-03	no est	2.9E+00
$m_e^{Trk,Dir,SimaPro}$	$\frac{g}{mile-bbl}$	2.6E-03	1.1E-03	1.7E-02	8.9E-02	1.1E-01	7.8E+01
$m_e^{Trk,Dir}$	$\frac{g}{mile-bbl}$	5.3E-03	2.1E+00	1.5E-02	9.8E-02	1.4E-01	3.5E+02
$m_e^{Trk,Ind}$	$\frac{g}{mile-bbl}$	1.2E-03	1.2E-01	6.6E-03	3.8E-02	2.8E-02	2.2E+01
m_e^{Trk}	$\frac{g}{mile-bbl}$	6.5E-03	2.3E+00	2.2E-02	1.4E-01	1.7E-01	3.7E+02

2.2 Central treatment

The direct emissions associated with central treatment, $m_e^{CT,Dir}$, were estimated through the electrical energy consumption. It was assumed that central treatment technology was mechanical vapor recompression (MVC). Al-Karaghouli and Kazmerski estimated the energy demand of MVC to be 7-12 $\frac{kwh}{m^3}$ and the average of 9.5 $\frac{kwh}{m^3}$ was used for this study.[6] The emission coefficients for electricity use was estimated using the data from the EIA for state electricity

production, EPA's National Emissions Inventory (NEI) for criteria air pollutants, and EPA's eGRID for greenhouse gas emissions. [7-9] The EIA provides estimates for the amount of electricity produced in the state of Pennsylvania in 2011 and 2012.The NEI provides NH_3, NO_x, $PM_{2.5}$, SO_2, and VOC emission estimates for the Pennsylvania electricity production in 2011. The EPA 2012 eGRID provides estimates for greenhouse gas emissions of CO_2, CH_4, and N_2O for the state of Pennsylvania in 2012. The greenhouse gas emissions were converted to CO_2e emission, by using the 100 year global warming potential of 34 and 298 for CH_4 and N_2O, respectively.[5] The electricity emission coefficients were calculated using equation (4).

$$m_e^{elec} = \frac{M_e^{elec}}{E_e^{elec}} \quad (4)$$

where m_e^{elec} is the electricity emission coefficient in units of $\left[\frac{g}{kwh}\right]$. The M_e^{elec} and E_e^{elec} are the estimated mass of emissions and electricity production for the state of Pennsylvania. The calculated electricity emission coefficient is shown in Table S2.

The direct emissions associated with the energy use of central treatment, $m_e^{CT,Dir}$, can be calculated by equation (5).

$$m_e^{CT,Dir} = m_e^{elec} r^{CT} \quad (5)$$

where $m_e^{CT,Dir}$ is the direct emission coefficient for central treatment and r^{CT} is the energy use of central treatment, 9.5 $\frac{kwh}{m^3}$. The calculated direct emission coefficient for central treatment is shown in Table S2.

The indirect emissions associated with central treatment, $m_e^{CT,Ind}$, was estimated in the same way as trucking. However, the economic sector and cost coefficient was different. The "Water,

Sewage and other systems" sector was used, which resulted in the indirect emissions from $1 million of activity was 0.041, 2.1, 0.82, 0.29, 2.84, 0.57, 1200 metric tons for NH_3, NO_x, $PM_{2.5}$, SO_2, VOC, CO_2e, respectively.[4] The $Cost\ Coefficient$ of central treatment for the case study is 5.5 $\frac{\$}{bbl}$. The calculated indirect emission coefficient is shown in Table S2. The sum of indirect and direct emission coefficient is the total emission coefficient, m_e^{CT}, as shown in table S2.

Table S2. *Central treatment emission coefficient*

	units	NH_3	NO_x	$PM_{2.5}$	SO_2	VOC	CO_2e
NEI	$\frac{g}{kWh}$	0.002	0.58	0.05	1.3	0.003	no est
eGRID2012	$\frac{g}{kWh}$	no est	0.54	no est	1.1	no est	484
m_e^{elec}	$\frac{g}{kWh}$	0.002	0.56	0.05	1.2	0.003	484
$m_e^{CT,Dir}$	$\frac{g}{bbl}$	0.01	3.09	0.25	6.73	0.02	2660
$m_e^{CT,Ind}$	$\frac{g}{bbl}$	0.23	11.6	1.6	15.6	3.1	6413
m_e^{CT}	$\frac{g}{bbl}$	0.24	14.7	1.8	22.3	3.2	9073

2.3 Storage, Piping, On-Site Treatment, and Disposal

The total emissions associated with storage, piping, on-site treatment, and disposal were estimated using EIO-LCA. The total emission coefficient can be calculated by equation (6).

$$m_e = m_e^{EIO} * Cost\ Coefficient \quad (6)$$

Where m_e is the total emission coefficient, m_e^{EIO} is the total emissions from economic input output, and the $Cost\ Coefficient$ relates the decision variables of an activity to the cost. The total emissions from economic input output for the associated economic sectors are shown in table S3. The $Cost\ Coefficient$, economic sector, and total emission coefficient for storage, piping, onsite treatment and disposal are shown in Table S4 and S5.

2.3.1 Storage: There are 3 costs for storage: freshwater impoundment, frac tanks, and wastewater storage. The associated emission coefficients for the frac tanks, m_e^{FT}, and wastewater storage, m_e^{WWT},are shown in Table S5. Since the impoundment cost is not proportional to the capacity of the impoundment, the emission coefficient based on the decision variable could not be calculated. Instead the emissions from impoundments were estimated by using the EIO emission coefficient and the cost of the impoundment.

2.3.2 Piping: There are 2 costs for piping: the capital costs of building a pipeline and the operating costs of pumping. The emission coefficient for the capital costs, m_e^{PipeC}, depend on whether the pipeline is buried (c1) or overland (c2+) and is shown in Table S5. The emission coefficient for the operating costs of pumping, m_e^{PipeO}, is shown in Table S5.

2.3.3 Onsite treatment: There is one cost associated with onsite treatment and the emission coefficient, m_e^{OT}, is shown in Table S5.

2.3.4 Disposal: There is one cost associated with disposal and the emission coefficient, m_e^{DP}, is shown in Table S5.

Table S3. *The economic input-output emission coefficient for the associated economic sectors.*

Sector/Cost	Units	NH_3	NO_x	$PM_{2.5}$	SO_2	VOC	CO_2e
Oil and gas extraction (1)	$\frac{tonne}{\$M}$	0.023	3.84	0.145	1.23	4.38	1990
Pipeline transportation (2)	$\frac{tonne}{\$M}$	0.039	2.7	0.17	1.4	4.9	4400
Support activities for oil and gas operations (3)	$\frac{tonne}{\$M}$	0.084	6.3	0.58	1.9	1.3	649

Table S4. *The cost coefficient and economic sector for activities estimated from EIO-LCA. Refer to table S3 for the numbering of the economic sectors.*

Activity	Emission Coefficient	Cost Coefficient	Units	Sector
Storage	m_e^{FT}	87	$\frac{\$}{bbl}$	1
Storage	m_e^{WWT}	0.525	$\frac{\$}{bbl-week}$	1
Piping	$m_e^{PipeC,c1}$	320	$\frac{\$K}{mile}$	2
Piping	$m_e^{PipeC,c2-c13}$	71.5	$\frac{\$K}{mile}$	2
Piping	m_e^{PipeO}	0.005	$\frac{\$}{bbl-mile}$	2
Onsite Treatment	m_e^{OT}	3	$\frac{\$}{bbl}$	3
Disposal	m_e^{DP}	1.5	$\frac{\$}{bbl}$	3

Table S5. *The cost coefficient and economic sector for activities estimated from EIO-LCA. Refer to table S3 for the numbering of the economic sectors.*

Activity	Emission Coefficient	Units	CO	NH3	NOx	PM2.5	SO2	VOC	CO2e
Storage	m_e^{FT}	$\frac{g}{bbl}$	4.5E+2	2.0E+0	3.3E+2	1.3E+1	1.1E+2	3.8E+2	1.7E+05
Storage	m_e^{WWT}	$\frac{g}{bbl-we}$	2.7E+0	1.2E-2	2.0E+0	7.6E-2	6.5E-1	2.3E+0	1.0E+03
Piping	$m_e^{PipeC,c1}$	$\frac{g}{mile}$	1.1E+6	1.2E+4	8.7E+5	5.5E+4	4.5E+5	1.6E+6	1.4E+09
Piping	$m_e^{PipeC,c2-c}$	$\frac{g}{mile}$	2.5E+5	2.8E+3	1.9E+5	1.2E+4	1.0E+5	3.5E+5	3.1E+08
Piping	m_e^{PipeO}	$\frac{g}{bbl-mi}$	1.7E-2	2.0E-4	1.4E-2	8.6E-4	7.1E-3	2.4E-2	2.2E+01
Onsite Treatment	m_e^{OT}	$\frac{g}{bbl}$	2.5E+1	2.5E-1	1.9E+1	1.7E+0	5.7E+0	3.8E+0	1.9E+03
Disposal	m_e^{DP}	$\frac{g}{bbl}$	1.2E+1	1.3E-1	9.5E+0	8.7E-1	2.8E+0	1.9E+0	9.7E+02

3. AP2 Modeling Parameters

The damages of air emissions associated with human health and environmental damages were estimated by using the AP2 model and value of a statistical life of $6.2 million in 2000 $ (8.5 million in 2015 $, calculated from the Bureau of Labor Statistics [http://www.bls.gov/data/inflation_calculator.htm]). The model reports county-level damages for marginal emissions at ground-level sources, low-stack heights, medium stack heights, tall-stack heights, and very-tall-stack heights.[10] Since all of the investigated activities emit at heights lower than the low-stack height, only the ground-level source data was used. The damages for the Pennsylvania counties were isolated and averaged to represent the damages across the state. The resulting HHE cost are shown in table S6.

Table S6. *Marginal air emission damages estimated from the AP2 model.*

Pollutant	Cost ($2015/metric ton)
NH_3	131,000
NO_x	5,540
$PM_{2.5}$	118,000
SO_2	44,500
VOCs	11,300

4. Case Study Details

The case study was adapted from Yang et al. (2015), which was based on the previous development of wellpads in the Utica play.[1] Yang et al. provided information on the spatial distribution of the wellpads, impoundments, water sources, central treatment, and disposal wells and the availability, frac fluid demand, gas production, and wastewater production for each wellpad. The major changes from the case study presented in Yang et al. are as follows:

1. The removal of the interruptible water sources and the addition of one uninterruptible source
2. The placement of an impoundment in wellpad area 1 and removal of an impoundment in area 2
3. The number of frac stages that could be fractured each week was kept constant at 30, instead of allowing it to be variable between 10-30 stages. This assumption is valid because without temporal variability in freshwater supply it is always more cost effective to fracture the wellpad as quickly as possible.
4. Increasing the distance to central treatment (from 35 miles to 50 miles) and the class 2 disposal wells (50 miles to 150 miles) to be more representative of the Marcellus play
5. The wastewater production was doubled. In the case study presented by Yang et al. the wastewater production was only 9.6% of the used frac fluid used, which would be low for the Marcellus play.
6. The gas production and wastewater production was allowed to start once a well was completed, instead of the production only starting after all of the wells on a wellpad were completed.

The wellpad availability dictates when hydraulic fracturing may start on a wellpad. Wellpads s1, s2, s7, and s8 were available immediately, while wellpads s3, s4, s9, s10, and s11 were available after week 18, and wellpads s5, s6, s12, s13, s14 were available after week 71, as presented in Yang et al.

The non-financial and financial parameters for the case study are shown in Table S7 and S8.

Table S7*. Non-financial parameters for the case study*

Parameter	Units	Value	Description	reference
SDW	bbl	240,000	Frac fluid use for 30 stages each week	[1]
ρ^{WW}	$unitless$	0.3	Maximum wastewater composition in frac fluid	[user defined]
η_{q1}	$unitless$	0.85	Central treatment efficiency	[11]
$CP_p^{min,IP}$	bbl	200,000	Impoundment minimum capacity	[12]
$CP_p^{max,IP}$	bbl	850,000	Impoundment maximum capacity	[12]
$CP_p^{min,WWT}$	bbl	1,000	Frac tank minimum capacity	[13]
$CP_p^{max,WWT}$	bbl	8,000	Frac tank maximum capacity	[13]
UF	$\frac{bbl}{week}$	1,000,000	upper flow for piping	[1]
Dis^o	$mile$	10	Distance from freshwater source	[14]
Dis^{CT}	$mile$	50	Distance from wellpads to central treatment facility	[15]
Dis^{DP}	$mile$	150	Distance from wellpads to disposal	[16,15]
Dis^{DP2}	$mile$	100	Distance from central treatment to disposal	[user defined]

***Table S8**. Financial parameters for the case study*

Parameter	Units	Value	Description	reference
OC_{o1}^{FW}	$\frac{\$}{bbl}$	0.2	Withdrawal cost from freshwater source	[1]
OC^{Pipe}	$\frac{\$}{bbl-mile}$	0.005	Pumping cost	[user defined]
IC_{c1}^{Pipe}	$\frac{\$}{mile}$	320,000	Buried pipeline cost	[1]
IC_{c2}^{Pipe}	$\frac{\$}{mile-week}$	5,500	Overland pipeline cost	[1]
OC^{Trk}	$\frac{\$}{bbl-mile}$	0.053	Trucking cost	[1]
$IC^{IP,Base}$	\$	800000	Impoundment base capital cost	[1]
$IC^{IP,Inc}$	$\frac{\$}{bbl}$	1.2	Impoundment incremental cost	[1]
IC^{WWT}	$\frac{\$}{bbl-week}$	0.525	Wastewater storage cost	[12]
IC^{FT}	$\frac{\$}{bbl}$	85	Frac tank cost	[1]
OC^{OT}	$\frac{\$}{bbl}$	3	Onsite treatment cost	[15]
OC_{q1}^{CT}	$\frac{\$}{bbl}$	5.5	Central treatment cost	[12,15]
OC^{DP}	$\frac{\$}{bbl}$	1.5	Disposal costs	[16]

The gas production for each wellpad after complete completion was presented in Yang et al. The data was adjusted so that the gas production could occur once wells were completed and not when the entire wellpad was completed. The gas production for each wellpad with respect to the start of hydraulic fracturing is shown in Figure S1. The gas production fluctuates as wells are being completed, but once all of the wells are completed the production steadily decreases.

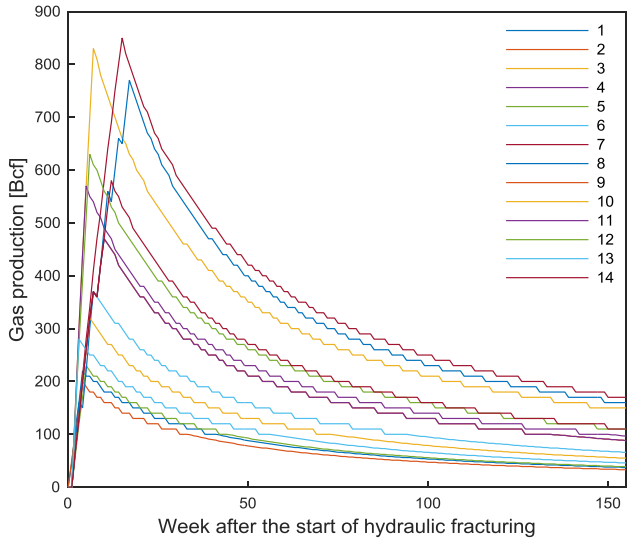

Figure S1. *Gas production for each wellpad.*

Wastewater production is similar to gas production and the original data is shown in Yang et al. The wastewater production after the adjustment to the allow production once wells are completed is shown in Figure S2. Some of the wells take more than 30 stages to fracture, so even when a wellpad is being fractured, a new well does not start producing every week. When a well does not come online in a week it has a large effect on the wastewater production because the majority of wastewater comes back in the first weeks of operation. Therefore, the wastewater production has high fluctuations from week to week.

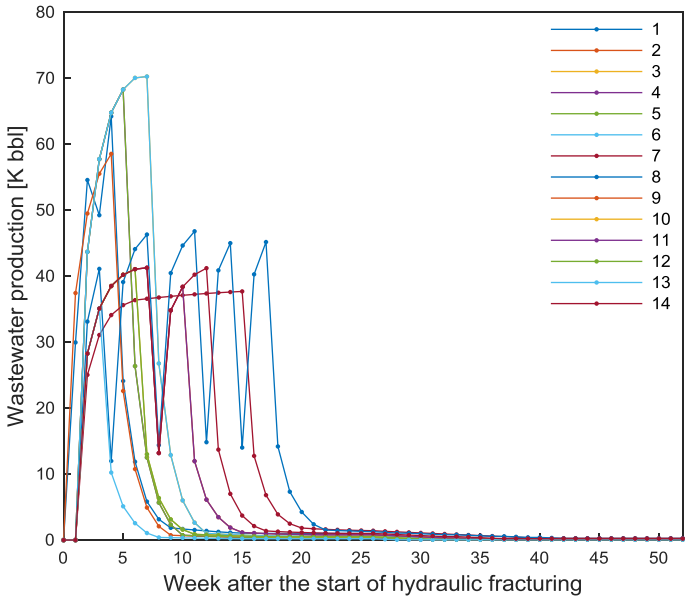

Figure S2*. Wastewater production after each wellpad starts being fractured.*

5. Additional Case Study Results

The optimal hydraulic fracturing schedule for maximizing profits (revenue minus financial water management costs) is shown in Figure S3. The wellpads are fractured as quickly as possible (only one transition week between wellpads) and the order of fracturing was 7, 1, 3, 4, 8, 9, 10, 12, 13, 14, 6, 11, 2, and 5. The resulting schedule is fixed for all other optimization runs.

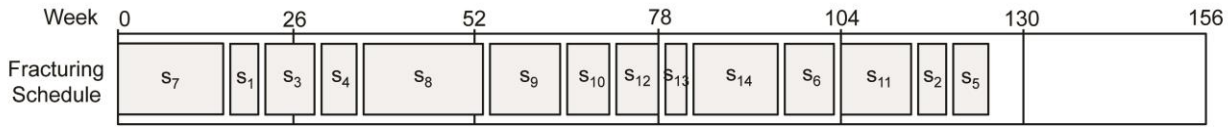

Figure S3. *Optimal hydraulic fracturing schedule over the 3 year, 156 week, time horizon.*

Financial Cost Minimization:

The freshwater piping arrangement for the cost optimal solution was presented in Figure 1C. In area 1, freshwater is supplied to the impoundment via overland pipeline rented in the second and eighth quarter (weeks 14 to 26 and 92 to 104). A buried pipeline carries freshwater from the source to the impoundment in Area 2, reflecting the high freshwater demand for the frac stages in this area (Figure S1). Overland pipelines rented in the first, fourth, fifth, and seventh quarter (weeks 1 to 13, 40 to 65, and 79 to 91) deliver water from impoundment 2 to wellpads 7, 8, 9, 12, 13, and 14. On a bbl-mile basis, 77% of the freshwater was transported via pipeline and 23% was transported via truck.

The financial cost optimal wastewater management solution maximized wastewater reuse, sending wastewater to central treatment only after all the wellpads were fractured. A total of 94% of the wastewater produced over the 3-year time horizon was reused in subsequent frac operations. This translates to an average frac fluid composition of 18% wastewater. In the financial cost optimal water management solution all of the wastewater was trucked because the high capital costs of wastewater pipelines could not be recovered by the relatively low volume of transported wastewater.

The financial cost optimal water management case for the fourteen wellpad case study provides total revenues of $1.2 billion, water and wastewater management costs of $36.4 million, and HHE costs of $10.9 million (Table S9). The financial costs and HHE costs were 3.1% and 0.9% of the revenue for the financial cost optimal water management scenario, which is substantially below the industry average. These reduced costs are likely to reflect the clustered location of the

wells, the high reuse percentage of the flowback and produced water, and the existence of a central treatment facility within 50 miles of the well clusters.

Water Management Scenarios:

As discussed in the report, the financial costs of water and wastewater management ranged from $36.4 to 65.1 million and the HHE costs ranged from $10.9 to 27.2 million (Table S9).

The scenarios can be described in three groups: low, moderate, and high financial and HHE costs. The low financial and HHE cost group included the optimal solution and scenarios 1, 5, 6, and 7: no wastewater piping (same as optimal), no freshwater trucking, no central treatment, and no direct disposal (same as optimal). Of these scenarios the cost optimal solution had the lowest cost and scenario 5, no freshwater trucking, had the lowest environmental costs. This finding demonstrates that further investment in freshwater pipelines in order to reduce trucking emissions may result in lower environmental costs. The financial and HHE cost tradeoff between the two strategies is a financial cost increase of $2.1 million and a HHE cost decrease of $0.7 million.

The moderate financial and HHE cost group included scenarios 2, 3, and 4: no wastewater trucking between wellpads, no wastewater storage, and no freshwater piping. No wastewater trucking between wellpads led to additional pipeline water transport, which increased the financial and HHE costs. This resulted in a reduction in the percentage of wastewater reuse to 81% from 94% in the cost-optimal scenario, and ultimately to additional costs and HHE damages associated with freshwater transport, wastewater transport, and wastewater disposal at central

treatment facilities and Class II injection wells. No wastewater storage decreased the amount of wastewater that was reused to 76%, similarly increasing the freshwater demand and transport of both fresh and wastewater. No freshwater piping increased transport via truck and led to additional financial costs and HHE damages.

The highest financial and HHE cost scenario was that of no wastewater reuse. When wastewater could not be reused, freshwater demand increased and all of the wastewater was transported to central treatment and disposal. This result emphasizes the importance of maximizing wastewater reuse to lower financial and HHE costs.

Further cost details of the scenarios are presented in Table S9.

Table S9. *The revenue, costs, and environmental costs for the financial cost optimal water management solution and the scenarios: SC 1) No WW piping (same as Opt), SC 2) No WW trucking, SC 3) No WW storage, SC 4) No FW piping, SC 5) No FW trucking, SC 6) No central treatment, SC 7) No direct disposal (same as Opt), and SC 8) No wastewater reuse.*

Category	Optimal	SC1	SC2	SC3	SC4	SC5	SC6	SC7	SC8
Revenue	1,181	1,181	1,181	1,181	1,181	1,181	1,181	1,181	1,181
FW withdrawal cost	4.2	4.2	4.3	4.4	4.2	4.2	4.2	4.2	5.1
Storage cost	4.3	4.3	4.7	3.4	4.3	4.3	4.3	4.3	3.4
On-site treatment cost	13.9	13.9	11.9	11.3	13.9	13.8	13.9	13.9	0.0
Central treatment cost	1.6	1.6	5.2	6.3	1.6	1.6	0.0	1.6	27.0
Disposal cost	0.06	0.06	0.21	0.26	0.06	0.07	0.43	0.06	1.10
Piping cost	6.9	6.9	10.1	6.9	0.0	12.5	6.9	6.9	7.5
Trucking cost	5.5	5.5	5.6	8.1	17.1	2.0	6.8	5.5	21.0
Total cost	36.4	36.4	42.1	40.6	41.1	38.5	36.5	36.4	65.1
Environmental cost	10.9	10.9	12.7	13.5	17.0	10.2	11.4	10.9	27.2

Human Health and Environmental Cost Minimization:

Further details on the water management difference between the financial cost minimization, HHE cost minimization, and the combined financial and HHE cost minimization are shown in the following Figures S4-S7.

The amount of transport for each mode is shown in Figure S4. Compared to the financial cost optimal solution, the combined cost optimal solution and HHE cost optimal solution had: an

8.3% and 29.9% increase in piping transport, a 16.0% and 53.4% decrease in trucking transport, a 29.1% and 90.9% decrease in freshwater trucking, a 0.6% and 9.5% decrease in wastewater trucking, respectively.

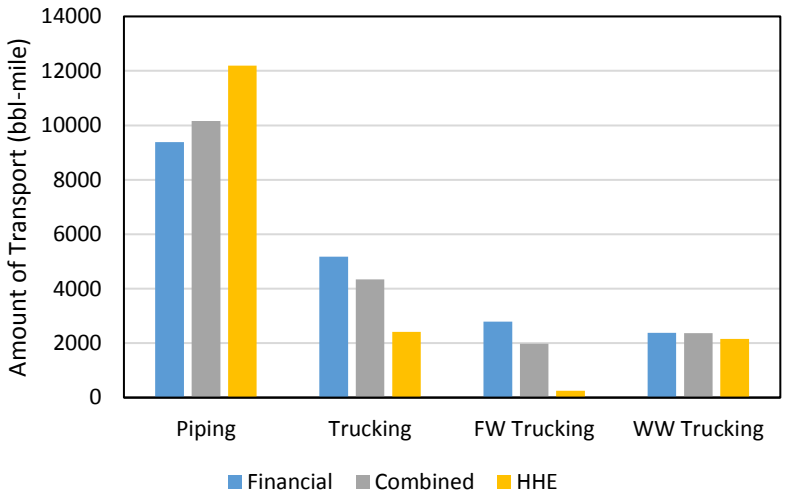

Figure S4. *The amount in bbl-mile for each mode of transport for the financial cost minimization, HHE cost minimization, and combined financial and HHE costs (combined) minimization. FW and WW stand for freshwater and wastewater respectively.*

The breakdown of freshwater volume transport is shown in Figure S5. Compared to the financial cost optimal solution, the combined and HHE cost optimal solution had: an 0.0% and 0.2% decrease in total freshwater use, 6.7% and 12.6% increase in volume of water piped to impoundment, 54% and 171% increase in volume of water piped from impoundments to wellpads, 53% and 100% decrease in volume of water trucked to impoundments, and a 22% and 84% decrease in volume of water trucked from impoundments to wellpads, respectively.

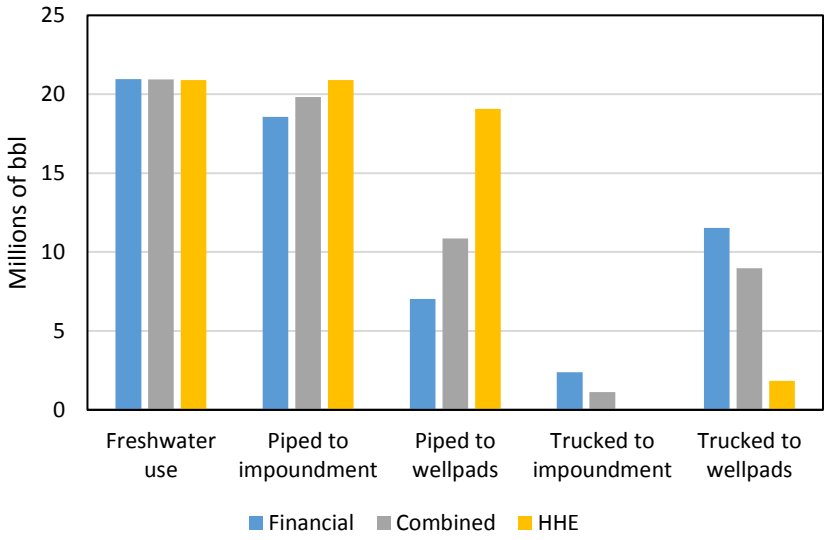

Figure S5. *The amount of freshwater transported for the financial cost minimization, HHE cost minimization, and combined financial and HHE costs (combined) minimization. All of the acquired freshwater is either piped or trucked to the impoundments and then from the impoundments to the wellpads.*

The production, reuse, and amount of wastewater handling is shown in Figure S6 and S8. Compared to the financial cost optimal solution, the combined and HHE cost optimal solution had: the same wastewater production, 0.0% and 1.1% increase in wastewater reuse and on-site treatment, 1.0% and 17.4% decrease in central treatment and disposal, respectively.

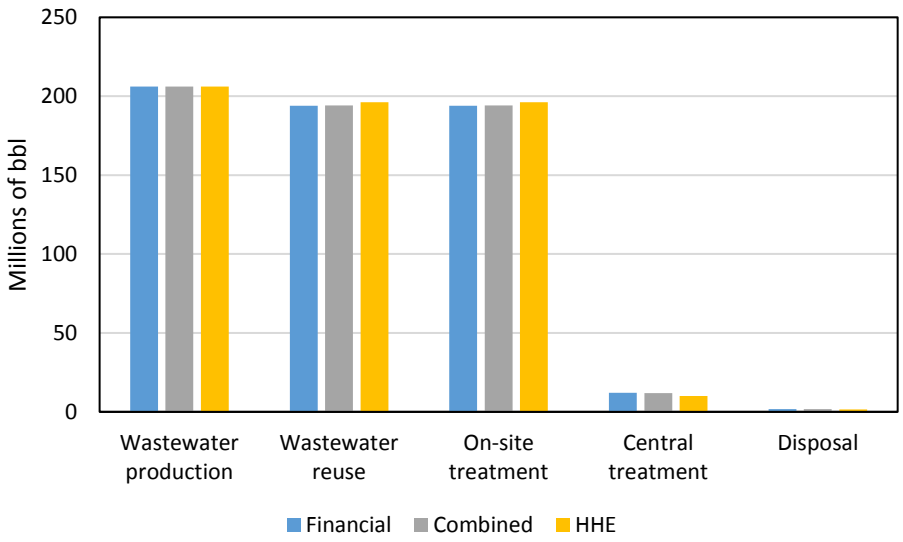

Figure S6. *The production, reuse, and amount of wastewater handling for the financial cost minimization, HHE cost minimization, and combined financial and HHE costs (combined) minimization.*

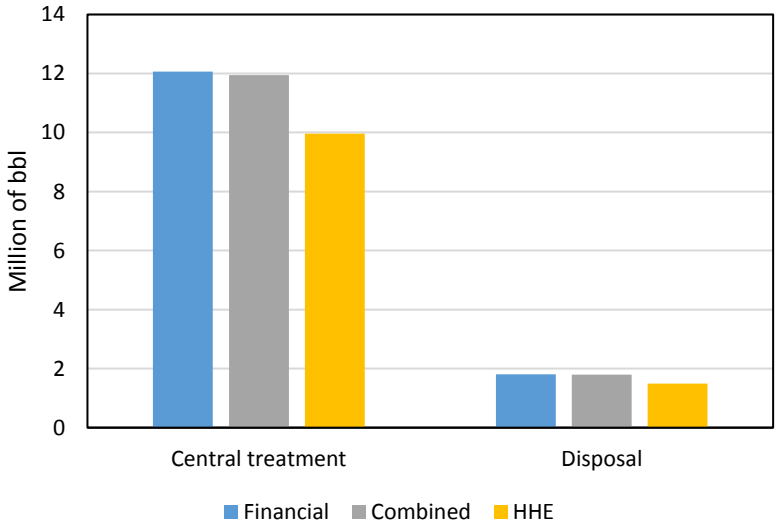

Figure S7. *The amount of central treatment and disposal for the financial cost minimization, HHE cost minimization, and combined financial and HHE costs (combined) minimization.*

6. References

(1) Yang, L.; Grossmann, I. E.; Mauter, M. S.; Dilmore, R. M. Investment optimization model for freshwater acquisition and wastewater handling in shale gas production. *Aiche J* **2015,** *61* (6), 1770.

(2) Jiang, M.; Hendrickson, C. T.; VanBriesen, J. M. Life cycle water consumption and wastewater generation impacts of a Marcellus shale gas well. *Environ Sci Technol* **2014,** *48* (3), 1911.

(3) Behrer, A.; Mauter, M. S. Allocating Damage Compensation in a Federalist System: Lessons from Spatially Resolved Air Emissions in the Marcellus. *In review* **2015**.

(4) Carnegie Mellon University Green Design Institute, Economic Input-Output Life Cycle Assessment (EIO-LCA) **2008**. http://www.eiolca.net/ (Accessed Aug 1, 2015)

(5) Myhre, G. et al. Anthropogenic and Natural Radiative Forcing. In: *Climate Change: The Physical Science Basis. Contribution of Working Group I to the Fifth Assessment Report of the Intergovernmental Panel on Climate Change*. (eds Stocker, T.F., *et al.*) Cambridge University Press, Cambridge, United Kingdom and New York, NY, USA. Ch. 8, 659-720 **2013**.
http://www.climatechange2013.org/images/report/WG1AR5_Chapter08_FINAL.pdf (Accessed Jan 10, 2016)

(6) Al-Karaghouli, A.; Kazmerski, L. L. Energy consumption and water production cost of conventional and renewable-energy-powered desalination processes. *Renewable and Sustainable Energy Reviews* **2013,** *24*, 343.

(7) U.S. Energy Information Administration, Net Generation by State by Type of Producer by Energy Source **2015**. https://www.eia.gov/electricity/data/state/ (Accessed Jan 7, 2016)

(8) U.S. Environmental Protection Agency, The 2011 National Emissions Inventory **2015**. http://www3.epa.gov/ttnchie1/net/2011inventory.html (Accessed Jan 7, 2016)

(9) U.S. Environmental Protection Agency. eGRID2012 Summary Tables **2015**. http://www.epa.gov/energy/egrid-2012-summary-tables. (Accessed Jan 7, 2016)

(10) Muller, N. Z.; Mendelsohn, R.; Nordhaus, W. Environmental Accounting for Pollution in the United States Economy. *American Economic Review* **2011,** *101* (5), 1649.

(11) Aqua-Pure Ventures Inc, Water Treatment Catolg and Decision Tool: Vendor Profile. http://www.all-llc.com/publicdownloads/FountainQuailProfile.pdf (Accessed Jan 15, 2016)

(12) Tipton, D. S., Water Management for Oil and Gas Operations. Oklahoma Water Survey Technical Workshop **2012**. http://oklahomawatersurvey.org/d1/wp-content/uploads/2012/10/06-NewfieldExploration.pdf (Accessed Jan 8, 2016)

(13) Allen, D. T.; Torres, V. M.; Thomas, J.; Sullivan, D. W.; Harrison, M.; Hendler, A.; Herndon, S. C.; Kolb, C. E.; Fraser, M. P.; Hill, A. D.et al. Measurements of methane emissions at natural gas production sites in the United States. *Proc Natl Acad Sci U S A* **2013,** *110* (44), 17768.

(14) Jiang, M; Griffin, W. M.; Hendrickson, C.; Jaramillo, P.; VanBriesen, J.; Venkatesh, A. Life cycle greenhouse gas emissions of Marcellus shale gas. *Environmental Research Letters* **2011,** *6* (3), 034014.

(15) Mauter, M. S.; Palmer, V. R. Expert Elicitation of Trends in Marcellus Oil and Gas Wastewater Management. *J Environ Eng* **2014,** *140* (5).

(16) Mauter, M. S.; Palmer, V. R.; Tang, Y.; Behrer, A. P. The Next Frontier in United States Shale Gas and Tight Oil Extraction: Strategic Reduction of Environmental Impacts. Belfer Center, Harvard Kennedy School **2013**.

APPENDIX F: SUPPORTING INFORMATION FOR CHAPTER 7 - ENERGY AND CO_2 EMISSIONS PENALTIES OF GEOLOGIC CARBON STORAGE BRINE MANAGEMENT

Supporting Information Summary:
The supporting information contains descriptions of 1) data and summary statistics for U.S. saline reservoirs, 2) energy consumption for pumping.

This supporting information is 8 pages long and contains 4 tables (Tables S1-S4).

S1) Data and summary statistics for U.S. saline reservoirs

As described in the main manuscript, we identify the U.S. saline reservoirs suitable for geologic carbon storage and their location, storage capacity, and depth using the National Carbon Sequestration Database and Geographical Information System database v1502 (NATCARB database).[1] We supplement the NATCARB database with empirical brine salinity distributions that we develop from brine samples in the U.S. Geological Survey national produced waters geochemical database v2.2 (USGS database).[2] In this section, we provide the cleaned data and present the summary statistics.

NATCARB database

The NATCARB database includes geospatial information on carbon storage potential of saline reservoirs across the U.S. and parts of Canada. The data is generated by Regional Carbon Sequestration Partnerships and the database is managed by the U.S. Department of Energy (DOE) with the purpose of aiding initial assessments of geologic carbon storage.

For our analysis, we modify the database in three ways. First, we geographically limit our analysis to data within the 48 contiguous states (excludes Canadian and offshore regions). By limiting the geographic area, we reduce the medium estimate of the total potential CO2 storage capacity from 8.4 to 5.6 trillion metric tonnes (33% decrease). Second, we collapse multiple labels for a single reservoir to a single label. For example, we relabel "Mt. Simon Sandstone" and "Basal Sands – Mt. Simon" to "Mt. Simon". Third, we do not consider the reservoirs that were labeled "Unnamed". In Table S.1, we present the 178 saline reservoirs identified from the NATCARB database.

Table S.1. *Saline reservoirs considered from the NATCARB database.*


Table S1.xlsx

USGS database

The USGS database includes roughly 170K brine samples across the U.S. The database was created from the combination of multiple datasets spanning several decades. The collection, analysis, and record keeping methods for these datasets were not standardized and they cannot be independently verified. Additionally, the sampling was not planned to accurately represent any specific region or reservoir. Despite these limitations, we choose to use the USGS database because it is the best available dataset that contains many brine samples for most U.S. saline reservoirs.

In order to develop empirical brine salinity distributions for the U.S. saline reservoirs, we pair GCS relevant USGS samples to the U.S. saline reservoirs identified in Table S.1. As described in the main manuscript, we limit our analysis to brine samples below 2500 feet to ensure there is sufficient pressure for supercritical CO_2 storage.[3] If the sample depth was not recorded, we use the average of the reported upper and lower perforation depth. By limiting the analysis to depths below 2500 feet, we reduce the number of brine samples by nearly 50%. We match the remaining brine samples to U.S. saline reservoirs by the name of the formation. Since the USGS formation names were not standardized there are many spelling variations that we manually identified as being the same. Oftentimes, multiple saline reservoir names appeared in a USGS formation label and we assigned that sample to both saline reservoirs. Through this matching process, roughly 35K brine samples were paired with saline reservoirs. Table S.2.

includes the paired saline reservoir name, USGS ID, formation and basin name, depth, and total dissolved solids and NaCl concentration for the matched USGS samples. Table S.3. provides the summarized data for each U.S. saline reservoir identified in Table S.1., including: CO_2 storage capacity, median depth, number of brine samples, 10th, 50th, and 90th percentile of TDS, and NaCl mass percentage of TDS.

Table S.2. *USGS brine sample data paired with U.S. saline reservoirs*


Table S2.xls

Table S.3. *Summarized data for each U.S. saline reservoir*


Table S3.xlsx

S2) Energy consumption for pumping

We base the energy demand of extraction, transport, and injection on the energy consumption of the pump. We estimate the pump energy consumption with equation S1.

$$EC_{pmp} = \frac{\rho g(\Delta H + H_L)}{\eta_1 \eta_2} \left[\frac{J\ s^2}{kg\ m^2}\right] \left[\frac{kWh}{3.6E6\ J}\right] \quad (S1)$$

Where EC_{pmp} is the pump energy consumption [kWh/m^3], ρ is density [kg/m^3], g is gravity [9.8 m/s^2], ΔH is head difference [m], H_L is the head loss [m], and η_1 and η_2 are the pump and motor efficiency. The head difference is determined with equation S2.

$$\Delta H = \frac{P_2 - P_1}{\rho g} + (h_2 - h_1) + \frac{v_2^2 - v_1^2}{2g} \quad (S2)$$

Where P is the hydraulic pressure [Pa], h is the height from some reference [m], v is the fluid velocity [m/s], and the fluid is pumped from subscript 1 to 2. In the applications we are considering, the kinetic head difference (last term with velocity) is negligible.

Extraction and injection

To estimate the pump energy consumption for brine extraction and injection with equation S1, we must determine the head loss and head difference. As stated in the manuscript, we assume the head loss for extraction and injection is 100 m.[4]

The head difference for brine extraction and injection will be dependent on the pressure and depth of the saline reservoir. While reservoir pressure and depth data can be obtained from the NATCARB database, we found that the vast majority (>90%) of the data points have no or negligible head difference between the surface and the reservoir. This result suggests that either saline reservoirs generally have neutral pressure (as opposed to over or underpressure) or that the pressure data is generated with a neutral pressure assumption. Instead of relying on the pressure and depth data in the NATCARB database, we use wellhead pressure data from wastewater disposal wells in the oil & gas industry to estimate the extent of overpressure for injection wells. The wellhead pressure of these injection wells ranged between 0-2.8 MPa for reservoirs in Oklahoma, which is equivalent to 0-285 m of head difference.[5] Without similar experience for deep brine extraction wells, we assume the reservoirs have neutral pressure and the head difference is negligible. When these head differences are combined with the assumed head loss, we estimate that the energy consumption of extraction is 0.4 kWh/m^3 and injection is between 0.4 and 1.5 kWh/m^3.

Transportation

The energy consumption of transporting the brine and product water can be determined by estimating the head difference and head loss. In our work, we assume there is no elevation change between the starting and final location, so the head difference is negligible. We estimate the transportation head loss per unit length of pipe with the Hazen-Williams equation shown in equation S3.

$$\frac{H_L}{L} = \frac{10.67\ Q^{1.852}}{C^{1.852}\ d^{4.8704}} \qquad (S3)$$

Where H_L is the head loss [m], L is the length of the pipe [m], Q is the flow rate [m3/s], C is the roughness coefficient, and d is the inside pipe diameter [m].

We use a range of realistic operating conditions to develop a range of head loss per unit length. These conditions include: cross sectional fluid velocities between 3 and 6 feet/s (0.9-1.8 m/s), pipe diameters between 6 and 12 inches (0.15-0.3 m), and a roughness coefficient of 120. The resulting head loss per unit length varies between 3 and 26 m/1000m. As suggested in Trautz et al., we roughly double this value to 5 and 50 m/1000m to account for bends, valves, and other features of pipelines.[4]

In order to estimate the total head loss across a pipeline, we need to estimate the pipeline length. However, there is great uncertainty in realistic transportation distances because there are no existing GCS brine management systems. Table S.7 provides the transportation distances assumed in this study and others. Using these distances and the head loss per unit length, we estimate that the energy consumption for extraction to treatment, concentrate to disposal, treated water to use range from 0-2.2, 0-11, 0.2-11 kWh/m^3-mile.

Table S7. *Distances for the three transportation activities in GCS brine management. NA means not they did not consider it.*

Transport activity	This work	Harto [6]	Trautz et al. [4]	Salih et al. [7]
Extraction to treatment	0-10	10	NA	NA
Concentrate to disposal	0-50	10-100	NA	1
Treated water to use	10-50	NA	15	NA

References

1. NETL, National Carbon Sequestration Database and Geographic Information System (NATCARB). v1502 ed.; Energy, U. S. D. o., Ed. 2015.

2. Blondes, M.; Gans, K.; Engle, M.; Kharaka, Y.; Reidy, M.; Saraswathula, V.; Thordsen, J.; Rowan, E.; Morrissey, E., U.S. Geological Survey National Produced Waters Geochemical Database v2.2. 2016.

3. Harto, C. B.; Veil, J. A. *Management of Water Extracted from Carbon Sequestration Projects*; Argonne National Laboratory: Chicago, Illinois, 2011.

4. Trautz, R. *Phase II Field Demonstration at Plant Smith Generating Station: Assessment of Opportunities for Optimal Reservoir Pressure Control, Plume Management and Produced Water Strategies.*; DE-FE0026140; Electric Power Research Institute: Palo Alto, CA, 2016.

5. Murray, K. *Class II Underground Injection Control Well Data for 2010-2013 by Geologic Zones of Completion, Oklahoma*; OF1-2014; Oklahoma Geological Survey: Norman, OK, 2014.

6. Harto, C. B. *Quantitative Assessment of Options for Managing Brines Extracted from Deep Saline Aquifers Used for Carbon Storage*; Argonne National Laboratory: 2014.

7. Salih, H. H.; Li, J.; Kaplan, R.; Dastgheib, S. A., Life cycle assessment of treatment and handling options for a highly saline brine extracted from a potential CO2 storage site. *Water Research* **2017,** *122* (Supplement C), 419-430.